nuclear technology®

CONTENTS / JUNE 1984–VOL. 65, NO. 3

TECHNICAL PAPERS

FISSION REACTORS

NUCLEAR SAFETY

RADIOACTIVE WASTE MANAGEMENT

MATERIALS

(Continued)

ON THIS COVER

This month's cover is taken from a figure in the paper by S-C. Yao et al. and shows noncoplanar, concentric sleeve blockage distribution and rod instrumentation.

CONTENTS / JUNE 1984–VOL. 65, NO. 3

(Continued)

HEAT TRANSFER AND FLUID FLOW

TECHNICAL NOTE

FISSION REACTORS

DEPARTMENTS

ENS European Nuclear Society nuclear technology®

AUTHORS — JUNE 1984

FISSION REACTORS

CORE STABILITY TEST ANALYSIS USING THE AUTO-REGRESSIVE MODEL

Tohru Mitsutake
Shigeaki Tsunoyama
Shigeru Kanemoto
Hideaki Namba
Shirley A. Sandoz

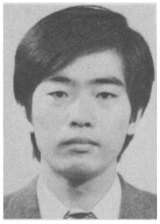
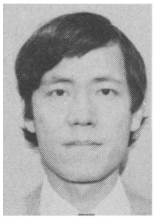
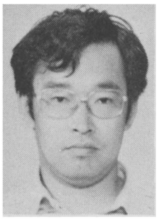
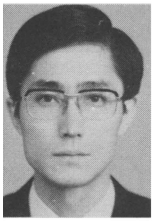


Tohru Mitsutake (top right) (BS, physics, 1976, and MS, nuclear engineering, 1979, Kyoto University) has been a staff engineer in the system analysis department at Nippon Atomic Industry Group Company, Ltd. since 1979, where he is involved in developing a parameter estimation method related to reactor dynamics. **Shigeaki Tsunoyama** (top left) (BS, physics, Tokyo University, 1967) is a senior researcher at Nippon Atomic Industry Group Company, Ltd. and has been engaged in the development of the physical model in the area of boiling water reactor (BWR) dynamics and safety. **Shigeru Kanemoto** (center right) (BS, 1974, and MS, 1976, nuclear engineering, Osaka University) joined Nippon Atomic Industry Group Company, Ltd. in 1976 and has been involved in the system identification research of BWRs with noise analysis. **Hideaki Namba** (bottom left) (BS, 1968, and MS, 1970, electrical engineering, Waseda University) is a deputy manager in the Reactor Control and Dynamics Section of Toshiba Corporation and is currently interested in the stability and abnormal operating transients of BWRs. **Shirley A. Sandoz** (bottom right) (PhD, mechanical engineering, Stanford University, 1973) has been employed by the Nuclear Energy Business Operation of the General Electric Company since 1971 in various areas involving fluids, heat transfer, and system dynamics technologies. She is currently manager of the system design methods group, responsible for BWR stability models and reactor tests.

REACTOR CORE STABILITY ANALYSIS FOR A BOILING WATER REACTOR BY A TRANSIENT MODEL

Shigeaki Tsunoyama
Tohru Mitsutake
Shigeo Ebata
Shirley A. Sandoz

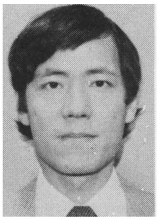
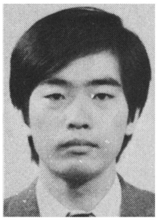
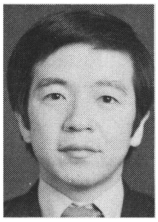


Shigeaki Tsunoyama (top right) (BS, physics, Tokyo University, 1967) is a senior researcher at Nippon Atomic Industry Group Company, Ltd. and has been engaged in the development of the physical model in the area of boiling water reactor (BWR) dynamics and safety. **Tohru Mitsutake** (top left) (BS, physics, 1976, and MS, nuclear engineering, 1979, Kyoto University) has been a staff engineer in the system analysis department at Nippon Atomic Industry Group Company, Ltd. since 1979, where he is involved in developing a parameter estimation method related to reactor dynamics. **Shigeo Ebata** (bottom right) (BS, 1973, and MS, 1975, electrical engineering, Nagoya University) is an engineer in the Reactor Control and Dynamics Section of Toshiba Corporation and works on the transient analysis and system design of BWRs. **Shirley A. Sandoz** (bottom left) (PhD, mechanical engineering, Stanford University, 1973) has been employed by the Nuclear Energy Business Operation of General Electric Company since 1971 in various areas involving fluids, heat transfer, and system dynamics technologies. She is currently manager of the system design methods group, responsible for BWR stability models and reactor tests.

AUTOMATED CONTROL ROD PROGRAMMING IN BOILNG WATER REACTOR CORES

Wan-Li Zhong
J. Weisman

Wan-Li Zhong (photo not available) [engineering physics, Qinghua University in Beijing (Peking), China, 1962] worked in the area of nuclear computations at the Reactor Engineering and Design Institute, Beijing, China. From September 1981 to September 1983 he was a visiting scholar in the Department of Chemical and Nuclear Engineering at the University of Cincinnati (UC). He has now returned to the Reactor Engineering and Design Institute. **J. Weisman** (right) (PhD, University of Pittsburgh) is a professor of nuclear engineering and director of the Nuclear Engineering Program at the UC. Prior to joining UC in 1968, Weisman spent 18 years in industry where his last position was manager of thermal-hydraulic analysis for the Westinghouse Electric Corporation, Pressurized Water Reactor Division.

NUCLEAR SAFETY

DEVELOPMENT OF A SODIUM VAPOR PRESSURE METER USING BETA-ALUMINA CERAMICS

Susumu Ninomiya
Fumio Ohtsuka
Hiromichi Nei
Osamu Takikawa
Mituo Harata

Susumu Ninomiya (top right) (MS, mechanical engineering, Osaka University, 1974) is a deputy manager in the Nuclear Engineering Laboratory at Toshiba Corporation. He has been engaged in studies on cold trap, vapor trap, and sodium cleaning. His current research interests include the study of sodium removal from narrow gap as crevice. **Fumio Ohtsuka** (top left) is a research engineer in the Nuclear Engineering Laboratory at Toshiba Corporation. His work has been the analysis of sodium vapor behavior in the fast breeder reactor cover gas system. **Hiromichi Nei** (center right) (BS, mechanical engineering, Hokkaido University, 1961; PhD, Tokyo Institute of Technology, 1978) is a manager in the Nuclear Engineering Laboratory, Toshiba Corporation. He has many years of experience with sodium technology, including experiments on sodium/water reaction and the development of sodium components. **Osamu Takikawa** (bottom left) (BS, physical chemistry, Nagoya University, 1973) is a researcher in the Research and Development Center at Toshiba Corporation. His current research interests include gas sensors, such as electrochemical sensors and semiconductor gas sensors. **Mituo Harata** (bottom right) (MS, crystal chemistry, Nagoya University, 1968) is a senior researcher in the Research and Development Center at Toshiba Corporation. He worked on the development of the beta-alumina solid electrolyte. His current research interests include the fabrication process of electronic ceramics.

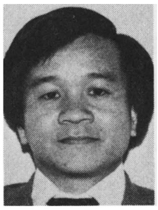
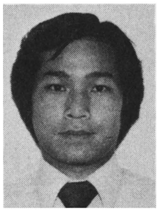
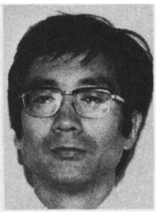
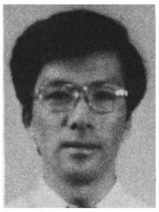
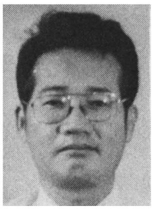

ELECTRICALLY ENHANCED DEPOSITION OF A CONFINED AEROSOL IN THE PRESENCE OF IONIZING RADIATION

Robert A. Fjeld
Thomas J. Overcamp

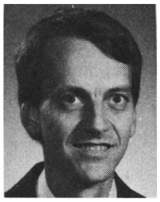

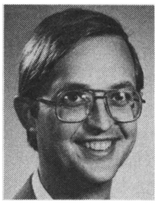

Robert A. Fjeld (top) (BS, nuclear engineering, North Carolina State University, 1970; MS, 1973, and PhD, 1976, nuclear engineering, The Pennsylvania State University) is an associate professor in the Department of Environmental Systems Engineering, Clemson University (CU). His primary technical interests are environmental aspects of nuclear technologies, aerosol physics, and radiation applications in environmental engineering. **Thomas J. Overcamp** (BS, mechanical engineering, Michigan State University, 1964; SM, 1970, and PhD, 1983, mechanical engineering, Massachusetts Institute of Technology) is an associate professor in the Department of Environmental Systems Engineering, CU. His interests include aerosol technology and air pollution control.

ANALYSIS OF COOLANT PRESSURE FLUCTUATION AND INDUCED VIBRATION OF LIQUID-METAL FAST BREEDER REACTOR FUEL PINS

Ken Amano
Kotaro Inoue

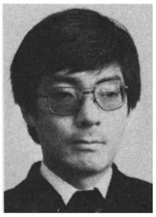

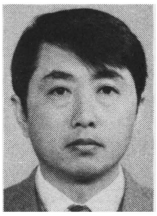

Ken Amano (top) (BE, electrical engineering, Yokohama National University, 1979; MS, plasma physics, Tokyo Institute of Technology, 1981) has been engaged in research on statistical mechanics of liquid metal in the fast breeder reactor (FBR) core system unit at the Energy Research Laboratory (ERL), Hitachi Ltd., Japan. **Kotaro Inoue** (BE, mechanical engineering, University of Tokyo, 1964; PhD, nuclear engineering, 1976) has engaged in reactor physics, safety analysis, systems design, solar energy development, and fusion systems research. He is presently a manager in the FBR core systems unit at the ERL, Hitachi Ltd., Japan.

DOMINANT FACTORS IN THE RELEASE OF FISSION PRODUCTS FROM OVERHEATED URANIA

C. D. Andriesse
R. H. J. Tanke

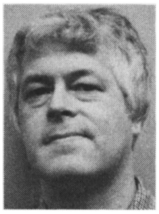

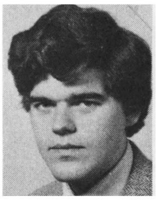

C. D. Andriesse (top) (PhD, Delft University of Technology, 1969) has worked as a research physicist in the KEMA Laboratories since 1980. He has published papers in the fields of neutron scattering, engineering of quantum solids, solid state astrophysics, and general astrophysics. His present work is on the behavior of fission products for the analysis of nuclear safety. **R. H. J. Tanke** (physics graduate, University of Utrecht, 1982) is performing his PhD thesis work in the KEMA Laboratories. His work concerns high-temperature mass spectrometry of irradiated UO_2 samples. He has studied problems in reactor physics at the Dodewaard Nuclear Power Station and at the Karlsruhe Nuclear Research Center.

RADIOACTIVE WASTE MANAGEMENT

LEACH TESTING OF IDAHO NATIONAL ENGINEERING LABORATORY WASTE FORMS IN A GAMMA FIELD

Robert P. Schuman

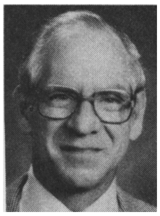

Robert P. Schuman (PhD, Ohio State University, 1946) works for EG&G Idaho, Inc., on the ultimate disposal of high-level defense and transuranium wastes. He worked for the Knolls Atomic Power Laboratory from 1947 to 1957 and at the National Reactor Testing Station from 1957 to 1969. He taught at Robert College, Boğaziçi Üniversitesi, Istanbul, from 1969 to

1977 and spent 1977-1978 as a visiting professor at Iowa State University. Among his interests are the chemical aspects of the nuclear fuel cycle, including waste management and actinide and fission product properties.

THE LEACHING BEHAVIOR OF ZIRCALOY CLADDING AND ITS IMPACT ON THE CONDITIONING OF WASTE FOR FINAL DISPOSAL

Berthold-Günter Brodda
Erich Richard Merz

Berthold-Günter Brodda (photo not available) [Dr.-Ing., chemistry, Technical University of Berlin, Federal Republic of Germany (FRG), 1968] is a section leader at the Institute for Chemical Technology of Kernforschungsanlage (KFA) Jülich. He is currently working on hot analytical chemistry and on the characterization and disposal of special nuclear waste types. **Erich Richard Merz** (photo not available) (Dr. rer. nat, nuclear chemistry, University of Mainz, FRG, 1957; professor of Nuclear Technology Rheinisch Westfälische Technische Hochschule Aachen, 1970) has been director of the Institute for Chemical Technology of KFA since 1968. He is a member of the German Reactor Safety Commission. His work has been in the area of the backend of the nuclear fuel cycle including radioactive waste disposal.

MATERIALS

RADIOACTIVE CONTAMINATION OF CARBON STEEL IN A BOILING WATER REACTOR

Takashi Honda
Akira Minato
Katsumi Ohsumi
Hideo Matsubayashi

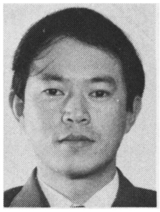

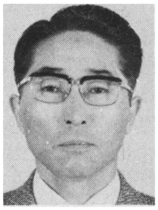

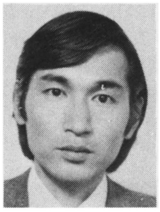

Takashi Honda (top right) (BS, electrochemical engineering, Yokohama National University, 1973) is a researcher at Hitachi Research Laboratory (HRL), Hitachi, Ltd. Since 1973 his general field of interest has been the corrosion of metals. His recent interests include the water chemistry of nuclear power plants. **Akira Minato** (top left) (BS, metallurgical engineering, Ibaraki University, 1953) is a senior researcher at HRL. Since 1970 he has been engaged in research on stress corrosion cracking of stainless steel and water chemistry of nuclear power systems. His current interests include the decontamination of nuclear plants. **Katsumi Ohsumi** (bottom right) (BS, nuclear engineering, Ohsaka University, 1970) is employed in the nuclear power plant engineering department, Hitachi, Ltd. His current technical interests include the water chemistry and radiation buildup control of nuclear power plants. **Hideo Matsubayashi** (bottom left) (BS, electrical engineering, Hiroshima University, 1957) is an assistant superintendent at Shimane Nuclear Power Plant, The Chugoku Electric Power Company, Inc. His current interests include the water chemistry and safety of nuclear power systems.

HEAT TRANSFER AND FLUID FLOW

HYDRAULICS OF BLOCKED ROD BUNDLES

Shi-chune Yao
M. J. Loftus
L. E. Hochreiter

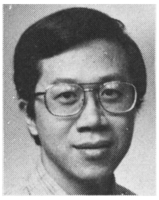

Shi-chune Yao (right) (BS, Tsing Hua University, Taiwan, 1968; MS and PhD, nuclear engineering, University of California, Berkeley, 1974) is a professor in the Department of Mechanical Engineering, Carnegie-Mellon University. His research interests are in the area of boiling heat transfer, two-phase flow, reactor safety analysis, and spray combustion. He has also been a consultant at Westinghouse Electric Corporation for many years. **M. J. Loftus** (top) (BSME, MSME, 1978, PE) has worked in thermal-hydraulic testing and analysis of pressurized water reactor safety related experiments for approximately 11 years at Westinghouse. **L. E. Hochreiter** (bottom) (BSME, University of Buffalo; MS and PhD, nuclear engineering, Purdue University, 1971) joined Westinghouse in 1971 and has been working in the light water reactor thermal-hydraulics areas, particularly as applied to reactor safety. He is also a lecturer at Carnegie-Mellon University.

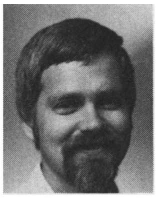

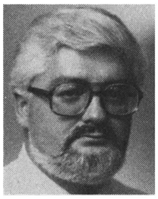

AN IMPROVED MULTIDIMENSIONAL FINITE DIFFERENCE SCHEME FOR PREDICTING STRATIFIED HORIZONTAL PIPE FLOW

Yassin A. Hassan
James G. Rice
Jong H. Kim

Yassin A. Hassan (top) (BSC, nuclear engineering, University of Alexandria, 1968; MSC, 1975, and PhD, 1979, nuclear engineering, University of Illinois) is a senior engineer at the Utility Power Generation Division, Babcock & Wilcox Company, Lynchburg, Virginia. He is responsible for developing, modifying, and maintaining various thermal-hydraulic computer codes, and is currently involved in the development and application of three-dimensional codes, especially those relevant to the thermal shock problem. **James G. Rice** (center) (BS, Old Dominion University, 1972; MS, 1974, and PhD, 1978, Virginia Polytechnic Institute and State University) is an assistant professor in the Department of Mechanical and Aerospace Engineering at the University of Virginia (UV). His research activities at UV are in the area of computational methods for problems in heat transfer and fluid flow. His computational work includes both finite element and finite difference methods for a variety of applications, ranging from thermal-hydraulic problems to turbomachinery fluid flow analysis. Prior to joining the faculty at UV, he was the supervisor of an industrial research group. This group was responsible for the development of computational methods for application to problems in the nuclear and fossil power industries. **Jong H. Kim** (bottom) (PhD, mechanical engineering, California Institute of Technology, 1971) is a project manager in the Nuclear Power Division of the Electric Power Research Institute. His interests include computational methods, testing and analysis in fluid flow, and heat transfer.

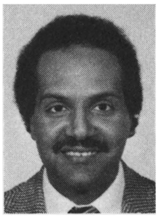

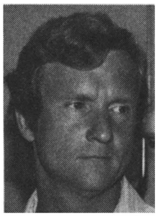

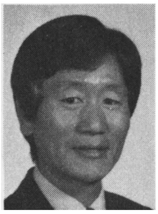

COMPARATIVE STUDY OF MEASUREMENTS BY MEANS OF GAMMA THERMOMETER STRINGS WITH FISSION CHAMBER MEASUREMENTS

Charles Hantouche

Charles Hantouche (BS, physics, Lebanese University, 1977; MS, 1980, and PhD, 1984, nuclear instrumentation, University of Grenoble, France) is a trainee scientist at the studies and research center of Electricité de France. His interests and activities are in developing and interpreting the signal provided by a new nuclear instrumentation in the pressurized water nuclear reactor.

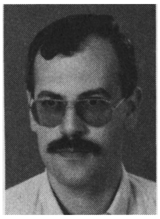

CORE STABILITY TEST ANALYSIS USING THE AUTOREGRESSIVE MODEL

TOHRU MITSUTAKE, SHIGEAKI TSUNOYAMA, and
SHIGERU KANEMOTO *Nippon Atomic Industry Group Company, Ltd.*
Ukishima-cho, Kawasaki-ku, Kawasaki, Japan

HIDEAKI NAMBA *Toshiba Corporation, Isogo Engineering Center*
Shinsugita-cho, Isogo-ku, Yokohama, Japan

SHIRLEY A. SANDOZ *General Electric Company*
175 Curtner Avenue, San Jose, California 95125

Received August 25, 1983
Accepted for Publication November 28, 1983

The multivariable autoregressive (AR) model identification technique has been applied in the study of the boiling water reactor core stability test analysis. It has been demonstrated through the analysis of core stability tests performed at the Peach Bottom-2 reactor, so that the AR model technique is effective in estimating core stability performance. Neutron flux to dome pressure open-loop stability performance is estimated by two methods, the ordinary correlation method and the AR model technique. Results obtained by both methods are in good agreement. The AR model technique can provide closed-loop decay ratios. This kind of decay ratio is considered to represent the actual core stability characteristic. Based on these test analysis results, the closed-loop in-reactor characteristic is more stable than the open-loop characteristic, which is usually considered to be the stability index for the reactor core. It was attempted to evaluate error in the AR model technique through indirect ways. It has been concluded that the AR model technique for the stability test data analysis is quantitatively highly effective in identifying and evaluating the core stability characteristics.

INTRODUCTION

Boiling water reactor (BWR) stability, which relates to coupled phenomena for thermal-hydraulic and void reactivity feedback dynamics, has been investigated by many analytical and experimental researchers and engineers since the beginning of BWR development.[1]

Among the BWR stability phenomena, which are usually divided into three categories, such as plant stability, core stability, and channel stability, the latter two are considered, from elementary mechanism, to take place due to the inherent system process. Hence, it is important for normal nuclear power plant operation to know where there might be any operational points beyond the stable boundary of the reactor core and coolant channels.

To make sure that the BWR plant is stable, a stability analysis was conducted based on a theoretical model. In the actual plant, core stability tests were conducted at Peach Bottom-2 by Philadelphia Electric Company, General Electric Company, and the Electric Power Research Institute in 1977 (Ref. 2). This project was aimed at confirming the stability margin for the reactor core during on-power operation. This paper reports on the procedure and results of this test data analysis, which is necessary for the qualification of reactor stability analysis codes.

Various techniques have been studied to identify the dynamic characteristics of nuclear reactor plants. Recently, the noise analysis technique proved to have some practical advantages, particularly, without any artificial disturbance, and also to provide information to support normal operation.[3] The autoregressive (AR) model analysis, a very efficient method in the system identification field, has been studied and applied to reactor noise analysis.[4] There is another way to examine the system characteristics, in which procedures are to add some artificial disturbances to the power plant and to observe the response signal characteristics. Pseudorandom binary sequences (PRBSs) have been examined in reactor kinetics investigation and plant dynamics estimation.[5,6] In the case of Peach Bottom-2 core stability tests, as mentioned above, small-pressure perturbation signals of PRBS were added to the pressure regulator reference set point.

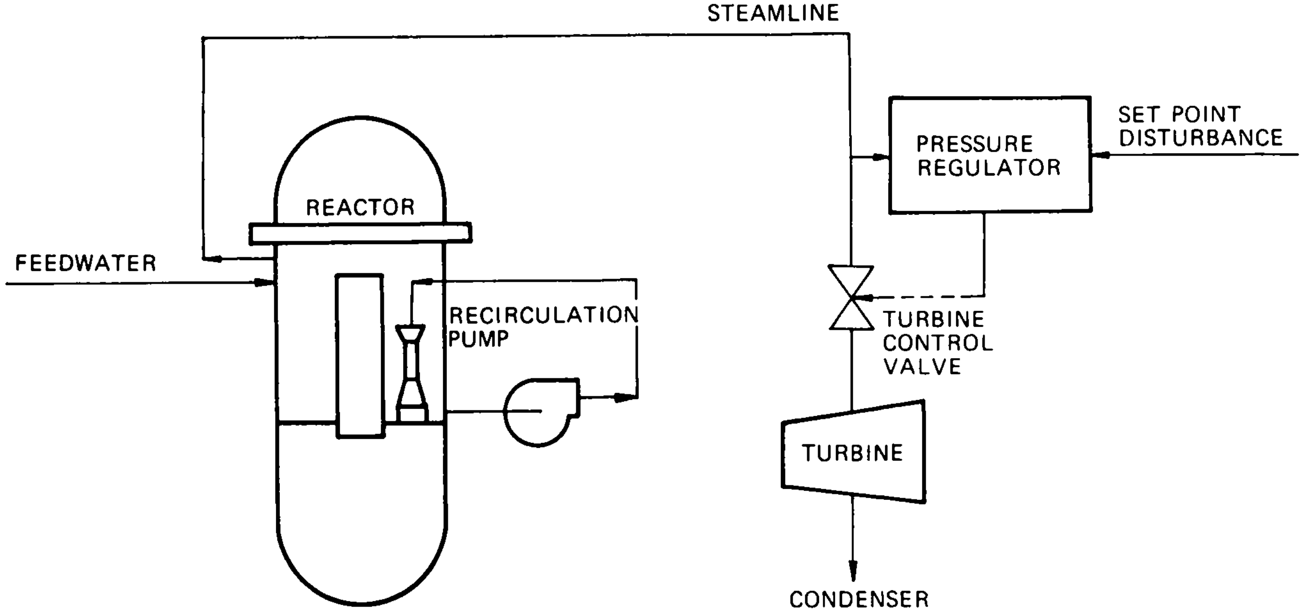

Fig. 1. Direct cycle BWR diagram.

In this paper, which follows previous papers,[7-9] the authors demonstrate that the AR model technique is the most practicable and effective to extract the required information about core stability performance.

HISTORICAL REVIEWS OF CORE STABILITY TESTS

In the past, the following methods have been applied to estimate BWR core stability through test data:

1. control rod oscillation test
2. noise analysis technique
3. small-pressure perturbation test.

The procedures involved in control rod oscillation tests are to oscillate one control rod in the reactor core and to measure the neutron flux responses to the reactivity perturbation induced by the oscillating rod.

These kinds of tests were conducted at Dresden-3 by the General Electric Company in 1973 (Ref. 10). Control rod oscillation tests have the following characteristics:

1. They add a direct reactivity perturbation to the nuclear core.

2. Movement by the essential control components, the control rods, needs to be repeated mechanically.

3. The local reactivity perturbation due to the control rod movements may not induce fluctuation in the whole core.

The last two characteristics are disadvantages, which could limit the applicability of this kind of test.

Many investigators have recently aimed to extract in-core information, including core stability, using the inherent reactor noise during normal operation. Considerable progress has been made.[3] Examples of the application to core stability analysis are described in Refs. 10 through 13.

In the small-pressure perturbation test, the pseudorandom signals are added to disturb the reactor core throughout with pressure perturbation, as shown in Fig. 1. In the test at Peach Bottom-2, PRBSs were used to produce the pressure perturbation input. This kind of signal produces a perturbation with sufficient gain over the frequency range expected to result in a large signal-to-noise ratio in a short testing time.

PRESSURE PERTURBATION TEST ANALYSIS METHOD

The core stability test method employed at Peach Bottom-2 is described in this section. Test points were four operating conditions, PT-1 through PT-4 in Fig. 2, which were chosen due to the smaller stability margin at low-flow/high-power conditions. There are two kinds of statistical data analysis in this paper, (a) the ordinary correlation method and (b) the AR method. The ordinary correlation method is a conventional way of estimating the input/output relation through power spectral densities in the frequency domain. The AR method, which is one practical method for nuclear power plant noise identification,[14] is a way to obtain the coefficients for the multivariate AR representation in the time domain. This paper shows the AR model practicability and compares the two methods.

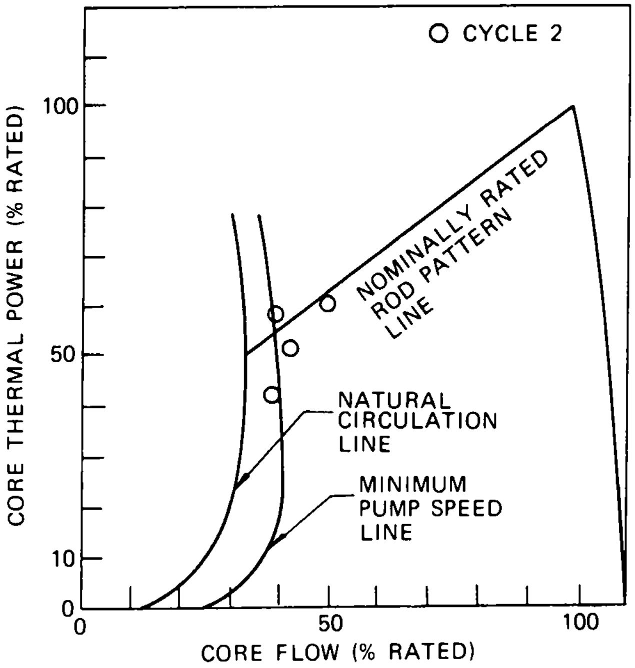

Fig. 2. Peach Bottom-2 stability test conditions.

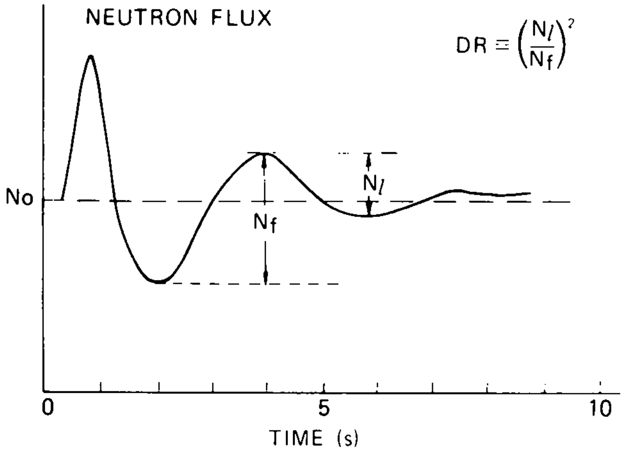

Fig. 3. Impulse response.

Stability Estimation by Correlation Analysis

Features of the ordinary correlation method are well known. Transfer function Gxy for output y to input x is calculated from the autospectral density Pyy for y and the cross-spectral density Pxy for y to x. The calculational conditions for data analysis are shown in Table I.

Sampling interval Δt and partitioned data length tp are selected so that the effective frequency range from $(tp)^{-1}$ to $(2\Delta t)^{-1}$ may broadly include the resonant frequency of the reactor core transfer function.

Assuming the dynamic relationship between dome pressure and average power range monitor (APRM) signal can be represented by an ordinary differential equation, the transfer function is found simply by Laplace transformation. The coefficients for this rational function can be calculated by fitting the measured transfer function to this model function by a least-squares method. The empirical form adopted is as shown in Eq. (1):

$$G(s) = \frac{K_p(\tau_l s + 1)}{s^2/w_l^2 + 2\delta_l s/w_l + 1} \quad . \tag{1}$$

TABLE I

Data Analysis Conditions

Sampling interval	$\Delta t = 0.25$ s
Data length	$T = 512$ s
Partitioned data length	$tp = 64$ s
Frequency range	$f = 0.02$ to 2.0 Hz
Input variable	Dome pressure
Output variable	Neutron flux

The inverse transform $g(t)$ for Eq. (1) has the behavior of a damped oscillation shown in Fig. 3, with the period $T = 2\pi/\beta$. The poles are S1, S2 = $\alpha \pm i\beta$ (α and β are constants). Therefore, the decay ratio (DR) is defined as follows[2]:

$$\mathrm{DR} = \exp\left[-\frac{2\pi\delta_l}{(1-\delta_l^2)^{1/2}}\right] \quad . \tag{2}$$

Note that sensitivity to parameter δ_l is relatively great near the resonant peak and quite small away from the peak.

Stability Analysis Using the AR Model

In recent years, stochastic models have been applied to the system identification problem for estimating, with better precision, dynamic relationships among system variables, including feedback. Also, in the reactor noise analysis field, much information has been obtained by time series analysis. One such method is the multivariate AR technique.[14,15]

The AR model analysis scheme in this paper is also shown in Ref. 14. The model technique has the following important advantages for reactor core stability test analysis:

1. A smoothed characteristic is obtained for the dynamic relation between model variables with feedback.

2. Stability margin can be estimated for both open and closed loops in a subsystem without any model assumptions.

The AR model coefficient matrix $\mathbf{A}(m)$ is a solution of the Yule Walker equation:

$$\sum_{j=1}^{K} \sum_{m=1}^{M_j} A_{ij}(m) R_{jh}(l-m) = R_{ih}(l) \ , \tag{3}$$

where

$i,h = 1,2,\ldots,K$

$R_{ih}(l)$ = cross-correlation functions between the h'th and i'th variables

K = number of model variables.

Note that model order M_j needs to be determined for each variable, according to Akaike's formalism,[16,17] that is called final prediction error criterion (FPEC). The description of the final prediction error (FPE) for a one-dimensional AR model is as follows:

$$FPE(M_j) = (N + M_j + 1)[N - (M_j + 1)]^{-1} \cdot SD(M_j)$$
$$(j = 1,2,\ldots,K) \ , \tag{4}$$

where N is the number of samples for each group of data (full time series length), and $SD(M) = \langle U^2 \rangle$, the variance in the innovation function, which is the residual

$$U = X(t) - \sum_{m=1}^{M} A(m) X(t-m) \ .$$

The FPEC has the following meaning. When the set of AR coefficients is applied to another time series with the same statistical characteristics as the data, the FPEC is the estimator for the mean-square prediction error. After obtaining AR coefficient matrix $\mathbf{A}(m)$, transfer function $G(f)_{ij}$ is calculated by finite Fourier transforming coefficient matrix $\mathbf{A}(f)$:

$$G(f)_{ij} = \frac{A(f)_{ij}}{A(f)_{ii}} \ . \tag{5}$$

Here,

$$A(f)_{ij} = I - \sum_{m=1}^{M_j} A(m)_{ij} \exp(-i \cdot 2\pi f \cdot m\Delta t) \ . \tag{6}$$

The initial or impulse response function is calculated by the inverse Fourier transform for the transfer function. This is an easy procedure to use in computing initial or impulse response behavior. Then, DRs are defined through the ratio of consequent overshoots, as shown in Fig. 3. In this paper, the core stability DR is estimated by averaging ten or more DRs, given in Fig. 3, to provide a more accurate estimate.

For stability evaluations, the BWR plant can be considered to contain two major components, the in-reactor vessel and the main steamline. The stability behavior of these components and the interface between them can be represented by the state variables, neutron flux, dome pressure, and turbine inlet pressure, as shown in Fig. 4. Symbols DR^{I} and $\mathrm{DR}^{\mathrm{II}}$ mean, respectively, the DR relating to the neutron flux to dome pressure open-loop G_1 and to the reactor core closed-loop G_F, excluding the part of the system downstream from the main steamline. While G_1 is equal to the one obtained by the ordinary correlation method, G_F, the new definition, is as follows:

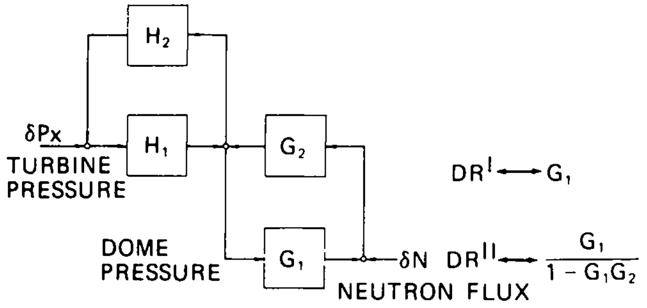

Fig. 4. The AR model for analysis.

$$G_F = \frac{G_1}{1 - G_1 G_2} \ , \tag{7}$$

where G_1 and G_2 are, respectively, the forward and feedback open-loop transfer functions from dome pressure to neutron flux. The DR^{I} and $\mathrm{DR}^{\mathrm{II}}$, shown in Fig. 4, are related to G_1 and G_F, respectively, as stated above.

This three-variable model is the simplest possible, except for a two-variable one consisting of two state variables, neutron flux and dome pressure. However, when analyzing Peach Bottom-2 data with this two-variable model, the AR modeling did not result in a good prediction of the raw time series for several reasons. One of them is that the model may be too simple, excluding the portion downward from the reactor dome outlet, that is the main steamline and reactor pressure regulator. That is the reason why the next simplest model, consisting of three variables, was adopted.

TEST DATA ANALYSIS RESULTS

The fluctuation in the reactor core neutron flux is induced mostly by the artificial pressure perturbation added to the initial pressure regulator reference set point. This PRBS signal has a binary value distribution. The peak-to-peak variations in neutron fluxes, i.e., the variations in APRM neutron flux signal readings, are 11 to 13% per rated power for an 8-psi pressure disturbance. The standard deviations during steady-state operation without pressure disturbance and pressure perturbation testing are listed in Table II. In all cases, the magnitudes of the fluctuations with pressure disturbance are increased by three to six times, compared to those in the steady states.

TABLE II

Fluctuation Amplitude

	PRBS		rms			
			PRBS[a]		Noise[b]	
Experimental Condition	1 bit (s)	Amplitude (psi)	Neutron Flux	Dome Pressure	Neutron Flux	Dome Pressure
PT-1	2	6	3.4% P	2.3×10^4 Pa	0.66% P	0.10×10^4 Pa
PT-2	2	8	3.4	2.2	0.47	0.08
PT-3	1	8	2.7	1.6	0.93	0.14
PT-4	1	8	3.0	1.7	0.43	0.09

[a] Pressure perturbation stability test.

[b] Steady-state noise without disturbance.

Stability Analysis by the Correlation Method

Stability estimation has been performed by the correlation method, i.e., by the dome-pressure/neutron-flux transfer function estimation and the least-squares fitting of the empirical transfer function model. These procedures are outlined in the previous section on the pressure perturbation test analysis method. The resulting DRs and the resonant frequencies are shown later. In Figs. 5 and 6, the measured and fitted transfer functions are compared with each other. The fitted values, described by the second-order damped oscillation model Eq. (1), are almost equal to the smoothly curved measured values. Therefore, the transfer function fitting method could provide a good estimation of DRs.

Stability Analysis Using the AR Model

The model of the whole BWR plant for AR model analysis, based on the plant dynamics model, has been shown in Fig. 4. The model variables are turbine inlet pressure, dome pressure, and neutron flux, which are considered to be the minimum number of measured variables for adequate description of the plant dynamics.

The open-loop transfer functions for the dome pressure to neutron flux are compared between the

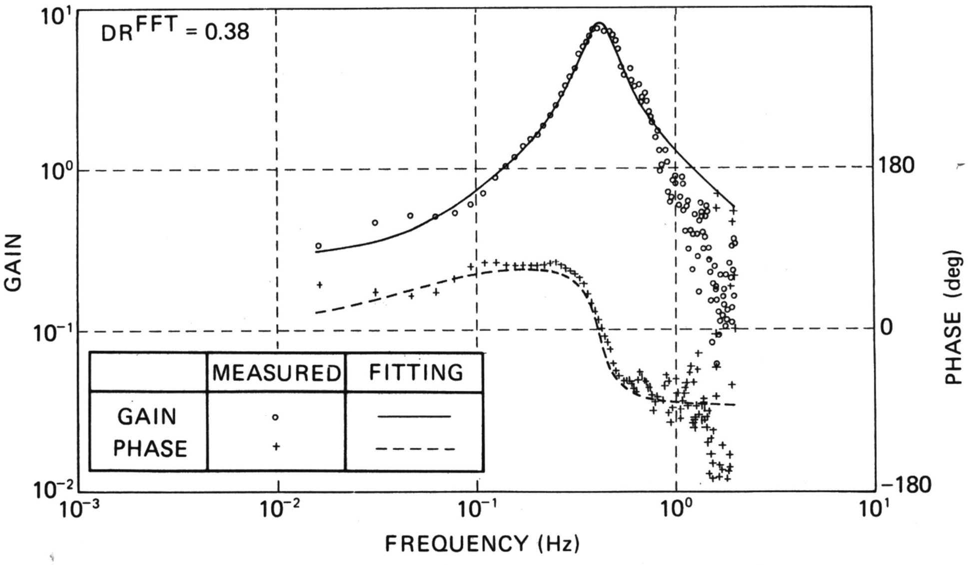

Fig. 5. Dome pressure to neutron flux transfer function (PT3).

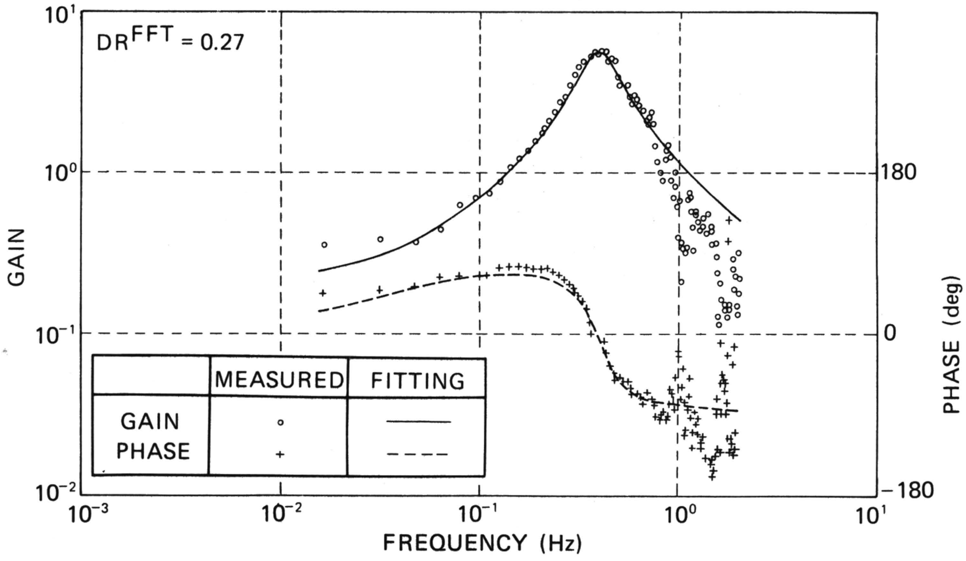

Fig. 6. Dome pressure to neutron flux transfer function (PT4).

correlation method and the AR model technique. In both PT-3 and PT-4, the transfer functions estimated by the AR model are more smoothed than the functions estimated by the correlation analysis. The open-loop transfer functions estimated by the two different methods are consistent.

The detailed results of core stability test analysis, using the three-dimensional multivariable AR model, are presented next.

Pressure Perturbation Test Data

The magnitudes of reactor fluctuation in pressure perturbation test data and steady-state data are shown in Table II. Considering these results, it was concluded that the magnitude of inherent noises within the core is significantly smaller than for the fluctuation induced by the artificial disturbance.

Optional order $M_j (j = 1, 2, \ldots, K)$ was obtained by the FPEC for each variable. Figure 7 shows an example of FPE performance, depending on the AR representation order. Here, σ_{N^2} is the mean square for the residual normalized by the autocovariance of its model variable, $\sigma_{N^2} = \sigma_{U^2}/\sigma_{X^2}$. Note that optimum order M_j, determined with FPE(M_j) for a single variable, is different in each variable.[14] Otherwise, it could result in either overestimated or underestimated order if the single optimal order M was determined, although it is usually adopted,[12] through multivariate FPE(M), which is defined by MFPE$(M) = [1 + (MK + 1)/N]^K[1 - (MK + 1)/N]^{-K} \cdot \|d_M\|$ (Ref. 16). Here, N is the sampling data number, and $\|d_M\|$ is the determinant of the residual covariance matrix.

From the definition, σ_N becomes smaller as the model order M becomes larger, but the FPE minimum principle can provide the optimum order in the way shown in Fig. 7. It is important to obtain an adequate representation wherein the FPEC is adopted for each variable.

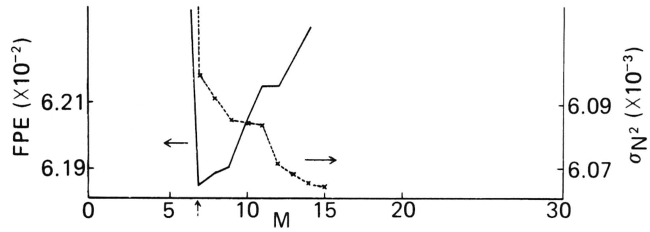

(a) NEUTRON FLUX

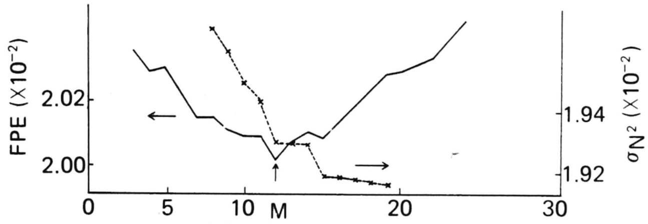

(b) DOME PRESSURE

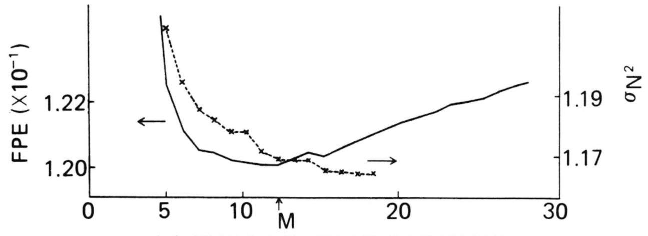

(c) TURBINE INLET PRESSURE

Fig. 7. Relation between FPE, variance in innovation $\langle \epsilon^2 \rangle$, and model order M (PT3).

Transfer Function

In Fig. 8, both open- and closed-loop transfer functions from dome pressure to neutron flux inside the reactor pressure vessel are compared at PT-3 and PT-4.

Decay ratios DR^I and DR^{II}, as shown in Fig. 4, correspond to the open- and closed-loop transfer functions, respectively. Explaining some differences between two kinds of transfer functions, the resonant frequencies for closed-loop transfer functions are a little lower than for open-loop functions, and the gain peaks are less sharp than for open-loop transfer functions. These differences can have a great effect on the stability performance index. These effects are probably caused by the large volume damping function in the steam dome in the vessel.

Impulse Response Function

Calculation of the impulse response function is the final step before obtaining DRs. The core stability DR is obtained by averaging all the DRs given in Fig. 3:

$$DR = \frac{1}{L}\sum_{i=1}^{L} DR^i \ , \qquad (8)$$

where L is the integer. The number L is ten or more. It is necessary to obtain smoothed behavior data for the impulse response function in DR computation.

Decay Ratio

The estimated DR results for the reactor core are shown in Table III. The DR^I and DR^{II} denote DRs for the open- and closed-loop characteristics, respectively, for the dome pressure to neutron flux; DR^{FFT} denotes the open-loop DRs estimated by the ordinary correlation method. The DR^I agrees well with DR^{FFT}.

The closed-loop stability performance estimated by DR^{II} is shown to be 30 to 40% more stable compared with DR^I, which is the usual design parameter for measuring the stability performance. The real reactor core response is provided by the closed-loop characteristics. The DR^{II} shows that consideration of the actual closed-loop behavior demonstrates a significant increase in the core design margin.

DISCUSSIONS

Decay Ratio Sensitivity Analysis—Correlation Method

In the preceding section on test data analysis results, DRs estimated by the AR technique were compared with DR^{FFT} by the ordinary correlation method. In the transfer function model fitting method, the DR can be described in terms of a model parameter δ_1.

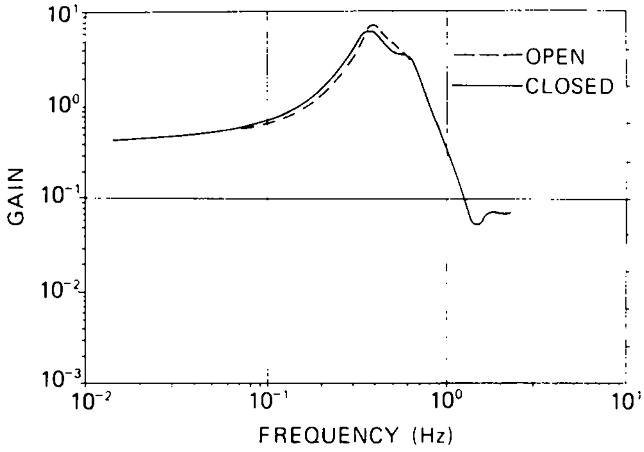

(a) PT3

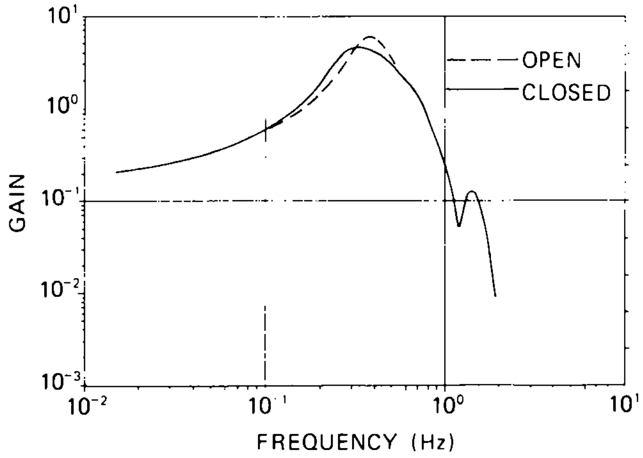

(b) PT4

Fig. 8. Comparison between open and closed loop transfer functions (PT3 and PT4).

The variation in δ_1 could cause only small changes in the phase characteristics, but would make significant changes in the gain around the resonant frequency. The sensitivity calculation results on the variation in $\delta_1 = 0.22 \pm 0.04$ are shown in Fig. 9. From these results, the relation between confidence interval $\delta\hat{G}$ for the estimated transfer function at the resonant frequency and the estimated error $\delta\overline{DR}$ for DRs are estimated:

$$\frac{\delta\overline{DR}}{\delta\hat{G}_{f=fR}} = \frac{0.03}{10\%} \ , \qquad (9)$$

where fR = resonant frequency. The result is evaluated at around DR = 0.3. At PT3 and PT4, statistical errors ΔM are transfer function gain, and biased errors $b_N[G(f)]$ are estimated in the neighborhood of the resonant frequency as follows:

$$\Delta M = 16\% \qquad (10)$$

TABLE III

Decay Ratio by the AR Model

Data	DR^{I}		DR^{FFT}		DR^{II}	
	DR^{I}	Resonant Frequency (Hz)	DR^{FFT}	Resonant Frequency (Hz)	DR^{II}	Resonant Frequency (Hz)
PT3	0.40	0.42	0.38	0.39	0.29	0.37
PT4	0.27	0.39	0.27	0.38	0.19	0.29

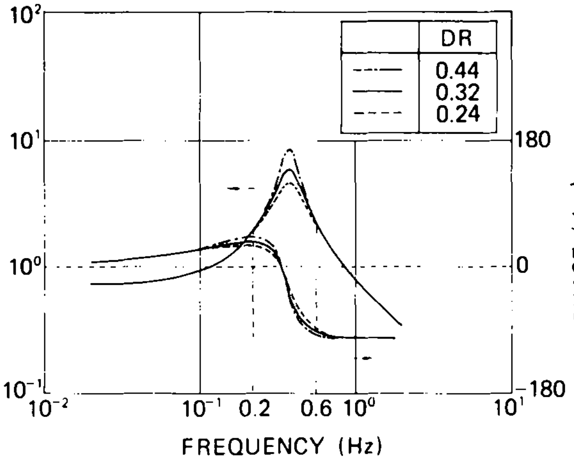

Fig. 9. Transfer function sensitivity to DR.

and

$$b_N[\hat{G}(f)] = \frac{\hat{G} - Gc}{Gc} = 2.0\% \ , \qquad (11)$$

where $\hat{G}$ is the predictor for true transfer function Gc. According to Eq. (10), error magnitude ΔDR for the estimated DR is calculated as

$$\Delta DR = \pm 0.05 \ . \qquad (12)$$

Therefore, DRs at PT3 and PT4, estimated by using the ordinary correlation method, are considered accurate to the extent shown by Eq. (12) and will be used later for the reference value.

Estimated DR Sensitivity Analysis—AR Model Technique

The section on test data analysis results shows that the AR model analysis provides stability performance index results that are consistent with those for the open-loop characteristics of neutron flux to dome pressure obtained by the ordinary correlation analysis.

There is no general way to estimate error involved in AR coefficients directly. Instead, the authors attempted to estimate how the DRs depend on these parameters. As one statistical fluctuation, it is important to estimate data length sensitivity.

TABLE IV

Sensitivity Study of DRs

DR Data	DR^{I}	DR^{FFT}	DR^{II}
Full data[a]	0.40	0.38	0.29
Half-length data	0.38	0.40	0.23
Half-length data	0.42	0.34	0.29

[a] Full data = 512 s.

Dividing total length into two equal lengths, 256 s, the dome pressure to neutron flux transfer function for each group of data is assumed to have the same frequency characteristics. Using the same procedures shown in the previous section, DRs were estimated for two parts of half-length data. Table IV shows the results of these DRs. Variation width values are 0.04 in DR^{I}, 0.06 in DR^{FFT}, and 0.06 in DR^{II}. These differences are practically allowable.

CONCLUSION

The multivariable AR model identification technique has been applied to data analysis in small-pressure perturbation tests for the core stability estimation performed at Peach Bottom-2. The core stability performance along the power-flow line, corresponding to minimum recirculation pump speed, was estimated with a three-variable AR model technique consisting of turbine inlet pressure, dome pressure, and neutron flux. The results show that these test points, which were considered to have a small stability margin, were very stable. The open-loop neutron flux to dome pressure results obtained by the AR model technique are in agreement with those obtained by the ordinary correlation method. It is possible to estimate the closed-loop core stability with the AR model, which is the new database for qualifying the core stability analysis code and identifying conservatism in the current stability design methods.[9]

It is concluded that the AR model technique for the stability test data analysis is quantitatively highly efficient for identifying and evaluating the core stability characteristics.

REFERENCES

1. J. A. THIE, "Dynamic Behavior of Boiling Reactors," ANL-5849, Argonne National Laboratory (May 1959).

2. L. A. CARMICHAEL et al., "Transient and Stability Tests at Peach Bottom Atomic Power Station Unit 2 at End of Cycle 2," NP-564, Electric Power Research Institute (1979).

3. A. TANABE et al., "Experience on BWR Plant Diagnosis System," IAEA-CN-39165, International Atomic Energy Agency, Stockholm (1980).

4. K. FUKUNISHI, "Diagnostic Analysis of a Nuclear Power Plant Using Multivariate Autoregressive Process," *Nucl. Sci. Eng.*, **62**, 215 (1977).

5. K. MATSUBARA et al., "A Multivariable Autoregressive Model of the Dynamics of a Boiling Water Reactor," *Nucl. Sci. Eng.*, **65**, 1 (1978).

6. T. W. KERLIN, *Frequency Response Testing in Nuclear Reactors*, Academic Press, New York (1974).

7. T. MITSUTAKE et al., "Application of Auto Regressive (A-R) Technique to BWR Stability Estimation," *Prog. Nucl. Energy*, **9**, 675 (1982).

8. S. TSUNOYAMA et al., "Peach Bottom-2 Reactor Stability Estimation Using PRBS and Noise Data," *Trans. Am. Nucl. Soc.*, **35**, 590 (1980).

9. S. TSUNOYAMA et al., "Peach Bottom-2 Reactor Stability Prediction with 1-D Transient Model," *Trans. Am. Nucl. Soc.*, **35**, 589 (1980).

10. R. O. NIEMI, "Dresden 3 Rod Oscillator Tests," NEDM-13381, General Electric Company (1973).

11. T. W. KERLIN et al., "Theoretical and Experimental Dynamic Analysis of the H. B. Robinson Nuclear Plant," *Nucl. Technol.*, **30**, 299 (1976).

12. B. R. UPADHYAYA et al., "Stability Monitoring of Boiling Water Reactors by Time Series Analysis of Neutron Noise," *Nucl. Sci. Eng.*, **77**, 480 (1981).

13. S. M. WU et al., "Stochastic Modeling of On-Line BWR Stability," NP-1753, Electric Power Research Institute (1981).

14. S. KANEMOTO et al., "Identification of Pressure Control System Dynamics in BWR Plant by Multivariate Auto Regressive Modeling Technique," *J. Nucl. Sci. Technol.*, **19**, 58 (1982).

15. S. KANEMOTO et al., "Multivariate Analyses for Neutron Noise Source Identification in BWR Plant," *J. Nucl. Sci. Technol.*, **20**, 13 (1983).

16. H. AKAIKE, "On the Use of Linear Model for the Identification of Feedback System," *Ann. Inst. Stat. Math.*, **20**, 425 (1968).

17. H. AKAIKE et al., "Statistical Analysis and Control of Dynamic Systems," Saiensu-sha (1972) (in Japanese).

REACTOR CORE STABILITY ANALYSIS FOR A BOILING WATER REACTOR BY A TRANSIENT MODEL

FISSION REACTORS

SHIGEAKI TSUNOYAMA and TOHRU MITSUTAKE
Nippon Atomic Industry Group Company, Ltd.
Ukishima-cho, Kawasaki-ku, Kawasaki, Japan

SHIGEO EBATA *Toshiba Corporation, Isogo Engineering Center*
Shinsugita-cho, Isogo-ku, Yokohama, Japan

SHIRLEY A. SANDOZ *General Electric Company*
175 Curtner Avenue, San Jose, California 95125

Received August 25, 1983
Accepted for Publication November 28, 1983

Applying an autoregressive (AR) technique to a boiling water reactor stability test yields two kinds of reactor stability performance indexes. One is characterized by the neutron flux to reactor pressure open-loop transfer function. The other is characterized by the closed-loop transfer function. Studies were performed on these reactor core stability indexes, using a one-dimensional transient model. To simulate these two kinds of stability characteristics in the time domain, the input/output relation for the system considered is important. In both cases, the output variable is the neutron flux. For the input state variable, in the case of the open-loop stability index, reactor pressure was chosen and adopted as a boundary variable to enable neglecting the feedback due to change in the reactor dome pressure. In the case of the closed-loop stability index, the vessel steam flow to the main steamline was adopted to separate the reactor response from the main steamline.

Employing this procedure, both stability indexes were estimated by the one-dimensional reactor transient model. Comparing these indexes to those evaluated by the AR fitting and Fourier transform of small perturbation test data, it was concluded that the one-dimensional transient model predicts well the open- and closed-loop stability performance. Further, it was shown that the open-loop index conventionally used is a somewhat conservative one.

INTRODUCTION

The stability phenomenon in the core of a boiling water reactor (BWR) has been studied since the start-up of early BWRs. As test methods have become more sophisticated, yielding higher quality data, comparison of details obtained from analytical investigation versus actual test data has given a better insight into the way in which neutron kinetics and thermohydraulic phenomena are coupled. The reactor core stability is an interaction phenomenon between the boiling process and the void-reactivity feedback. Small pressure perturbation tests were conducted at a BWR/4 by the Philadelphia Electric Company, the General Electric Company, and the Electric Power Research Institute,[1] where the open-loop reactivity feedback of the neutron flux to the reactor pressure was employed to describe the stability performance, fitting the measured data by an empirical transfer function.

Using an autoregressive (AR) model, Tsunoyama et al.[2] offer an alternative technique to analyze the pressure perturbation test. In AR fitting, the neutron flux to reactor pressure closed-loop transfer function can be obtained in addition to the open-loop transfer function.

Wu et al.[3] applied the single-input/single-output AR moving average fitting to analyze the stability. In their study, *a priori* knowledge that the stability resonant frequency is between 0.2 and 0.6 Hz is assumed. However, more detailed study on the transfer function, i.e., the open- and closed-loop stability characteristics, was not carried out.

Most previous theoretical studies on BWR core stability have been conducted with a lumped neutronic kinetic model and a frequency domain analysis.[4,5] Recently, the space-dependent effect was studied by Park et al.[6]

This paper reports on a one-dimensional BWR transient model that was employed to study core stability. Using the one-dimensional model, both neutron flux to reactor pressure open- and closed-loop responses are compared[7] and the adequacy of the representation of the stability performance, in terms of the closed-loop response, is discussed.

OBJECTIVES

In this study, the reactor core stability performance was studied using a time domain analysis code. Resulting stability indexes (decay ratios) are compared with those for the pressure perturbation test yielded by the AR and Fourier transform techniques. Test data used here were measured at the Peach Bottom-2 reactor, a BWR/4 plant, perturbing the reactor pressure. In the time domain analysis, the step or impulse response technique is generally adopted. The technique employed here is basically the latter. In the time domain analysis, the ideal impulse cannot be used, so a perturbation of small duration is added to the system.

In assessing the stability performance, the Fourier transform technique gives the neutron flux to reactor pressure open-loop stability index.[1] However, as discussed in Refs. 2 and 8, the AR technique gives both open- and closed-loop decay ratios (DRs).

In AR fitting, the system response is represented in the form of

$$X(n) = \sum_{m=1}^{M} \mathbf{A}(m) \cdot X(n-m) + U(n) \ , \tag{1}$$

and fitting coefficient matrix **A** is calculated by Akaike's[8] criteria. In this study, the physical relation between the time series $X(n)$ obtained by the AR fitting and the response obtained by the transient model was studied in terms of reactor stability performance.

After obtaining fitting coefficient matrix **A**, the transfer function was calculated by the finite Fourier transform. By inverse Fourier transforming this transfer function, the impulse response function is calculated. This is an easy procedure to use in computing impulse response. Comparing this impulse response and the response obtained by the transient model, the core stability damping characteristics were studied.

Further, the difference in the stability performances, based on the open- and closed-loop modeling of the reactor, is discussed at a marginally stable low-flow and high-power condition. It is shown that the closed-loop response, corresponding to actual reactor behavior, is still stable, even if the open-loop response shows an onset of a limit cycle oscillation.

REACTIVITY FEEDBACK TRANSFER FUNCTION FOR REACTOR CORE STABILITY

As mentioned in the Introduction, two kinds of transfer functions were used in the reactor core stability analysis. In this section, each transfer function category is explained.

Open-Loop Transfer Function for Pressure Perturbation Test

A block diagram of the pressure perturbation test is shown in Fig. 1. In this case, transfer function G_{f_p} for the void reactivity change to the reactor pressure change is itself unknown. Hence, Carmichael and Niemi[1] assumed an empirical transfer function model to identify the open-loop transfer function of the neutron flux to the reactor pressure. The assumed empirical transfer function model is

$$G_{CF} = \frac{Kp(\tau_1 s + 1)}{S^2/\omega_1^2 + 2\delta_1 S/\omega_1 + 1} \ . \tag{2}$$

Fitting a measured open-loop transfer function from the reactor pressure to the core-averaged neutron flux by the above empirical model, the stability performance index was obtained.

On the other hand, Tsunoyama et al.[2] and Mitsutake et al.[8] applied the AR fitting technique to identify the stability characteristic in the time domain in the form represented by Eq. (1). The stability performance was calculated by an impulse response of the system model with coefficient matrix **A** without assuming an empirical transfer function. This approach yields the neutron flux to reactor pressure closed-loop characteristic in addition to the open-loop characteristic shown in Fig. 1. The closed-loop response is described next.

Closed-Loop Transfer Function for the Pressure Perturbation Test

Figure 2 shows a closed-loop block diagram for the reactor, including the core, recirculation loop, separator, and dryer. The feedback loop in the closed loop consists of three parts (see Fig. 2). The first part is the loop from the neutron flux to the dryer exit steam flow. The second is the model of the dome steam mass balance. The third is from the dome pressure to the neutronic reactivity.

Of concern is a stability margin for an in-reactor response. Therefore, the core, recirculation loop, and reactor dome pressure responses are mainly taken into account in the closed-loop transfer function, separating the steamline dynamics, as was done in the AR analysis.[2,8]

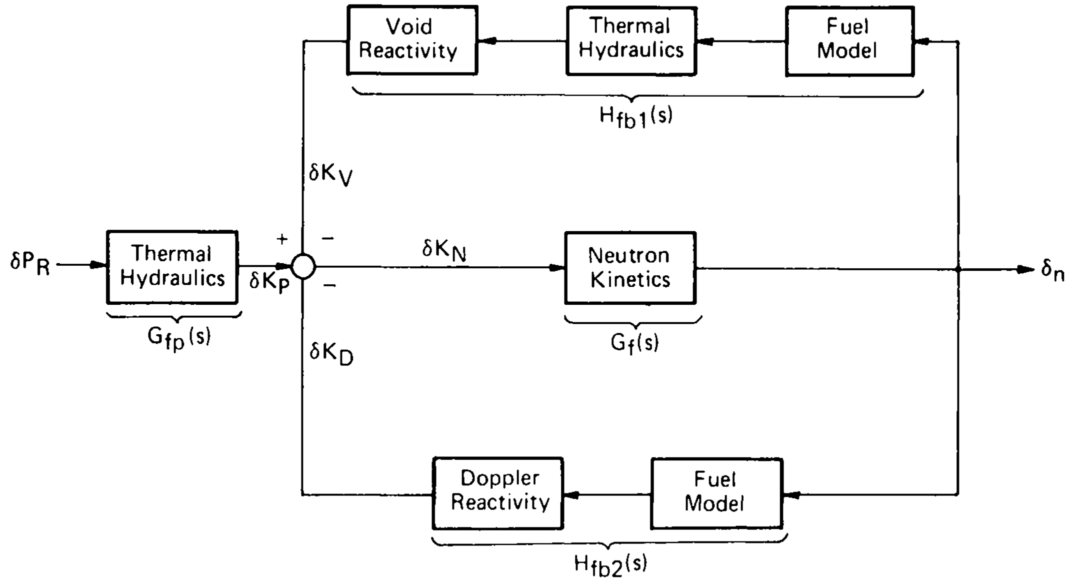

Fig. 1. The BWR reactivity feedback transfer function pressure perturbation test (open loop).

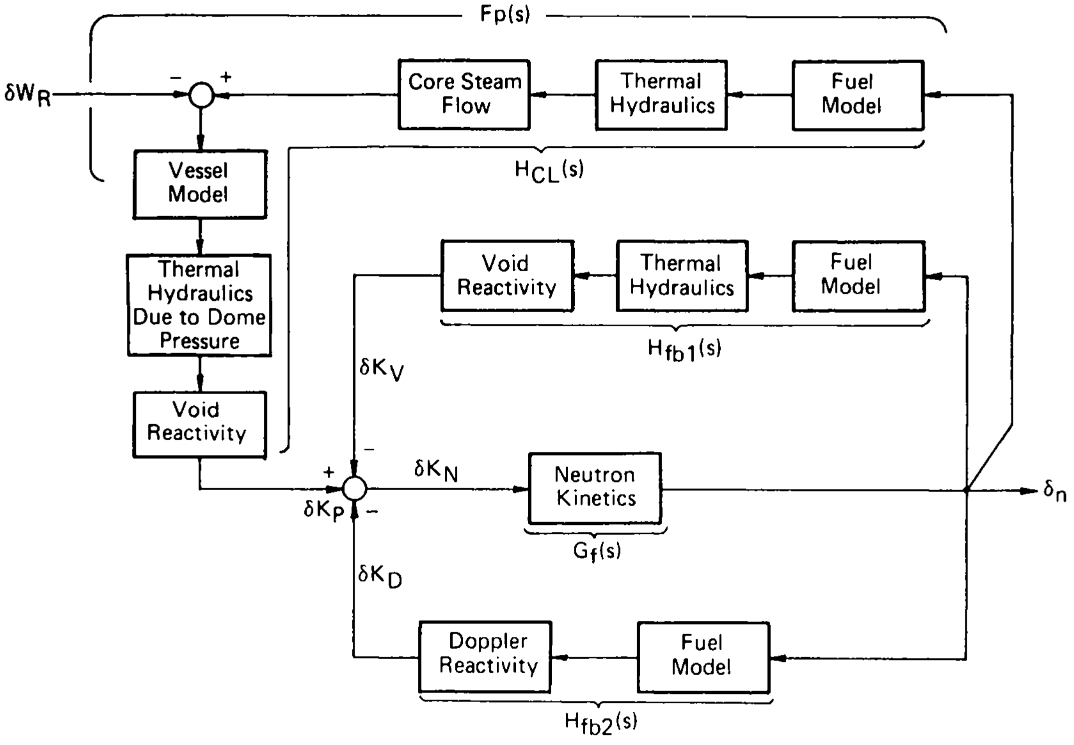

Fig. 2. The BWR reactivity feedback transfer function pressure perturbation test (closed loop).

One-Dimensional Transient Model Description

The transient model consists of a one-dimensional neutronic and thermohydraulic core model and major component models to simulate actual plant dynamics. Physical model details are described in Ref. 9.

The major assumptions employed in this model are described in the following three subsections.

Neutronic Kinetics

The time-dependent neutron flux is calculated assuming one energy group, six delayed-neutron groups, and time-dependent diffusion only in the axial direction. The three-dimensional neutron diffusion parameters are collapsed into equivalent one-dimensional parameters, using a steady-state radial neutron flux distribution, as a measure of radial importance similar to Henry's[10] procedure.

In the core stability simulation, control rod positions are fixed, so the steady-state radial distribution is a good weighting factor.

A neutronic parameter is fit as a quadratic function of relative water density U, i.e.,

$$\Sigma = \Sigma_0(Z)\ [1 + a(Z)(U - U_0) + b(Z)(U - U_0)^2]\ , \tag{3}$$

where U_0 is a steady-state relative water density.

Core Thermal-Hydraulics Model

The core thermal-hydraulics model allows for spatial variation in the coolant flow, coolant density, and pressure in the axial direction. The thermal-hydraulics model is based on a five-equation model, which includes separate continuity and energy equations for each phase, a total momentum equation, and a drift flux void correlation, as reported in Ref. 11.

This model has a feature, from the viewpoint of two-phase stability analysis, wherein a net vapor generation point is calculated simultaneously with the conservation equations for a two-phase separated flow model in a fully implicit donor-cell technique similar to that for the KACHINA code.[12]

Comparison to experimental data for two-phase instability showed this model can closely predict the density wave oscillation, the propagation of change in the void fraction.[11] Accurately determining propagation of void fraction change is important in assuring reactivity feedback stability. Hence, this model is also applicable to reactivity feedback stability prediction.

Fuel Model

Heat transfer to the moderator and fuel temperature are calculated, assuming an average cylindrical fuel and model for each axial location in the core.

OPEN-LOOP STABILITY PERFORMANCE

The one-dimensional model is applied to simulate the BWR/4 stability test data. To clarify applicability of the one-dimensional model in this analysis, phase differences between local power range monitor (LPRM) readings at the same axial location are evaluated. As typical LPRMs, central and peripheral LPRMs, marked with circles in Fig. 3a, are used. Figure 3b shows the phase difference between LPRM level B readings of the pressure perturbation test data located at central and peripheral regions. This indicates that the LPRM readings are in phase. Phase differences among LPRM readings at other axial levels were the same as shown in this figure. This result means the one-dimensional model is adequate to simulate the stability test data.

As a stability performance index for the BWR, a DR is usually used. The definition of the DR is a ratio of the first overshoot A to the second overshoot B of the step response, as shown in Fig. 4a.

The response in Fig. 4a appears in an ideal linear system and the reference line is straight. However, in the actual physical phenomena or in a time domain analysis, the reference line curves slightly, as shown in

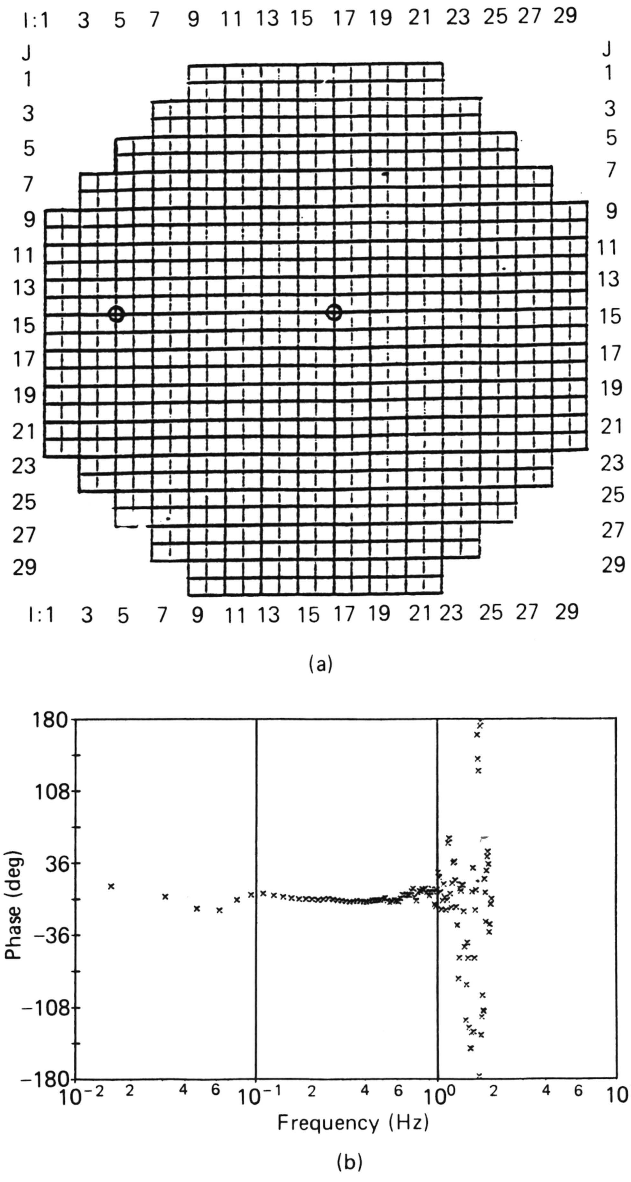

(a)

(b)

Fig. 3. The LPRM phase difference: (a) LPRM positions to evaluate phase difference and (b) phase difference between LPRMs (level B).

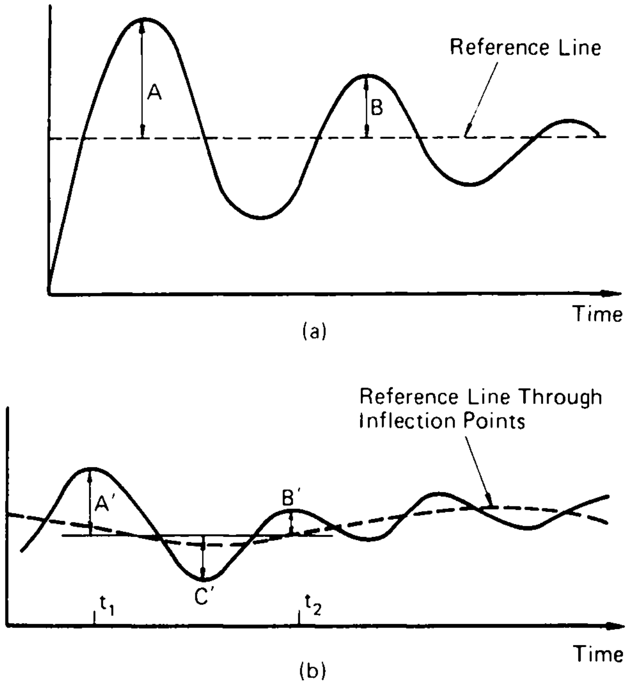

(a)

(b)

Fig. 4. Determining decay ratio: (a) response in linear system and (b) actual response.

TABLE I

Test Conditions

Test Point	Power		Core Flow	
	MW(thermal)	%	ton/h	%
PT1	1995	60.6	2430	52.3
PT2	1702	51.7	2040	43.8
PT3	1948	59.2	1880	40.4
PT4	1434	43.5	1870	40.3

Fig. 4b. Also, time domain analysis usually takes much computer time until the system response settles in order to obtain a settled value, i.e., the final reference line. Hence, DR is defined in the following way, using values A', B', and C' in Fig. 4b:

$$\mathrm{DR} = \left(\frac{B' + C'}{A' + C'}\right)^2 , \tag{4}$$

which is the same as the DR for Fig. 4a, if the reference line is linear, because (C'/A') is equal to (B'/C'). Natural oscillation frequency (FR) is defined as

$$\mathrm{FR} = \left(\frac{1}{t_2 - t_1}\right) . \tag{5}$$

The neutron flux to reactor pressure open-loop response is described by the in-reactor block diagram in Fig. 1. To simulate this response, the reactor pressure was chosen as a boundary condition during a transient. By first perturbing the reactor pressure and then holding it constant, as shown in Fig. 5, the open-loop response was simulated. Test data used here were measured at the BWR/4 plant.[1] Test conditions are shown in Table I. Input data regarding nuclear constants and power distribution are based on the actual reactor conditions at each test point. Table II shows the open-loop DRs by the AR analysis. Fourier transform results of the test data agree well with results of the one-dimensional simulation. The one-dimensional model frequencies are somewhat smaller than the others. Test points PT1 and PT2 could not be analyzed by the AR model, because the pseudo-random signal bit length was 2 s, which is long compared to the reactor stability characteristic frequency, 0.3 to 0.5 Hz. The DR is defined only in the system linearity range. Linearity was verified by increasing the PT3 disturbance to 0.09 MPa in the analysis. The result in Fig. 6 shows the system remains linear to 0.07 MPa. This tendency is the same in the other cases.

TABLE II

The DRs and Resonant Frequencies

	Open Loop					
	Fourier		AR Model		One-Dimensional Model	
	DR	Resonant Frequency (Hz)	DR	Resonant Frequency (Hz)	DR	Resonant Frequency (Hz)
PT1	0.19	0.44	---	---	0.18	0.38
PT2	0.17	0.40	---	---	0.21	0.33
PT3	0.38	0.42	0.40	0.39	0.39	0.33
PT4	0.27	0.39	0.27	0.38	0.27	0.34

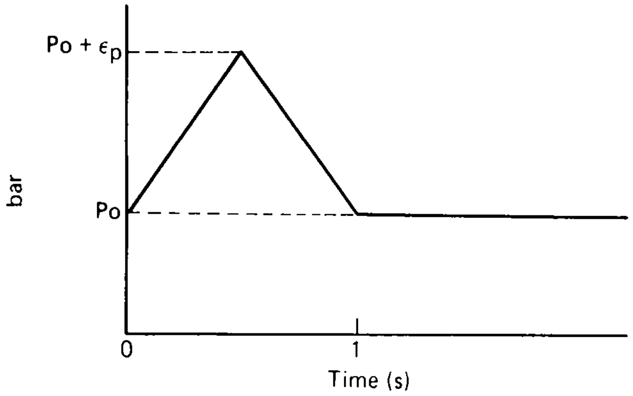

Fig. 5. Reactor pressure disturbance to simulate open-loop response.

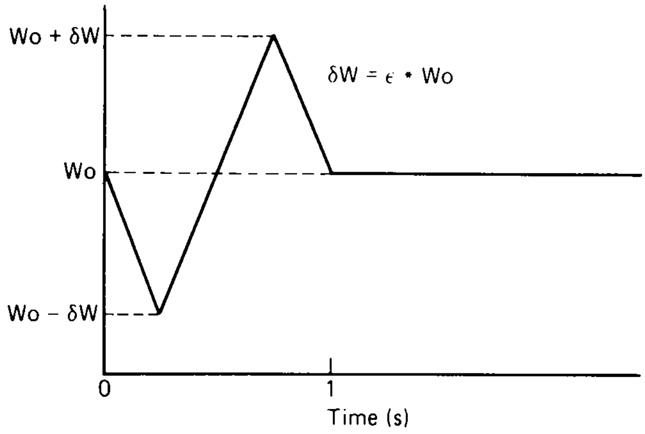

Fig. 7. Vessel steam flow disturbance to simulate closed-loop response.

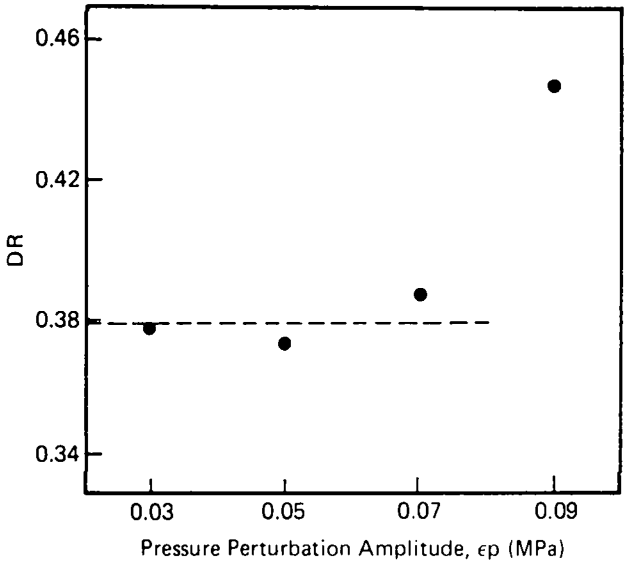

Fig. 6. Open-loop response linearity.

TABLE III

The DRs and Resonant Frequencies

	Closed Loop			
	AR Model		One-Dimensional Model	
	DR	Resonant Frequency (Hz)	DR	Resonant Frequency (Hz)
PT1	---	---	0.16	0.40
PT2	---	---	0.23	0.33
PT3	0.29	0.37	0.32	0.35
PT4	0.19	0.29	0.19	0.33

CLOSED-LOOP STABILITY PERFORMANCE

The main objective of this part of the study is to verify the closed-loop DR obtained by the AR model. The reactor model is separated from the main steamline model by suppressing changes in the steam flow (see Fig. 2).

The vessel steam flow is adopted as the boundary condition variable. A disturbance was introduced into the vessel steam flow, as shown in Fig. 7. The integrated change in energy for the steam flow must be zero, since the final steady state for the reactor must be the same as the initial condition. The results are listed in Table III. The agreement between the one-dimensional prediction and AR model is satisfactory. The closed-loop DRs tend to be smaller than the open-loop DRs.

To examine the linearity of the DR to the input disturbance, the disturbance amplitude was changed in the case of PT3. Figure 8 indicates the system response is linear with an amplitude <40% of the initial main steam flow. This is the same as in the other cases. The perturbation duration effect was also examined (Fig. 9). When the duration was 0.5 s, higher harmonics were induced and the amplitude was small because of the small energy in the added perturbation. On the other hand, as the duration became about the same as the natural frequency, the system response was smoother, making it easier to evaluate the DR. The DRs agree well for calculation with 1- and 2-s input durations.

OPEN- AND CLOSED-LOOP CHARACTERISTICS AROUND STABILITY BOUNDARY

The comparison between the open- and closed-loop DRs in Tables II and III indicates the closed-loop

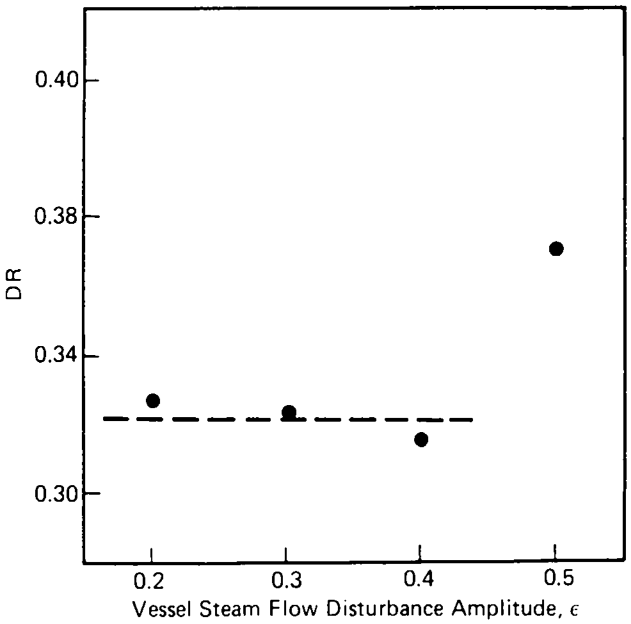

Fig. 8. Closed-loop response linearity.

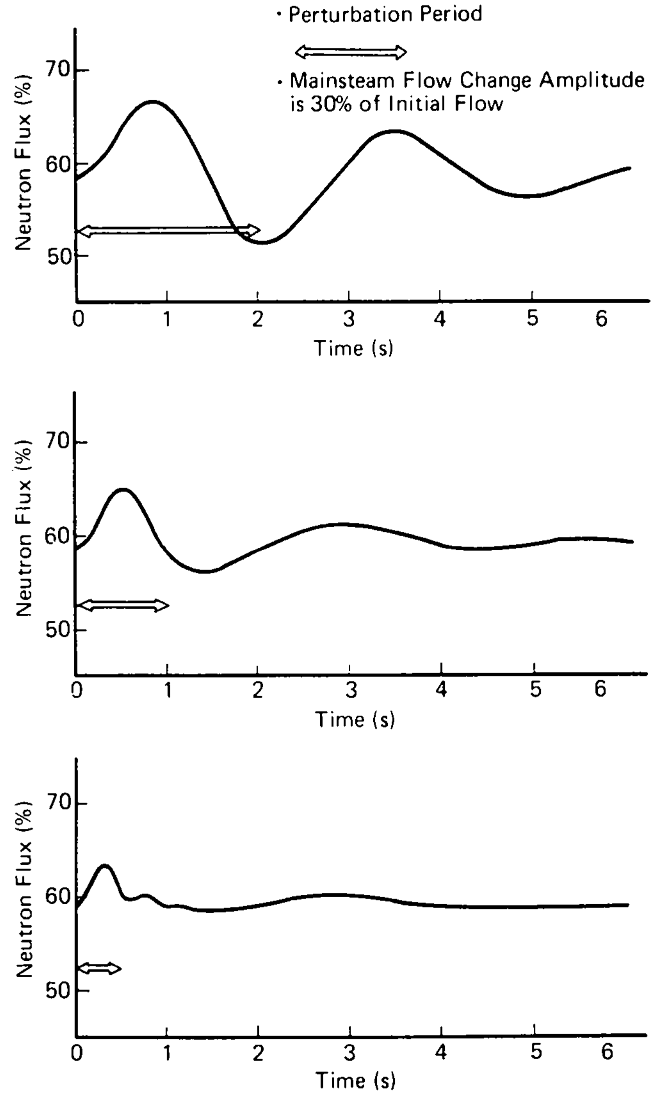

Fig. 9. Change in neutron flux due to main steam flow perturbation (PT3).

DRs are smaller than the open-loop DRs by ~30%. This comparison is based on data with large stability margins, within or just above the normal operational range. Of interest is the relationship between both DRs and behavior or response at onset of a limit cycle condition.

As a dominant and underdamped pole of the reactor core transfer function is considered to be in the open loop in Fig. 1, not in the feedback loop H_{CL} in Fig. 2, both open- and closed-loop DRs might be similar at the oscillation onset condition if the dome response is insensitive to the neutron flux change.

In order to study this possibility, the open- and closed-loop characteristics were compared near the oscillatory condition, using the one-dimensional transient model mentioned before.

The modern BWR is designed to be very stable under normal operating conditions. Zircaloy-clad UO_2 fuel pins have a thermal time constant of ~10 s and the period of change in voids is characterized by coolant transit time in the fuel assembly, which is ~2 s. This difference strongly damps the change in reactivity feedback due to changes in voids. Hence, to simulate the oscillatory condition, a virtual core condition was chosen, i.e., a higher power and lower flow condition (70% rated power and 35% rated flow). This core condition was made by virtually shifting the core condition from the normal operational range, adjusting the neutron balance by the neutron multiplication factor.

Open- and closed-loop system responses are shown in Fig. 10. The open-loop response shows a standing wave, which means the DR is ~1. However, the closed-loop response is still stable and the decay ratio is 0.82. This comparison shows that, even if the open-loop response starts to oscillate, the physical reactor core is still in a stable operating condition. The gain in the feedback loop from the neutron flux to the reactor dome pressure is usually small. However, as mentioned previously, it plays an important role in predicting the measure of reactor core stability. Therefore, this feedback loop was studied next.

The reactor dome pressure response to neutron flux is designated by *Fp*(*s*) in Fig. 2. This open-loop *Fp* has been studied three ways in the case of test point PT3. The results are shown in Fig. 11. The first result was estimated by Carmichael and Niemi[1] and is used to evaluate the bias error for the neutron flux to reactor pressure open-loop transfer function. The feedback transfer function *Fp*(*s*) can be approximated by the

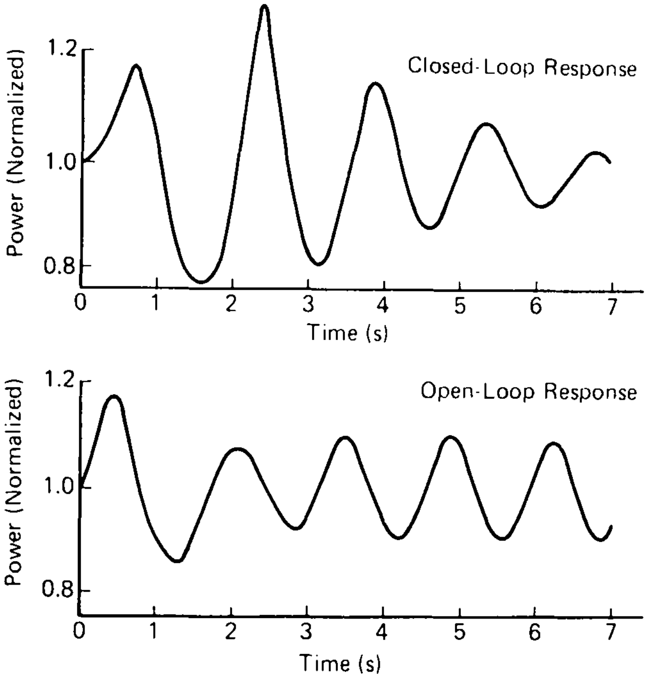

Fig. 10. Power response versus time.

effective fuel time constant τ_{fl} and an integrator representing the effective mass and energy storage in the vessel. Hence,

$$Fp(s) \cong \frac{Kp}{S(1+\tau_{fl}\cdot S)}\ \mathrm{MPa}/\% \ , \qquad (6)$$

where

$Kp \cong 0.01\ \mathrm{MPa/s}\cdot\%$

$\tau_{fl} \cong 7\ \mathrm{s}.$

The second result is calculated by sinusoidally changing the amplitude of neutron flux in the one-dimensional transient model. The initial neutron flux distribution is fixed. Only the amplitude is oscillated without any reactivity feedback, i.e., the void and Doppler feedback. Further, the steam flow from the reactor vessel to the main steamline is also kept constant, since the inherent reactor core stability is defined by the in-reactor response. The latter condition may cause a small drift in the dome pressure response, due to an initial mismatch in the energy balance inside the reactor vessel. Hence, the transfer function is computed with the following function:

$$\Delta P_D(t) = P_{D,S}(t) - P_{D,D}(t) \ , \qquad (7)$$

where $P_{D,S}$ and $P_{D,D}$ are the dome pressure response enhanced by the sinusoidal power perturbation and that drifted from the steady state without any perturbation. The third is the AR fitting test data result.[7]

These results are in fairly good agreement, as shown in Fig. 11. Consequently, it can be said that the gain in the feedback loop is small, as Carmichael pointed out. However, it still affects and stabilizes the reactor core characteristic.

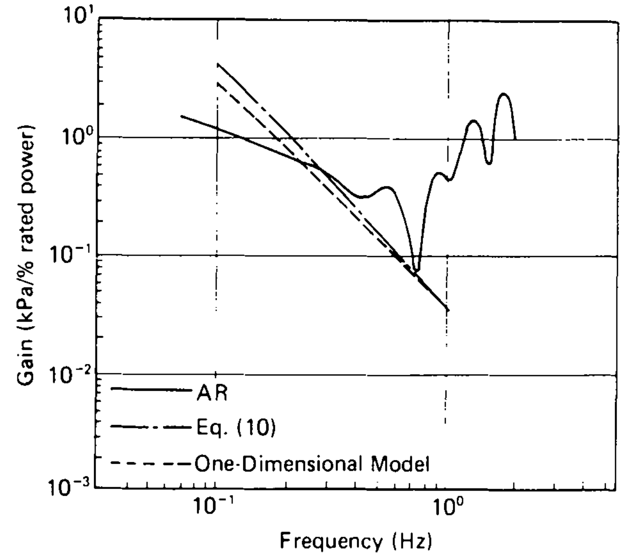

Fig. 11. Feedback loop $Fp(s)$ from neutron flux to reactor pressure.

SUMMARY

Comparing the one-dimensional transient model to the AR fitting and Fourier transform technique, the following conditions can be reached.

The one-dimensional model predicts well the decay ratios for the open- and closed-loop reactor core stability characteristics. The model represented by the closed-loop reactor response for the autoregression was verified. Further, it was shown that the closed-loop DR closely describes the actual reactor response and that the open-loop DR employed in the reactor design is a somewhat conservative index.

ACKNOWLEDGMENT

The authors are much indebted to General Electric Company for access to test and nuclear data.

REFERENCES

1. L. A. CARMICHAEL and R. O. NIEMI, "Transient and Stability Tests at Peach Bottom Atomic Power Station Unit 2 at End of Cycle 2," NP-564, Electric Power Research Institute (1978).

2. S. TSUNOYAMA, S. KANEMOTO, T. MITSUTAKE, and H. NAMBA, "Peach Bottom-2 Reactor Stability Estimation Using PRBS and Noise Data," *Trans. Am. Nucl. Soc.*, **35**, 590 (1980).

3. S. M. WU, M. S. OUYANG, and T. UNGPIYAKUL, "Stochastic Modeling of On-Line BWR Stability," NP-1753, Electric Power Research Institute (1981).

4. L. A. CARMICHAEL and G. J. SCATENA, "Stability and Dynamic Performance of the General Electric Boiling Water Reactors," APED-5652, General Electric Company (1969).

5. R. T. LAHEY, Jr. and F. J. MOODY, *The Thermal-Hydraulics of a Boiling Water Nuclear Reactor*, American Nuclear Society (1977).

6. G. PARK, M. BECKER, and R. T. LAHEY, "The Effect of Radial Nonuniformity on BWR Stability Margins," *Trans. Am. Nucl. Soc.*, **35**, 647 (1980).

7. S. TSUNOYAMA, T. MITSUTAKE, S. EBATA, and K. NONTA, "Peach Bottom-2 Reactor Stability Prediction with 1-D Transient Model," *Trans. Am. Nucl. Soc.*, **35**, 589 (1980).

8. T. MITSUTAKE, S. TSUNOYAMA, S. KANEMOTO, H. NAMBA, and S. A. SANDOZ, "Core Stability Test Analysis Using the Autoregressive Model," *Nucl. Technol.*, **65**, 365 (1984).

9. R. B. LINFORD, "Qualification of the One-Dimensional Core Transient Model for Boiling Water Reactors, Vol. I," NEDO-24154, General Electric Company (1978).

10. A. F. HENRY, "Nuclear Reactor Analysis," MIT Press, Cambridge, Massachusetts (1975).

11. B. S. SHIRALKER, S. TSUNOYAMA, S. P. CONGDON, and T. KAGAWA, "A Momentum Coupled Transient Thermal-Hydraulic Model for BWRs," *Trans. Am. Nucl. Soc.*, **32**, 291 (1979).

12. F. H. HARLOW and A. A. AMSDEM, "A Numerical Fluid Dynamics Calculation Method for All Flow Speeds," *J. Comp. Physica*, **8**, 197 (1971).

AUTOMATED CONTROL ROD PROGRAMMING IN BOILING WATER REACTOR CORES

WAN-LI ZHONG* and J. WEISMAN *University of Cincinnati*
Department of Chemical and Nuclear Engineering, Cincinnati, Ohio 45221

Received August 30, 1983
Accepted for Publication December 8, 1983

The decreased number of rods that are moved for power shaping in a boiling water reactor (BWR) with a control cell core (CCC) design make automated control rod programming feasible. A three-dimensional computer code, RODPRO, has therefore been developed for automatically generating a long-term control rod program for a BWR utilizing a CCC design. The program, which conforms to the general industrial practice for BWRs with CCCs, moves individual control rods so as to bring the core to criticality at each burnup step. By the use of heuristic rules, the procedure avoids complex theoretical approaches while eliminating tedious trial-and-error studies. The rod patterns so generated are shown to be consistent with real world requirements.

INTRODUCTION

In contrast to a pressurized water reactor where chemical shim control is used, the reactivity change in a boiling water reactor (BWR) core during operation is primarily compensated for by the withdrawal of control rods. Control rod programming is therefore important to the economy and safety of a BWR power plant operation.

Prior to the present effort, a number of theoretical studies had been undertaken in attempts to determine optimum control rod programs. The optimization strategy required to minimize the power peaking throughout lifetime was studied by several authors.[1-5] On the other hand, another group of workers focused their attention on the strategy needed to maximize the reactor lifetime or average burnup.[6-9] While these studies were helpful in defining the general nature of the control rod programming problem, they were usually too simplified for actual needs. Furthermore, the application of these optimization procedures to an accurate three-dimensional BWR simulator cannot be effected because of excessive computer time requirements. In addition, the resulting optimum poison distribution determined by a theoretical approach is almost impossible to achieve by discrete bottom-entering control rods. In practice, one is compelled to be content with a suboptimum solution.

The foregoing difficulties may be the major reason why the control rod programs really used for BWR cores have been generated by trial and error using a three-dimensional simulator and following general heuristic rules for guidance. The trial and error procedures generally use the axial power distribution resulting from the application of the Haling Principle[1] as a target. This principle states that the lowest possible axial peaking factor will be obtained if the axial power shape of a given assembly remains invariant over the cycle. Since all rods are withdrawn at the end of a cycle (EOC), the principle implies that the EOC burnup and power distribution must be consistent. The limitations inherent in rod programming prevent the Haling target from being achieved at all times during life, and the axial peaking factors are generally significantly higher than the ideal Haling values.

In view of the appreciable manpower required by trial and error procedures, various attempts have been made to develop a completely automated procedure. Kawai et al.[10] tried to develop a practical automated procedure for an actual BWR core considering three-dimensional behavior. The strategy adopted was, for each burnup step, to seek a power distribution that best fit a modified Haling target power distribution. The approach required the solution of a nonlinear programming problem that was treated by the method of "approximation programming." However, the

---

*Visiting scholar from Reactor Engineering and Design Institute, Beijing, China.

recomputation of the large number of linear programming coefficients required by this method is very time consuming. Furthermore, the control rod program so obtained led to the tips of a number of control rods being located near the central part of the core. Such a position would significantly distort the ideal Haling power distribution.

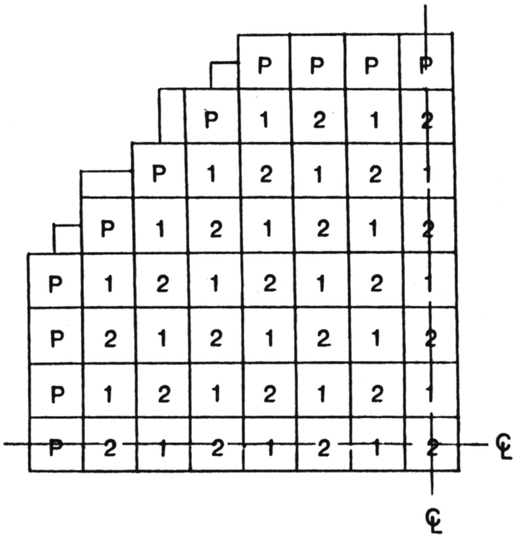

Fig. 1. Control cell configuration.

With recent developments in BWR fuel management, in particular the new control cell core[11-15] (CCC), the control rod programming problem has been simplified. We have therefore attempted the development of a new fully automated three-dimensional control rod programming code, based on the CCC design, that does not have the previously cited disadvantages.

The four fuel assemblies surrounding a given control rod are called a "control cell." In the minimum-shuffle control cell core (MSCCC) arrangement,[14] the control cells are divided into three groups (Fig. 1): Group one contains first- (fresh) and second-cycle fuel, group two third- and fourth-cycle fuel. The remaining cells are peripheral control cells that may contain a mixture of burnups. The MSCCC refueling strategy will

1. discharge fourth-cycle fuel or move it to peripheral locations
2. move second-cycle fuel into the previous fourth-cycle fuel's positions
3. load fresh fuel into positions previously occupied by second-cycle fuel
4. keep the first and third fuel positions fixed (but fuel is interchangeable).

This strategy leads to two successive core configurations designated as A- and B-type cores (shown in Figs. 2a and 2b, respectively). It is seen from Figs. 2a

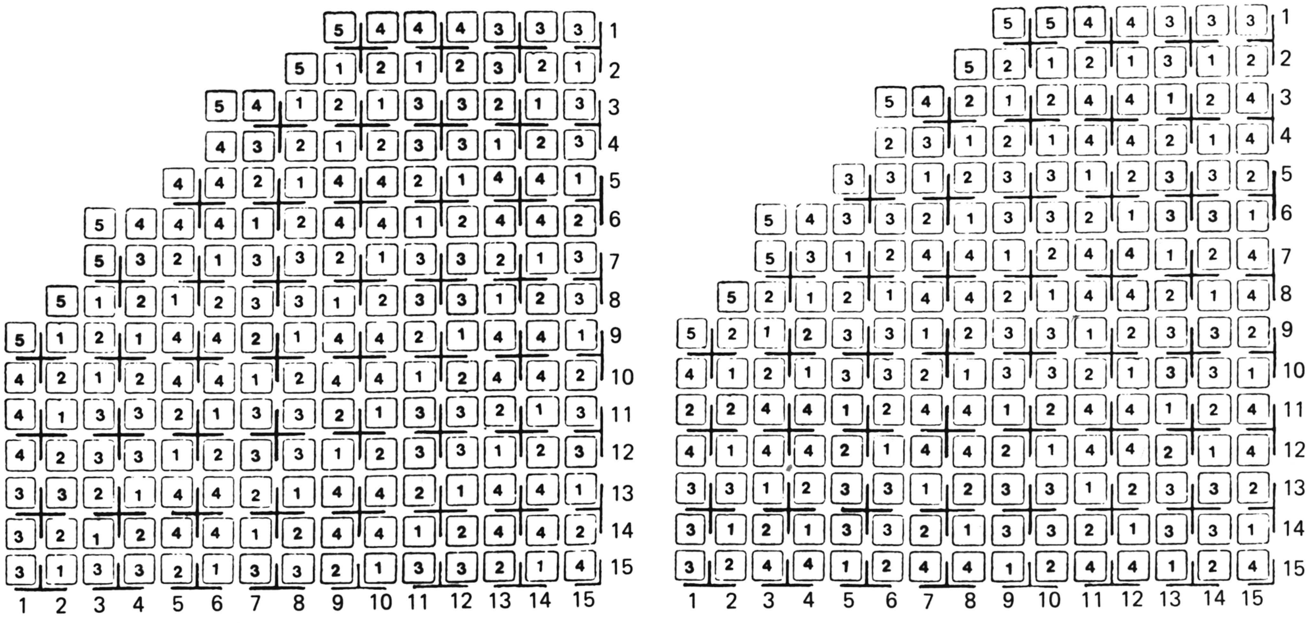

Assembly Residence Time Key:

1 = Fresh Fuel
2 = First Burned Fuel
3 = Second Burned Fuel
4 = Third Burned Fuel
5 = Fourth Burned Fuel

Fig. 2. (a) A-type core configuration and (b) B-type core configuration.

and 2b that the radial positions of both group one control cells (first- and second-cycle fuel) and group two control cells (third- and fourth-cycle fuel) remain unchanged. However, the positions of the first- and second-cycle and third- and fourth-cycle assemblies are interchanged within each group when the core is switched from A to B type or vice versa. The key to control rod programming for a BWR with CCC design is that only the control rods that are surrounded by the third-cycle fuel are moved for reactivity compensation and power shaping during operation. That is to say, the control rods within first- and second-cycle fuel (group one) are always withdrawn during operation. The rods surrounded by third- and fourth-cycle fuel (group two) are used alternately in the A- and B-type core. Note that the position of the third-cycle fuel changes as one goes from an A- to B-type core (see Figs. 1b and 1c) so that the rods actually moved are always surrounded by third-cycle fuel. In sum, by taking into account the peripheral control rods, which are always withdrawn during operation, only about one-fifth of the total number of control rods need to be considered in either cycle. This significantly reduces the number of control rod arrangements that must be evaluated.

It was found that the simplification occasioned by the CCC design together with a rapid three-dimensional simulator enabled a practical automated procedure to be developed. The resulting computer program, RODPRO, which follows heuristic rules, replaces the trial and error approach without requiring the use of a formal optimization procedure.

BWR CORE SIMULATOR

Nuclear Model

Since RODPRO endeavors to simulate the behavior of a real BWR core, a three-dimensional BWR nuclear simulator interfacing with core thermal-hydraulic characteristics is required. Based on an extension of the $1\frac{1}{2}$ group, two-dimensional model used by Lin et al.,[16] such a three-dimensional coarse-mesh BWR core simulator has been developed. In this simulator, a node is considered to be a 0.3-m (1-ft) section of a fuel assembly. By following a development essentially identical to that of Lin et al.,[16] the finite difference form of the fast-group diffusion equation at interior node I is (see Nomenclature on p. 393)

$$\beta \sum_{K=1}^{6} \frac{A_K}{l_K} (\phi_{f,I} - \phi_{f,K}) + (1-\beta) \sum_{j=1}^{4} \frac{A_J}{l_J} (\phi_{f,I} - \phi_{f,J}) + \frac{\phi_{f,I} V_I}{L_{f,I}^2} = \frac{k_{\infty,I}}{k_{eff}} \frac{1}{L_{f,I}^2} \phi_{f,I} \ . \tag{1}$$

The quantity L_f^2 is given by

$$L_f^2 = D_f \bigg/ \left(\Sigma_f^a + \Sigma_t^a \frac{\phi_t}{\phi_f} \right) \ , \tag{2}$$

and the quantity β is an empirical weighting factor between zero and one that allows the effect of diagonally placed assemblies to be taken into account. By recognizing that thermal leakage is negligible from the large size nodes used, we obtain the thermal flux from

$$\Sigma_t^a \phi_t = \Sigma_{f \to t}^s \phi_f \ . \tag{3}$$

The scheme adopted by Lin et al.[16] for the reflector boundary, where the reflector is replaced by albedo-type boundary conditions, is also used here. This yields for either radial or axial boundary nodes:

$$\begin{aligned} &\beta \sum_{K=1}^{6-M} \frac{A_K}{l_K} (\phi_{f,I} - \phi_{f,K}) + \beta \sum_{K=1}^{M} \frac{A_K'}{D_I} \gamma_k + (1-\beta) \\ &\quad \times \sum_{J=1}^{4-H} \frac{A_J'}{l_J} (\phi_{f,I} - \phi_{f,J}) + (1-\beta) \sum_{J=1}^{H} \frac{A_J'}{D_I} \gamma_J \\ &\quad + \frac{\phi_{f,I} V_I}{L_{f,I}^2} = \frac{k_{\infty,I}}{k_{eff}} \frac{1}{L_{f,I}^2} \phi_{f,I} \ , \end{aligned} \tag{4}$$

where

$$\gamma_K = \frac{1}{\alpha_{ff}(1 - h_K / D_f \alpha_{ff})} \tag{5}$$

and

$$\alpha_{ff} = [1/(D_f \kappa_f)] \tanh[\kappa_f (x_2 - x_1)] \ . \tag{6}$$

The derivation of the finite difference equations for the one-group model is the same as for the $1\frac{1}{2}$ group model except L_f^2 is replaced by the one-group neutron migration area M^2.

If I is an interior node, Eq. (4) will reduce to Eq. (1). Equation (4) can be rearranged to obtain an explicit form for the flux at node I. It is then used in an inner and an outer iteration scheme. The eigenvalue is evaluated from both the total neutron balance and the Rayleigh quotient. The difference between these two values determines the eigenvalue convergence in the source iteration.

The flux-source iteration is imbedded within the outer void iteration required for all BWRs. To keep the computational time at a minimum, a partial convergence scheme (described previously by Refs. 17 and 18) is introduced in the void iteration. When partial convergence of flux and eigenvalue is reached, the void iteration is deliberately turned to the next cycle to renew nuclear parameters. With these more accurate parameters, the partial convergence of both flux and eigenvalue is again achieved. After several iterations with increasingly rigid convergence criteria, the desired final convergence criteria are then applied. As previously noted, this approach reduces computation time by more than a factor of 2.

Computation of assembly voids requires calculation of the power production at each node. Previous observations have shown[19] that improved power estimates are achieved by basing the power on a flux which is a weighted average of the node flux and fluxes at surrounding node interfaces. The average flux for power estimation and void production is therefore obtained from

$$\bar{\phi} = W\phi_I + \frac{1-W}{6}\sum_{j=1}^{6}\phi_J^I \ , \tag{7}$$

where

$$\phi_J^I = \frac{\phi_I D_I + \phi_J D_J}{D_I + D_J} \ . \tag{8}$$

The difference between the eigenvalues of two successive void iterations determines the convergence of void iteration, i.e., the convergence of the three-dimensional simulation. Convergence of the void iteration is required following every rod movement until criticality is reached. The burnup over a given time interval is then calculated, and the same computation process is repeated for the end of the step. Control rods are then interchanged and the procedure is repeated. Details of the numerical model may be found in Ref. 20.

Thermal-Hydraulic Model

For the most part, the thermal-hydraulic subroutine follows that previously developed by Lin et al.[16] However, the previous scheme in which channel flows were adjusted in accordance with an input table is no longer used. Flows are adjusted by requiring uniform pressure drops across each channel and across the passage between channels. It is believed that this is more accurate than the previous approach.

The flow adjustment is embodied in the void loop. By a set of assumed flow rates and an assumed power distribution, the void fraction for each channel is estimated along with the mixture density. The pressure drop through a channel is then calculated. An arbitrary perturbation of flow rates (2% increment in each channel) is introduced, and the same procedure as above is repeated to get the channel pressure drop after the perturbation. The results of these calculations are used to obtain the change of flow rate per unit pressure drop change, i.e., $(\partial G/\partial \Delta p)$, for each channel. The pressure drops across channels are averaged over all channels to obtain the average pressure drop $\overline{\Delta p}$. The deviation of pressure drop of an individual channel i from the average value, i.e., $(\Delta p_i - \overline{\Delta p})$, is then used to calculate the flow rate change ΔG_i of that channel as follows:

$$\Delta G_i = (\Delta p_i - \overline{\Delta p}) \times (\partial G/\partial \Delta p)_i \ , \tag{9}$$

and the modified flow rate for the n'th void iteration is

$$G_i^n = G_i^{n-1} + \Delta G_i \ . \tag{10}$$

The total flow through all channels is calculated by

$$w_{total}^n = a_c \times \sum_{i=1}^{NA} G_i^n \ , \tag{11}$$

and the average channel flow rate is

$$\bar{w}^n = w_{total}^n / NA \ . \tag{12}$$

The normalized relative flow rate for channel i, F_i^n, is then given by

$$F_i^n = (a_c \times G_i^n)/\bar{w}^n \ . \tag{13}$$

The bypass flow rate, w_{bypass}, is calculated in accordance with the average channel pressure drop $\overline{\Delta p}$. The new total flow through all channels is then

$$w_{new}^n = w_{core} - w_{bypass} \ . \tag{14}$$

The final flow rate for channel i at the n'th void iteration is then given by

$$G_i^n = \left(\frac{w_{new}^n}{NA}\right) \times F_i^n / a_c \ . \tag{15}$$

This scheme avoids solving a set of simultaneous equations for channel flow rates under the condition of uniform pressure drop across the core. Moreover, by following the partial convergence idea mentioned previously, we omit an iterative procedure for obtaining a consistent pressure drop-channel flow rate relationship in each void loop. Such consistency is only required at the end of the computations; hence, computer time is saved. The flow rates are revised following each void iteration until convergence of the three-dimensional simulation is achieved.

CONTROL ROD PROGRAMMING

Present BWR control rod programming practice divides the control rods used for power shaping and control of reactivity with lifetime into two groups. One group is either inserted deeply [~3 to 3.6 m (~10 to ~12 ft)] or is withdrawn. The other group is inserted to a shallow depth [0 to ~1.2 m (0 to ~4 ft)] or is fully withdrawn. After approximately every 1000 h of effective full power operation, the deep and shallow rod groups are interchanged (rod swap). This allows a more even fuel assembly burnup.

The present automated scheme is designed to be fully consistent with current practice. The power shaping rods are still divided into deep and shallow groups, and these groups are interchanged at preset (by user) intervals. Furthermore, in conformity with the CCC design principles, only these rods that are surrounded by third-cycle fuel are moved for power shaping and control of reactivity. The remaining rods are used only for startup and shutdown and are fully withdrawn when the reactor is at power. Rod motion is constrained by the core thermal limits. For the present case, the limit was based on a maximum linear power of 52.5 kW/m (16 kW/ft). A total peaking factor of 2.91 was found to be consistent with this limit. The ratio of the power of the hottest rod in the assembly to the power of the average rod (local peaking factor) was taken as 1.30. This results in a limiting three-dimensional peaking factor, based on assembly powers of 2.24. This value is slightly lower than that used by Kawai et al.[10]

On the basis of separate computations, values of k_∞ are determined as a function of moderator density for a cell with no control rod, a rod fully inserted, and a rod inserted halfway into the cell. The results are then fitted with polynomials having the same form as used in the NODE-B (Ref. 21) program. We write

$$k_\infty = B_{1j}(1 + B_{2j}U + B_{3j}U^2) \;, \quad j = 1,2,3 \;, \tag{16}$$

with the index j indicating the degree of rod insertion.

The RODPRO, the trial and error adjustment of the position of the power shaping rods is replaced by an automated procedure. Heuristic rules govern the actions of the computer program. Several sets of heuristic rules were examined in a preliminary study to find the best approach to be used. The strategies examined were

1. Deep and shallow principle. (To shift the power peak toward the bottom of the core, rod programmers often try to keep the deep rods as deep as possible and the shallow rods as shallow as possible.)
2. Keeping the location of axial peak as close to the location of the peak of the Haling distribution as possible. (If the assumption of a smooth axial power distribution is valid, then this scheme should be a way of approximating the Haling distribution.)
3. Keeping the radial power distribution as close as possible to the radial power distribution found when all assemblies follow the appropriate Haling distribution axially.
4. Keeping the magnitude of the peak power as low as possible. (In this scheme, rods were moved to suppress the highest peak power whenever it occurred.)

From the preliminary results obtained, it was observed that

1. The first option kept the power peak at the lower part of the core approximately during the first half of the operational period (as can be seen in Fig. 3), and created a bottom overburned axial burnup distribution at EOC. This avoided an unacceptably high power peak at the EOC with all rods out.

2. Since the second option tried to match the locations of the Haling axial peaks, the shallow rods were not necessarily kept as shallow as possible at the early stages of operation. This procedure also created a bottom overburned axial burnup distribution at EOC. However, it was found that this strategy was very difficult to follow using only a limited number of isolated control rods. The rod arrangement required to bring the reactor just critical would often result in a significant deviation of the axial power distribution from the ideal Haling shape.

3. The third and fourth options tended to insert the control rods more evenly than the first two options, because the deep and shallow principle would not naturally be applied in following these strategies. Therefore, the EOC axial burnup peaking tended to be shifted upward as shown in Fig. 3. A continuation of the same strategies for successive cycles tends to aggravate the top overburned condition, and thus leads to an unallowable power peak at EOC with all rods withdrawn.

4. The first option had a slightly higher value of EOC reactivity than that of the core whose assemblies followed the ideal Haling distribution. The increased reactivity was obtained at the cost of a higher design power peak than obtained when following the Haling distribution. The second option provided almost the

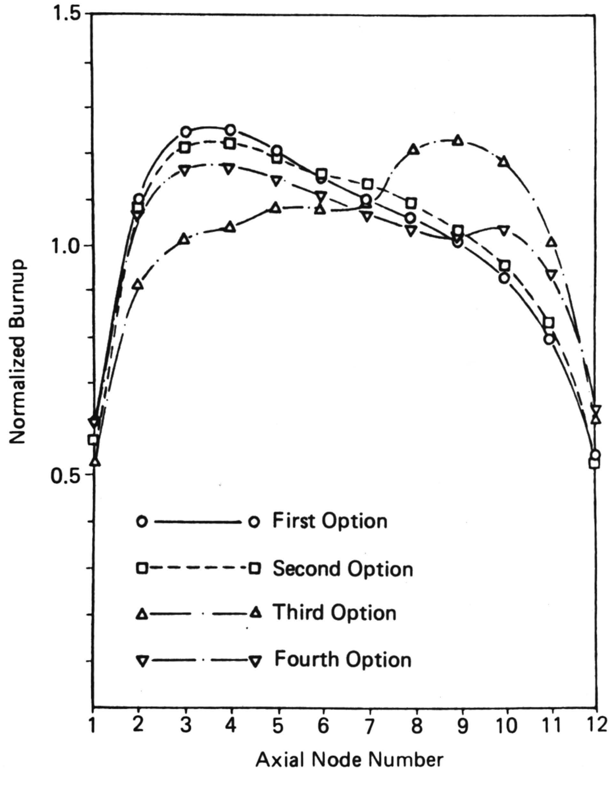

Fig. 3. Comparison of typical EOC burnup distributions.

same EOC reactivity as the ideal Haling distribution. The third and fourth options provided lower values than the Haling distribution.

In view of these observations, it was decided to discard the third and fourth options. Both the first and second options were then examined in detail.

Deep and Shallow Option

The deep and shallow control rod programming option is begun by assigning rod positions in accordance with a set of heuristic rules. At beginning of cycle, the position of the first deep rod is determined by the location of the third-cycle fuel having the highest axial power with all rods out. The remaining rods that are to be used in the cycle are then arranged in alternating deep [3.35-m (11-ft)] and shallow [0.3-m (1-ft)] positions. The reactivity is then adjusted to bring the core to criticality while avoiding any violation of thermal limitations, flattening radial power, and maintaining the deep/shallow arrangement as much as possible. To do this, rods are inserted to suppress unacceptable peaking. If the core is supercritical after such rod insertion, the rod in the region with the highest axial power peak is inserted. If the depth of the inserted rod is more than 1.2 m (4 ft), the rod will be inserted to 3.35 m (11 ft). If the core is not far from criticality ($k_{eff} <$ EIGVUP), a deep rod (if any) will be chosen for insertion to maintain the deep/shallow arrangement. On the other hand, if the core is considerably subcritical ($k_{eff} <$ EIGVLO), the rod in the region of lowest axial power peak is almost totally withdrawn. If the core is slightly subcritical, a shallow rod will be chosen as the one to be withdrawn. The process of adjustment continues until the core is brought to criticality while meeting all constraints and the critical rod pattern so obtained is stored. By using this scheme, the ends of control rods will be located as far from the central part of the core as possible therefore minimizing the distortion of the Haling distribution.

After the core accumulates a burnup of ~1000 h, the deep and shallow rods are interchanged and the starting rod pattern for this burnup step is then obtained by the previously described procedure.

In many cases, the rod pattern at the end of first step (i.e., the rod pattern before swap of deep and shallow rods) is required in order to understand the rod pattern change during that period of operation. The previously obtained rod pattern for the first step (i.e., the stored startup rod pattern of the first step) is used, for the sake of saving computational time, to begin a criticality search at the end of the burnup step. Generally, only a few rod movements are needed to bring the core to criticality. The entire procedure is then repeated at roughly 1000-h intervals until the end of life is reached.

Location of Axial Peaks as Close to Position of Haling Distribution Peaks as Possible

As previously indicated, this option attempts to follow the axial Haling distribution. Since a smooth variation in axial power shapes is assumed, the deviation of the actual locations of the axial peaks from those for the ideal Haling locations was used to guide rod movement subject to meeting the required reactivity and thermal constraints. The scheme for assigning initial rod patterns for each burnup step was basically the same as that used for the deep/shallow option. Any violation of thermal limits was first suppressed by appropriate rod insertion. The deviations of axial peak locations from those of ideal Haling distributions were then mainly used to govern the rod adjustment. That is, after eliminating any violation of thermal constraints, if the core is slightly supercritical, the rod in the region with the axial peak location lower than that of the Haling distribution will be chosen to be inserted so as to shift the peak location upward. For the considerably supercritical condition, however, the rod in the region of highest axial peak may be deeply [3.35 m (11 ft)] inserted. On the other hand, if the core is considerably subcritical, the rod in the region of lowest axial peak will be almost totally [0.3 m (1 ft)] withdrawn. For a slightly subcritical core, a shallow rod in the region with the axial peak location higher than that of the Haling distribution will be chosen for withdrawal to shift the peak location downward. However, during the process of criticality adjustment, it may be found that no rod movements bring the axial power shape to a better fit of the Haling distribution. In that case, the magnitude of axial peak is used to guide the rod movement as done in the case of deep/shallow option. It was observed that in many cases the control rod pattern providing the best fit of the axial Haling distribution did not lead to a critical core. The criticality requirement will often distort the ideal Haling distribution. The principal flow diagram for this approach is shown in Fig. 4.

RESULTS

The Peach Bottom BWR was selected as the reference core, and six successive cycles (i.e., three A-type cores and three B-type cores) were examined on the basis of a refueling scheme for the CCC design provided by REFUEL (Ref. 18). The control rod banks are defined in Fig. 5, and a set of rod patterns for a typical A core based on one-eighth core symmetry is illustrated in Fig. 6. From the rod bank axial positions in Fig. 6, it is seen that the deep and shallow principle was followed rather well throughout the core lifetime. However, during the operational period from 1000 to 2000 h, shallow rod bank 4 was obliged to stay at the central part of the core in order to keep the power

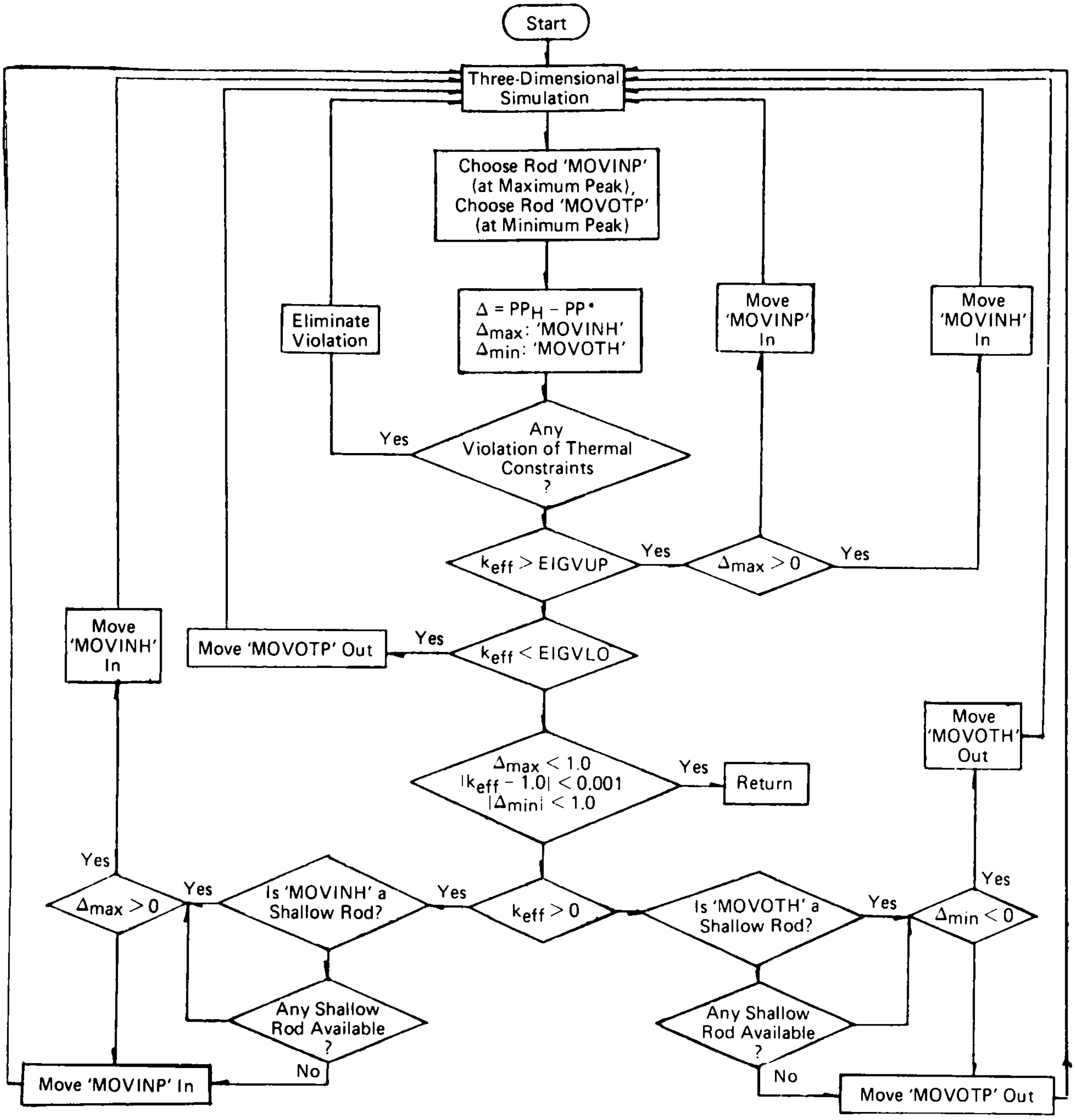

*PP_H = Axial Peak Position of Ideal Haling Distribution
PP = Axial Peak Position Calculated

Fig. 4. Principal logic flow chart for scheme 2.

peak from exceeding the limiting three-dimensional peaking factor.

It can also be seen from Fig. 6 that the rod pattern does not change very much during the 1000-h operational time interval for each burnup step. The difference between the starting pattern and the ending pattern indicates to the reactor operators which rods to move and how far to move them during operation. On the other hand, a dramatic change of rod pattern occurs at the end of a burnup step (i.e., the beginning of the next step) where the interchange of deep and shallow rods takes place (rod swap).

Figure 7 shows the comparison between a typical time-dependent average axial power distribution obtained by the deep and shallow scheme and that of the ideal Haling distribution. It is seen that the average axial power distribution varies considerably from step to step, and that none entirely agrees with the Haling

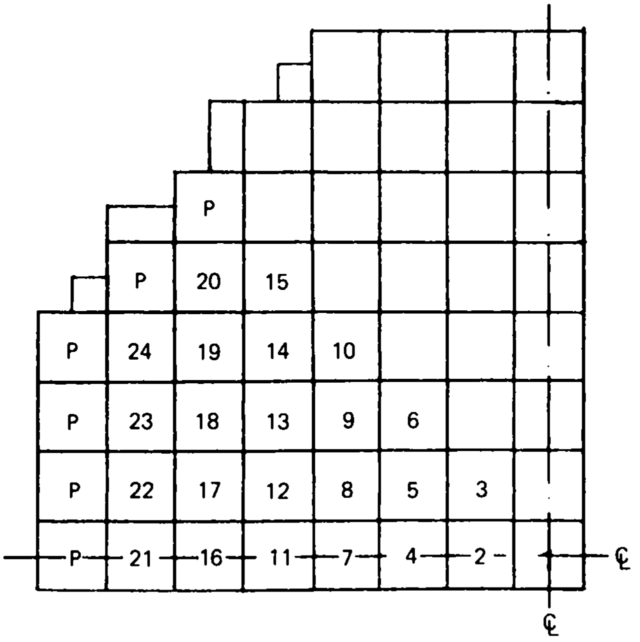

Fig. 5. Control rod bank designation.

distribution. However, as a whole, the time average axial power distribution over a cycle for the same cases are in fairly good agreement with the ideal Haling distribution as shown in Fig. 8.

It can also be seen from Fig. 7 that the operational strategy adopted here keeps the axial location of the peak power as low as possible. In the latter portion of the cycle, the larger depletion at the lower elevations pushes the axial location of the peak power upward. Both strategies tend to create bottom overburned assemblies as shown in Fig. 8, and thus avoids unallowable peaking at EOC with all rods out. Figure 9 illustrates the axial burnup shapes of different cycle fuel in a core at EOC for both schemes as well as those of the ideal Haling option. It may also be observed in Fig. 9 that the application of scheme 2 (Haling target) tends to shift the axial peak location 0.3 to 0.6 m (1 to 2 ft) above the locations obtained in scheme 1 (deep/shallow). This may result from the fact that during the early stages of the operation of the deep/shallow scheme (scheme 1) the requirement that the rod depth be as deep and as shallow as possible will create axial peaks at lower positions than those of the ideal Haling distribution and thus more depletion at the lower portion of the core.

Examination of the multicycle EOC reactivities shows that the EOC reactivities for both schemes are nearly identical to the reactivities of the Haling option at the end of the A cycles. Scheme 1 provides reactivities that are slightly higher than those of the Haling cores at the end of B cycles (i.e., 0.9992 versus 0.9988); scheme 2 provides slightly lower reactivities at the end of the B cycles.

TABLE I

Comparison of Maximum Peaking Factors

Cycle	A1	B1	A2	B2	A3	B3
Ideal Haling	1.56	1.52	1.55	1.50	1.55	1.50
Scheme 1	2.14	2.19	1.99	2.21	2.01	2.16
Scheme 2	2.18	2.15	1.93	2.17	2.00	

The maximum peaking factors found during the entire operational time of each cycle are compared in Table I. It can be seen from Table I that the peaking factors for both schemes are significantly higher than those of the ideal Haling distribution. However, the peaking factors are well within the limiting three-dimensional assembly peaking factor of 2.24. It was also observed that the actual peaking factor can be reduced by setting a lower limit but at the cost of slightly lower EOC reactivity.

DISCUSSION AND CONCLUSION

The RODPRO code has been programmed to utilize either the deep/shallow scheme or the scheme that keeps the axial location of the peak power close to the Haling power peak location. It was found that the deep/shallow scheme is the easiest to implement. Both schemes provide an almost identical axial burnup distribution for the fourth-cycle fuel (discharged fuel) at EOC. However, the deep and shallow scheme provides slightly higher reactivities at the end of the B cycles. It is therefore recommended.

The work done indicates that achieving the target of an ideal Haling distribution at all times during operation by using only a limited number of discrete control rods is almost impossible. The present approach is believed to be a reasonable compromise. In it, the reactor is operated with a high power density in the lower regions of the core while attempting to obtain a whole cycle average power distribution, which would be in agreement with the ideal Haling distribution.

This computer code is made possible by the recent CCC fuel management concept, which simplifies BWR operation and considerably reduces the number of control rods that need to be moved in a given cycle. This, together with a rapid three-dimensional core simulator, allows the computations to be completed in a reasonable time. The rod patterns thus obtained are believed highly acceptable.

As noted previously, the fuel arrangement used in the CCC design examined in this study corresponds to the MSCCC configuration proposed by Fennern et al.[14] It is possible that, in some reactor plants, group

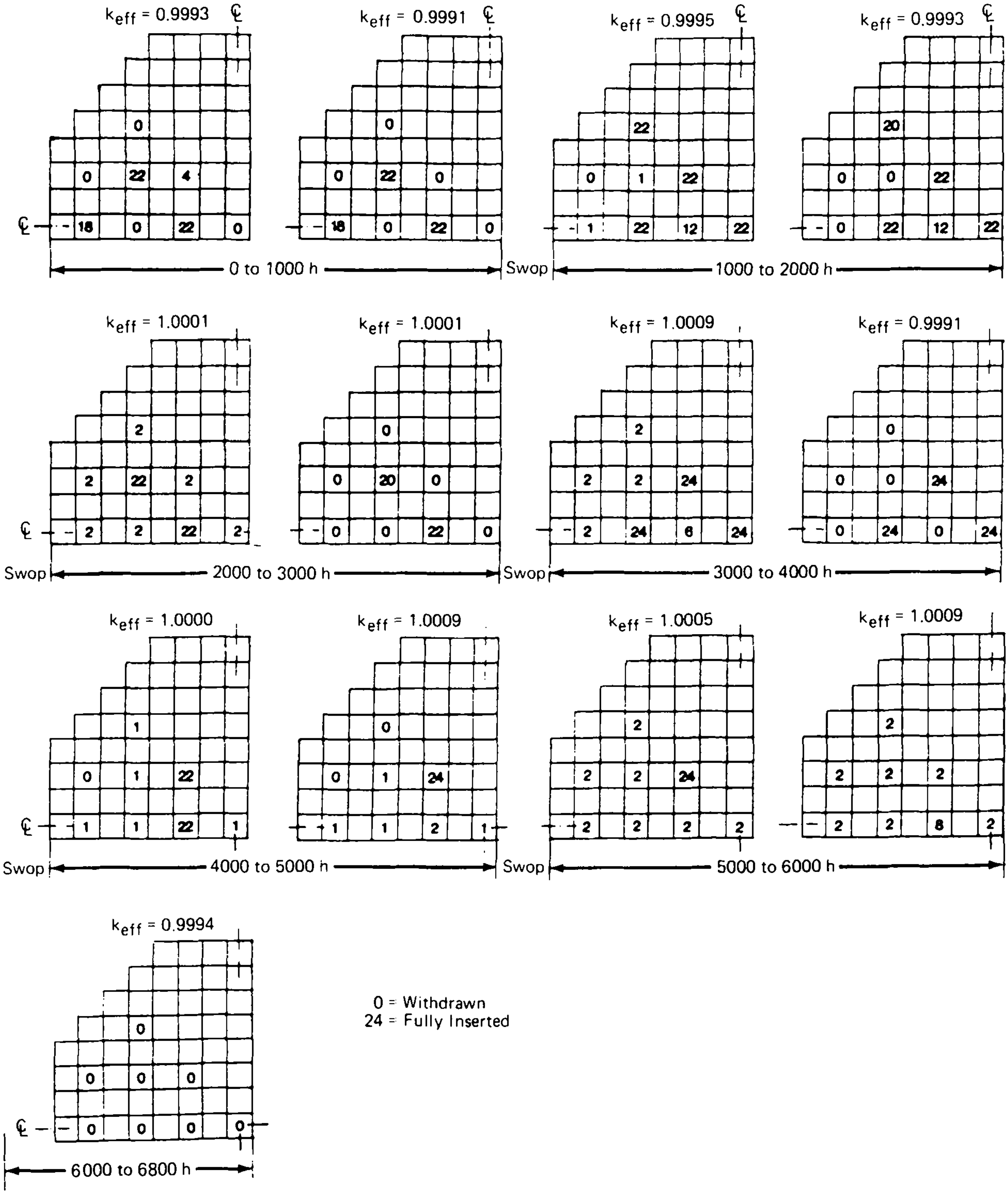

Fig. 6. Control rod program for a typical A-type core.

1 control cells could lead to shutdown margin violations. The MSCCC fuel arrangement could then not be used. However, the basic CCC concept, in which less than one-fourth of the control rods are moved during operation and those rods moved are surrounded by low reactivity fuel, could still be applied. Since the logic of RODPRO is tied only to the CCC concept, and not to a particular refueling scheme, the program should remain applicable. A study of the behavior of RODPRO with another CCC would be desirable.

The 1000-h period between rod swaps was arbitrarily chosen without any attempt to optimize this

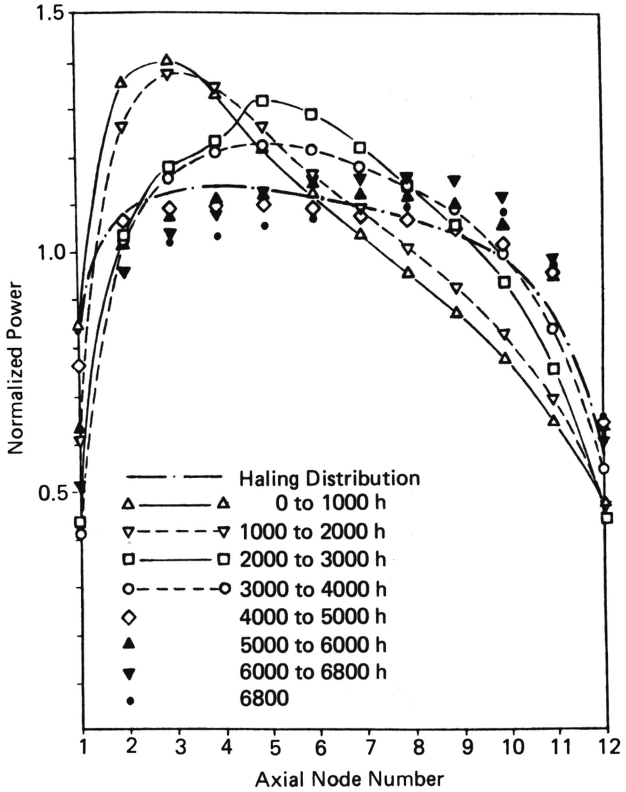

Fig. 7. Time-dependent axial power distribution from scheme 1.

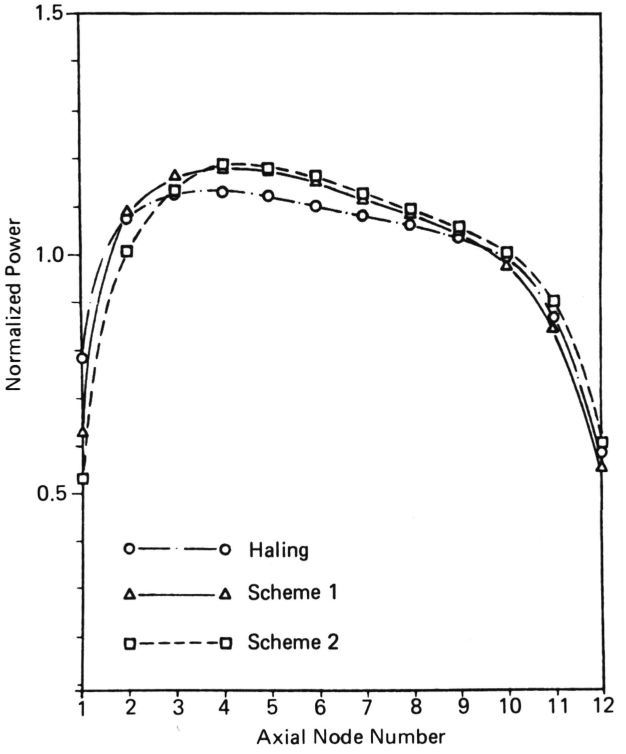

Fig. 8. Time-averaged axial power distribution.

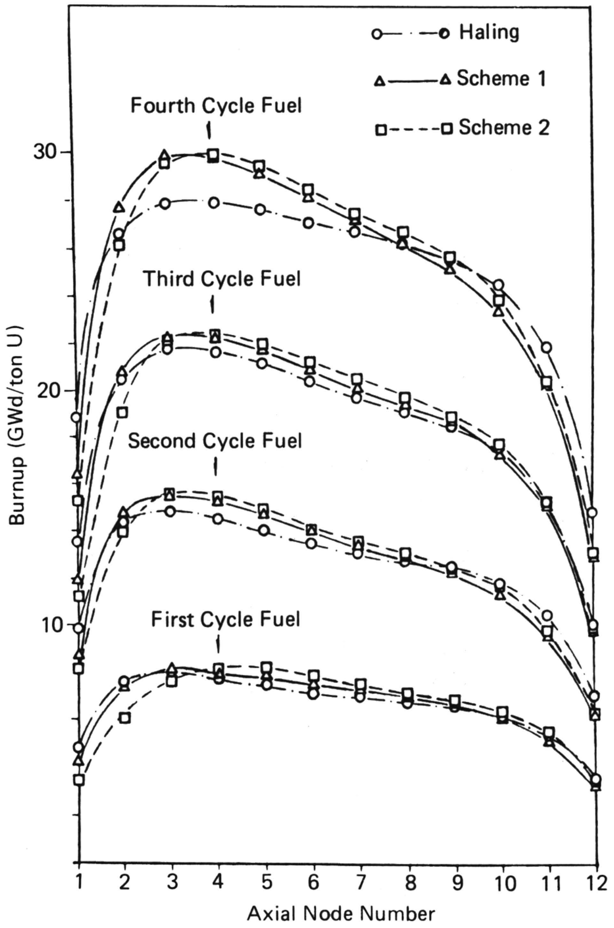

Fig. 9. EOC axial burnup shapes as a function of core residence.

period. A few preliminary runs indicated that longer periods between rod swaps could certainly be accommodated in the latter part of the cycle. A study of the optimal times between rod swaps, balancing the cost of derating during a rod swap against poorer power distributions, would be useful.

Although the nuclear model used in RODPRO has been compared with other results, these comparisons have not been made specifically for a CCC design. It is possible that the increased core heterogeneity might require some adjustments to group parameters to achieve the degree of precision desired. However, in the core configuration examined, tighter restrictions on peak power could be met. Any power distribution inaccuracies might therefore be dealt with by simply requiring a slightly lower peak power.

The RODPRO code avoids the simplifications that have made previous theoretical work impractical; RODPRO can greatly reduce the engineering time required for BWR control rod programming. The computational time for examination of a one-eighth core on an AMDAHL 470/V6 computer is only ~15 to 20 min. It is believed that a practical automated control rod programming procedure has been developed.

NOMENCLATURE

a_c = flow area per channel (length squared)

A_K = area of the boundary separating nodes I and K (cm^2)

A'_K = surface area of reflector boundary (cm^2)

$B_{i,j,k}$ = correlation constants

D_f = fast group diffusion coefficient (cm)

D_t = thermal group diffusion coefficient (cm)

F = relative channel flow rate (core average is 1.0)

G = mass velocity (mass/area·time)

h_K = distance from the center of node to the core-reflector boundary (cm)

H = number of diagonal assemblies replaced by the reflector

i = channel index

I = node index

J = node index

K = node index

k_∞ = infinite multiplication factor

k_{eff} = effective multiplication factor

l_K = distance between nodes I and K (cm)

m = total number of nodes under consideration

M = number of faces surrounded by the reflector

n = void iteration index

N = source iteration index

NA = number of assemblies in the whole core

Δp = pressure drop across channel (force/area)

$\overline{\Delta p}$ = average pressure drop over the entire core (force/area)

U = relative moderator density (dimensionless)

W = weighting factor

w = flow rate through channel (mass/time)

x_1 = location of core-reflector boundary (cm)

x_2 = location at which flux goes to zero (cm)

β = empirical weighting factor

κ_f = $K_f^2 = (\Sigma_f^a/D_f)^{1/2}$ (cm^{-1})

Σ_f^a = fast group macroabsorption cross section (cm^{-1})

Σ_f^f = fast group macro-fission cross section (cm^{-1})

Σ_t^a = thermal group macroabsorption cross section (cm^{-1})

Σ_t^f = thermal group macro-fission cross section (cm^{-1})

Σ_f^R = fast group macro-removal cross section (cm^{-1}) $= \Sigma_f^a + \Sigma_{f\to t}^s$

$\Sigma_{f\to t}^s$ = macro-scattering cross section from fast group to thermal group (cm^{-1})

ν_f = neutrons produced per fast fission

ν_t = neutrons produced per thermal fission

ϕ_f = fast group flux (1/cm^2·s)

ϕ_t = thermal group flux (1/cm^2·s)

ϕ_J^I = flux at interface between nodes I and J (1/cm^2·s)

$\bar{\phi}$ = node and surfaces average flux (1/cm^2·s)

ACKNOWLEDGMENT

The authors wish to express their thanks to Tom Crawford of R.D.I. for his helpful discussions and suggestions.

REFERENCES

1. R. K. HALING, "Operating Strategy for Maintaining an Optimum Power Distribution Throughout Life," *Proc. ANS Topl. Mtg.*, TID-7672, U.S. Atomic Energy Commission (1964).

2. R. L. CROWTHER, "Extensions of the Power-Control Method for Solution of Large Inhomogeneous Reactor Problems," ANL-7050, Argonne National Laboratory (1965).

3. W. B. TERNEY and H. FENECH, "Control Rod Programming Optimization Using Dynamic Programming," *Nucl. Sci. Eng.*, **39**, 109 (1970).

4. B. SYNDER and E. E. LEWIS, "Optimal Control Rod Policies for an Operating Cycle of a Simulated BWR Core," CONF-730414, p. II-56, U.S Atomic Energy Commission (1973).

5. W. C. WADE and W. B. TERNEY, "Optimal Control of Nuclear Reactor Depletion," *Nucl. Sci. Eng.*, **45**, 199 (1971).

6. H. MOTODA and T. KAWAI, "A Theory of Control-Rod Programming Optimization in Two-Region Reactors," *Nucl. Sci. Eng.*, **39**, 114 (1970).

7. A. SUZUKI and R. KIYOSE, "Maximizing the Average Fuel Burnup Over Entire Core: A Poison Management Optimization Problem for Multizone Light Water Reactor Cores," *Nucl. Sci. Eng.*, **44**, 121 (1971).

8. H. MOTODA, "Optimization of Control Rod Programming and Loading Pattern in Multiregion Nuclear Reactor by the Method of Approximation Programming," *Nucl. Sci. Eng.*, **49**, 515 (1972).

9. M. KITAMURA and H. MATODA, "Burnup Optimization Using Modal Expansion Method," *J. Nucl. Sci. Technol.*, **9**, 512 (1972).

10. T. KAWAI et al., "A Method for Generating a Control Rod Program for Boiling Water Reactors," *Nucl. Technol.*, **28**, 108 (1976).

11. R. L. CROWTHER et al., "Recent BWR Fuel Management Reactor Physics Advances," *Proc. Topl. Mtg. Advances in Reactor Physics and Core Thermal Hydraulics*, Kiamesha Lake, New York, September 22-24, 1982, NUREG/CP-0034, p. 271, U.S. Nuclear Regulatory Commission (1982).

12. S. R. SPECKER et al., "The BWR Control Cell Core Improved Design," *Trans. Am. Nucl. Soc.*, **30**, 336 (1978).

13. T. G. PIASCIK et al., "BWR Operating Experience at Millstone I with the Control Cell Core Improved Design," *Trans. Am. Nucl. Soc.*, **32**, 706 (1979).

14. L. E. FENNERN et. al., "Improved BWR Control Cell Core Design Concept," *Trans. Am. Nucl. Soc.*, **33**, 642 (1979).

15. R. L. CROWTHER et. al., "Advances in BWR Design for Extended Burnup," *Trans. Am. Nucl. Soc.*, **43**, 156 (1982).

16. B. LIN, B. ZOLOTAR, and J. WEISMAN, "An Automated Procedure for Selection of Optimal Refueling Policies for Light Water Reactors," *Nucl. Technol.*, **44**, 258 (1979).

17. W. L. ZHONG, "Partial Convergence Scheme for BWR Computations," *Research Annals of U.C. College of Engineering*, **83**, *118* (1983).

18. S. H. YEH, A. YING, and J. WEISMAN, "An Automated Procedure for Selecting BWR Refueling Policies Following Operational Problems or Changes," *Nucl. Technol.*, **61**, 78 (1983).

19. S. BORRESEN, "A Simplified, Coarse-Mesh, Three-Dimensional Diffusion Scheme for Calculating the Gross Power Distribution in a Boiling Water Reactor," *Nucl. Sci. Eng.*, **44**, 37 (1971).

20. W. L. ZHONG and J. WEISMAN, "RODPRO: A Computer Code for Automated Control Rod Programming in CCC Designs," *Research Annals of U.C. College of Engineering*, **83**, *117* (1983).

21. "EPRI NODE-B Code Manual," Electric Power Research Institute (1976).

DEVELOPMENT OF A SODIUM VAPOR PRESSURE METER USING BETA-ALUMINA CERAMICS

SUSUMU NINOMIYA, FUMIO OHTSUKA, and HIROMICHI NEI
Toshiba Corporation, Nuclear Engineering Laboratory
Ukishima-cho, Kawasaki-ku, Kawasaki 210, Japan

OSAMU TAKIKAWA and MITUO HARATA *Toshiba Corporation*
Research and Development Center, Komukai-Toshiba-cho
Saiwai-ku, Kawasaki 210, Japan

Received July 20, 1983
Accepted for Publication November 28, 1983

A program was carried out to develop a sodium vapor pressure measuring system using beta-alumina ceramics for use in developing sodium vapor traps and monitoring sodium mist in cover gas for fast breeder reactors (FBRs) and test facilities. The sensor device was tested in a vacuum glass capsule. Its output agreed well with theoretical results. Moreover, it proved to have the capability of measuring a lower vapor pressure near 10^{-5} Torr without any calibrations.

The measuring system, consisting of a beta-alumina sensor device, gas circulating pump, gas heater, and mist trap, is applicable to FBR plants and test facilities that contain much sodium mist and to a transient monitoring system. This system was tested in an isothermal sodium vapor circulation test loop under conditions involving much sodium mist.

INTRODUCTION

In sodium-cooled fast breeder reactors (FBRs), large amounts of sodium vapor and mist in a cover gas adhere to the inner walls of pipings, valves, and various equipment in the cover gas system. Together with the gas movement, the vapor, mist, and moving gas combination becomes a cause of plugging and functional disorder in the system. In order to prevent these problems, traps are widely used for the removal of sodium vapor or mist from the FBR.

Generally, high efficiency sodium removal, low pressure drop, and long service life are required for the vapor trap performance. The sodium vapor concentration measurement has been a key element, especially in transient phases, such as cover gas absorption, in developing a basic understanding of the phenomena.

An analysis of sodium vapor or mist concentration in the gap of the reactor roof has also been important when designing a reactor roof. Recently, in the sodium leak detection field, the need for a sodium concentration measurement technology has also arisen.

In regard to continuously monitoring the sodium concentration in cover gas, several different methods, including the electric discharge method,[1] had been suggested as being useful. Actually, however, a sampling method has been used because of the simplicity, which requires no calibration. However, a measurement by the sampling method usually takes 1 to 2 h, and it is impossible to continuously measure the sodium vapor concentration in the transient state.

Moreover, a large amount of gas must be sampled for a gas flowing system with low sodium concentration before it becomes feasible to use an analytic instrument. This fact is also unfavorable from the point of view of affecting the system conditions.

For this reason, the continuous on-line sodium vapor pressure meter development was planned using a beta-alumina solid electrolyte. Sodium ions are able to transmit through beta-alumina ceramics. The equilibrium electromotive force (emf) is proportional to the sodium vapor pressure difference between the two sides of ceramics. Beta-alumina has been applied to high-energy density sodium-sulfur batteries as electrolytes, whose characteristics have been published in some reports.[2,3]

A sodium vapor pressure measuring system, developed on a trial basis, proved to be fully usable without calibration in a sodium vapor and mist atmosphere.

BACKGROUND

When sodium vapor pressures are different on the two sides of a beta-alumina sheet, sodium ions have a tendency to transmit from the high-pressure to the low-pressure side, as shown in Fig. 1. In this case, a kind of sodium battery is formed so that the high pressure side becomes an anode and the other side becomes a cathode. The reaction equations are expressed by:

$$Na \rightarrow Na^+ + e^- \tag{1}$$

and

$$Na^+ + e^- \rightarrow Na \ . \tag{2}$$

The equilibrium emf E (in volts) is predicted by the Nernst equation:

$$E = \frac{RT}{nF} \ln \frac{P_1}{P_2} \ , \tag{3}$$

where

R = gas constant

T = sensor temperature (K)

n = number of charges at electrode reaction (n = 1 here)

F = Faraday constant

P_1 = primary sodium vapor pressure

P_2 = secondary sodium vapor pressure.

Therefore, if the primary sodium vapor pressure is kept at a known value, the secondary pressure can be calculated easily by using Eq. (3).

BETA-ALUMINA SENSOR

Figure 2 shows the sodium vapor pressure sensor. The beta-alumina cell is connected to an alpha-alumina tube with solder glass, and the alpha-alumina tube is hermetically sealed to a Kovar flange. The beta-alumina sensor is evacuated and ~3 g of sodium is enclosed in it. The inside sodium vapor pressure is calculated by the following formula[4]:

$$\log P = 6.354 - \frac{5567}{T_{Na}} - 0.5 \log T_{Na} \ , \tag{4}$$

where

P = saturated sodium vapor pressure (atm)

T_{Na} = sodium temperature (K).

The inner sodium temperature is measured by an inserted thermocouple. The thermocouple well, made of stainless steel, is also used as an inner cathode. A stainless steel mesh is wrapped around the beta-alumina cell for the anode.

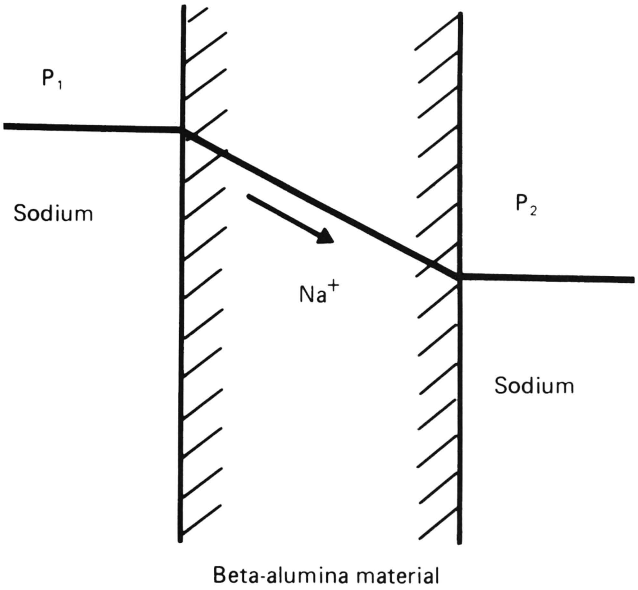

Fig. 1. Sodium ion current in a beta-alumina solid electrolyte.

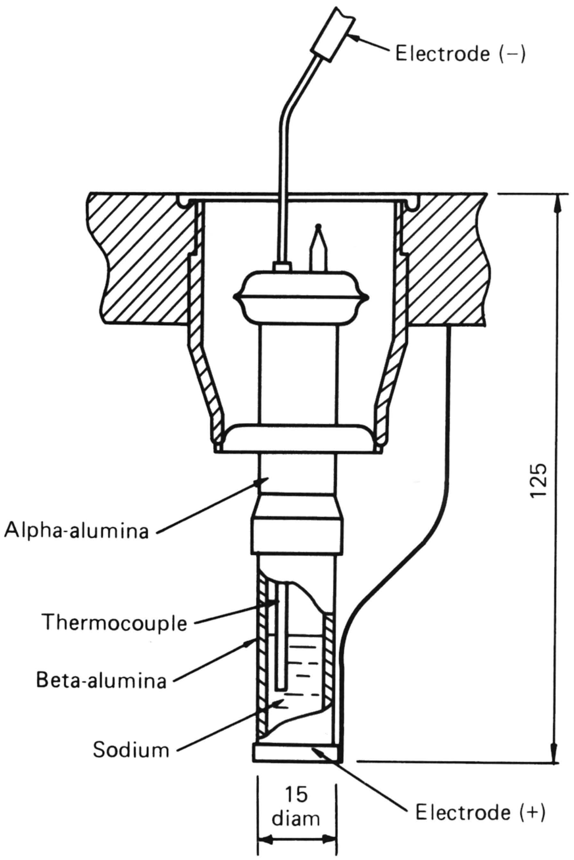

Fig. 2. Sodium vapor pressure sensor device configuration (measurements are in millimetres).

EXPERIMENT IN A GLASS CAPSULE

A preliminary test was performed in a glass capsule, as shown in Fig. 3, in order to check the emf from the beta-alumina sensor in a pure sodium vapor environment without inert gas or generated sodium mist. The glass capsule is 100 mm in diameter and 500 mm high, in which 30 g of sodium is inserted. The capsule was evacuated and baked at 400°C for 1 h to degas the construction material. The capsule was then hermetically sealed. Residual gas pressure was $<10^{-5}$ mm Hg at room temperature. The sodium was heated by a heater wrapped around the capsule so that it was filled with saturated sodium vapor at that temperature. The sensor temperature is always kept higher than the capsule sodium temperature, with separate controls for the two heaters around the sensor and the sodium in order to avoid sodium condensation on the beta-alumina sensor surface.

Therefore, as the reference vapor pressure is always kept higher than the outside pressure, a small amount of sodium permeates through the beta-alumina wall. Figure 4 shows test results indicating the relation between the output (emf) and the sodium vapor pressure, with changing sodium temperature in the capsule as a parameter. The lines show calculated sodium vapor pressures from Eq. (3) and agree with the experiments. Although it was hard until now to measure such a low sodium vapor pressure as 10^{-4} to 10^{-6} Torr, it has become possible to detect as far as 10^{-6} Torr orders of magnitude. Moreover, it was proved that calibration is unnecessary for this method.

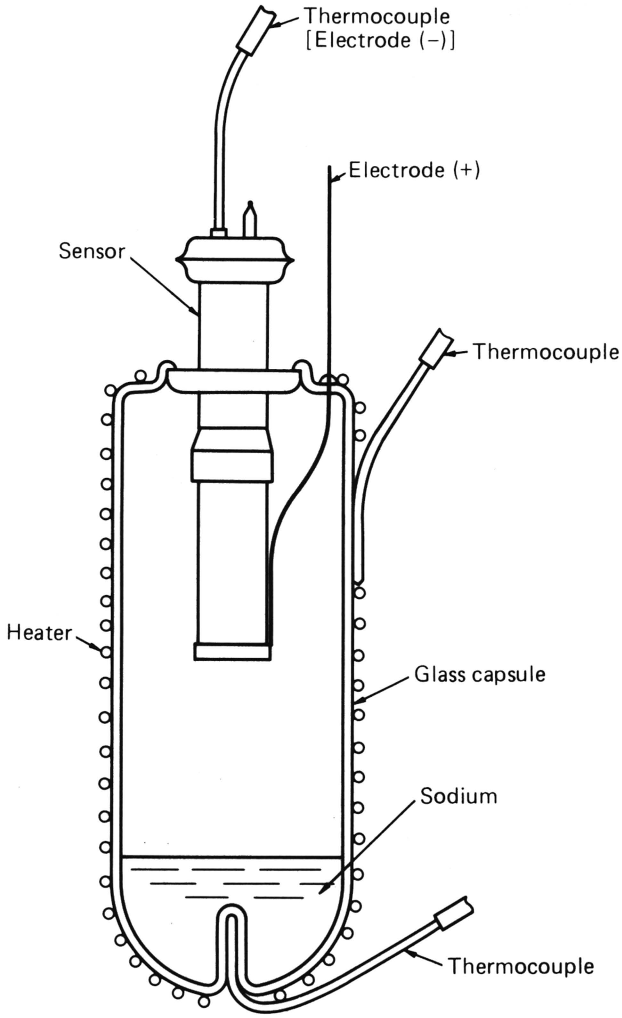

Fig. 3. Laboratory apparatus for testing a sensor in a vacuum glass capsule.

EXPERIMENT IN A TEST LOOP CIRCULATING SODIUM VAPOR/MIST AND COVER GAS

Sodium Vapor Concentration Measuring Unit

Generally, a large amount of sodium mist exists in the cover gas in actual sodium loops and FBR plants. The amount is estimated to increase exponentially with temperature increase.

On the other hand, the emf for this beta-alumina sensor is in proportion to the vapor pressure, only as described previously. Therefore, sodium mist must be vaporized completely around the beta-alumina sensor surface in order to measure all the sodium accurately.

If liquid sodium or sodium mist adheres on the beta-alumina surface, the sodium vapor pressure around the device becomes saturated at surface temperature, so that the difference between inner and outer surface sodium vapor pressure becomes zero.

Therefore, the sodium vapor concentration measurement unit was designed considering these factors, as shown in Figs. 5 and 6. A heating vessel with a beta-alumina sensor on the upper part was installed to completely vaporize the sodium mist. A circulation

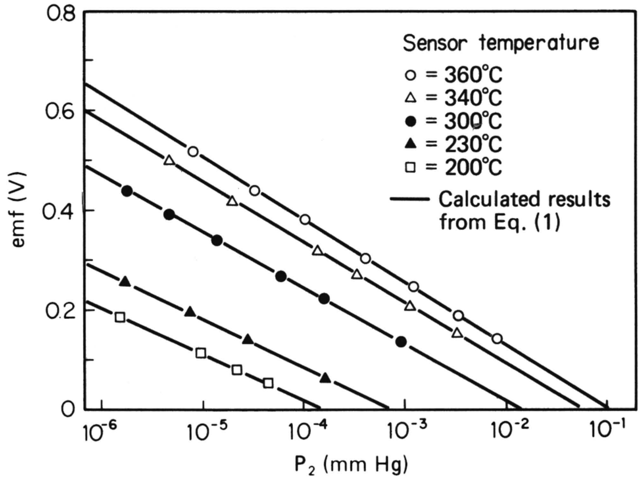

Fig. 4. The emf versus sodium vapor pressure in a vacuum glass capsule calculated from sodium pool temperature.

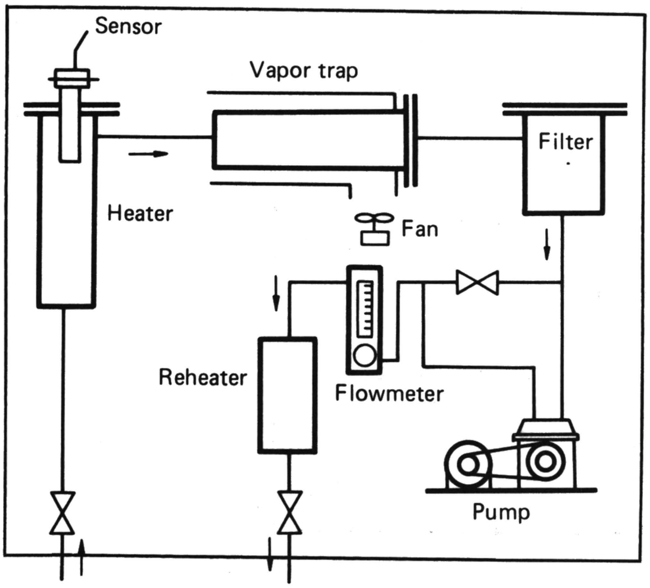

Fig. 5. Sodium vapor concentration measuring unit layout.

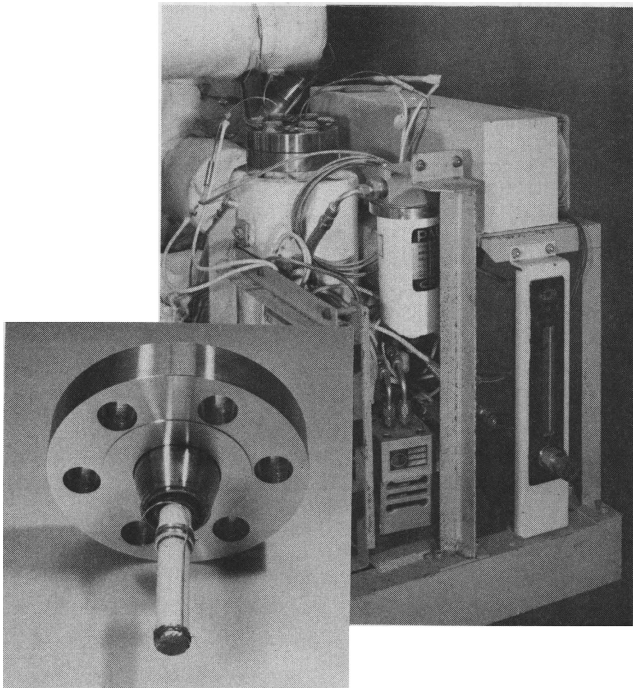

Fig. 6. Sodium vapor sensor and measuring unit.

pump was installed to introduce the gas from the system at a constant flow rate.

Measurement in an Isothermal Sodium Vapor Circulation Loop

A test was performed using an isothermal sodium vapor forced circulation test loop that included a sodium evaporator, as shown in Fig. 7. The sodium vapor concentration measuring unit, shown in Fig. 5 by the box, was installed at the nozzle. The objective of this experiment was to compare the sensor output emf in an actual sodium vapor circulation loop with calculated results. In this test run, the same kind of beta-alumina sensor was also set up on the top of the sodium evaporator in order to confirm the reproducibility of the sensor and the reappearance of the output from the sensor itself in the sodium vapor circulation loop after the preceding glass capsule test. On the other hand, the purpose of the unit sensor is to check and develop the total system for the measurement unit, i.e., to test the sampling and the vaporization of the sodium mist, to confirm the reliability of the filter and the pump, and to check the control method and the level of the unit temperature.

Figure 8 shows the two sensor emfs brought about by changes in the sodium evaporator temperature. The emf from the sensor set up on the evaporator agrees with calculated saturated values at sodium temperature. As the sodium temperature decreases, the emf becomes lower, in comparison with calculated value. This situation is assumed to be caused by the low sodium evaporating rate from the sodium surface in the evaporator under 5 ℓ/min argon gas circulating flow rate conditions. The actual sodium vapor pressure around the sensor was estimated to be lower than

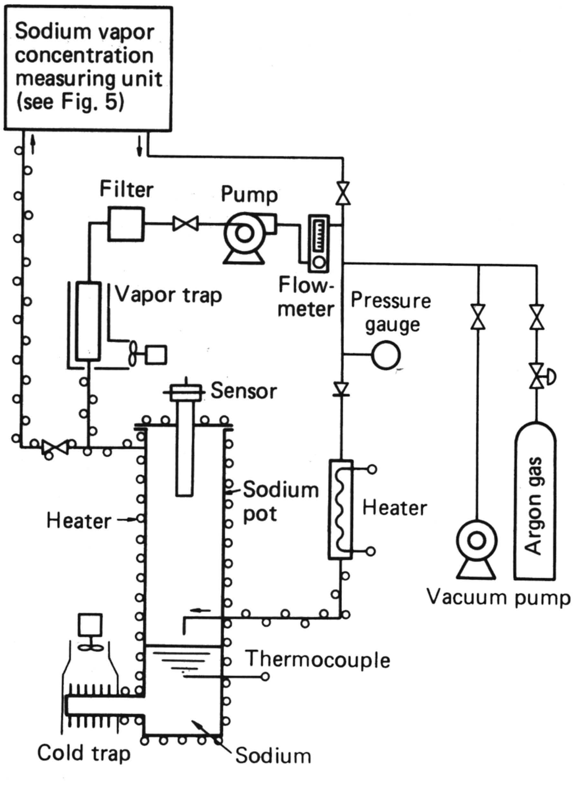

Fig. 7. Sodium vapor forced circulation test loop.

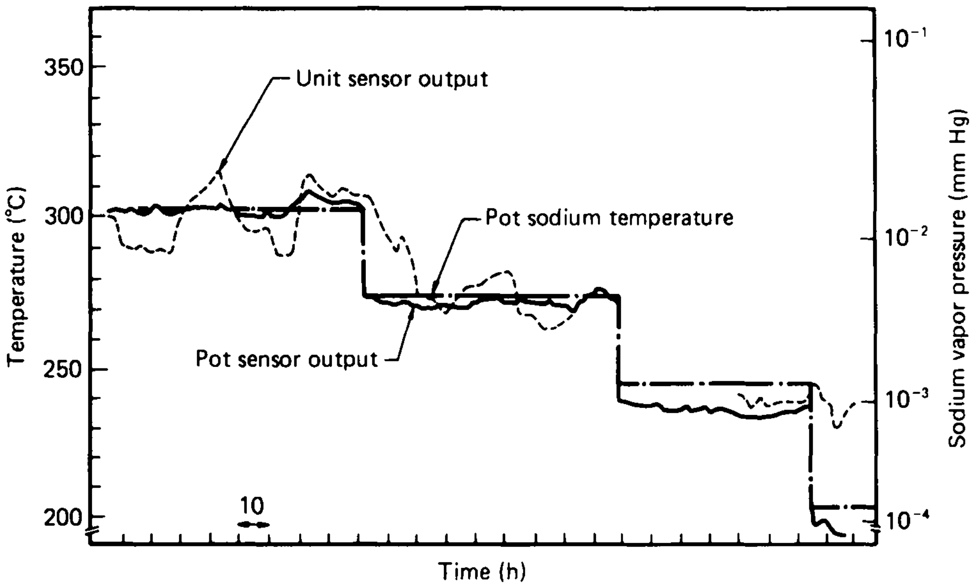

Fig. 8. Comparison between continuous measurement results from pot and unit sensors.

the saturated value calculated from the sodium temperature in the evaporator, so that the indicated emf is probably a correct value. Otherwise, the sensor emf in the unit is fluctuated in comparison with the other sensor. The reason is that the temperature at the unit entrance nozzle is disturbed a little, so sodium condenses and evaporates alternately on the inner surface of the nozzle. This phenomenon is also caused by the fact that the average emf value is close to the value calculated from the local sodium temperature. Therefore, the sensor emf probably indicates the true vapor pressure around it.

Figure 9 shows the relation between detected sodium vapor pressure and the sodium pool temperature.

Figure 10 shows the sensor response curve at

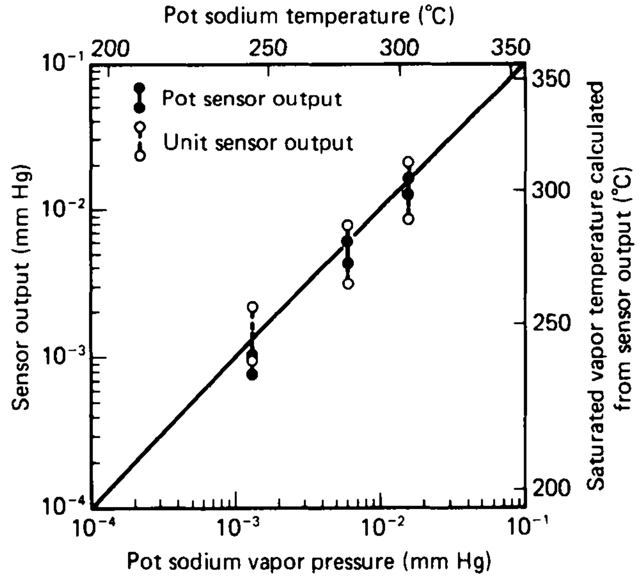

Fig. 9. Fluctuation range in the forced circulation test loop.

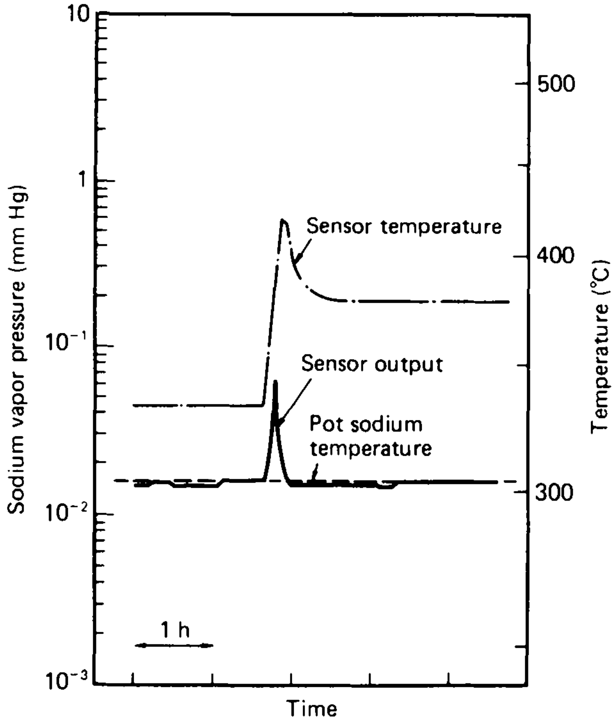

Fig. 10. Sensor output with changing sensor temperature.

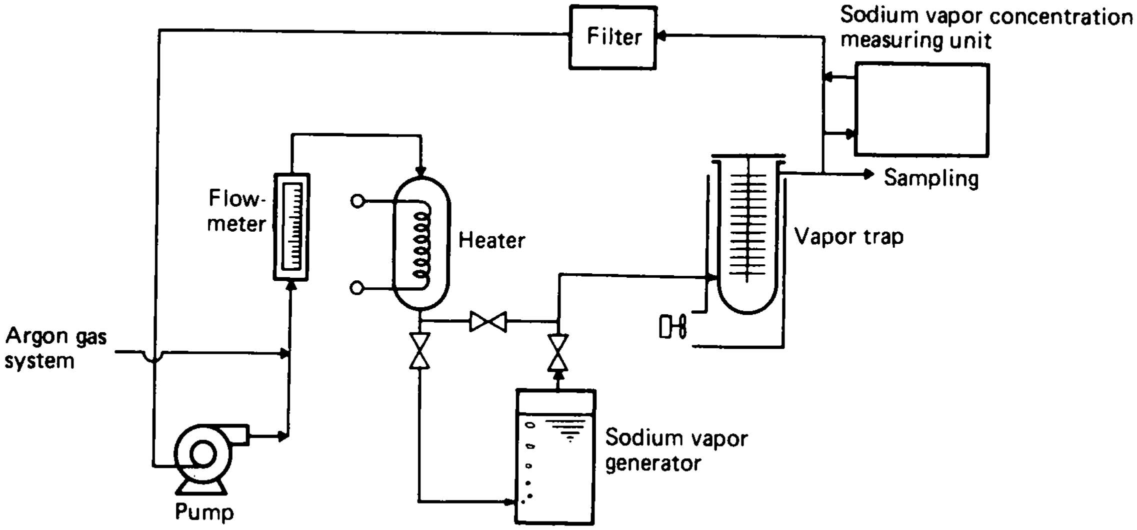

Fig. 11. Vapor trap test loop.

changed sodium reference temperatures in the beta-alumina cell, while keeping the circulated sodium vapor and gas constant. In this run, the sensor temperature was changed from 330 to 380°C. The sensor emf was the same value as that calculated from Eq. (1) when both sensors were in the steady state.

Experiment in the Sodium Loop Containing Sodium Mist

This test was performed to check whether or not the sodium mist sampled from the sodium loop was completely vaporized in the heater and indicates the total sodium concentration.

A vapor trap test loop, shown in Fig. 11, was used in this test, because a constant supply of sodium vapor and mist was required. Saturated sodium vapor at ~500°C flowed into the vapor trap and was cooled to 130°C at the outlet. Some sodium vapor was trapped in the vapor trap and the rest was carried over. The sodium vapor detector unit, shown in Fig. 5, was set up at the vapor trap outlet nozzle. Some vapor and mist was introduced into the unit. The nozzle temperature was kept at 350°C at the small vapor trap in the unit, and the gas flow rate was regulated to 5 ℓ/min.

Figure 12 shows the device emf from the beginning of the test. The dots show results obtained from the other nozzle at the vapor trap outlet, using the usual sampling method. The dotted line shows the average value during this run calculated from the measurement of all the sodium deposited on the small vapor trap and filter in the unit.

Since the vapor trap outlet temperature was kept at 130°C, the amount of sampled sodium mist in the unit was several thousand times that of sodium vapor. It was proved to be completely vaporized and detected.

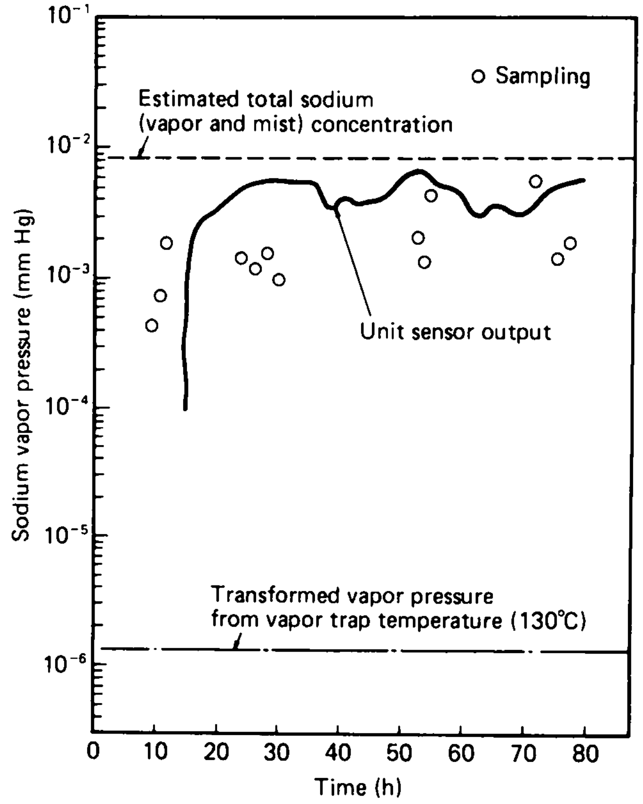

Fig. 12. Unit sensor output in the vapor trap outlet.

DISCUSSION

When processing a sodium vapor detector with a beta-alumina solid electrolyte, the problem is the amount of heat that the seal material used between beta- and alpha-alumina can withstand. The maximum operating temperature for this sensor device is limited by the seal material. Therefore, the maximum measurable sodium vapor concentration is the saturated value in equilibrium with the maximum temperature. This temperature is ~350°C. The sensor has been used for ~1000 h at 350°C and a few hours at 420°C in steady state. No trouble, however, occurred.

When the beta-alumina sensor device is used for a sodium system in which the sodium vapor or mist concentration changes momentarily, the device response time becomes an important problem. Since the electrochemical transport time for sodium ions in beta-alumina itself is estimated to be a few milliseconds, it seems to suggest that the critical delay time is generally induced by sodium vapor diffusion to the sensor surface. For this problem, since a forced absorption unit was adopted in this test, the sodium vapor transport delay time could be short.

On the other hand, it is reported that beta-alumina has a property whereby it responds sensitively to oxygen. Therefore, if an oxidized layer adheres on the sensor device surface, it does not indicate sodium vapor pressure exactly and accurately. In this test, the emf became a very high voltage during 20 to 50 h from the beginning of the test, as shown in Fig. 12. After that, the sensor device indicated normal voltage. This seems to be because the sensor device's surface had been cleaned by sodium vapor/mist.

CONCLUSION

A sodium vapor pressure detector and a measuring unit have been developed using a beta-alumina solid electrolyte. The results obtained in this study can be summarized as follows:

1. Sodium vapor pressures from 1.65×10^{-1} to 2.78×10^{-6} Torr at equivalent saturated sodium temperatures from 305 to 140°C were measured continuously without any calibrations.

2. Sampled sodium mist was vaporized completely by the heater in the measuring unit. This measuring unit is useful for measuring sodium concentration in a sodium loop that includes sodium mist.

REFERENCES

1. K. ONODERA et al., "Sodium Vapor Detector," Preprint 1971 Fall Meeting, Atomic Energy Society of Japan(I), E5 (1971) (in Japanese).

2. N. WEBER and J. T. KUMMER, "A Sodium-Sulfur Secondary Battery," *Proc. ASME Conf. Intersociety Energy Conversion Engineering*, Miami Beach, Florida, August 13-17, 1967, p. 913, American Society of Mechanical Engineers (1967).

3. A. IMAI and M. HARATA, "Ionic Conduction of Impurity/Doped Beta-Alumina Ceramics," *Japan J. Appl. Phys.*, **11**, 180 (1972).

4. R. W. DITCHBURN and J. C. GILMOUR, "The Vapor Pressure of Monatomic Vapors," *Rev. Mod. Phys.*, **13**, 310 (1941).

ELECTRICALLY ENHANCED DEPOSITION OF A CONFINED AEROSOL IN THE PRESENCE OF IONIZING RADIATION

ROBERT A. FJELD and THOMAS J. OVERCAMP
Clemson University, Environmental Systems Engineering
Clemson, South Carolina 29631

Received September 6, 1983
Accepted for Publication November 28, 1983

The effect of an electric field on the deposition of a confined aerosol in the presence of ionizing radiation is determined experimentally. A method to determine depositional rate coefficients from measurements of steady-state relative aerosol concentrations in a continuously reinforced chamber is used to obtain experimental data for monodisperse aerosols. Results were obtained for 0.1- and 0.5-μm-diam polystyrene aerosols in a 6000-cm^3 container in which the average air absorbed dose rate is 0.22 Gy/h (22 rad/h). Data are obtained in the absence and in the presence of an externally applied electric field of 10^5 V/m.

Significant reductions in aerosol concentration were observed in the chamber upon application of the electric field. In the absence of ionizing radiation, the depositional rate coefficient increases by a factor of 5 to 10. In the presence of ionizing radiation it increases by more than two orders of magnitude. Based on these results, it is concluded that electrical deposition may have potential use as the basis for a technique to reduce concentrations of nuclear aerosols.

INTRODUCTION

The behavior of the aerosol produced in a degraded core accident is governed by a number of physical processes—nucleation, condensation, coagulation, gravitational settling, and various depositional mechanisms.[1-3] In the normal evolution of the postaccident aerosol, electrical effects are generally considered unimportant because particles are assumed to be neutralized by positive and negative ions that are continuously produced by the ionizing radiation.[4] However, if an electric field is present, the situation changes. The field serves to separate positive and negative ions, creating regions where particles can acquire substantial levels of charge. Once charged, particles can be influenced by the electrophoretic force, and electrical effects can play a significant role in the evolution and fate of the aerosol.

One electrical effect of potential importance is enhanced deposition. From experiments in a flow system,[5,6] it is known that ionizing radiation and an electric field can be used to remove suspended particles from a gas stream. A logical extension in the nuclear safety context is the use of an electric field as the basis for an engineered feature to reduce the aerosol source term. To assess the scientific feasibility of the idea, data are needed for demonstrating the effect of ionizing radiation and an electric field on aerosol concentrations in a confined space and for quantifying the effects. Presented in this paper are results of bench-scale experiments conducted on 0.1- and 0.5-μm-diam aerosol in an electric field of 10^5 V/m and an ion generation rate on the order of $10^{13}/\text{m}^3\cdot\text{s}$ (~22 rad/h). It is found that the electric and radiation fields combine to reduce significantly aerosol concentrations and that the effect can be quantified experimentally in terms of a depositional rate coefficient.

THEORY

The postaccident aerosol in containment evolves as a consequence of a variety of particle growth and removal processes along with convective mixing. The behavior of particles of a given size may be described by the following kinetic equation[7]:

$$\begin{aligned}\frac{\partial n}{\partial t}(\bar{r},t) + \nabla\cdot n(\bar{r},t)\bar{v} &= \nabla\cdot(D+\epsilon)\nabla n(\bar{r},t) - \nabla\cdot n(\bar{r},t)\bar{c} \\ &\quad + g(\bar{r},t) - l(\bar{r},t)\ , \qquad (1)\end{aligned}$$

where

n = particle concentration

$\bar{r}$ = position vector

dV = volume element

$\bar{v}$ = fluid velocity vector

D = particle diffusion coefficient

ϵ = turbulent eddy diffusivity

$\bar{c}$ = particle velocity due to external forces

g, l = particle gain or loss rate per unit volume.

The first term on the left side of Eq. (1) is the rate of change of particle concentration in dV at time t. The second term represents convective transport, assuming that the particles move with the fluid. The first term on the right side represents transport due to Brownian plus turbulent diffusion, and the second represents transport due to external forces. The gain and loss terms represent particle generation and processes such as coagulation, nucleation, and condensation.

A mixed chamber is one in which convective mixing maintains a uniform aerosol concentration, N, everywhere except within a small distance, δ, of surfaces. An equation for the concentration as a function of time in a mixed chamber can be obtained by operating on Eq. (1) with the volume integral, $\int dV$, and subsequently applying the divergence theorem to the first two terms on the right side of the equation. The result is

$$\begin{aligned}\frac{dN(t)}{dt} &- S_i(t) + S_0(t) \\ &= G(t) - L(t) - \frac{N(t)}{V} \\ &\times \oint\!\!\!\oint_A \left[\left(\frac{D+\epsilon}{\delta}\right) + c_n\right] dA \ , \end{aligned} \tag{2}$$

where

$$N(t) = \frac{1}{V}\int n(\bar{r},t)\,dV$$

$$G(t) = \frac{1}{V}\int g(\bar{r},t)\,dV$$

$$L(t) = \frac{1}{V}\int l(\bar{r},t)\,dV \ ,$$

and where

S_i and S_0 = aerosol input and leakage, respectively

V = chamber volume

δ = boundary layer thickness

c_n = normal component of particle velocity due to external forces.

The third term on the right side of Eq. (2) represents particle deposition on surfaces in the chamber. This term may be written as NR, where R is a depositional rate coefficient. If the depositional mechanisms are assumed to be independent, $R = \Sigma R_i$, where the R_i are rate coefficients for the various mechanisms. Diffusional, gravitational, and electrical depositions are given by

$$R_d = \frac{D+\epsilon}{\delta}\left(\frac{A_s}{V}\right) \tag{3a}$$

$$R_g = v_t\left(\frac{A_f}{V}\right) \tag{3b}$$

$$R_e = Z_p E\left(\frac{A_e}{V}\right) \ , \tag{3c}$$

where

v_t = gravitational settling velocity

Z_p = particle electrical mobility

E = electric field strength

A_s, A_f, and A_e = chamber surface area, floor area, and electrode area, respectively.

In terms of the depositional rate coefficients, Eq. (2) becomes

$$\frac{dN}{dt} - S_i + S_0 = G - L - R_d N - R_g N - R_e N \ . \tag{4}$$

As seen in Eq. (3c), electrical deposition depends on particle mobility and electric field strength. Particle electrical mobility is proportional to particle charge, namely,

$$Z_p = \frac{n_c q_e}{3\pi\eta D_p C} \ , \tag{5}$$

where

n_c = number of elementary charges carried by a particle

q_e = elementary charge unit (1.6×10^{-19} coul)

η = absolute viscosity

D_p = particle diameter

C = Cunningham correction factor.

Particles acquire charge from gaseous ions produced by ionizing radiation in the presence of an external electric field. The electric field causes positive and negative ions to drift in opposite directions and results in the creation of regions where there exist imbalances in positive and negative ion conductivity. In regions where positive ions dominate, the net charging rate is positive. In regions of negative ion dominance, it is negative. The spatial variation of positive and negative ion conductivities depends on the electric field strength and the ion generation rate. For example, the positive conductivity due to uniform ion generation between parallel plate electrodes increases linearly, from zero at the positive plate to a maximum at the negative plate. The negative conductivity decreases from a maximum of the positive plate to zero at the negative plate. In general, the conductivities are determined by solving simultaneously the positive and negative ion continuity equations and Poisson's equation.[8]

The charge acquired by a particle exposed to bipolar ions ultimately reaches a steady-state level, the magnitude of which depends on the positive to negative ion conductivity ratio, electric field strength, particle size, and particle dielectric constant.[9] The conductivity ratio varies from zero (unipolar negative) at the positive plate to unity (equal bipolar) at a point between the plates and then to infinity (unipolar positive) at the negative plate. The corresponding net particle charge changes from highly negative to zero to highly positive. Particle charge increases with increasing electric field strength and particle diameter, and it is higher for conducting particles than it is for insulating particles.

When the positive and negative conductivities are equal, the aerosol obtains a state of minimum charge. This minimum, or "neutral," charge state is referred to as Boltzmann equilibrium and is characterized by a distribution having a mean of zero and decreasing numbers of particles with ±1, ±2, ±3, etc. charges.[10]

In a mixed chamber, the particle charging and deposition problem is difficult to address theoretically because mixing causes particles to traverse regions where the charging conditions vary. In fact, the possibility exists for particles to move from a region where the net charging rate changes sign from positive to negative or vice versa. Complicating the situation is the superposition of electrical transport on fluid transport, once the particles acquire charge. The electrical force causes particles to move toward regions where the magnitude of charge increases. Thus, once electrical transport begins to dominate convective transport, a particle should quickly be deposited.

EXPERIMENT

Laboratory experiments were conducted to determine if significant electrical deposition could be observed for submicrometre aerosols and to measure the depositional rate coefficients. The apparatus (Fig. 1) consisted of an aerosol generation system, a test chamber, and an aerosol detector. The apparatus, experimental procedure, and data analysis are discussed below.

Apparatus and Procedure

Highly monodisperse 0.1- or 0.5-μm-diam aerosols of polystyrene spheres[a] were generated by air blast atomization[11] of dilute (~0.1% solids by mass) aqueous suspensions. The liquid feed rate to the atomizer ranged from 0.5 to 1 cm^3/min. The liquid was

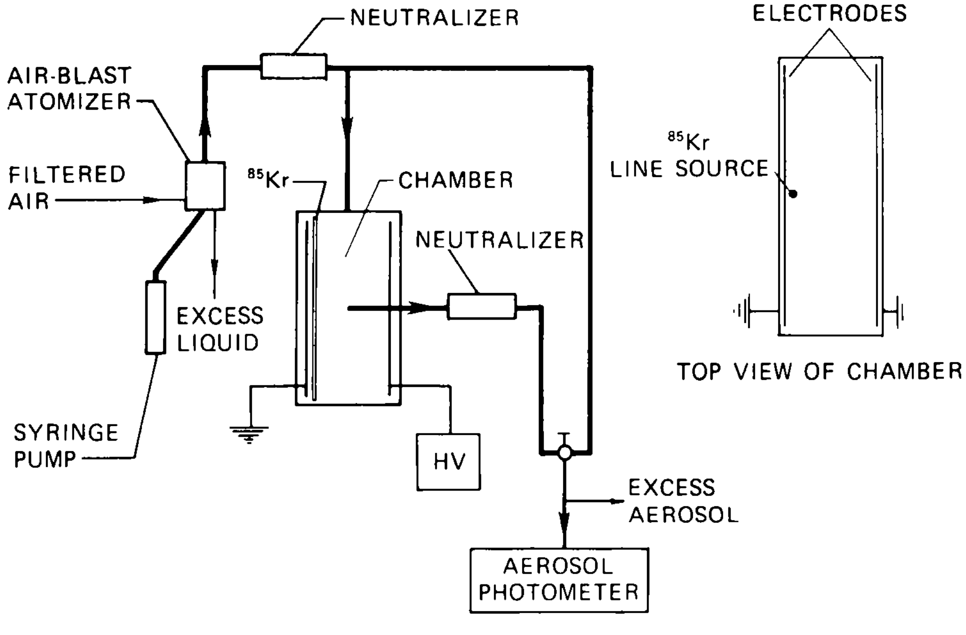

Fig. 1. Schematic of the experimental apparatus, including a top view of the chamber.

---

[a] Dow Chemical Company.

atomized by filtered air supplied through a 0.34-mm orifice at a flow rate of ~50 cm^3/s. The aerosol then flowed through a ^{210}Po charge neutralizer to minimize aerosol charge before entering the chamber. The aerosol concentration in the inlet stream was 500 to 1000/cm^3 for 0.5-μm-diam particles and ~10^4/cm^3 for 0.1-μm-diam particles.

The aerosol was introduced into the top of a 6000-cm^3 chamber (10 cm wide × 20 cm long × 30 cm high). Parallel plate electrodes (20 × 30 cm) were located on two opposing walls of the chamber. One plate was connected to a dc high voltage supply and the other one was grounded. The plate separation was 10 cm. Guard wires were situated on the periphery of the test region, between the plates, to maintain a uniform electric field in the chamber. A 3.7×10^8 Bq (10-mCi) line source of ^{85}Kr[b] could be inserted into the chamber, adjacent to the grounded electrode. The average absorbed dose rate in the chamber, based on measurement of the net saturation current to the grounded plate, was ~0.22 Gy/h (22 rad/h).

The chamber concentration was measured continuously through a tube inserted into the center of the chamber. The aerosol was immediately sent through a neutralizer to prevent electrostatic removal in subsequent sampling lines or in the aerosol detector. A photometer,[c] modified by routing the output current from the photomultiplier tube to a more sensitive electrometer,[d] was used to detect the aerosol. Although the response of the photometer decreases significantly between 0.5 and 0.1 μm, the concentration of 0.1-μm-diam particles was sufficiently large to yield a detectable current.

The test procedure was as follows. First, the inlet concentration was measured. With $E = 0$, the steady-state concentration in the chamber was measured. The inlet concentration was then checked and the electric field ($E = 10^5$ V/m) was applied. The chamber concentration was subsequently measured as a function of time until steady state was again reached. The inlet concentration was then rechecked. The above procedure was followed both with the source absent and with the source present.

Data Analysis

In the experiments, particles are fed into the chamber from the aerosol generator and extracted for sampling. The flow terms in Eq. (4) thus become $S_i = N_i Q/V$ and $S_0 = NQ/V$, where N_i is inlet concentration, N is chamber concentration, and Q is volumetric flow rate. The only gain or loss mechanism of possible significance is coagulation. However, even if coagulation is enhanced by electrical forces, calculations based on theory[7,12] indicate it to only become important for a particle concentration on the order of 10^8/cm^3. This is well in excess of particle concentrations in these experiments. This leaves deposition as the only process within the chamber that affects the aerosol concentration, and Eq. (4) reduces to

$$\frac{dN}{dt} = \frac{Q}{V}(N_i - N) - RN \ . \tag{6}$$

In terms of the relative concentration, $f = N/N_i$, Eq. (6) becomes

$$\frac{df}{dt} = \frac{Q}{V} - f\left(R + \frac{Q}{V}\right) \ . \tag{7}$$

Depositional rate coefficients are determined from steady-state measurements of f. The steady-state relative concentration is

$$f_{ss} = \frac{Q/V}{(R + Q/V)} \ . \tag{8}$$

Since the flow rate and chamber volume are known, Eq. (8) can be used to determine the rate coefficient, namely,

$$R = \frac{Q}{V}\left(\frac{1 - f_{ss}}{f_{ss}}\right) \ . \tag{9}$$

Equation (9) gives the total depositional rate coefficient. The electrical depositional rate coefficient is determined by finding R in the absence of the electric field and R' in its presence. Since the diffusional and gravitational coefficients are the same in each test, the electrical coefficient is obtained by subtraction:

$$R_e = R' - R \ . \tag{10}$$

RESULTS

Results of an experiment with 0.1-μm-diam aerosol are shown in Fig. 2, where the ratio of chamber concentration to inlet concentration is displayed as a function of time. An initial steady-state concentration of 0.8 was observed under conditions of negligible radiation dose rate (i.e., background levels) and zero electric field strength. On application of an electric field of 10^5 V/m, the concentration decreased to ~0.4. It returned to the initial level of 0.8 when the electric field was removed. Following insertion of the source, the concentration climbed to ~0.9. Then, on application of the electric field, the concentration decreased rapidly to a steady-state level of 0.05. This latter decrease was observed again following a subsequent off/on cycle of the field.

Data for 0.5-μm-diam aerosol are presented in Fig. 3. Shown here is relative concentration following application of the electric field in the absence (Fig. 3a)

---

[b] 3-M Corporation.

[c] Royco 230.

[d] Keithley 610B.

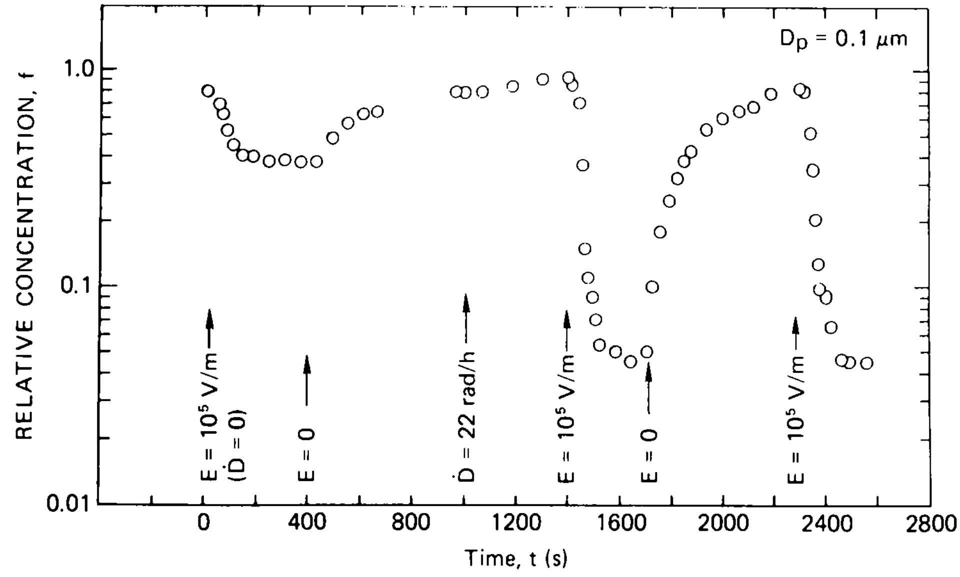

Fig. 2. Relative concentration as a function of time for 0.1-μm-diam aerosol.

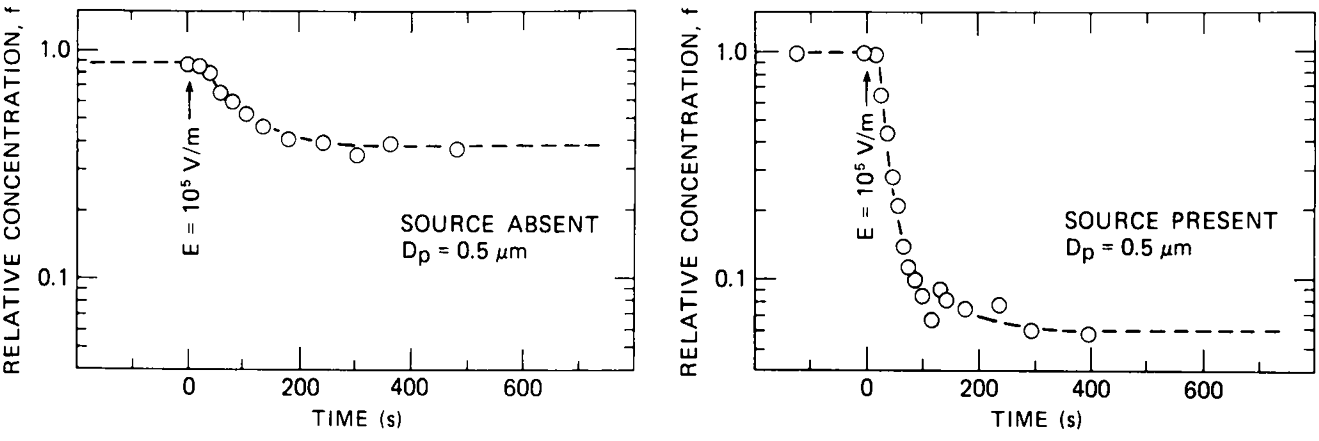

(a) (b)

Fig. 3. Relative concentration as a function of time for 0.5-μm-diam aerosol following application of a 10^5 V/m electric field.

and in the presence (Fig. 3b) of the source. In the absence of ionizing radiation, the concentration decreased from ~0.87 to <0.4 after application of the field. In the presence of ionizing radiation, it decreased from 1.0 to 0.07.

From these data it is seen that the electric field had a significant impact on aerosol concentration and that the effect was enhanced by ionizing radiation. These effects can be explained by particle charge levels. In the absence of ionizing radiation, those particles in the entering aerosol that possess a sufficient number of charges are deposited on the electrodes by the electric field. The particles are given charge in the process of being atomized. This charge is then reduced as the aerosol passes through the neutralizer. (However, as noted later, complete neutralization to Boltzmann equilibrium may not have occurred.) In the presence of ionizing radiation and the electric field, particle charge levels are increased and a greater fraction of the particles are deposited. As explained in the theory section, a region of positive ion dominance adjacent to the negative electrode and a region of negative ion dominance near the positive electrode are responsible for the increase in particle charge.

The observations of relative aerosol concentration can be used to quantify deposition processes through Eqs. (9) and (10). Results are given in Table I. The total depositional rate coefficient increased by a factor of between 5 and 10 when the field was applied in the absence of ionizing radiation. It increased more

TABLE I

Total and Electrical Depositional Rate Coefficients

D_p (μm)	E (V/m)	Dose Rate (rad/h)	f_{ss}	R (s^{-1})	R_e (s^{-1})
0.1	0	0	0.8	0.0025	0.0
0.1	10^5	0	0.38	0.016	0.014
0.1	0	22	0.9	0.0009	0.0
0.1	10^5	22	0.05	0.19	0.19
0.5	0	0	0.87	0.0014	0.0
0.5	10^5	0	0.36	0.016	0.015
0.5	0	22	1.0	<0.0005	0.0
0.5	10^5	22	0.072	0.12	0.12

TABLE II

Particle Charge Calculated from the Electrical Depositional Rate Coefficient

D_p (μm)	E (V/m)	Dose Rate (rad/h)	R_e (s^{-1})	Z_p ($m^2/V \cdot s$)	N_c
0.1	10^5	0	0.014	7×10^{-9}	0.27
0.1	10^5	22	0.19	9.5×10^{-8}	3.6
0.5	10^5	0	0.015	7.5×10^{-9}	3.0
0.5	10^5	22	0.12	6×10^{-8}	24

than two orders of magnitude when the field was applied in the presence of ionizing radiation.

Estimates of particle charge using the experimental electrical depositional rate coefficients and Eqs. (3c) and (5) are given in Table II. The charge levels are reasonable based on comparisons with aerosol charging data available in the literature.[9,10,13]

Although the principal objective of these experiments was to determine the effects of ionizing radiation and an electric field on aerosol deposition, effects of ionizing radiation alone are suggested by the data. For both particle sizes, there was a small but measureable reduction in aerosol concentration in the absence of both radiation and the electric field. Since gravitational settling and coagulation were negligible, it is likely that this was due to diffusive deposition. The experimental depositional rate coefficient calculated for 0.1-μm-diam particles is larger than that for 0.5-μm-diam particles. Qualitatively, this is consistent with theory for deposition by convective diffusion.[12] With ionizing radiation present, aerosol concentration increased (Figs. 2 and 3 and Table I). In fact, for 0.5-μm-diam particles the chamber concentration was equal to the inlet concentration, indicating negligible deposition. A possible explanation for this reduction of deposition is that particle charge, through the electrical image force, played a role in deposition. It is conjectured that the input aerosol either was not fully neutralized or possessed a broader charge distribution than the Boltzmann equilibrium distribution and that deposition of particles in the high charge portion of the distribution was enhanced by the electrical image force. In the ionized chamber, however, the charge distribution was reduced to Boltzmann equilibrium, with a consequent reduction in image force deposition. A direct measure of particle charge distributions would need to be made to confirm the suspicion of non-Boltzmann charge on the input aerosol.

DISCUSSION

To evaluate the use of an electric field as the basis for an engineered safeguard, the dependence of the electrical depositional rate coefficient would need to be determined as a function of electric field strength, absorbed dose rate, and mixing intensity. The electrical effects are expected to vary as the square of electric field strength. This is because the electrical depositional coefficient is proportional to the product of electric field strength and particle electrical mobility. Particle mobility is proportional to particle charge, which, in turn, is proportional to electric field strength. At the very high dose rates expected following a degraded core accident, space charge effects would decrease the electric field in the central region of the chamber, but would increase the field near the electrodes. Since it is likely that most of the enhanced removal is due to charging and electrical transport occurring near the plates, rather than in the bulk of the chamber, electrical deposition should increase with increasing dose rate. With increasing mixing intensity, it is expected that the electrical effects would decrease in importance. This is due to an increase in convective transport of charged particles of one polarity to regions where ions of opposite polarity are dominant, the result being a lowering of particle charge.

Another consideration in evaluating electrical effects is aerosol concentration. A very dilute aerosol was used in these experiments in order to isolate and thereby quantify the effect of ionizing radiation and an electric field. The aerosol in containment following a degraded core accident could be over a million times more concentrated. A thick layer of high resistivity particles on an electrode could cause a significant reduction of electric field strength. In addition, at high concentrations coagulation can play a major role in aerosol dynamics. Electrical effects could either enhance or retard coagulation, depending on the extent of mixing of positively and negatively charged particles. In very high electric fields, coagulation could be enhanced, especially for particles that may have agglomerated to form a colinear chain.

The well-mixed model, because it is based on the assumption of homogeneity throughout the bulk of the chamber, may not be appropriate for electrical effects. Particle mobilities are not constant across the chamber, and they depend on the intensity of mixing in the chamber. The electrical mobilities and particle charges, given in Table II, are probably representative of particles near the plates and are much higher than mobilities and charges on particles located in the central portion of the chamber. However, the well-mixed model is a useful tool for quantifying the experimental measurements. The electrical deposition coefficients measured in laboratory experiments can be scaled to estimate electrical deposition in larger systems through the A_e/V factor in Eq. (3c). However, this is only valid for comparable absorbed dose rates, electric fields, and mixing intensities.

This research has been confined to a study of electrical deposition of nuclear aerosols in the presence of an external electric field. Electrical effects are also possible in the absence of an external field if particles possess charge. Particles frequently acquire charge upon being generated, and may be influenced by electrical forces before being neutralized. Also, radioactive particles can be self-charged.[14,15] As mentioned earlier, the presence of charge on particles enhances deposition and can affect coagulation, retarding it when the particles have the same sign and enhancing it when they have the opposite sign.

CONCLUSIONS

It is demonstrated that an electric field can significantly reduce the concentration of a confined aerosol in the presence of ionizing radiation. Using a well-mixed model for aerosol behavior, deposition is quantified experimentally in the form of a depositional rate coefficient. The rate coefficient is determined from measurements of the steady-state aerosol concentration in a continuously reinforced chamber.

In the absence of ionizing radiation, the depositional rate coefficient increases by a factor of 5 to 10 upon application of an external electric field of 10^5 V/m. In the presence of a radiation absorbed dose rate of $\sim$22 rad/h, the depositional rate coefficient increases by more than two orders of magnitude. Estimates of particle charge calculated from the rate coefficient are consistent with published aerosol charging data.

ACKNOWLEDGMENTS

The authors express their appreciation to Jay Vandeven for his assistance in fabricating the experimental chamber.

This work was supported in part by the College of Engineering at Clemson University and received funds from NSF Grant No. ISP-8011451.

REFERENCES

1. L. D. REED, K. W. LEE, and J. A. GIESEKE, "The Behavior of Contained Radioactive Suspensions," *Nucl. Sci. Eng.*, **75**, 167 (1980).

2. H. A. MOREWITZ, "Fission Product and Aerosol Behavior Following Degraded Core Accidents," *Nucl. Technol.*, **53**, 120 (1981).

3. H. BUNZ, W. SCHIKARSKI, and W. SCHOCK, "The Role of Aerosol Behavior in Light Water Reactor Core Melt Accidents," *Nucl. Technol.*, **53**, 141 (1981).

4. L. D. REED, H. JORDAN, and J. A. GIESEKE, "Effects of Radiation on Aerosol Behavior," BMI-NUREG-1943, Battelle Columbus Laboratories (1975).

5. W. DICKTER and M. A. SCHULTZ, "Investigation of a Device Using Radiation to Charge and Collect Particulate Matter," *Nucl. Technol.*, **12**, 243 (1971).

6. M. A. SCHULTZ, M. E. CROTZER, and W. R. KNAPICK, "Collection of Particulate Matter from Smokestacks Using Gamma-Ray Ionization," *Nucl. Technol.*, **17**, 38 (1973).

7. S. K. FRIEDLANDER, *Smoke, Dust and Haze, Fundamentals of Aerosol Behavior*, John Wiley & Sons, New York (1977).

8. J. D. COBINE, *Gaseous Conductors*, McGraw-Hill Book Company, Inc., New York (1941).

9. R. A. FJELD, R. O. GAUNTT, and A. R. McFARLAND, "Continuum Field-Diffusion Theory for Bipolar Charging of Aerosols," *J. Aerosol Sci.*, **14**, 541 (1983).

10. B. Y. H. LIU and D. Y. H. PUI, "Equilibrium Bipolar Charge Distribution of Aerosols," *J. Colloid Interface Sci.*, **49**, 305 (1974).

11. B. Y. H. LIU and K. W. LEE, "An Aerosol Generator of High Stability," *Am. Ind. Hygiene Assoc. J.*, **36**, 861 (1975).

12. N. A. FUCHS, *The Mechanics of Aerosols* (English Translation), Pergamon Press, Oxford (1964).

13. G. W. HEWITT, "The Charging of Small Particles for Electrostatic Precipitation," *AIEE Trans.*, **76**, 300 (1957).

14. H. C. YEH, G. J. NEWTON, O. G. RAABE, and D. R. BOOR, "Self-Charging of Au-198 Labelled Monodisperse Gold Aerosols Studied with a Miniature Electrical Mobility Spectrometer," *J. Aerosol Sci.*, **7**, 245 (1976).

15. L. D. REED, H. JORDAN, and J. A. GIESEKE, "Charging of Radioactive Aerosols," *J. Aerosol Sci.*, **8**, 457 (1977).

ANALYSIS OF COOLANT PRESSURE FLUCTUATION AND INDUCED VIBRATION OF LIQUID-METAL FAST BREEDER REACTOR FUEL PINS

NUCLEAR SAFETY

KEN AMANO and KOTARO INOUE
Energy Research Laboratory, Hitachi Ltd.
1168 Moriyama-cho, Hitachi-shi, 316 Japan

Received July 5, 1983
Accepted for Publication November 28, 1983

An analytical model describing pressure fluctuation of turbulent flow in liquid-metal fast breeder reactor (LMFBR) fuel assemblies has been proposed, and the oscillation amplitude of a fuel pin thus caused has been calculated. In the treatment, the statistical model for pressure fluctuation in stable turbulent flow was assumed, and the fluctuation was estimated from pressure loss of flow and velocity gradient. The vibration amplitude was calculated by solving a Langevin equation. According to the comparison of the calculated results with experimental data, this model realistically describes the fuel pin vibration in LMFBR fuel assemblies.

INTRODUCTION

Many experimental and theoretical studies have been performed on fluid-induced vibration. Their cause mechanisms can be roughly classified into flow elastic vibration, vortex shedding, and statistical pressure fluctuation. In the case of fluid-induced vibration for a liquid-metal fast breeder reactor (LMFBR) fuel assembly, vortex shedding and flow elastic vibration rarely occur. The flow condition in the fuel assembly is axial external flow along the fuel pins, accompanied with swirl flow caused by a wire spacer. The vortex shedding often occurs under cross-flow conditions against fuel pins but rarely under axial flow conditions.[1] The flow elastic vibration can occur under both axial and cross flows. But it is known that there is a threshold of mean flow velocity above which the flow elastic vibration occurs.[2] Because the threshold is much higher than the mean velocity in an LMFBR, the flow elastic vibration rarely occurs.

On the other hand, the pressure fluctuation caused by turbulent flow appears where the Reynolds number is high. The character of vibration caused by the pressure fluctuation is the small amplitude, which coincides with the realistic vibration of LMFBR fuel pins.

For theoretical studies, Reavis[3] calculated the amplitude of fuel pin vibration caused by the pressure fluctuation in turbulent flow. He evaluated the power spectrum of pressure fluctuation from experimental correlation functions about space and time and from the power amplitude in turbulent boundary layer pressure fluctuation. He solved a Langevin equation to get the response of the vibration amplitude from the pressure fluctuation. The vibration amplitude by his model, however, was much smaller than experimental data, so he proposed a calibrating factor, i.e., the ratio of the measured oscillation to the theoretical oscillation.

Chen and Wambsganss[4] indicated that the statistical method is very accurate if the measured excitation spectrum is used. Paidoussis[5] proposed empirical expression of the vibration amplitude.

In this paper, a modified theoretical model for pressure fluctuation is proposed. For the modified model, the magnitude of pressure fluctuation is estimated from turbulent flow energy loss by using the relation of fluctuation to dissipation.

For wrapping a wire spacer type of fuel assembly, the problem of fluid-induced vibration is significant in terms of wear on fuel pin cladding. Using this model, the fuel pin vibration amplitude in an LMFBR fuel assembly is calculated from the linear response to random pressure fluctuation around the fuel pin and compared with a water fluid vibration test.

THEORETICAL MODEL

Only pressure fluctuation in turbulent flow was assumed to be the cause of fuel pin vibration. Nonlinear vibration, i.e., vortex-induced vibration and aerodynamic instability were neglected, because measured oscillations from water fluid vibration tests were so small as to make the nonlinear vibration force negligible. Therefore, the statistical method for pressure fluctuation in turbulent flow could be adopted, and the equation describing vibration could be separated from the fluid equation.

For the pin vibration equation, a fuel pin vibrates with an eigenfrequency and an eigenmode, and the vibration equation is linear. Therefore, spatial integration of this equation after multiplying it by an eigenvalue function leads to an ordinary differential equation dependent only on time.

This ordinary differential equation could be further transformed into a Langevin equation with a pressure fluctuation force. The fuel pin oscillation could be obtained from the Langevin equation as a linear response of pressure fluctuation.

Fuel Pin Vibration Model

The fuel pin vibration equation was only assumed as (see Nomenclature on p. 414)

$$(m+M)\frac{\partial^2 y}{\partial t^2}+\gamma\frac{\partial y}{\partial t}+EI\frac{\partial^4 y}{\partial x^4}=P'(x,t) \ , \qquad (1)$$

where $P'(x,t)$ was the pressure fluctuation force. The eigenfrequency ω_n and eigenmode function $y_n(x)$ were given as

$$\omega_n=\left(\frac{n\pi}{L}\right)^2\left[\frac{EI}{(m+M)}\right]^{1/2} \qquad (2)$$

and

$$y_n(x)=\sin\frac{n\pi x}{L} \ , \qquad (3)$$

where L was a distance between two fixed points. Measured eigenfrequencies indicated that L was some multiple of the wire spacer pitch.[6] Using Eq. (3), oscillation $y(x,t)$ was given as

$$y(x,t)=\sum_n q_n(t)y_n(x) \ . \qquad (4)$$

Equation (1) was integrated over space after multiplication in Eq. (3), and an ordinary differential equation was given as

$$\frac{L}{2}(m+M)\left(\frac{d^2q_n}{dt^2}+2\omega_n\xi\frac{d^2q_n}{dt}+\omega_n^2q_n\right)$$
$$=\int_0^L P'(x,t)y_n(x)\,dx \ , \qquad (5)$$

where ξ was the damping ratio.

The right term of Eq. (5), which was pressure fluctuation force, was transformed into power spectrum $S(\omega)$. From the Wiener-Khinchin theorem, the mean-square fuel pin oscillation $\langle q_n^2\rangle$ was given as

$$\langle q_n^2\rangle=\int_{-\infty}^{+\infty}\frac{S(\omega)\,d\omega}{\frac{L^2}{4}(m+M)^2[(\omega^2-\omega_n^2)^2+4\xi^2\omega_n^2\omega^2]} \ . \qquad (6)$$

Model of Pressure Fluctuation Power Spectrum

Pressure fluctuation P' was a function of time t, axial distance x, and azimuthal direction θ (see Fig. 1). The correlation function was assumed to have the following form:

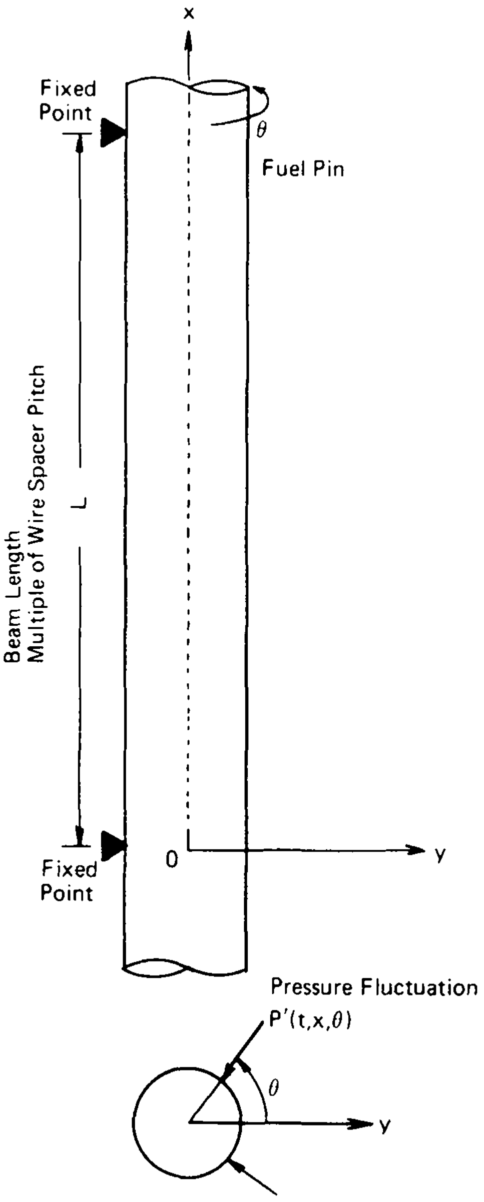

Fig. 1. Fuel pin vibration model.

$$\langle P'(t_1,x_1,\theta_1)P'(t_2,x_2,\theta_2)\rangle = \langle P'\rangle\phi_\tau(|t_1-t_2|)\cdot\phi_\xi(|x_1-x_2|)\cdot\phi_\theta(|\theta_1-\theta_2|) \ . \tag{7}$$

The values $\langle P'\rangle$, ϕ_c, ϕ_ξ, and ϕ_θ were given in the following.

1. The quantities $\phi_\xi(|x_1-x_2|)$ and $\phi_\theta(|\theta_1-\theta_2|)$ were given by Bakewell's experiments[7] for turbulent air flow around a cylinder:

$$\phi_\xi(|x_1-x_2|) = \exp[(-0.7\omega)|x_1-x_2|/2\pi U_c] \times \cos(\omega|x_1-x_2|/U_c) \tag{8}$$

and

$$\phi_\theta(|\theta_1-\theta_2|) = \exp(-3\omega D|\theta_1-\theta_2|/2\pi U) \ . \tag{9}$$

Equation (8) was integrated over the x direction after multiplication by an eigenmode function $y_n(x)$, so that

$$\Psi_\xi(\omega) = \int_0^L dx_1 y_n(x_1)\int_0^L \phi_\xi(|x_1-x_2|)\cdot y_n(x_2)\,dx_2 \ . \tag{10}$$

Equation (9) was integrated over the θ direction after multiplication by $(D/2)\cos\theta$:

$$\Psi_\theta(\omega) = \int_{-\pi}^{\pi}\frac{D}{2}\cos\theta_1\,d\theta_1\int_{-\pi}^{\pi}\frac{D}{2}\cos\theta_2\phi_\theta(|\theta_1-\theta_2|)\,d\theta_2 \ . \tag{11}$$

2. The form of the time correlation function $\phi_\tau(|t_1-t_2|)$ was assumed based on the data of a fluid vibration test in a fuel assembly.[6] The experimental data have shown that the power spectrum of pressure fluctuation was almost flat over a wide region, except for many little peaks relating to eigenmodes of structure in the assembly. Therefore, the time correlation function was assumed in the following form:

$$\phi_\tau(|t_1-t_2|) = \exp(-|t_1-t_2|/\tau_0) \ , \tag{12}$$

where τ_0 must be very small. The order of τ_0 is estimated later. The Fourier transform of Eq. (12) is

$$\Psi_\tau(\omega) = \frac{2}{\pi}\frac{\alpha}{\omega^2+\alpha^2} \ , \tag{13}$$

where

$$\alpha = 1/\tau_0 \ .$$

3. The magnitudes of the pressure fluctuation P'_{rms} $[=(\langle P^{2\prime}\rangle)^{1/2}]$ and time constant τ_0 in Eq. (12) were estimated theoretically as follows. It could be assumed that P'_{rms} had the same order as turbulent flow energy $\frac{3}{2}\rho\langle u'^2\rangle$, so that

$$P'_{\text{rms}} = \frac{3}{2}\rho\langle u'^2\rangle \ . \tag{14}$$

The loss of turbulent energy per unit time was given as $\Delta P\cdot\bar{U}$ and could be represented by using the turbulent kinematic viscosity K, giving

$$\epsilon = \Delta P\cdot\bar{U} = \frac{1}{2}\rho K\sum_\alpha\sum_\beta\left(\frac{\partial\bar{u}_\alpha}{\partial x_\beta}+\frac{\partial\bar{u}_\beta}{\partial x_\alpha}\right)^2 \ . \tag{15}$$

Equation (15) was also the definition of K. The time constant τ_0 was defined as

$$\tau_0 = \frac{3}{2}\rho\langle u'^2\rangle/\epsilon \ . \tag{16}$$

The value K had the same order as $\langle u'^2\rangle\tau_0$, so that

$$K = \langle u'^2\rangle\tau_0 \ . \tag{17}$$

Pressure loss per unit length ΔP was calculated by Rehme's expression,[8] which is used for evaluating the pressure drop in the wire spacer type of fuel assembly. The quantity $\partial\bar{u}_\alpha/\partial x_\beta$ could be estimated by hydraulic diameter D_{eq} and mean flow velocity $\bar{U}$ as $\bar{U}/D_{eq}$. Equation (15) gave ϵ and K, while τ_0 and P'_{rms} were obtained from Eqs. (16) and (17):

$$\tau_0 = \left(\frac{3\rho K}{2\epsilon}\right)^{1/2} \tag{18}$$

and

$$P'_{\text{rms}} = \left(\frac{3}{2}\rho\epsilon K\right)^{1/2} \ . \tag{19}$$

The ΔP was expressed by pressure loss coefficient C_D,

$$\Delta P = \frac{1}{2}C_D\frac{\bar{U}^3}{D_{eq}}\ \text{(per unit length)} \ , \tag{20}$$

and Eq. (19) was represented as

$$P'_{\text{rms}} = \left(\frac{3}{4}C_D\right)^{1/2}\frac{\bar{U}^{1.5}}{D_{eq}^{0.5}}\rho K^{0.5} \ . \tag{21}$$

Equations (10), (11), (13), and (21) yielded the power spectrum of the pressure fluctuation,

$$S(\omega) = P'^2_{\text{rms}}\cdot\Psi_\tau(\omega)\cdot\Psi_\xi(\omega)\cdot\Psi_\theta(\omega) \ . \tag{22}$$

CALCULATION RESULTS

The fuel pin oscillation was numerically calculated using geometric parameters listed in Table I. Table II shows turbulent flow parameters calculated by Eqs. (18) through (21).

Reavis has used the pressure fluctuation expression[3]

$$P'_{\text{rms}} = 0.17\frac{\bar{U}^{1.5}}{D_{eq}^{0.5}}\rho\nu^{0.5} \ , \tag{23}$$

where ν indicates molecule kinematic viscosity. Our results, calculated using Eq. (21), gave a P'_{rms} value

TABLE I

Geometric Data of a Fuel Pin

Outer/inner pin cladding diameter	0.65/0.56 cm
Total length of fuel pin	283.4 cm
Equivalent hydraulic diameter of fuel bundle	0.34 cm
Mass of fuel pin per unit length	3.65 g/cm

TABLE II

Features of Turbulent Flow in a Fuel Assembly

($\bar{U} = 500$ cm/s)

Pressure loss per length, ΔP	6.1×10^3 dyn/cm^2
Reynolds number, Re	4.5×10^5
Turbulent kinematic viscosity, K	0.78 cm^2/s
Turbulence damping time constant, τ_0	5.6×10^{-4} s
Pressure fluctuation (root-mean-square), P'_{rms}	1.39×10^3 dyn/cm^2

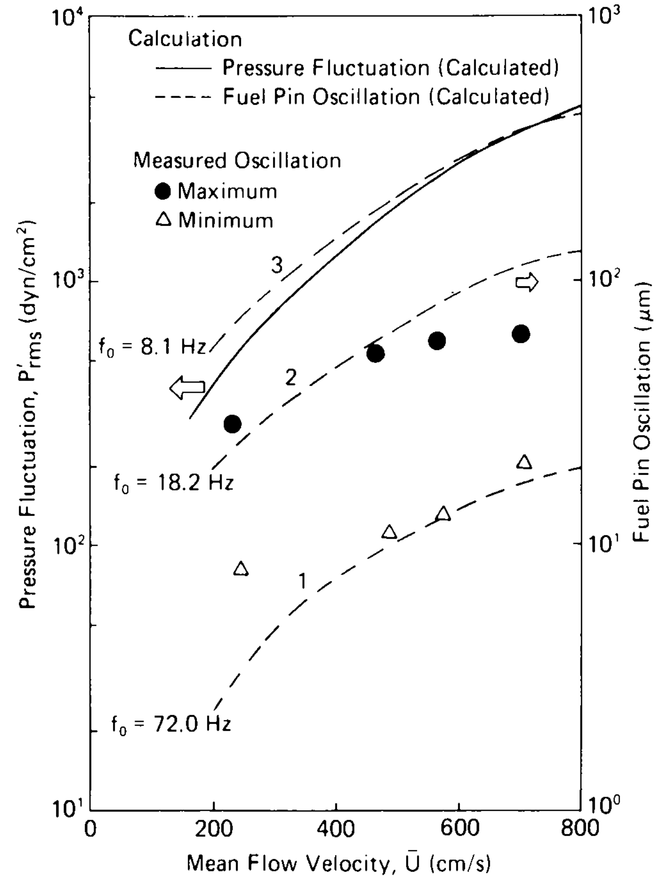

	Beam Length, L (cm)	Eigenfrequency, f_0 (Hz)
1	30.7 (1 Wire Pitch)	72.0
2	61.4 (2 Wire Pitch)	18.2
3	92.1 (3 Wire Pitch)	8.1

Fig. 2. Pressure fluctuation and fuel pin oscillation.

~200 times larger than that obtained by Reavis, because Eq. (21) incorporated turbulent kinematic viscosity K, while Eq. (23) used molecule kinematic viscosity. The time constant of turbulent flow τ_0 was 0.56 ms, so the characteristic frequency of turbulence ($\frac{1}{2}\pi\tau_0$) was ~300 Hz. Therefore, the power spectrum [Eq. (13)] was almost flat from 0 to ~300 Hz.

Figure 2 shows the fuel pin oscillation versus mean flow velocity for various distances between fixed points. In this figure, the damping ratio ξ in Eq. (6) was 0.01. Figure 2 also shows the oscillations measured by Sasaki[6] for the same conditions as given in Table I. He reported that the eigenfrequency for fuel pin oscillation was ~20 Hz, which corresponds with two wire pitches of beam length. Our calculation of the same parameter as 18.2 Hz showed good agreement with measured maximum oscillation in the region of $\bar{U} < 600$ cm/s, but for $\bar{U} > 600$ cm/s, the oscillation was overestimated in the analysis.

The fuel pin oscillations calculated by Reavis[3] were one-tenth to one-hundredth smaller than measured ones. To compensate for this, he proposed a calibrating factor C defined as the ratio of the measured oscillation to the theoretical oscillation.

Oscillations, for the same conditions as Tables I and II, were calculated using Eqs. (6) and (23). Then, two ratios were evaluated, i.e., measured oscillations (M) to Reavis's predicted oscillations (C.R), and Reavis's predicted oscillations (C.R) to our predicted oscillations (C.O). Finally, the ratio of M/C.O was indirectly calculated from the product of M/C.R and C.R/C.O.

Figure 3 shows the ratios M/C.R and M/C.O. Our calculations are much closer to measured ones, which came from the use of Eq. (21) instead of Eq. (23).

In our calculation, because velocity gradient $\partial u_\alpha/\partial x_\beta$ is estimated as $\bar{U}/D_{eq}$, K increases in proportion to the square of D_{eq} from Eq. (15) at given ΔP and $\bar{U}$. So our calculated oscillations using Eqs. (6) and (21) increase as D_{eq} increases, while calculated oscillations using Eqs. (6) and (23) decrease as D_{eq} increases. Therefore, our calculation values follow the trend of the measured oscillation for increasing D_{eq}.

The same figure indicates that in the region of $D_{eq}/L < 10^{-2}$ our calculation is not in good agreement with the measured oscillation. Here, the Reynolds numbers are small and flow is laminar, rather than turbulent. In the region of $D_{eq}/L > 10^{-2}$, our

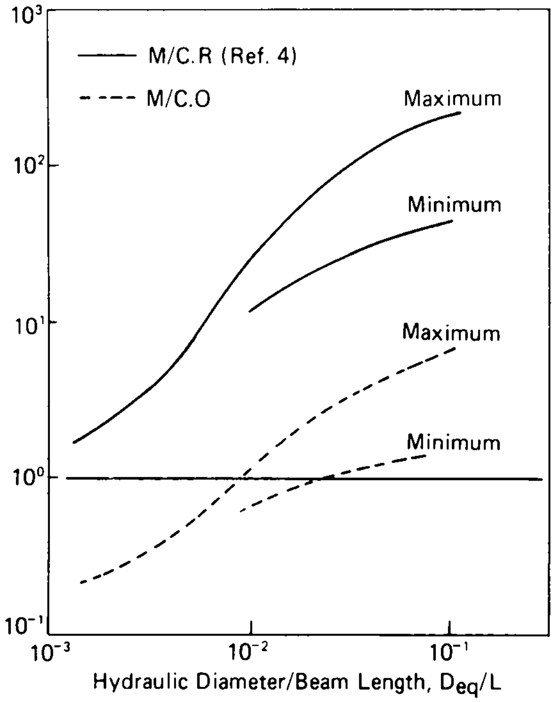

Fig. 3. Average disparity between theoretical and experimental displacements [M = measured oscillation, C.R = calculated (Reavis, Ref. 3), and C.O = calculated (present study)].

calculated results are of the same order as the measured oscillations.

The fuel pin oscillations are also calculated using Paidoussis's empirical relationship,[5] as given below:

$$\delta = \frac{1}{\pi 4}\,\frac{(u^2\cdot \mathrm{Re}\cdot\epsilon^2)^{0.8}}{1+2u^2}\left(\frac{\beta^{2/3}}{1+4\beta}\right)\times 10^{-5} \ , \qquad (24)$$

where δ is the dimensionless displacement amplitude of vibration and equals the amplitude divided by the pin diameters,

$$u = \bar{U}L\left(\frac{M}{EI}\right)^{1/2} \ ,$$

$$\epsilon = L/D \ ,$$

and

$$\beta = \frac{m}{m+M} \ .$$

Figure 4 plots fuel pin oscillations calculated by Eqs. (6) and (21) and those by Eq. (24). The conditions of the two calculations are as given in Tables I and II. Both equations gave results of the same order; thus Paidoussis's empirical expression could be represented theoretically. The oscillation amplitude by Paidoussis is proportional to $U^{2.3}$, while it is proportional to U^2 by this model.

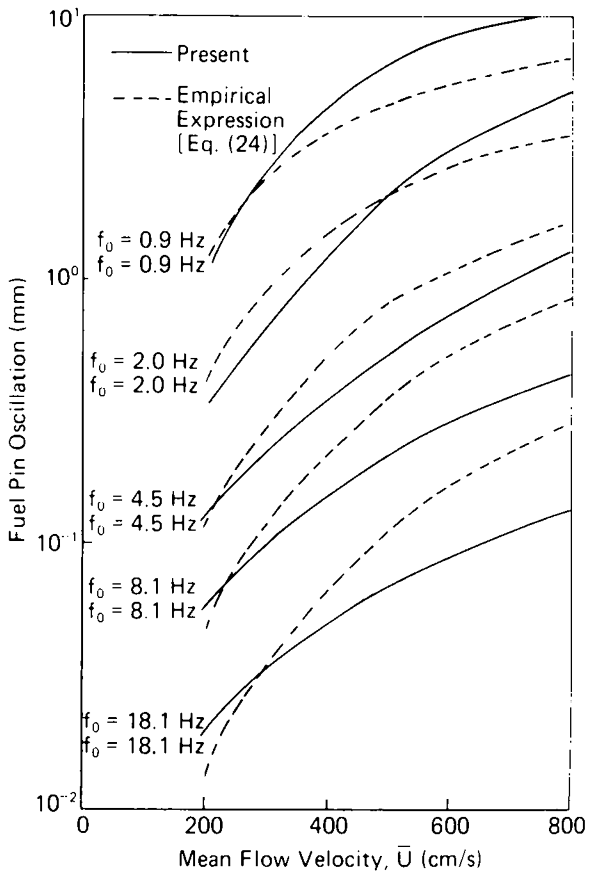

Fig. 4. Comparison between present calculations and empirical expression for fuel pin oscillations.

The differences between Reavis's model and the proposed one are the time correlation function and the amplitude of pressure fluctuation. As for the time correlation function, there is no reason to assume Eq. (12) in every boundary condition. In the LMFBR fuel assembly, Eq. (12) was used because the spectrum in the experiment was broad. In addition, τ_0 was estimated from Eq. (18). But in other cases, the time correlation may be transformed by other different boundaries and different influences of upstream.

For the amplitude of pressure fluctuation, the turbulent boundary layer pressure fluctuation is estimated in Reavis's model, while the whole turbulent energy in fluid volume is estimated in this model. Indeed almost turbulent energy is generated in the turbulent boundary layer, but the pressure fluctuation in the layer is smaller than that in the whole fluid volume. So the amplitude of pressure fluctuation in this model is much larger than that in Reavis's model. This model is in good agreement with the realistic oscillation amplitude, at least in the fuel bundles.

CONCLUSION

The pressure fluctuation in LMFBR fuel assemblies and the fluid-induced vibration of fuel pins caused by the pressure fluctuation have been estimated. A modified model for pressure fluctuation was proposed. First, the turbulent energy and turbulent kinematic viscosity were estimated from pressure loss and flow velocity gradients. A power spectrum of Lorentz's type was assumed. Next, the damping ratio was calculated from a theoretical description of column motion resistance in viscous fluid. Finally, the linear response of the vibration equation was obtained.

Pressure fluctuation by the modified model increases as the pressure loss increases, as is expected from the fluctuation/dissipation theorem. This model yields an amplitude of fuel pin vibration of the same order as measured ones.

NOMENCLATURE

D = fuel pin diameter (cm)

D_{eq} = hydraulic diameter of bundle (cm)

E = Young's modulus (dyn/cm^2)

I = two-dimensional moment (cm^4)

f_0 = eigenfrequency (1/s)

K = turbulent kinematic viscosity (cm^2/s)

L = beam length (cm)

M = mass of fluid per unit length (g/cm)

m = mass of a fuel pin per unit length (g/cm)

ΔP = pressure loss per unit length (dyn/cm^3)

P'_{rms} = pressure fluctuation (root-mean-square) (dyn/cm^2)

$\langle q_n^2 \rangle$ = displacement amplitude of vibration (mean square) (cm^2)

Re = Reynolds number (dimensionless)

$\bar{U}$ = mean flow velocity (cm/s)

u' = fluctuation of flow velocity (cm/s)

U_c = fluctuation transport velocity ($U_c \approx 0.8\bar{U}$) (cm/s)

γ = damping factor (g/s·cm)

δ = dimensionless displacement amplitude of vibration

ϵ = energy loss per unit volume per unit time (erg/cm^3·s)

ρ = fluid density (g/cm^3)

τ_0 = damping time constant of turbulence (s)

ω = angular frequency (1/s)

ξ = damping ratio ($\gamma = 2\omega_n \xi$) (g/s^2)

$\langle\ \rangle$ = average value

ACKNOWLEDGMENTS

The authors would like to acknowledge the continuous encouragement of K. Taniguchi and H. Yamamoto of the Energy Research Laboratory, Hitachi Ltd., during this study. Acknowledgment is also given A. Suzuoki for his valuable discussions and advice.

REFERENCES

1. M. J. PETTIGREW, Y. SYLVESTRE, and A. O. COMPAGNA, "Vibration Analysis of Heat Exchanger and Steam Generator Designs," *Nucl. Eng. Des.*, **48**, 95 (1979).

2. M. J. HANNOYER and M. P. PAIDOUSSIS, "Instabilities of Tubular Beam Simultaneously Subjected to Internal and External Axial Flows," *J. Mech. Des.*, **100**, 328 (1978).

3. J. R. REAVIS, "Vibration Correlation for Maximum Fuel-Element Displacement in Parallel Turbulent Flow," *Nucl. Sci. Eng.*, **38**, 63 (1969).

4. S. S. CHEN and M. W. WAMBSGANSS, "Parallel Flow Induced Vibration of Fuel Rods," *Nucl. Eng. Des.*, **18**, 253 (1972).

5. M. P. PAIDOUSSIS, "The Amplitude of Fluid-Induced Vibration of Cylinders in Axial Flow," AECL-2225, U.S. Atomic Energy Commission (Mar. 1965).

6. Y. SASAKI, "The Hydraulic Vibration Testing of FBR Fuel Pin Bundle," *Trans. Fall Mtg. Japan Atomic Energy Society*, Kōōbe, September 1978, A30.

7. H. P. BAKEWELL, "Narrow-Band Investigations of the Longitudinal Space-Time Correlation Function Turbulent Air Flow," *J. Acoust. Soc. Am.*, **36**, 146 (1964).

8. K. REHME, "Pressure Drop Correlation for Fuel Element Spacers," *Nucl. Technol.*, **17**, 15 (1973).

NUCLEAR SAFETY

DOMINANT FACTORS IN THE RELEASE OF FISSION PRODUCTS FROM OVERHEATED URANIA

C. D. ANDRIESSE and R. H. J. TANKE *KEMA Laboratories*
Utrechtseweg 310, Arnhem, The Netherlands

Received August 25, 1983
Accepted for Publication November 28, 1983

Existing data on the release of fission products (FPs) from UO_2 above 1000°C show that the dominant transport process consists of elementary diffusion within grains. For many FPs, the noble gases among them forming an exception, this diffusion is characterized by an activation energy of ~2.6 eV, which is close to the one for oxygen and very different from the one for uranium. Assuming that oxygen diffusion represents the diffusion of FPs, it can be predicted that diffusion is enhanced when there is excess oxygen in the lattice. An empirical relation between the pertinent activation energy and the overstoichiometry induced by uranium fission (burnup) is given. The transport by diffusion has to be driven by some gradient, and it is argued that the temperature gradient dominates over the concentration gradient. This argument leads to a complete description of the release rate in terms of the grain size, the central and surface temperatures, and the heat of transport. The heat of transport plays a crucial role as it varies greatly for the various FPs. Existing data allow estimation of values ranging from 0.1 eV for refractory products to more than 100 eV for volatile products. These variations appear to be correlated with variations in the bond strengths between FPs and oxygen, being the more reactive element in UO_2. An empirical model of the dependence of the heat of transport on this bond strength is given, so that release rates for all the FPs can be derived from chemical tables. Finally, consistency of the measured release data with other independently obtained fuel parameters is proven.

INTRODUCTION

When the core of a nuclear reactor is overheated, it can become a source of radiotoxic matter. For this reason it is important to study the release rate of fission products (FPs) from urania (UO_2) at high temperatures. These rates set the pace in the interaction of the released products with fuel cladding and the surroundings of the reactor. However, the physics and chemistry are only partially understood, despite the fact that many detailed codes have been proposed. For example, a recent code,[1] FASTGRASS, only addresses the release of noble gases and the volatile iodine and cesium. In this situation a simpler approach to the problem of high-temperature releases can still be useful, if it aims at an understanding of the dominant processes for all FPs. Such an approach involves rough approximations, but it tries to grasp the essential. The object of this paper is to contribute to such an understanding. Elementary diffusion in UO_2, temperature gradients, and bond strengths are briefly discussed, and in conclusion an empirical relation is given for the release rate of all relevant FPs.

ELEMENTARY DIFFUSION

Existing data on the release rates at temperatures between 1000 and 3000°C have been reviewed in Ref. 2. We have transferred the curves of Fig. 4.3 of Ref. 2 to those in the Arrhenius plot of Fig. 1. The latter can be well represented by

$$\log(f) = -c_1/T + c_2 \ , \tag{1}$$

where

f = fraction of a particular FP, at any moment present in the fuel, released per second

T = absolute temperature

c_1 and c_2 = constants given in Table I.

The case for iodine, krypton, and xenon is ambiguous (see Fig. 1); for temperatures above 1300 K (or ~1000°C), it may be identical to the case for cesium.

It is striking that the values of c_1 are all close to the average value $\bar{c}_1$ of 1.3×10^4 K, which points to a rather common energy equivalent $\bar{c}_1 \cdot k \cdot \ln(10)$ of 2.6 eV (k is the Boltzmann constant; 1 eV corresponds with 23 kcal/mol). This energy is only slightly smaller than the activation energy for oxygen diffusion in

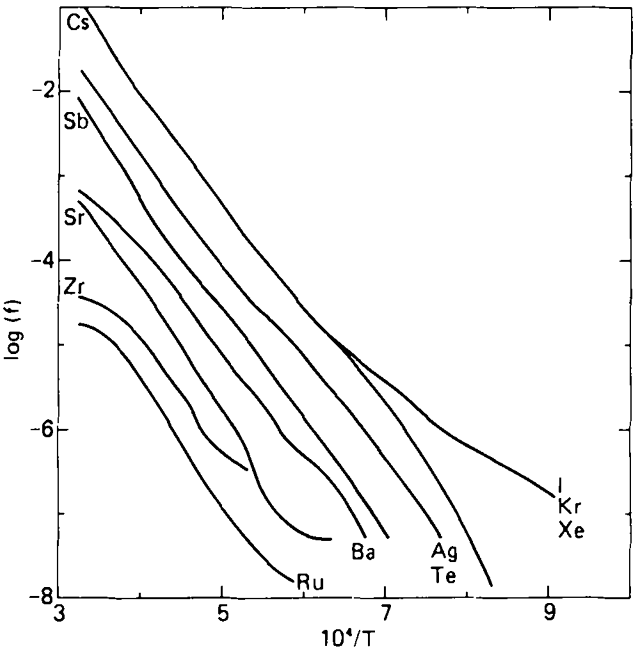

Fig. 1. Data on the release rate f as a function of the inverse temperature $1/T$.

TABLE I

Values of the Constants c_1 and c_2 in Relation (1) Derived from Fig. 1*

Element	c_1 (10^4 K)	c_2
Silver	1.3	2.3
Barium	1.3	1.3
Cesium	1.2	2.8
Iodine	(0.7)	(−0.8)
Krypton	(0.7)	(−0.8)
Ruthenium	1.5	0.5
Antimony	1.3	2.0
Strontium	1.5	1.8
Tellurium	1.3	2.3
Xenon	(0.7)	(−0.8)
Zirconium	1.3	0.3

*The error in c_1 is ~0.1 and in c_2 ~0.5; the values in parentheses do not apply for temperatures above 1000°C, and they may be replaced by those for cesium.

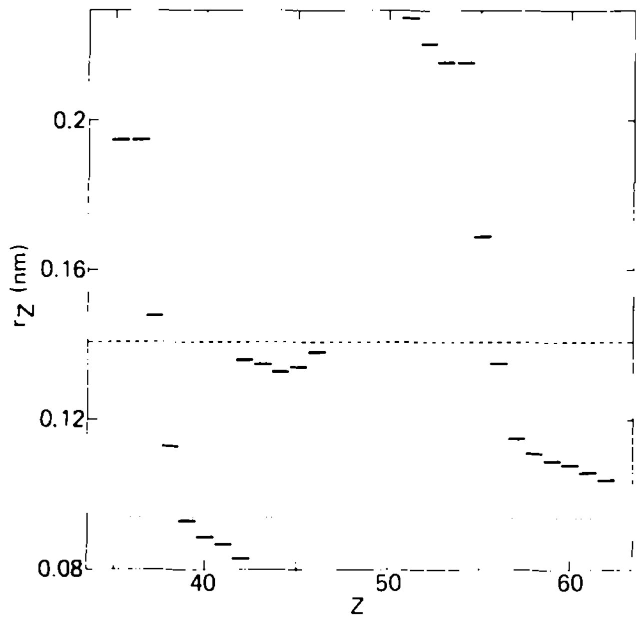

Fig. 2. Radii r_Z of FP atoms and ions as a function of the atomic number Z; for comparison the radii are indicated of the oxygen anion (dashed line) and of the uranium cation (dotted line).

UO_2, being 2.8 eV (±10%) (Ref. 3). We return to this difference later. Uranium diffusion in UO_2 has the much larger activation energy of 3.8 eV (±13%) (Ref. 4).

The diffusion mechanism of FPs seems to be related to that of oxygen. Like oxygen, most FPs are large atoms or ions compared to uranium. Figure 2 shows Pauling's radii of atoms or ions, which are probably formed in the UO_2, with the case at $Z = 42$ double because of the double role of molybdenum in balancing the oxygen potential, either as an element or as an oxide. They occupy a small fraction of the interstitial sites in the fluorite-type lattice, which has an open space that would fit uranium. As the FPs do not fit these open spaces, they deform the lattice locally, thereby lowering the energy threshold to neighboring sites. The relatively large oxygen, if interstitial, plays a similar role (discussed later). The interstitial sites are understood to be crucial in the diffusive motion of oxygen, which apparently has easier access to them than uranium. The similarity in effect on the lattice at interstitial sites suggests a similarity in the diffusion of oxygen and FPs. This implies a roughly similar activation energy for diffusion, despite the fact that oxygen forms the predominant anion, and FPs occur with negative, zero, and positive charges.

In view of the above, we associate the release of FPs from UO_2 at high temperatures with elementary anion diffusion, characterized by a threshold energy q. The fractional release rate f should then be proportional to the diffusion coefficient D with, as required by the dimension of both quantities, a proportionality constant $1/A^2$, where A is a length. As the diffusion coefficient depends on the temperature and q by the Arrhenius factor, one can write

$$f = D/A^2 = [D_\infty \exp(-q/kT)]/A^2 \ , \qquad (2)$$

where D_∞ is the high-temperature limit of the diffusion coefficient. The difference between the value of q for oxygen and FPs is explained as follows.

It has long been known[5] that oxygen atoms diffuse more rapidly when the parameter for nonstoichiometry x in UO_{2+x} is increased. This has strengthened the hypothesis that the excess (interstitial) oxygen carries the diffusion current and thus that the diffusion is an interstitial mechanism. If FPs diffuse in association with oxygen, we expect that the pertinent dependence of q on x holds for them also. Empirically

$$q = q_0/(1 + 15x) \ , \tag{3}$$

with q_0 the activation energy of 2.8 eV. For $x = 0.063$ this gives $q = 1.4$ eV, whereas at that value of x an energy of 1.3 eV (±10%) has been measured.[5] For other values of x, Eq. (3) gives semiquantitative agreement.[6] One obtains the above average value of 2.6 eV for the FPs if $x = 0.005$. This modest value for the nonstoichiometry may well be representative for the irradiated fuel from which the Ref. 2 data are obtained. Thus, Eq. (3) inserted in Eq. (2) will give realistic predictions of the increase of the release rate when UO_2 is oxidized. This effect has recently been discussed in terms of sintering in steam.[7] Another cause for oxidation is burnup of the UO_2 fuel, as not all oxygen, orphan after fission of uranium, binds to an FP. If β is the burnup (as a fraction of the initially present uranium atoms), empirical data point at[8]

$$x = 1.3\beta \ , \quad \beta < 0.03 . \tag{4}$$

(For $\beta > 0.03$ the increase of x with β is stronger.) Thus, Eqs. (4) and (3), inserted in Eq. (2), will give a prediction of the release rate with burnup. These increases turn out to be important, as shown later in Figs. 4 and 5.

Elementary diffusion theory[9] shows that D_∞ is not a free constant but that it is determined by

$$D_\infty = \frac{1}{6} a^2 \nu \exp[q/(3kT_m)] \ , \tag{5}$$

where

a = length of one diffusive step in the lattice

ν = Debije frequency

T_m = melting temperature.

This relation is based on a theory of the activation entropy by Zener, which at least for metals has turned out to be correct. One can expect therefore that $D_\infty = 6 \times 10^{-6}$ m^2/s for all atoms diffusing with the activation energy $q = 2.8$ eV. It cannot vary more than by 40% for all atoms given in Table I. Yet the product D_∞/A^2, which is given by 10^{c_2}, varies over about two orders of magnitude! This implies that diffusion is not the only important mechanism and that the length A, instead of being a simple size parameter, contains significant physics. We study additional factors in the following section.

TEMPERATURE GRADIENTS

Before they can escape, the FPs have to travel through the fuel matrix. This travel includes

1. capture in interstitial lattice sites near the end of fission tracks
2. atomic diffusion in grains
3. slipping along grain boundaries
4. capture in closed porosity or holes
5. hole migration
6. transport to open porosity or cracks.

This need not be a strict series; part of the modes can go on in parallel. Modes 3 through 6 have been described in considerable detail.[10] At normal fuel temperatures some can be slow, notably mode 5. At abnormal high fuel temperatures, however, mode 2 is probably the slowest and thus limits the release rate. This cannot be proven, but it is suggested by the above-discussed similarity between elementary diffusion and the release rate. Let us discuss the agents behind this diffusion.

Atomic diffusion in grains can be driven by concentration gradients and by temperature gradients. Concentration gradients lead to normal diffusion and temperature gradients to thermal diffusion. Fission does not lead to significant differences in concentration, except in a thin surface layer within the stopping range of fission fragments. However, the temperature differences in the fuel are large. For homogeneous (self-)heating of a spherical fuel sample with radius R (or an irregular sample with the equivalent radius R), the temperature is given by

$$\frac{T - T_R}{T_0 - T_R} = 1 - \frac{r^2}{R^2} \ . \tag{6}$$

Here, T_0 and T_R are the temperatures in the center and at the surface, respectively, and they can differ by hundreds of degrees at a radius of ~10 mm. One may expect therefore that thermal diffusion dominates over normal diffusion.

The atomic flux J obeys[11]

$$J = -D\nabla C - D\frac{QC}{kT^2}\nabla T \ , \tag{7}$$

where

C = concentration

Q = heat of transport.

If thermal diffusion dominates the flux, we set $\nabla C = 0$ and simplify the above relation to

$$J = -D\frac{QC}{kT^2}\nabla T \ . \tag{8}$$

Using Eq. (6), we determine the temperature gradient ∇T, integrate the atomic flux J over the spherical sample, and divide the result by the total number of atoms inside this sample $(4/3\pi R^3 C)$. This yields the fractional release rate:

$$f = 6\,\frac{D}{R^2}\,\frac{Q(T_0 - T_R)}{kT_R^2} \quad . \tag{9}$$

With the explicit relation for the diffusion coefficient D, given in Eq. (2), this can also be written as

$$\log(f) = -\frac{q\log(e)}{kT_R} + [\log(Q) + c_3] \quad , \tag{10}$$

and

$$c_3 = \log\left[6\,\frac{D_\infty}{R^2}\,\frac{(T_0 - T_R)}{kT_R^2}\right] \quad . \tag{11}$$

The comparison with Eq. (1) gives us

$$c_1 = q\log(e)/k \quad , \tag{12}$$

and

$$c_2 = \log(Q) + c_3 \quad . \tag{13}$$

Note that c_3 is not a true constant. It depends on the temperature in a much slower fashion than c_1/T, however, so that it can be approximated by a constant for practical applications.

The above analysis clarifies the physics in the length A appearing in Eq. (2). The physical size one must address is that of the fuel sample R. But is R the (equivalent) radius of a grain or of a coherent bit in (cracked) fuel or of a fuel pellet? The above reasoning, based on elementary diffusion, excludes the last possibility. It does not clearly discriminate between the first two possibilities. The size of coherent fuel fragments can be millimetres, while the grain sizes are more than one order of magnitude smaller. Unfortunately, we are left with this ambiguity. There is clear evidence[12] for a reduction in release rates when grains have grown, in accordance with Eq. (9).

The analysis also clarifies the important role of temperature gradients. They should be known to assess release rates and often this is not the case. The value of $(T_0 - T_R)$ can be much larger for fuel in a reactor under accident conditions, when there is strong self-heating, than for used fuel outside a reactor, which is externally heated. This means that the values of c_2, given in Table I and pertaining to used fuel outside a reactor, have to be increased for fuel in a reactor under accident conditions. The likely value of this increase is 0.5 to 1.0, depending on the nature of the accident.

The analysis finally clarifies the decisive role of the heat of transport, which is a fundamental microscopic transport property of the UO_2 lattice. We examine this factor next.

BOND STRENGTHS

For the sake of clarity, the heat of transport Q has little if anything to do with the activation energy for diffusion q, being the threshold the atom or ion has to step across when it moves from one lattice site to the next. Rather it expresses the pull or push the atom or ion experiences from its neighbors as the indirect result of a temperature gradient. A direct effect of this gradient can be easily understood. As the chance of making a diffusive step, being proportional to $C \cdot \exp(-q/kT)$, is highest at hot lattice sites, atoms or ions leave those sites more easily than cool sites. The concentration C thus tends to be peaked at the cool sites so that the chances are everywhere the same, that is when C is proportional to $\exp(q/kT)$. The hypothetical density that follows would be extremely high toward the surface of the sample, whereas in the bulk it would be very low. Of course the atoms or ions in the lattice will firmly resist such a large-scale inhomogeneity. This resistance will depend on the strength of the binding of the various elements to their neighbors. Therefore we can understand how binding forces enter in the heat of transport (this thermally induced pulling or pushing), but also that the phenomenon is quite complicated. In fact, the value of Q is hard to predict. For oxygen in slightly substoichiometric UO_2, its value is ~ 1 eV (Ref. 13). For FPs no information is available apart from the rough guesses we make in the next section.

The above discussion leads us to the following argument. Chemically there can hardly be question of an interaction of FPs with uranium. As the FPs only form a dilute solution in the UO_2 (at the high temperatures of interest precipitates being unlikely), interactions among them can be left aside as well. The interaction that will prevail is the one between FPs and oxygen. (Barten has suggested that we look at the bond with oxygen.[14])

Figure 3 shows that a fair correlation exists between c_2 (Table I) and the energy E of a chemical bond between the various FPs and oxygen[15]; apart from the constant c_3 is c_2 equal to $\log(Q)$, see Eq. (13). This correlation does not imply that such bonds indeed are formed in the UO_2 lattice. Depending on the Gibbs potential, some bonds are formed, others not. However, these bond energies do measure how firmly the FPs stick to the interstitial sites surrounding the oxygen anions. The better they stick, the more difficult it is to push or to pull them away, that is, the smaller the heat of transport. In view of the inverse nature of sticking and moving, we propose

$$Q/Q_0 = (E/E_0)^{-n} \quad , \tag{14}$$

where

Q_0 and E_0 = normalized values of the heat of transport and of the bond energy, respectively

n = constant.

Substituting this in Eq. (13), we get

$$c_2 = -n\log(E) + \log(Q_0E_0^n) + c_3 \quad . \tag{15}$$

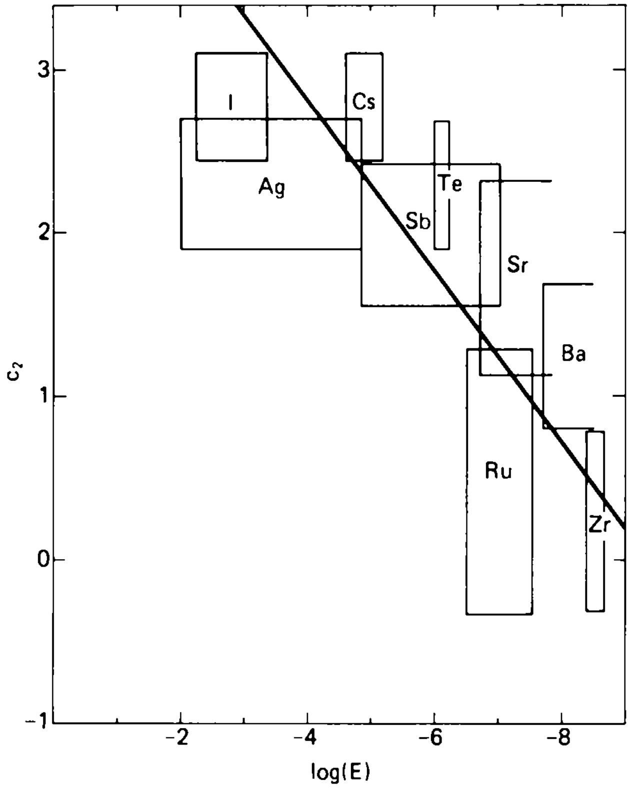

Fig. 3. Correlation between empirical data on c_2 and the binding energy E of FPs with oxygen; the line is according to $c_2 = -5.2 \log(E) + 4.9$, if E is expressed in electron volts.

From Fig. 3, we can find a value for n:

$$n = 5.2 \pm 25\% \ . \tag{16}$$

From Fig. 3, we can also find that, if the energy is expressed in electron volts,

$$\log(Q_0 E_0^n) + c_3 = 4.9 \pm 10\% \ . \tag{17}$$

With these values we have found the physicochemical interpolation formula $c_2 = -5.2 \log(E) + 4.9$. (Keep in mind that this c_2 depends on temperature gradients, which need not be the same as for the experimental data in Fig. 3.) Using this formula, we have calculated values of c_2 for all FPs of radiotoxical relevance from measured values of the bond strength[15] (Table II). The agreement with the values of Table I is reasonable, given the error in c_2 of 0.5, however, there are discrepancies.

TABLE II

Values of the Bond Energy of Oxygen with Various FPs and the Derived Values of c_2 [Eqs. (15), (16), and (17)]

Element	E (eV)	c_2
Silver	2.22	3.1
Barium	>5.85	<0.9
Bromine	2.44	2.9
Cerium	8.26	0.1
Cesium	3.09	2.4
Iodine	1.91	3.4
Krypton	<0.09	>10.3
Lanthanum	8.30	0.1
Molybdenum	6.31	0.7
Niobium	7.83	0.3
Palladium	2.43	2.9
Rhodium	3.91	1.8
Ruthenium	5.00	1.3
Antimony	3.87	1.8
Tin	5.70	1.0
Strontium	>4.72	<1.4
Tellurium	4.06	1.7
Xenon	0.38	7.1
Yttrium	7.43	0.4
Zirconium	7.90	0.2

According to our analysis, silver, krypton, ruthenium, and xenon are released faster (that is, have a larger value of c_2) than according to the data in Ref. 2. For the noble gases, the discrepancy may not be real, as experimental data above 1000°C are scarce and conflicting. For silver and ruthenium the discrepancy may be significant. The release rate of these elements has recently been determined by heating corium, a simulant fuel with appropriate amounts of FPs (Ref. 16). These recent data are given in Table III, together with those for some other elements (we have converted them to the logarithm of the fraction released per second, and we have averaged over the two cases studied). Also shown are the predictions by

$$\log(f) = -\frac{1.4 \times 10^4}{T} \frac{1}{1 + 15x} - 5.2 \log(E) + 4.9 \ , \tag{18}$$

the complete interpolation formula as can be formed from Eqs. (1) and (12) with Eq. (3), and Eq. (15) with Eqs. (16) and (17); for comparison with corium we have put $x = 0$.

Taking into account that the error in the predicted $\log(f)$ has to be larger than the error in c_2, being 0.5, the agreement between experiment and prediction is good for antimony, reasonable for silver and tellurium, and bad for molybdenum and ruthenium. In the case of silver, doubt arises therefore about the validity of the pertinent data base in Ref. 2. In contrast to the case of silver, the case of tellurium is curious as less release is predicted than is measured. The measured release data of silver and tellurium are similar, whereas the predictions are dissimilar because the bond strengths of AgO and TeO are dissimilar. If one accepts the alternative value of 2.7 eV for the TeO

TABLE III

Comparison of the Prediction, Eq. (18), with Averaged Experimental Data of Release Rates from Corium at 2400°C

Element	log(*f*)	
	Experiment	Prediction
Silver	−2.65	−2.1
Molybdenum	−5.78	−4.5
Ruthenium	<−7.13	−3.9
Antimony	−3.24	−3.4
Tellurium	−2.93	−3.5

bond,[17] the predictions become similar, however. The discrepancy between predicted and measured release rates of ruthenium remains, and it is even larger than in comparison with the data in Ref. 2. It is conceivable that the differences in the experimental data have to do with differences in the chemical forms of ruthenium in or on the real fuel and the corium, respectively. We recall that oxidized ruthenium is more volatile than elemental ruthenium, the form expected to occur inside the fuel. In our analysis no weight is given to chemical retention mechanisms, so that in the case of ruthenium (and molybdenum) more release is predicted than actually can occur. If, contrary to our expectation, metal precipitates are possible at temperatures up to 2400°C, the release has to be characterized by a much larger bond strength E than given in Table II.

DISCUSSION AND CONCLUSION

Plausibility arguments were given for two important approximations, namely Eqs. (8) and (14), but no proofs of their validity. We can show, however, that the results calculated from Eqs. (8) and (14) are not only consistent with release data, but also with other fuel parameters. To this end we first obtain an estimate of the constant c_3 from Eq. (17) and then show that this is consistent with the value given by Eq. (11).

The energies E_0 and Q_0, introduced in Eq. (14), are normalized values. Let us normalize to oxygen, for which there is at least an indication for the heat of transport. Assuming that the value as quoted above is also valid for overstoichiometric UO_2, which is by no means certain, we put $Q_0 = 1$ eV. The bond energy of oxygen to oxygen is known,[15] so that $E_0 = 5.17$ eV. With $n = 5.2$ we get $\log(Q_0 E_0^n) = 3.7$, if the energies are expressed in electron volts, and then, from Eq. (17), the estimate

$$c_3 = 1.2 \ . \qquad (19)$$

This result (of which the validity is by no means certain) allows us to estimate heats of transport by virtue of Eq. (13). It turns out that $\log(Q) = c_2 - 1.2$, and that the data on c_2 given in Table II give direct answer for the values of Q. Thus, the found values vary between 0.1 and 160 eV, if the extreme cases of the noble gases are excluded, and they are largest for the most volatile FPs, as they should. Since further information is not available, we cannot judge whether they are realistic.

Turning now to Eq. (11), we have to be cautious not to make errors in the dimension. The dimension of c_3 is the negative log(energy·time), and we have consistently used the electron volt as the unit for energy. If the pertinent shift in the log scale is made and 6×10^{-6} m^2/s is used for the value of D_∞, we can rewrite Eq. (11) as

$$c_3 = 0.6 - 2\log\left(\frac{R}{1\ \mathrm{mm}}\right) + \log\left(\frac{T_0 - T_R}{10\ \mathrm{K}}\right) - 2\log\left(\frac{T_R}{1000\ \mathrm{K}}\right) \ . \qquad (20)$$

This means that consistency with Eq. (19) is achieved if the fuel can be characterized by coherent bits of ~0.5 mm in size and temperature differences of ~10°C. By making somewhat different choices of fuel parameters, one finds that it is hard to shift c_3 by more than a few units. In view of the speculative nature of Eq. (19), the errors in the experimental data, and the simplicity of our model, this result is quite satisfactory.

We conclude that the above analysis leads to a consistent and useful prediction of actual release rates. Presently available data suggest that interpolation formula (18) cannot give more than the order of magnitude of these rates. The temperature gradient, hidden in the constant 4.9 of this formula, may be higher during accident situations, so that under these conditions the release can be higher. Whether or not the formula is more precise remains to be proven by further experiments on the release rate of FPs from real fuel at high temperatures. We stress that the formula does not include eventual chemical retention on the fuel surface. Finally, to facilitate the comparison with the data in Ref. 2, we present Figs. 4 and 5 with release constants in the format of Fig. 3.4 of Ref. 2. They pertain to UO_2 and $UO_{2.04}$, respectively, and show the important increase of the release when UO_2 is oxidized. It is easy and straightforward to calculate cases for other FPs contained in Table II and for other cases of the nonstoichiometry.

ACKNOWLEDGMENT

This work has profited from a study contract of the Commission of the European Communities, Brussels, in the indirect action program on nuclear safety.

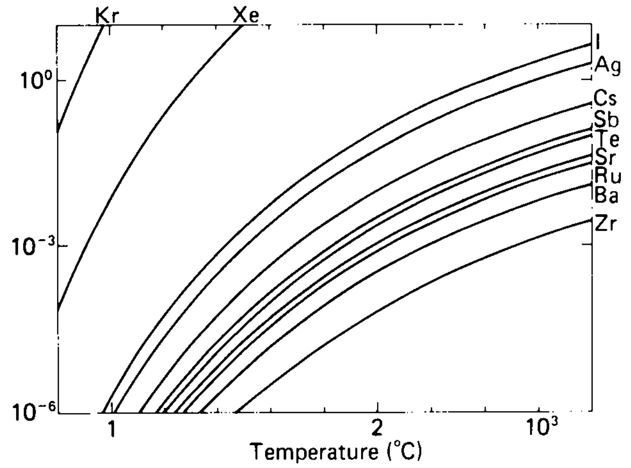

Fig. 4. Release rate constant, expressed in 1/min, as a function of the temperature, expressed in degrees Celsius, from UO_2, for various FPs, calculated from Eq. (18) and Table II.

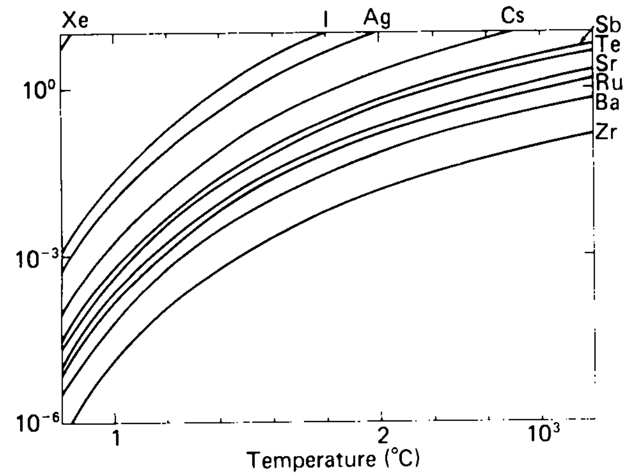

Fig. 5. Release rate constant, expressed in 1/min, as a function of the temperature, expressed in degrees Celsius, from $UO_{2.04}$, for various FPs, calculated from Eq. (18) and Table II.

REFERENCES

1. J. REST, "Evaluation of Volatile and Gaseous Fission Product Behavior in Water Reactor Fuel Under Normal and Severe Accident Conditions," *Nucl. Technol.*, **61**, 33 (1983).

2. "Technical Bases for Estimating Fission Product Behavior During LWR Accidents," NUREG-0772, U.S. Nuclear Regulatory Commission (1981); see also background material in document NUREG/CR 2507.

3. J. BELLE, A. B. AUSKERN, W. A. BOSTROM, and F. S. SUSKO, "Diffusion Kinetics in Uranium Dioxide," *Reactivity of Solids*, p. 452, J. H. DE BOER, Ed., Elsevier Publishing Company, Amsterdam (1961).

4. J. BELLE, Ed., "Uranium Dioxide—Properties and Nuclear Application," 3rd ed., p. 308, U.S. Atomic Energy Commission (1955).

5. R. HAUL, D. JUST, and G. DUEMBGEN, "Sauerstoffdiffusion in Oxyden," *Reactivity of Solids*, p. 65, J. H. DE BOER, Ed., Elsevier Publishing Company, Amsterdam (1961).

6. J. REKOLA, "Isothermal Sintering Kinetics of UO_{2+x}," *INIS Atomindex*, 11, RN 496545, International Atomic Energy Agency (1980).

7. D. CUBICCIOTTI, "A Model for Release of Fission Gases and Volatile Products from Irradiated UO_2 in Steam Environment," *Nucl. Technol.*, **53**, 5 (1981).

8. D. R. OLANDER, "Fundamental Aspects of Nuclear Reactor Fuel Elements," pp. 152 and 183, U.S. Department of Energy Technical Information Center (1976); these data strictly refer to mixed-oxide fuel.

9. P. G. SHEWMON, *Diffusion in Solids*, Secs. 2-5, McGraw-Hill Book Company, Inc., New York (1963).

10. M. O. TUCKER and R. J. WHITE, "The Release of Unstable Fission Products from UO_2 During Irradiation," *J. Nucl. Mater.*, **87**, 1 (1979).

11. D. R. OLANDER, "Fundamental Aspects of Nuclear Reactor Fuel Elements," p. 78, U.S. Department of Energy Technical Information Center (1976).

12. C. A. FRISKNEY and J. A. TURNBULL, "The Characteristics of Fission Gas Release from Uranium Dioxide During Irradiation," *J. Nucl. Mater.*, **79**, 184 (1979).

13. D. R. OLANDER, "Fundamental Aspects of Nuclear Reactor Fuel Elements," p. 164, U.S. Department of Energy Technical Information Center (1976).

14. H. BARTEN, KEMA Laboratories, Personal Communication (1983).

15. *Handbook of Chemistry and Physics*, 66th ed., p. F180, CRC Press (1982).

16. H. ALBRECHT and H. WILD, "Investigation of Fission Product Release by Annealing and Melting of LWR Fuel Pins in Air and Steam," ANS/ENS Meeting on Reactor Safety Aspects of Fuel Behavior, Sun Valley, Idaho (1981).

17. LANDOLT-BOERNSTEIN, *Atom- und Molekularphysik*, **2**, 27, Berlin (1951).

RADIOACTIVE WASTE MANAGEMENT

LEACH TESTING OF IDAHO NATIONAL ENGINEERING LABORATORY WASTE FORMS IN A GAMMA FIELD

ROBERT P. SCHUMAN *EG&G Idaho, Inc.*
Idaho National Engineering Laboratory
P.O. Box 1625, Idaho Falls, Idaho 83415

Received July 11, 1983
Accepted for Publication November 28, 1983

Two leach-resistant waste forms, a borosilicate glass developed for the high-level waste calcines from reprocessed uranium fuels and iron-enriched basalt, a fused ceramic developed for americium plus plutonium wastes, have been leach tested. The specimens were leached in distilled deionized water and in a saturated salt brine at ~30°C for 28, 63, and 126 days; one set was leached in a gamma field of $\sim 10^4$ *Gy/h (*$\sim 10^6$ *rad/h). The specimens were simulated high-level waste forms prepared from inactive ingredients and spiked with* ^{22}Na, ^{60}Co, ^{95}Zr-^{95}Nb, ^{137}Cs, ^{133}Ba, ^{144}Ce, *and* ^{241}Am. *The components were melted and heat treated, and specimens were sawed from the solidified material.*

The gamma field increased the leach rates in water (pH ~3 after irradiation) typically by a factor of ~10 and increased the leach rates in salt brine (pH decreased much less during irradiation) by a factor of ~2. The leach rate of cobalt from glass was about seven times that from iron-enriched basalt. The leach rates usually decreased with increasing leach time. Both waste forms were still leach resistant in irradiated brine at 30°C, $<2\ \mu g/cm^2 \cdot day$, *and fairly leach resistant in irradiated water at 30°C,* $<25\ \mu g/cm^2 \cdot day$.

INTRODUCTION

Leach-resistant glass waste forms for immobilizing calcined high-level waste from the Idaho Chemical Processing Plant[1] (ICPP) and a durable fused ceramic for immobilizing the alpha-contaminated wastes temporarily stored in the Waste Management Complex[2] have been developed at the Idaho National Engineering Laboratory (INEL). The fused ceramic also shows promise for immobilizing high-level reprocessing wastes. The primary purpose of these waste forms is to contain the fission products (FPs), activation products, and actinides in case the waste forms should be exposed to groundwater. Extensive tests (in the absence of a radiation field) have been made on the waste forms and have shown them to be leach resistant in distilled deionized water and simulated salt repository brines.[3,4] However, waste forms prepared from typical high-level reprocessing wastes containing FPs and activation products will produce a high radiation field and subject the groundwater to radiolysis. Pure water in a gamma field produces largely H_2 and O_2 gases and H_2O_2 in solution. If air is present, the N_2 and O_2 will combine in the radiation field to produce oxides of nitrogen that dissolve and oxidize in the water to form nitric acid.[5,6] If CO_2 is dissolved in the water, it is possible to produce organic acids, especially HCOOH and $H_2C_2O_4$, by the radiolytic reduction of CO_2 (Refs. 7 and 8). A number of studies have been made of the radiation chemistry of salt brines.[9,10] Leach tests in gamma-irradiated water have shown an enhancement of leaching due primarily to the radiolytically produced nitric acid in the leachant.[11,12]

The purpose of this study is to determine the leach resistance of the INEL waste forms in a gamma radiation field. Leach tests were run in distilled deionized water and in a saturated salt brine with a composition typical of Waste Isolation Pilot Plant (WIPP) brines. The gamma field was produced by the FPs from Advanced Test Reactor (ATR) spent fuel.

PREPARATION OF SAMPLES

The glass waste form was prepared from simulated calcined ICPP reprocessing waste.[13] The fused ceramic waste form, iron-enriched basalt (IEB), was prepared from simulated commercial high-level reprocessing waste.[14-16] The glass was prepared from inactive ingredients spiked with $\sim 10^4$ Bq/g each of 2.6-yr ^{22}Na, 5.26-yr ^{60}Co, 64-day ^{95}Zr plus 35-day

^{95}Nb daughter, 10.6-yr ^{133}Ba, 30.2-yr ^{137}Cs, 284-day ^{144}Ce plus 17-min ^{144}Pr daughter, and 432-yr ^{241}Am. These ingredients were melted at 1100°C in alumina crucibles; then the melt was poured on a graphite block and annealed. Table I lists the composition of the glass. The IEB was prepared by melting an optimized mix[17] with a simulated commercial high-level waste[14-16] and the same radioactive tracers in alumina crucibles at 1500°C. The melt was heat treated by cooling to 1000°C, held at 1000°C overnight, then slowly cooled to room temperature. Table II gives the composition of the IEB. This composition

TABLE I

Composition of ICPP Zirconia Calcine Glass

Frit 127 (66.7 wt%)	wt%	Zirconia Calcine (33.3 wt%)	wt%	Zirconia Calcine (33.3 wt%)	wt%
SiO_2	46.9	CaF_2	13.0	B_2O_3	0.67
B_2O_3	5.7	ZrO_2	7.0	Fe_2O_3	0.47
Na_2O (as Na_2CO_3, 14.5 wt%)	8.5	Al_2O_3	4.5	MgO	0.60
Li_2O (as Li_2CO_3, 10.2 wt%)	4.1	UO_2	0.03	NiO	0.07
CuO	1.4	ThO_2	0.03	Na_3PO_4	0.07
		$CaCO_3$	5.4	K_2CrO_4	0.10
		$NaNO_3$	0.77	Fissium (see next section)	0.67

Composition of Fissium

Addition	Weight Added per 100 g Fissium (g)	Element Represented	10-yr Decay ^{235}U Fission Yield (%)
SeO_2	0.17	Selenium	0.39
Rb_2CO_3	1.47	Rubidium	3.17
$SrCO_3$	4.36	Strontium	7.35
ZrO_2	15.88	Zirconium	32.12
MoO_3	14.04	Molybdenum	24.32
Ruthenium	7.01	Ruthenium	11.04
		Technetium	6.14
NiO	1.38	Rhodium	3.00
		Palladium	1.60
Antimony	0.10	Silver to antimony	0.21
TeO_2	1.36	Tellurium	2.13
Cs_2CO_3	11.84	Cesium	12.12
$BaCO_3$	6.41	Barium	8.10
La_2O_3	11.01	Lanthanum	6.55
		Yttrium	4.79
		Praseodymium	5.50
CeO_2	8.42	Cerium	12.91
Nd_2O_3	16.56	Neodymium	20.46
		Promethium	0.15
		Samarium	3.62
		Europium	0.30
Volatile and lost, none added to fissium		Bromine	0.14
		Krypton	5.41
		Iodine	0.93
		Xenon	21.72

TABLE II

Composition of IEB Prepared with Simulated High-Level Reprocessing Waste

IEB Mix, 80 wt%	wt%
SiO_2	39.9
Al_2O_3	7.8
Fe_2O_3	11.8
FeO	3.4
TiO_2	0.23
CaO	6.7
MgO	2.9
K_2O	1.9
Na_2O	5.2
P_2O_5	0.09
SO_3	0.01
Simulated Waste, 20 wt%	**wt%**
Al_2O_3	2.0
$K_2Cr_2O_7$	0.2
Fe_2O_3	2.0
MgO	0.8
Na_3PO_4	2.0
NiO	0.2
UO_2	0.8
Fissium (see Table I)	12.0

of IEB contains two major crystalline phases, spinel (magnetite) and augite, (Ca,Fe,Mg)(Si,Al)O_3, plus an aluminosilicate glass comprising 30 to 50% of the volume.[4,17]

Leach specimens with an area of 3 to 4 cm^2 were diamond sawed from the solidified melts. The saw gave a 400- to 600-grit finish, which met the Materials Characterization Center's MCC-1 leach test specifications.[18] Because of the activity of the spiked samples, the cutting was done in a glove box. The leach specimens were then cleaned in an ultrasonic bath with water and ethanol, their areas measured, and the weight of the dried specimens determined with a microbalance. The tracer content of the specimens was determined by counting the specimens at a 9-cm distance with a standardized Ge(Li) gamma spectrometer.

LEACH TESTING

The tests were patterned after the MCC-1 static leach test procedure,[18] with modifications necessary because of the high radiation for those tests in the gamma radiation field. The leachants used were distilled deionized water (in equilibrium with air) and salt brine. The distilled deionized water was prepared by distilling deionized water. The preparation was made according to MCC-1 specifications. The brine was WIPP brine B with a few minor components omitted (see Table III) (Ref. 19). For each specimen, a volume of leachant in cubic centimetres equal to ten times the sample surface area in square centimetres was used. The containers used for the leach tests in the gamma field had to be radiation resistant in a field of $\sim 10^4$ Gy/h ($\sim 10^6$ rad/h). The distilled deionized water was contained in 150-mm-high, 27-mm-diam, 0.5-mm-thick stainless steel tubes, and the brine was contained in 180-mm-high, 27-mm-diam glass-stoppered Pyrex test tubes. The stoppers for the tubes could leak slightly so that radiolytic gas pressure would not build up.

The gamma facility consisted of a dry aluminum tube placed in the ATR canal and surrounded by an array of ATR spent fuel elements. The leach tubes were held in a thin-walled, open, stainless steel can and suspended in the region of maximum gamma dose. A stream of air was passed over the tubes and manually adjusted to keep the temperature fairly constant. The temperature in the gamma facility averaged ~30°C, but did reach a maximum of 40°C when the gamma heating was greatest.

For comparison tests in the absence of the gamma field, MCC-1-specified Teflon jars[18] were used for the distilled deionized water, while the glass-stoppered Pyrex test tubes were used for the brine. The comparison samples were leached in a laboratory oven, which was maintained at the same temperature, ±2°C, as the samples in the gamma facility.

Samples were leached for 28, 63, and 126 days. The gamma field was measured with an ionization chamber every time spent fuel elements around the facility were changed. The total dose was calculated by multiplying the log mean of the initial and final gamma dose rates by the exposure time:

$$\log R_{lm} = \frac{\log Ri + \log Rf}{2} \ ,$$

where

R_{lm} = log mean dose

Ri = initial dose

Rf = final dose.

TABLE III

Composition of Simulated Salt Brine

	g/ℓ
NaCl	292.0
$CaSO_4$	2.7
NaBr	0.5
Na_2SO_4	2.0
$MgSO_4 \cdot 7H_2O$	0.1
H_2O	To make 1.00 ℓ

At the conclusion of the leach period, the tubes were removed and weighed to check for leachant evaporation. Then the tubes were opened and the samples removed, rinsed, dried, and weighed to determine weight loss. The pH of the leachates was then determined and the leachates transferred to polystyrene counting bottles and diluted to 50 ml with water rinses of the leach vessel. The entire 50 ml of solution was counted by placing the bottle on the 1-cm shelf of the standardized Ge(Li) gamma spectrometer. After the unacidified leachate was counted, the leachate was transferred back into the leach vessel, made 1% in HCl (brine) or HNO_3 (water) as specified by MCC-1, then digested overnight at 90°C. During digestion the leachate was allowed to evaporate a little. After digestion, the leachate was transferred back to the same counting bottle and the volume made up to 50 ml with 1% HCl or HNO_3 rinses. The solution was then recounted. The relative counting efficiencies of the nuclides in the thin specimens on the 9-cm shelf and in 50 ml of solution on the 1-cm shelf were determined by counting the same amount of tracer evaporated on a thin inactive glass sheet at 9 cm and in a 2% acid solution on the 1-cm shelf. The leach rates determined from the counts of the 1% acidified solutions gave the leach rates as specified by MCC-1 (Ref. 18).

Usually the counting rates of the unacidified and acidified solutions were the same, but for some samples the counting rate from the unacidified solution was significantly greater than that from the acidified solution, due most likely to the settling of solid alteration product, carrying activity to the bottom of the counting bottle. In only a few cases did the acid digestion increase the activity, indicating that usually very little activity was adsorbed on the leach containers.

A few distilled deionized water leachates, after acidification and counting, were analyzed for aluminum, calcium, sodium, silicon, lithium, boron, and iron by inductively coupled plasma (ICP) emission or atomic absorption (AA). No ICP or AA analyses were made of the brines because leaching of the Pyrex glass could add silicon and boron, and the sodium and calcium contents of the brine would mask the small concentration increase from leaching.

LEACH RATES

The weight loss leach rates were determined by dividing the weight loss by the measured sample area and the leach time. The standard deviation of the leach rates is estimated from a ±10-μg uncertainty in the weight loss and a ±10% uncertainty in the area. The weight loss leach rates are given in Table IV. The IEB samples typically showed a slight gain in weight when leached in brine, probably due to adsorption or ion exchange of Na^+ and other ions on the sample.

TABLE IV

Static Weight Loss Leach Rates, ~30°C, and Leachate pH

Time (day)	Gamma Dose (Gy)	IEB		Glass	
		Leach Rate ($\mu g/cm^2 \cdot day$)	pH of Leachate	Leach Rate ($\mu g/cm^2 \cdot day$)	pH of Leachate
Distilled Deionized Water					
28	5.2×10^6	1.8 ± 0.2	3.1	17 ± 2	3.4
28	0	>5.5[a]	7.4	0.39 ± 0.11	7.1
63	1.6×10^7	5.5 ± 0.6	2.7	<3.7[b]	---
63	0	0.21 ± 0.05	7.0	0.56 ± 0.09	6.3
126	3.1×10^7	1.91 ± 0.20	2.4	1.18 ± 0.12	4.8
126	0	0.12 ± 0.02	6.7	0.07 ± 0.02	7.5
Brine					
28	5.2×10^6	0.30 ± 0.09	---	0.40 ± 0.11	---
28	0	(Gain)	5.9	0.62 ± 0.13	---
63	1.6×10^7	0.06 ± 0.04	4.4	0.62 ± 0.08	5.0
63	0	(Gain)	6.8	0.30 ± 0.07	6.3
126	3.1×10^7	0.11 ± 0.03	4.0	0.12 ± 0.03	6.7
126	0	(Gain)	6.6	0.10 ± 0.03	6.5

[a] *A small piece broke off.*

[b] Leachant lost during test.

Weight loss leach rates are, therefore, not a good indicator of the durability of the materials.

The pH of each leachate at the end of the leach period is also given in Table IV. The low pH of the irradiated leachates, especially the distilled deionized water, shows the presence of radiolytic HNO_3.

The elemental leach rates of sodium, cobalt, zirconium, niobium, barium, cesium, cerium, and americium were determined from the 9-cm photopeak count rates of the leach specimens and the 1-cm count rates of the solutions in the counting bottles. The fraction leached was calculated by dividing the gamma photopeak count rate (corrected for background and decay) from the 50 ml of solution counted on the 1-cm shelf by the relative efficiency (peak counting rate of tracer in 50 ml of solution at 1 cm divided by peak counting rate of the same amount of tracer evaporated on glass at 9 cm) and the gamma photopeak count rate (corrected for background and decay) from the leach sample on the 9-cm shelf. The leach rate was then calculated by multiplying the fraction leached by the weight of the sample (in grams) and dividing by the area (in square centimetres) and the time of leach (in days). The standard deviation of the leach rates was estimated from a ±10% uncertainty in the area and counting efficiency ratio and the counting statistics. The activities were assumed to be uniformly distributed in the solution. If the activity were absorbed on a solid that settled to the bottom of the bottle, the counting rate would be high, giving a high leach rate. The elemental leach rates are given in Table V for IEB and Table VI for the glass. The leach rates are calculated from the counts on the acidified leachates; the leach rates calculated from the counts on the unacidified leachates are included in parentheses. The leach rates determined from the acidified leachates should have a minimal error from the settling of solids carrying absorbed activity.

The leach rates from the ICP-AA analyses were also calculated from the fraction leached (total weight leached divided by total weight of material in sample as estimated from composition of mixture melted). The results are given in Table VII. The standard deviation is calculated assuming a uniform melt and no loss of element or gain of aluminum during melting.

DISCUSSION OF RESULTS

The leach rates of both IEB and glass in distilled deionized water were markedly increased by the gamma irradiation of the leachant. The decrease in pH of the leachant showed the buildup of radiolytic nitric acid. The pH decrease was greater for the IEB leachates than the glass leachates, probably because the higher leachable alkali and alkaline earth contents of the glass helped neutralize the nitric acid. The leach rates of both IEB and glass in the irradiated water appeared to be due mainly to congruent dissolution, since the leach rates of sodium, barium, cesium, cerium, calcium, and silicon (plus cobalt, americium, lithium, and boron for the glass) and weight loss were roughly the same. The niobium leach rate (and the cobalt rate from IEB) was less but still appreciable, and the zirconium leach rate was almost always less than twice the detection limit. The americium leach rates from IEB tended to be higher than those of the other elements in irradiated water, but were usually low and often less than twice the detection limit in unirradiated water. The leach rates of aluminum in irradiated water were also higher than those of the other elements for both glass and IEB, while in unirradiated water they were only slightly greater than the detection limit. Pickup of aluminum from the alumina crucibles during sample preparation could give the specimens a higher aluminum content than assumed and help account for the high aluminum leach rates. The total amount of material leached, both in irradiated and unirradiated water, tended to increase little (especially for glass) with leach time; in fact, considerably more material was leached from the 28-day glass leach sample than from the 126-day glass sample, perhaps due to the higher final pH of the 126-day leachant, or perhaps due to the expected large variation of leach rates from different samples. The highest leach rates observed ($\sim 20\ \mu g/cm^2 \cdot day$), those for glass in irradiated water for 28 days (final pH 3.4), were much less than those ($\sim 600\ \mu g/cm^2 \cdot day$) from the same glass in pH 3.8 acetic-acid/sodium-acetate buffer at 25°C (Ref. 20). A summary of the leach results, expressed in micrograms leached per square centimetre during the total leach period, is given in Table VIII.

The gamma radiation field increased the leaching in salt brine much less than it did in water, and the pH of the brine decreased less. The leaching of sodium was essentially unchanged while the leaching of cobalt, cesium, and barium was roughly doubled (see Table VIII). Again the leach rate of americium was significantly increased, especially for IEB. In the absence of the radiation field, the leach rates in brine are roughly the same as those in water; sodium tends to be somewhat more leachable in brine.

The leach containers that were used in the gamma field had to be radiation resistant. Both the Pyrex glass and stainless steel containers that we used were satisfactory and showed no detectable corrosion or physical damage other than the coloration of the glass. The retention of radioactivity on the containers after washing with dilute acid and alkaline ethylene diamine tetraacetic acid was barely detectable and no more than that on Teflon containers. The glass tubes were easier to fabricate and allowed almost no evaporation of the leachant. The irradiated water leachates showed some iron. If all the iron in the 63-day leachate (final pH 2.7) was due to corrosion of the stainless steel, the corrosion was 6 μg iron/cm^2. Iron from the

TABLE V

Static Elemental Leach Rates from IEB, ~30°C

($\mu g/cm^2 \cdot day$)

Element	Leach Time					
	28 days		63 days		126 days	
	Gamma Dose					
	5.2 × 10^6 Gy	0 Gy	1.6 × 10^7 Gy	0 Gy	3.1 × 10^7 Gy	0 Gy
Distilled Deionized Water						
Sodium	1.78 ± 0.20[a] (1.71 ± 0.20)	0.86 ± 0.12 (0.81 ± 0.11)	9.6 ± 1.1 (8.8 ± 1.0)	0.39 ± 0.05 (0.39 ± 0.06)	2.6 ± 0.3 (2.7 ± 0.3)	0.36 ± 0.04 (0.33 ± 0.04)
Cobalt	0.43 ± 0.05 (0.45 ± 0.05)	0.096 ± 0.015 (0.073 ± 0.018)	0.80 ± 0.08 (0.90 ± 0.09)	0.048 ± 0.008 (0.032 ± 0.008)	0.52 ± 0.06 (0.59 ± 0.06)	0.032 ± 0.005 (0.029 ± 0.005)
Zirconium	0.19 ± 0.14 (0.16 ± 0.12)	0.00 ± 0.12 (0.08 ± 0.12)	0.0 ± 0.2 (0.3 ± 0.3)	0.00 ± 0.08 (0.00 ± 0.06)	0.65 ± 0.18 (0.07 ± 0.13)	0.00 ± 0.08 (0.00 ± 0.07)
Niobium	3.7 ± 0.4 (1.3 ± 0.2)	0.04 ± 0.02 (0.06 ± 0.03)	2.4 ± 0.3 (5.7 ± 0.6)	0.00 ± 0.03 (0.02 ± 0.03)	1.88 ± 0.20 (1.55 ± 0.18)	0.00 ± 0.03 (0.00 ± 0.02)
Barium	1.24 ± 0.25 (1.27 ± 0.28)	0.19 ± 0.04 (0.12 ± 0.03)	10.5 ± 2.6 (9.3 ± 1.5)	0.10 ± 0.02 (0.12 ± 0.02)	2.5 ± 0.5 (2.5 ± 0.5)	0.094 ± 0.020 (0.086 ± 0.016)
Cesium	0.99 ± 0.12 (1.18 ± 0.25)	1.33 ± 0.14 (1.43 ± 0.15)	7.0 ± 0.7 (6.9 ± 0.7)	0.20 ± 0.03 (0.20 ± 0.03)	2.2 ± 0.3 (2.2 ± 0.3)	0.17 ± 0.02 (0.16 ± 0.02)
Cerium	2.9 ± 0.3 (2.9 ± 0.3)	0.16 ± 0.04 (0.17 ± 0.04)	10.9 ± 1.1 (9.1 ± 1.0)	0.14 ± 0.04 (0.04 ± 0.04)	3.2 ± 0.4 (3.2 ± 0.4)	0.09 ± 0.02 (0.05 ± 0.02)
Americium	12.0 ± 1.3 (10.9 ± 1.2)	0.41 ± 0.12 (0.27 ± 0.10)	17.5 ± 2.0 (14.2 ± 1.7)	0.09 ± 0.09 (0.06 ± 0.07)	7.8 ± 0.9 (7.6 ± 0.9)	0.03 ± 0.03 (0.01 ± 0.02)
Salt Brine						
Sodium	1.85 ± 0.21 (1.89 ± 0.21)	1.91 ± 0.23 (1.96 ± 0.23)	1.82 ± 0.20 (1.56 ± 0.20)	1.83 ± 0.20 (1.75 ± 0.19)	0.90 ± 0.10 (0.91 ± 0.10)	1.22 ± 0.18 (1.22 ± 0.18)
Cobalt	0.054 ± 0.009 (0.049 ± 0.009)	0.083 ± 0.017 (0.094 ± 0.014)	0.064 ± 0.007 (0.039 ± 0.007)	0.032 ± 0.006 (0.019 ± 0.005)	0.043 ± 0.005 (0.059 ± 0.006)	0.013 ± 0.004 (0.022 ± 0.003)
Zirconium	0.0 ± 0.1 (0.0 ± 0.1)	0.18 ± 0.16 (0.00 ± 0.14)	0.0 ± 0.2 (0.0 ± 0.1)	0.00 ± 0.13 (0.00 ± 0.09)	0.00 ± 0.07 (0.00 ± 0.05)	0.00 ± 0.10 (0.00 ± 0.08)
Niobium	0.07 ± 0.03 (0.04 ± 0.02)	0.15 ± 0.05 (0.11 ± 0.03)	0.04 ± 0.06 (0.02 ± 0.03)	0.03 ± 0.05 (0.00 ± 0.03)	0.05 ± 0.02 (0.04 ± 0.02)	0.00 ± 0.04 (0.00 ± 0.02)
Barium	0.20 ± 0.03 (0.13 ± 0.04)	0.16 ± 0.03 (0.17 ± 0.03)	0.17 ± 0.02 (0.14 ± 0.02)	0.080 ± 0.013 (0.067 ± 0.013)	0.113 ± 0.012 (0.113 ± 0.012)	0.038 ± 0.009 (0.050 ± 0.006)
Cesium	0.21 ± 0.04 (0.25 ± 0.04)	0.27 ± 0.06 (0.23 ± 0.05)	0.41 ± 0.05 (0.35 ± 0.05)	0.15 ± 0.03 (0.18 ± 0.03)	0.14 ± 0.02 (0.12 ± 0.02)	0.030 ± 0.012 (0.034 ± 0.010)
Cerium	0.00 ± 0.05 (0.00 ± 0.05)	0.00 ± 0.06 (0.12 ± 0.06)	0.00 ± 0.04 (0.00 ± 0.03)	0.00 ± 0.02 (0.00 ± 0.02)	0.044 ± 0.014 (0.068 ± 0.014)	0.00 ± 0.02 (0.00 ± 0.02)
Americium	1.9 ± 0.2 (1.6 ± 0.2)	0.33 ± 0.14 (0.20 ± 0.11)	0.73 ± 0.12 (0.73 ± 0.10)	0.00 ± 0.06 (0.00 ± 0.05)	0.22 ± 0.07 (0.30 ± 0.07)	0.00 ± 0.04 (0.05 ± 0.03)

[a] The first value is from acidified leachates; the second, in parentheses, is from unacidified leachates.

TABLE VI

Static Elemental Leach Rates from Glass, ~30°C

($\mu g/cm^2 \cdot day$)

Element	Leach Time					
	28 days		63 days		126 days	
	Gamma Dose					
	5.2×10^6 Gy	0 Gy	1.6×10^7 Gy	0 Gy	3.1×10^7 Gy	0 Gy
Distilled Deionized Water						
Sodium	21 ± 3[a] (20 ± 3)	0.39 ± 0.07 (0.36 ± 0.07)	--- ---	0.25 ± 0.04 (0.22 ± 0.04)	0.86 ± 0.11 (0.95 ± 0.11)	0.13 ± 0.02 (0.14 ± 0.02)
Cobalt	22 ± 3 (22 ± 3)	0.35 ± 0.04 (0.35 ± 0.04)	--- ---	0.25 ± 0.03 (0.19 ± 0.02)	1.19 ± 0.13 (1.21 ± 0.13)	0.092 ± 0.010 (0.098 ± 0.010)
Zirconium	0.09 ± 0.07 (0.00 ± 0.10)	0.12 ± 0.10 (0.00 ± 0.10)	--- ---	0.0 ± 0.1 (0.0 ± 0.1)	0.17 ± 0.16 (0.00 ± 0.10)	0.00 ± 0.05 (0.00 ± 0.06)
Niobium	6.5 ± 0.7 (1.2 ± 0.2)	0.05 ± 0.04 (0.04 ± 0.04)	--- ---	0.06 ± 0.04 (0.00 ± 0.03)	0.22 ± 0.05 (0.11 ± 0.04)	0.00 ± 0.02 (0.02 ± 0.02)
Barium	23 ± 3 (24 ± 3)	0.13 ± 0.03 (0.14 ± 0.03)	--- ---	0.21 ± 0.04 (0.12 ± 0.02)	0.90 ± 0.10 (0.91 ± 0.10)	0.046 ± 0.006 (0.049 ± 0.008)
Cesium	20 ± 3 (22 ± 3)	0.30 ± 0.06 (0.28 ± 0.06)	--- ---	0.27 ± 0.05 (0.22 ± 0.03)	0.74 ± 0.08 (0.72 ± 0.08)	0.080 ± 0.012 (0.078 ± 0.012)
Cerium	21 ± 3 (22 ± 3)	0.00 ± 0.05 (0.04 ± 0.05)	--- ---	0.17 ± 0.05 (0.03 ± 0.03)	0.38 ± 0.04 (0.38 ± 0.04)	0.018 ± 0.011 (0.010 ± 0.011)
Americium	24 ± 3 (27 ± 3)	0.00 ± 0.10 (0.00 ± 0.10)	--- ---	0.16 ± 0.08 (0.00 ± 0.05)	0.89 ± 0.11 (0.65 ± 0.10)	0.00 ± 0.02 (0.00 ± 0.02)
Salt Brine						
Sodium	1.02 ± 0.14 (1.01 ± 0.14)	0.82 ± 0.12 (0.78 ± 0.11)	0.18 ± 0.03 (0.13 ± 0.02)	0.085 ± 0.032 (0.10 ± 0.02)	0.44 ± 0.05 (0.43 ± 0.05)	0.33 ± 0.04 (0.31 ± 0.05)
Cobalt	0.88 ± 0.09 (0.84 ± 0.09)	0.59 ± 0.06 (0.58 ± 0.06)	0.34 ± 0.04 (0.24 ± 0.03)	0.080 ± 0.009 (0.081 ± 0.009)	0.28 ± 0.03 (0.30 ± 0.03)	0.21 ± 0.03 (0.22 ± 0.03)
Zirconium	0.08 ± 0.10 (0.00 ± 0.10)	0.11 ± 0.14 (0.00 ± 0.14)	0.00 ± 0.07 (0.00 ± 0.06)	0.00 ± 0.10 (0.00 ± 0.06)	0.00 ± 0.10 (0.00 ± 0.07)	0.00 ± 0.10 (0.07 ± 0.07)
Niobium	0.08 ± 0.04 (0.10 ± 0.05)	0.09 ± 0.05 (0.12 ± 0.03)	0.03 ± 0.03 (0.00 ± 0.02)	0.00 ± 0.04 (0.01 ± 0.02)	0.00 ± 0.03 (0.03 ± 0.02)	0.00 ± 0.03 (0.01 ± 0.02)
Barium	0.97 ± 0.10 (0.88 ± 0.09)	0.61 ± 0.11 (0.64 ± 0.19)	0.10 ± 0.02 (0.11 ± 0.02)	0.078 ± 0.013 (0.048 ± 0.009)	0.40 ± 0.05 (0.37 ± 0.05)	0.24 ± 0.03 (0.28 ± 0.03)
Cesium	0.76 ± 0.09 (0.81 ± 0.09)	0.56 ± 0.08 (0.46 ± 0.07)	0.091 ± 0.022 (0.104 ± 0.020)	0.029 ± 0.022 (0.062 ± 0.015)	0.28 ± 0.04 (0.32 ± 0.04)	0.22 ± 0.03 (0.22 ± 0.03)
Cerium	0.00 ± 0.05 (0.00 ± 0.05)	0.07 ± 0.07 (0.12 ± 0.07)	0.00 ± 0.02 (0.00 ± 0.02)	0.03 ± 0.03 (0.00 ± 0.02)	0.032 ± 0.017 (0.044 ± 0.017)	0.000 ± 0.015 (0.006 ± 0.014)
Americium	0.56 ± 0.12 (0.47 ± 0.12)	0.04 ± 0.12 (0.18 ± 0.12)	0.23 ± 0.05 (0.15 ± 0.05)	0.04 ± 0.04 (0.00 ± 0.03)	0.07 ± 0.03 (0.08 ± 0.03)	0.00 ± 0.02 (0.00 ± 0.02)

[a] The first value is from acidified leachates; the second, in parentheses, is from unacidified leachates.

corrosion of ductile cast iron has been found to accelerate leaching from a zinc borosilicate glass at 90°C (Ref. 21). The leaching conditions were much different from those of this experiment: final pH 9 to 10 compared to 3, temperature 90°C rather than 30°C, and a cast iron rather than corrosion-resistant stainless steel. Also, iron silicates would not be expected to form in the low pH of this experiment. No significant effect on the leaching due to the stainless steel would be expected, although it has not been ruled out.

Since Pyrex glass tubes were used for the brine leaching both with and without the gamma field, the effect, if any, on leaching due to silicon saturation by silicon leaching from the Pyrex will be the same for both tests. Some early leach experiments made in Pyrex containers gave the same leach rates (silicon was not determined) as those made in polypropylene containers.[20]

TABLE VII

Static Elemental Leach Rates in Distilled Deionized Water, ~30°C, as Determined by ICP ($\mu g/cm^2 \cdot day$)

	Material Leached								
	IEB	IEB	Glass	IEB	IEB	IEB	Glass	IEB	Glass
	Gamma Dose (Gy)								
	5.2×10^6	0	0	1.6×10^7	0	3.1×10^7	3.1×10^7	0	0
	Leach Time (days)								
Element	28	28	28	63	63	126	126	126	126
Lithium	---	---	0.48 ± 0.22	---	---	---	1.16 ± 0.18	---	0.14 ± 0.07
Boron	---	---	---	---	---	---	1.09 ± 0.14	---	0.26 ± 0.10
Sodium	1.14 ± 0.21	0.51 ± 0.13	0.55 ± 0.08	4.4 ± 0.7	0.28 ± 0.05	1.5 ± 0.3	1.24 ± 0.18	0.25 ± 0.10	0.24 ± 0.04
Aluminum	10 ± 3	0.20 ± 0.08	0.43 ± 0.22	14.7 ± 2.3	0.11 ± 0.07	5.3 ± 0.9	52 ± 6	0.07 ± 0.03	0.23 ± 0.08
Silicon	0.64 ± 0.09	0.17 ± 0.04	0.21 ± 0.07	5.5 ± 0.7	0.00 ± 0.03	1.48 ± 0.18	0.89 ± 0.13	0.08 ± 0.03	0.08 ± 0.03
Calcium	2.8 ± 0.3	0.81 ± 0.10	0.56 ± 0.18	7.8 ± 0.8	0.44 ± 0.07	2.9 ± 0.5	0.84 ± 0.15	0.09 ± 0.04	0.09 ± 0.04
Iron	<15[a]	0.06 ± 0.03	1.5 ± 1.5	<13[a]	0.00 ± 0.02	---	---	---	---

[a] The iron leach rates in the radiation field are meaningless because of iron from the corrosion of the stainless steel leach tubes.

CONCLUSIONS

The experiments allowed comparison of a high quality glass and IEB for immobilizing high-level waste. Except for the 28-day leach in irradiated distilled deionized water, where the glass was considerably more leachable, both the glass and IEB had about the same leach rates under the same conditions. The IEB gave consistently lower leach rates for cobalt, however, since the cobalt in the IEB was probably incorporated isomorphously in the magnetite, (Fe,Co) Fe_2O_4, phase. For glass, cobalt was about as leachable as barium and cesium, while for IEB it was only about one-seventh as leachable. The use of tracer-spiked specimens simplified leachate analysis, especially for the brine.

The experiments showed that both the IEB and the glass are leach resistant in saturated WIPP brine, even in the presence of a high gamma radiation field.

ACKNOWLEDGMENT

This work was supported by the U.S. Department of Energy under contract DE-AC07-761D01570.

REFERENCES

1. B. A. STAPLES, D. A. PAVLICA, and H. S. COLE, "Properties of Formula 127 Glass Prepared with Radioactive Zirconia Calcine," ENICO-1120, Exxon Nuclear Idaho Company, Inc. (Sep. 1982).

2. J. M. WELCH, P. V. KELSEY, S. P. HENSLEE, R. L. TALLMAN, R. P. SCHUMAN, R. M. HORTON, C. W. SILL, D. E. OWEN, and J. E. FLINN, "Iron-Enriched Basalt for Containment of Nuclear Waste," *Scientific Basis for Nuclear Waste Management*, Vol. 4, p. 23, S. TOPP, Ed., Plenum Press, New York (1982).

TABLE VIII

Total Amount Leached, $\mu g/cm^2$

Element	Time							
	28 days				133 days			
	Dose (Gy)							
	5.3×10^6		0		3.1×10^7		0	
	Material							
	IEB	Glass	IEB	Glass	IEB	Glass	IEB	Glass
30°C Distilled Deionized Water								
Weight	50	480	---	11	240	150	15	8.8
Sodium	50	590	24	11	330	110	45	16
Cobalt	12	620	2.7	10	66	150	4	12
Niobium	100	180	[a]	[a]	240	28	[a]	[a]
Barium	35	640	5.3	3.6	310	110	12	5.8
Cesium	28	560	37	8.4	280	93	21	10
Cerium	81	590	4.5	[a]	400	48	11	[a]
Americium	340	670	11	[a]	980	110	[a]	[a]
Lithium	---	---	---	14	---	150	---	18
Boron	---	---	---	---	---	140	---	33
Aluminum	280	---	5.6	12	670	6600	9	29
Silicon	18	---	4.8	5.9	190	110	10	10
Calcium	78	---	23	16	370	110	11	11
30°C Salt Brine								
Sodium	52	29	53	23	110	55	150	42
Cobalt	1.5	25	2.3	16	5.4	35	1.6	26
Niobium	2.0	[a]	4	[a]	6.3	[a]	[a]	[a]
Barium	5.6	27	4.5	17	14	50	4.8	30
Cesium	5.9	21	7.6	16	18	35	3.8	28
Americium	53	16	9.2	[a]	28	9	[a]	[a]

[a] Less than 2σ from zero.

3. R. P. SCHUMAN, "Leach Testing of the Idaho Chemical Processing Plant Final Waste Forms," *Nucl. Technol.*, **56**, 254 (1982).

4. R. P. SCHUMAN, J. M. WELCH, and B. A. STAPLES, "Preparation and Leaching of Radioactive INEL Waste Forms," *Waste Management, 82*, Vol. 3, p. 355, R. G. POST, Ed., University of Arizona, Nuclear Engineering Department (1982).

5. A. R. JONES, "Radiation-Induced Reactions in the N_2-O_2-H_2O System," *Radiat. Res.*, **10**, 655 (1959).

6. G. R. CHOPPIN and J. RYDBERG, *Nuclear Chemistry, Theory and Applications*, pp. 322-326, Pergamon Press, New York (1980).

7. A. BARKATT, A. BARKATT, and W. SOUSANPOUR, "Effects of γ Radiation on the Leaching Kinetics of Various Nuclear Waste-Form Materials," *Nature*, **300**, 339 (Nov. 1982).

8. A. BARKATT, A. BARKATT, and W. SOUSANPOUR, "Gamma Radiolysis of Aqueous Media and Its Effects on the Leaching Processes of Nuclear Waste Disposal Materials," *Nucl. Technol.*, **60**, 218 (1983).

9. G. H. JENKS and J. R. WALTON, "Radiation Chemistry of Salt-Mine Brines and Hydrates," ORNL-5726, Oak Ridge National Laboratory (July 1981).

10. G. H. JENKS, "Review of Information on the Radiation Chemistry of Materials Around Waste Canisters in Salt and Assessment of the Need for Additional Experimental

Information," ORNL-5607, Oak Ridge National Laboratory (Mar. 1980).

11. W. G. BURNS, A. E. HUGHES, J. A. C. MARPLES, R. S. NELSON, and A. M. STOREHAM, "Radiation Effects and the Leach Rates of Vitrified Radioactive Waste," *Nature*, **295**, 130 (Jan. 1982).

12. G. L. McVAY and L. R. PEDERSON, "Effects of Gamma Radiation on Glass Leaching," *J. Am. Ceram. Soc.*, **64**, 154 (Mar. 1981).

13. B. A. STAPLES, G. S. POMIALE, and E. L. WADE, "Properties of Radioactive Calcine Retrieved from the Second Calcined Solids Storage Facility at ICPP," ICP-1189, Allied Chemical-Idaho Chemical Programs (1979).

14. R. BONNIAUD, "La Vitrification en France des Solutions de Produits de Fission," *Nucl. Technol.*, **34**, 449 (1977).

15. P. TEMPEST, "A Comparison of Borosilicate Glass and Synthetic Minerals as Media for the Immobilization of High-Level Radioactive Waste," *Nucl. Technol.*, **52**, 415 (1981).

16. H. T. BLAIR, "Full-Scale In-Can Melting for Vitrification of Nuclear Wastes," *Nucl. Technol.*, **49**, 267 (1980).

17. J. E. FLINN, S. P. HENSLEE, P. V. KELSEY, R. L. TALLMAN, and J. M. WELCH, "Characterization of Iron-Enriched Synthetic Basalt for Transuranic Containment," *Scientific Basis for Nuclear Waste Management*, Vol. 3, p. 201, J. G. MOORE, Ed., Plenum Press, New York (1981).

18. D. M. STRACHAN, R. P. TURCOTTE, and B. O. BARNES, "MCC-1: A Standard Leach Test for Nuclear Waste Forms," *Nucl. Technol.*, **56**, 306 (1982); see also J. E. MENDEL, "MCC-IP Static Leach Test Method," *Nuclear Waste Materials Handbook*, DOE/TIC-11400, Battelle-Pacific Northwest Laboratories (1981).

19. J. W. BRAITHWAITE and M. A. MOLECKE, "Nuclear Waste Canister Corrosion Studies Pertinent to Geological Isolation," *Nuclear and Chemical Waste Management*, Vol. 1, p. 37 (1980).

20. R. P. SCHUMAN, "Leach Testing of Idaho Chemical Processing Plant Final Waste Forms," ENICO-1064, Exxon Nuclear Idaho Company, Inc. (Oct. 1980).

21. G. L. McVAY and C. Q. BUCKWALTER, "Effect of Iron on Waste-Glass Leaching," *J. Am. Ceram. Soc.*, **66**, 170 (Mar. 1983).

THE LEACHING BEHAVIOR OF ZIRCALOY CLADDING AND ITS IMPACT ON THE CONDITIONING OF WASTE FOR FINAL DISPOSAL

BERTHOLD-GÜNTER BRODDA and ERICH RICHARD MERZ
Kernforschungsanlage Jülich GmbH
Institut für Chemische Technologie der Nuklearen Entsorgung
Postfach 1913, D-5170 Jülich, Federal Republic of Germany

Received August 1, 1983
Accepted for Publication December 5, 1983

The leaching behavior of real Zircaloy cladding hulls, originating from the pressurized water reactor nuclear power station at Obrigheim, Federal Republic of Germany, was investigated using distilled water; nitric acid; sodium hydroxide solution; Portland, alumina, and Sorel cement lye solutions; and a potassium pyrosulfate melt as leachants.

The leached fraction was determined for six gamma-emitting isotopes and two actinides.

The distributions of the radionuclides in the hulls were determined using a potassium pyrosulfate melt. The results indicated that actinides (plutonium and curium) were concentrated on the surface; the diffusing species (ruthenium and cesium) had high concentrations at the surface but also appeared in the inner portions of the hulls. The distribution of activation products (cobalt and antimony) was very nearly homogeneous throughout the hulls.

It is recommended that, prior to reprocessing, the Zircaloy-clad fuel rods be separated from the fuel assembly to facilitate handling of the alpha-contaminated waste stream. The results of this study show that decontamination with nitric acid should be sufficient for further conditioning prior to disposal if conditioning is required.

INTRODUCTION

Zircaloy cladding hulls leached with semiconcentrated nitric acid become radioactive waste in reprocessing fuel elements from light water reactors (LWRs). The Zircaloy amounts to almost 300 kg/ton of heavy metal (HM) or UO_2. There is an additional 60 kg of structural material (head and support pieces, spacers, guide tubes, etc.) in the case of complete boiling water fuel elements, or 120 kg in the case of pressurized water reactor (PWR) fuel elements. These additional parts are fabricated from stainless steel or Inconel, and it is appropriate to deal with them as separate waste streams, although currently, this is not the practice everywhere.

The use of a single-rod shear makes it possible to separate the Zircaloy cladding hulls almost completely from the other structural materials. However, this is not possible to the same extent if a bundle shear is used. In this case the head and support pieces can easily be sawed off prior to shearing and separated from the main material flow. The other structural sections (e.g., spacers and guide tubes), whose weight is about two-thirds that of the head and support pieces and contain several times as many activation products, cannot be separated from the cladding so easily. After a decay time of 5 to 7 yr, the most important radioisotopes in these components are ^{55}Fe, ^{60}Co, ^{63}Ni, and, at a somewhat lower level, ^{125}Sb. Detailed computations of the radioactivities and thermal power levels for these parts can be found in Ref. 1.

The primary point is, however, that all structural sections—apart from low external contaminations—are free of alpha emitters, and thus can be put into a lower classification with respect to their long-term radiotoxicity than the Zircaloy cladding hulls, which contain higher levels of actinides. These actinides result partly from residues of undissolved fuel retained on the fuel cladding and partly from trace amounts of actinides adsorbed or bonded on the surface layers.

If it were possible to make the cladding hulls largely free of alpha contamination by a suitable purification step, this would simplify the final storage design.

OBJECTIVES

The present investigation was concerned with the leaching behavior of Zircaloy cladding hulls under various conditions on real experimental material. The goal was to develop suggestions for improvements in the handling of reprocessing waste, using the results from the present study and the findings of earlier works.[2-6] These earlier works discussed the impact of tritium and krypton (isotopes not included in this study) on the handling of reprocessing waste.

EXPERIMENTAL MATERIAL

Two types of Zircaloy cladding hulls with different pretreatments were available for the experimental studies. Both types originated from fuel used in the PWR nuclear power station at Obrigheim, Federal Republic of Germany. The major characteristics of the two types of hulls are given in Table I.

The Kraftwerk Union (KWU) cladding hulls specimens (hereafter referred to as type P-1) were obtained in the hot cells at the KWU in Karlstein by cutting a fuel rod into ~6-cm-long sections and mechanically ejecting the UO_2 pellets. Although the inside surfaces were mechanically buffed after ejection, the cladding hulls still contained trace amounts of fuel. For this reason, the leached fractions measured in the experiments were higher than those from cladding hull sections obtained from the Karlsruhe reprocessing facility (WAK). Two different hull types (designated P-2a and P-2b) were available from WAK. They had different levels of contamination (see the initial radioactivities in Tables II and III) due to differences in the dissolving and washing steps at the reprocessing facility. For use in the experiments, cladding hulls were subsequently cut into 1-cm sections.

All cladding hulls displayed a dark coloration on both the inside and outside surfaces. This is a very thin oxide layer, several microns in thickness. These oxide layers resist acid or alkaline leachant attack but can be dissolved in a pyrosulfate melt.

EXPERIMENTAL PROCEDURE

Measurements of the alpha and gamma radioactivities were carried out using standard procedures. Whereas the gamma radioactivities of the individual specimens could be directly measured with a Ge(Li) semiconductor detector, alpha spectrometry required the preparation of thin samples by electrodeposition.[7]

The cladding hulls were boiled under a reflux condenser for 3 h using 50 ml of the solutions described below. The solutions were filtered after cooling and their radioactive inventories measured. The cladding hulls were directly measured by gamma spectrometry.

The following aqueous solvents were used:

1. double distilled water (H_2O)
2. 7 *M* HNO_3
3. 1 *M* NaOH
4. Portland cement (PC) solution produced by agitating a mixture of 60 g PC and 110 g H_2O in a tumbler for several days (the clear filtrate had a pH value of 12.6)
5. alumina cement (AC) solutions produced by agitating a mixture of 60 g AC with 200 g H_2O for several days (the clear filtrate had a pH value of 11.6)
6. Sorel cement (SC) leach simulate produced by agitating a mixture of 150 g of a saturated aqueous $MgCl_2$ solution with a 1 g MgO for 24 h (the pH value of the clear filtrate was 5.9).

Molten salt decompositions with potassium pyrosulfate were carried out by heating in a nickel crucible at 400°C. The solidified melts were then dissolved in warm 1 *M* H_2SO_4. Radionuclide distributions in the hulls were obtained from sequential molten salt decompositions. Measurements of activity and hull weight were made at various times during the course of the experiment starting at 0.25 h and ending at 110 h. The activity of the gamma emitters was determined from gamma spectrometry of the residual cladding

TABLE I

Characteristics of Hulls Investigated in the Present Study

Type	KWU (P-1)	WAK (P-2a and P-2b)
Initial enrichment	3.1%	3.02%
Burnup	30 000 MWd·ton^{-1}	28 200 MWd·ton^{-1}
Mean power density of fuel rod	180 W·cm^{-1}	200 W·cm^{-1}
Discharge from reactor	May 1977	August 1975
Reprocessing date	Not applicable	1977
Cladding hull material	Zircaloy-4	Zircaloy-4
Separation fuel-cladding hulls	Mechanical	Chemical

TABLE II

The Behavior of Gamma-Emitting Nuclides in Zircaloy Cladding Hulls Under the Action of Different Aqueous Leachants

Sample	Nuclide	Initial Radioactivity (μCi·g^{-1})	Radionuclide Fraction Leached (%)					
			H_2O	HNO_3	NaOH	PC	AC	SC
P-1	^{134}Cs	181	7.8	10.9	15.4	9.8	13.8	12.7
	^{137}Cs	936	7.2	11.0	14.9	9.9	13.8	12.7
	^{106}Rh	414	ND[a]	21.4	1.1	ND	ND	1.7
	^{154}Eu	33	ND	0.4	ND	ND	ND	ND
	^{125}Sb	1234	0.8	2.3	3.5	0.2	0.9	0.5
	^{60}Co	69	ND	0.3	1.5	ND	ND	ND
P-2a	^{134}Cs	41	1.5	12.4	3.7	2.4	3.2	1.3
	^{137}Cs	498	1.5	12.5	3.7	2.3	3.0	1.4
	^{106}Rh	13	ND	99.5	1.8	NM[b]	NM	NM
	^{154}Eu	14	ND	2.8	ND	ND	ND	ND
	^{125}Sb	222	0.9	30.2	7.7	0.1	1.0	1.8
	^{60}Co	26	ND	40.7	2.9	ND	ND	ND
P-2b	^{134}Cs	0.4	49.8	81.9	56.1	NM	NM	NM
	^{137}Cs	3.8	75.8	95.6	86.1	NM	NM	NM
	^{106}Rh	2.5	24.0	99.5	2.7	NM	ND	NM
	^{154}Eu	ND	ND	ND	ND	ND	ND	ND
	^{125}Sb	45	23.2	28.3	10.3	ND	28	NM
	^{60}Co	8	9.1	48.4	4.3	NM	ND	NM

[a] ND = not detectable.
[b] NM = not measured.

TABLE III

Leaching Behavior of Actinides in Zircaloy Cladding Hulls

Hull Type	Initial Radioactivity		Leachant	Leached Fraction	
	^{239,240}Pu (μCi·g^{-1})	^{244}Cm (μCi·g^{-1})		^{239,240}Pu (%)	^{244}Cm (%)
P-1	150	260	HNO_3	60	46
			$K_2S_2O_7$	40	54
			NaOH	ND[a]	ND
			$K_2S_2O_7$	57	52
P-2a	1100	570	HNO_3	90	40
			$K_2S_2O_7$	10	60
			NaOH	ND	ND
			$K_2S_2O_7$	59	100
P-2b	440	10	HNO_3	98	100
			$K_2S_2O_7$	2	ND
			NaOH	ND	ND
			$K_2S_2O_7$	70	80

[a] ND = not detectable.

hulls; the activity of the actinides was obtained from the filtered solutions.

EXPERIMENTAL RESULTS

Table II shows the results, in terms of the fraction leached, for the most important gamma-emitting nuclides in Zircaloy cladding hulls. The values of initial radioactivity for each hull type were obtained from measurements on composite samples of the hulls. Any individual hull specimen may, then, differ slightly from the value shown. It is evident that the alkaline element cesium dissolves relatively well in both alkaline and acidic solvents, in contrast to the other elements studied.

Table III gives the initial levels of the actinides ^{239,240}Pu and ^{244}Cm and their behavior under successive leaching with HNO_3, NaOH, and $K_2S_2O_7$. The experiments were performed with separate specimens in the order HNO_3-$K_2S_2O_7$ and NaOH-$K_2S_2O_7$, respectively. The HNO_3 treatment effects a considerable decontamination while the alkaline leachant does not seem to exert any measurable influence.

Figure 1 shows the radionuclide distributions within the Zircaloy cladding tubes for the whole series of experiments. The cladding hulls were dissolved in stages by successive potassium pyrosulfate melt treatment. Although the individual measurements displayed some scatter, it was possible to construct enveloping curves. The graphic representation then results in three clearly divided groups:

1. the actinides that are concentrated in a thin surface layer
2. diffusing species, whose highest concentration is clearly to be found in the inner surface layer but which also penetrate into deeper material layers to a considerable extent
3. activation products that are, in part, located on the external Zircaloy surface as corrosion products, but which otherwise display a homogeneous distribution.

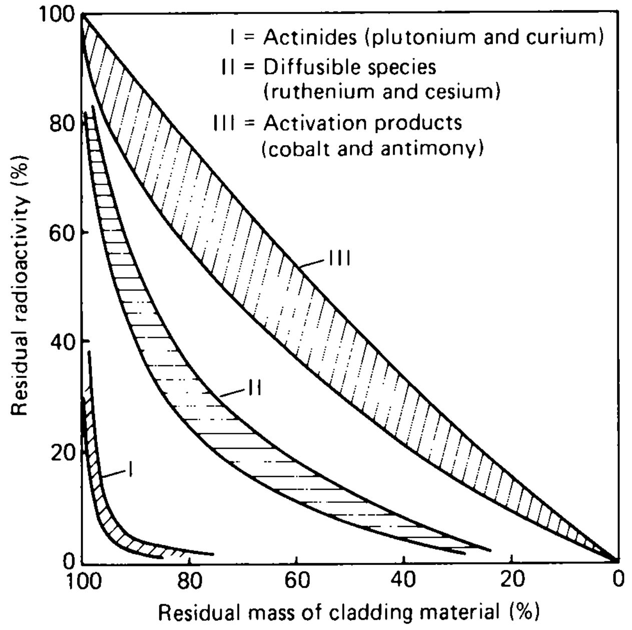

Fig. 1. Radionuclide distributions in Zircaloy cladding hulls.

DISCUSSION OF RESULTS

The experimental results indicate that the measured radioactivities of the Zircaloy cladding tubes come from two different sources:

1. Surface contamination or surface nuclide implantation due to nuclear recoil effects—the observed leaching of various nuclides by different aqueous solvents indicates that the radioactivity must in part be pure surface contamination. However, some fraction is also firmly implanted in the oxide layer. Although the actinides, like the rare earths, display very low diffusion velocities in Zircaloy, the opposite is true of some fission product (FP) elements. The depth distribution measured for ruthenium and cesium leads one to suppose that similar diffusion behavior may also be valid for other chemically related elements. It thus becomes clear that a surface decontamination of the Zircaloy cladding tubes, removing some material, would almost completely eliminate the actinides but not all fission nuclides.

2. Activation products of the cladding tube material, which are distributed fairly evenly through the whole thickness of the material—the radionuclides ^{60}Co and ^{125}Sb are characteristic of this group.

The results of this study indicate that placement of well decontaminated Zircaloy cladding hulls in concrete represents an acceptable solution. The cement product effects an improvement in the radionuclide leaching resistance. Cement products do not, however, provide any gain or loss with respect to long-term protective effects in the case of contact of the final disposal product with aqueous solutions, which is very improbable but cannot be completely excluded. The alkaline environment of the cement products does promote leaching of the relatively short-lived alkaline and, possibly, the alkaline earth elements, but it does suppress considerably the mobility of a whole series of other elements, especially the very long-lived actinides. The basic character of the cement products and their crystal water content promotes corrosive attack on the Zircaloy cladding hulls, which may possibly be intensified by tritium and krypton degassing. Further studies are still required here. The formation of hydrogen radiolysis gas, which can lead to an increase in tritium release, must also be taken into consideration.[8] Cementing can have advantages in suppressing a possible spontaneous ignition of the fine Zircaloy particles adhering to the cladding hulls.

In deciding on appropriate conditioning for final disposal of the Zircaloy cladding hulls, it should be noted that the levels of tritium and ^{85}Kr also play an important role. Depending on burnup and rod power density, typical LWR Zircaloy cladding hulls contain between 700 and 1400 μCi T/g of Zircaloy.[3,8] This tritium is rather firmly bound into the Zircaloy matrix in the form of zirconium tritide and is released only at relatively high temperatures (800 to 1000°C). On the other hand, zirconium tritide exchanges its hydrogen isotopes when in contact with aqueous solutions or hydrated solids, such as cement products. An isotope exchange process of this type can lead to an increased tritium release from the cemented final disposal products of Zircaloy cladding hulls. This is particularly true if the product comes into contact with aqueous solutions.

The behavior of the inert gas ^{85}Kr, which enters the Zircaloy cladding hulls by means of recoil effects, is especially interesting. A mean ^{85}Kr inventory of 62 μCi/g of Zircaloy was measured for PWR cladding hulls with a burnup of 31 000 MWd/ton U. This corresponds to ~0.1% of the total inventory in the fuel rod. Furthermore, it has been shown that the ^{85}Kr activity is almost completely restricted to the inner corrosion layer of the cladding tubes, which is ~10 μm thick. Similar to the case of tritium, ^{85}Kr release only takes place at temperatures above 800°C (Ref. 5). The application of aqueous solutions does not show any leaching effect.

A critical evaluation of leaching behavior under various conditions indicates that a thorough pretreatment with semiconcentrated nitric acid of the cladding hulls leaving the dissolver of a reprocessing facility is an effective measure for minimizing the surface contamination of Zircaloy cladding hulls by FPs and actinides. Decontamination factors of between 2 and 20 can be achieved. These observations are in agreement with the findings of earlier English studies.[9] However, the actinide content remaining in the Zircaloy after this treatment is still higher than the limit of 10 nCi/g recommended by various authorities. Therefore, the cladding hulls must still be classified as alpha-contaminated waste.

A further important result of the present study is the discovery that actinides cannot be put into solution by alkaline solvents and thus cannot be made mobile. Therefore, embedding the Zircaloy cladding hulls in cement products for the purpose of conditioning for final disposal can be regarded as a useful procedure. Cement products do not display any permanent effect in improving the leaching resistance of the alkaline and alkaline earth elements, nor presumably, that of ruthenium. They simply bring about a delay in release.

CONCLUSIONS ON CONDITIONING FOR FINAL DISPOSAL

The first recommendation should be to mechanically separate the Zircaloy-clad fuel rods as cleanly as possible from the remaining metallic structural sections in order to be able to handle each as a separate waste stream. In this way, the fraction containing alpha contamination would be restricted to the Zircaloy cladding hulls. Insofar as possible, alpha contamination of the structural material otherwise free of alpha emitters must be avoided during the dismantling operation. The separation of structural materials free of alpha contamination from a waste stream containing such contamination can be achieved most effectively by using a single-rod shear, although this may present an economic penalty.

This fact is important if very strict demands are made on the final disposal of waste containing alpha contamination. The fraction containing alpha contamination would be placed in deep geologic formations, while the majority of activated structural components with relatively short decay times could be buried close to the surface. Direct incorporation in concrete without compacting in drums would seem to be the most appropriate method for burial of the activated structural components.

Further treatment of the Zircaloy cladding hulls after reprocessing depends on the safety philosophy adopted. If dilution is favored, then the Zircaloy cladding hulls only superficially contaminated with actinides and FPs will not require any further treatment. They can be embedded in a matrix material to provide dilution (e.g., a mixture of cement and sand). In this way, large volumes of waste with low specific radioactivities result, and the radiolysis and heat dissipation problems are greatly reduced. If, however, concentration of the waste and safe containment of the minimized volumes is the preferred strategy, then a further decontamination of the Zircaloy cladding hulls before final disposal may provide a gain in safety. In this type of treatment, a waste product of medium radioactivity is divided into a small volume of highly radioactive material and a larger volume with lower specific radioactivity. This measure can be attractive if it is possible to economically carry out the final disposal of the larger volume.

If postreprocessing treatment of the hulls is desirable, the results of this study indicate that decontamination of the leached cladding hulls with nitric acid would be beneficial, but further decontamination, for example, by dissolution of the oxidized surface layers by treatment with pyrosulfate salt melt, is not recommended. The remaining Zircaloy cladding hulls would likely be practically free of alpha contamination, and final disposal would be easier, but the resulting secondary waste would be similar, from the point of view of volume and quality, to that of the primary waste. Therefore, a net benefit would not be realized.

Other suggestions for conditioning of Zircaloy cladding hulls (e.g., abrasive conditioning) have been proposed. They do not, however, seem to offer any significant gain in safety. In the end, only experiments with genuine waste canisters can provide the information required for a final decision on the best process.

ACKNOWLEDGMENTS

We would like to thank D. Herz, G. Jahn, and S. Wolters for carrying out the experimental work and J. Ganley for his help in preparing the manuscript.

REFERENCES

1. H. D. HAUG, "Zerfallsrechnungen verschiedener mittelaktiver und aktinidenhaltiger Abfälle des LWR-Brennstoffkreislaufes, Teil I," KfK-3221, Kernforschungszentrum Karlsruhe (1981).

2. K. KROTH, D. HERZ, H. LAMMERTZ, and U. WENZEL, "Classification of Cladding Hulls with Regard to Their Conditioning and Disposal," *Proc. Management of Alpha-Contaminated Wastes*, Vienna, January 2-6, 1980, IAEA-SM-246/15, p. 425, International Atomic Energy Agency (1981).

3. B. MÜLLER, F. KREUTZ, and K. KROTH, "Tritiumgewinnung aus Zircaloy-Hüllrohren abgebrannter LWR-Brennelemente," JÜL-1715, Kernforschungsanlage Jülich GmbH (1981).

4. L. N. GROSSMANN and J. O. HEGLAND, "Tritium Distribution in High Power Zircaloy Fuel Elements," GEAP-12205, General Electric Company (1971).

5. K. KROTH, "Kr-85-Inventar in Zircaloy-Hüllrohren abgebrannter LWR-Brennelemente," *Wissenschaftlicher Ergebnisbericht der KFA-Jülich*, p. 221, Kernforschungsanlage Jülich GmbH (1981).

6. J. H. GOODE and V. C. A. VAUGHEN, "ORNL Experiments on the Behavior of Tritium During Head-End Processing of Irradiated Reactor Fuels," ORNL-TM 2793, Oak Ridge National Laboratory (1970).

7. U. WENZEL and D. HERZ, "α-Spectrometry in Nuclear Fuel Analysis," *J. Radioanal. Chem.*, **21**, 473 (1974).

8. H. FROTSCHER, H. GRÄBNER, and H. KAPULLA, "Konditionierung von Hüllen bestrahlter Brennelemente durch Walzen und Einbetten in Beton," EUR-7728-DE, Commission of European Communities (1982).

9. R. L. DILLON, "Decontamination and Melt Densification of Fuel Hull Wastes," *Proc. OECD/NEA Technical Seminar on Treatment, Conditioning and Storage of Solid Alpha-Bearing Waste and Cladding Hulls*, Paris, December 5-7, 1977, p. 299, Organization for Economic Cooperation and Development (1978).

RADIOACTIVE CONTAMINATION OF CARBON STEEL IN A BOILING WATER REACTOR

TAKASHI HONDA and AKIRA MINATO
Hitachi, Ltd., Hitachi Research Laboratory
4026 Kuji-cho, Hitachi-shi, Ibaraki-ken, 319-12 Japan

KATSUMI OHSUMI *Hitachi, Ltd., Nuclear Power Generation Division*
3-1-1 Saiwai-cho, Hitachi-shi, Ibaraki-ken, 317 Japan

HIDEO MATSUBAYASHI *The Chugoku Electric Power Company, Inc.*
Shimane Nuclear Power Station, 654-1 Kataku
Kashima-cho, Yatsuka-gun, Shimane-ken, 690-03 Japan

Received October 17, 1983
Accepted for Publication January 16, 1984

Deposition of ^{60}Co contained in reactor water results in contamination of boiling water reactor out-of-core components. To elucidate the deposition mechanism, the deposition kinetics of radionuclides on carbon steel were evaluated through exposure tests in actual reactor water. On the basis of the data, a radiation buildup model was developed. Cationic ^{60}Co and ^{58}Co were difficult to transmit through the oxide film, which was probably charged positively, and incorporate into the inner oxide layer; consequently these amounts on the steel did not increase even after 1000 h. However, anionic ^{51}Cr was easily captured by the growing oxide film, and the amount showed an increasing trend up to 500 h.

INTRODUCTION

Deposition of several radionuclides, which are contained in reactor water, results in contamination of boiling water reactor (BWR) out-of-core components. Radioisotopic analyses of actual piping have identified ^{60}Co as the primary cause of radiation buildup.[1-3] This cobalt isotope exhibits a relatively long half-life and large gamma activity.

The components are primarily made of stainless steel, except part of the piping in the reactor water cleanup line for which carbon steel is used. Radiation buildup on stainless steel in actual reactor water has been previously described.[4,5] These references revealed that the deposition rate of ^{60}Co was controlled mainly by the growth of an oxide film on the steel. However, as the growth rate and morphology of oxide film formed on carbon steel are assumed to differ from those of stainless steel, elucidation of the deposition mechanism for radionuclides on both steels would be useful. It is the purpose of this paper to present results from carbon steel exposure tests carried out at a commercially operating BWR.

EXPERIMENTAL

This study was conducted in a test facility, which was connected to the reactor water flow. Facility details have been described elsewhere.[5]

The chemical composition of carbon steel used as test material is shown in Table I. The test coupons were solid rods, 370 mm in length and 6.4 mm in diameter. They were machine polished, rinsed with acetone, and kept in a desiccator until exposure.

TABLE I

Chemical Composition of Carbon Steel Used as Test Coupons

Element	wt%
Carbon	0.19
Silicon	0.20
Manganese	0.56
Phosphorus	0.016
Sulfur	0.014
Cobalt	0.0063
Nickel	0.022
Chromium	0.012

Exposure tests were carried out at a neutral pH (6.9 to 7.2) reactor water at 230°C containing 150- to 170-ppb oxygen and flowing at 0.5 m/s for 25 to 4200 h. The conductivity of water was in the range of 0.10 to 0.12 μS/cm. Reactor operations were very stable during experiment runs. Table II shows the concentrations of radionuclides and elemental metals in the reactor water sampled at the facility inlet. A major part of the radionuclides existed as soluble species, which was assumed to be closely related to the low concentration of insoluble iron.[6] The so-called soluble species were those that could pass through a 0.45-μm Millipore filter and be collected on ion exchange membranes. The insoluble species were those collected on the Millipore filter. Soluble ^{51}Cr and elemental chromium were collected on anion exchange membranes, while the other soluble radionuclides and elemental metals were collected on cation exchange membranes.

TABLE II

Average Concentration of Radionuclides and Elemental Metals in Reactor Water

Radionuclide	Soluble Species (μCi·m^{-3})	Insoluble Species (μCi·m^{-3})
^{60}Co	100	5
^{58}Co	200	10
^{51}Cr	10	5
^{54}Mn	20	0.6
^{59}Fe	Not detected	Not detected

Elemental Metal	Soluble Species (ppb)	Insoluble Species (ppb)
Iron	0.034	0.035
Cobalt	0.16	Not detected
Nickel	2.3	Not detected
Chromium	0.075	Not detected

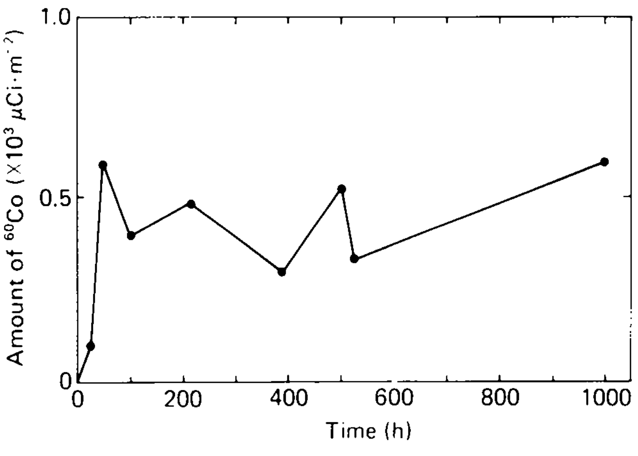

Fig. 1. Deposition of ^{60}Co on carbon steel exposed in reactor water at 230°C.

After exposure, coupons were removed from the facility and gamma scanned immediately. They were divided into small segments, and the oxide films on the segments were then analyzed.[5]

RESULTS

Radiation Buildup with Time

The deposition kinetics of ^{60}Co on carbon steel are shown in Fig. 1. The amount of ^{60}Co always varied, but did not tend to increase even after 1000 h. On the other hand, the oxide film grew on steel, as shown in Fig. 2. Oxide film weights and descaled weight losses fit the following equation:

$$\Delta W = \Delta W_0 + kt \ ,$$

where

ΔW = oxide film weights or descaled weight losses

ΔW_0 = empirical extrapolation to zero time

k = rate constant

t = exposure time.

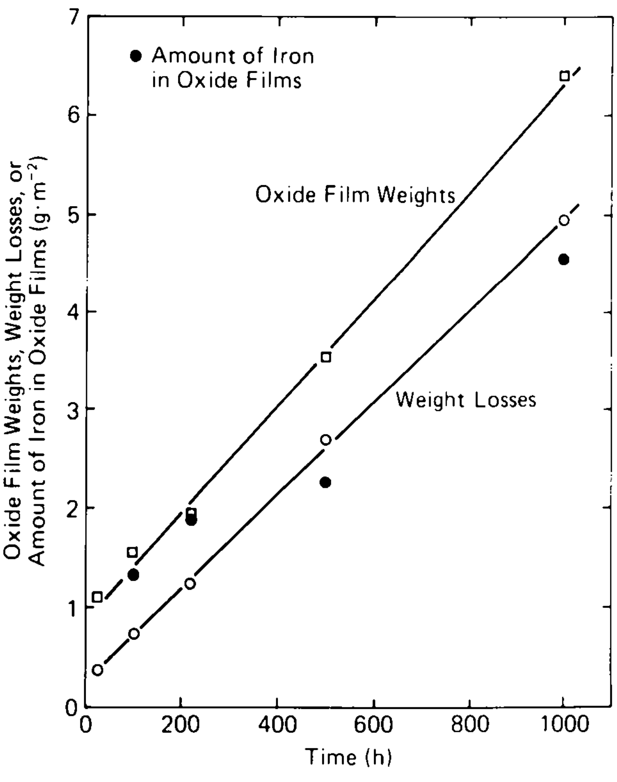

Fig. 2. Corrosion behavior of carbon steel exposed in reactor water at 230°C.

This equation for corrosion implied a linear rate control that became effective after an initial nonlinear period. The corrosion rate was 1.1 $mg \cdot dm^{-2} \cdot day^{-1}$. In general, elemental metals contained in the steel were left on it as an oxide film or released to system flow through corrosion. Figure 2 shows in the oxide film that the amount of iron, a major component of carbon steel, approximately matched the weight loss of the steel. This indicated that the amount released was small; most metal atoms formed an oxide film.

By comparison of the first two figures, the deposition of ^{60}Co was shown to be independent of the oxide film growth. This differed from the deposition kinetics on stainless steel, in which the deposition rate of ^{60}Co was mainly controlled by the film growth.

Characterization of Oxide Films

Figure 3a shows a scanning electron micrograph (SEM) of an oxide film formed after a 1000-h exposure. About 1-μm platelike crystals, which were assumed to be hematite, were uniformly visible. These crystals could be easily removed by ultrasonic cleaning (Fig. 3b). Subsequently, the adhered oxide layer was removed from the metal by electrolytical descaling (Fig. 3c). These two oxide layers, removed by the two-step descalings, were then analyzed chemically.

The chemical compositions of these layers are shown in Table III. Iron occupied over 95% of all metal sites in the films. The amounts of cobalt, nickel, and chromium, which were minor elements in the films, were much higher than those of the base material. Therefore, these three must have come from the reactor water.

The specific activity of ^{60}Co in the outer layer was several times higher than that in the inner layer, as shown in Table IV. This was assumed to be a result of the deposition of crud suspended in reactor water, as the specific activity of crud was several orders of magnitude higher than that of oxide film. However,

TABLE III

Weights of Metals and Chemical Compositions of Oxide Layers Formed on Carbon Steel Exposed for 1000 h at 230°C

($\times 10^4$ $\mu g \cdot m^{-2}$, weight percent in parentheses)

Oxide Film	Iron	Cobalt	Nickel	Chromium
Outer oxide layer	14.3 (97.3)	0.0189 (0.129)	0.0928 (0.631)	0.312 (2.12)
Inner oxide layer	437 (95.6)	0.108 (0.0236)	6.64 (1.45)	13.5 (2.95)

TABLE IV

Comparison of ^{60}Co Specific Activity of the Suspended Crud and Oxide Layers

(Curies per gram of iron)

Suspended Crud	Outer Oxide Layer	Inner Oxide Layer
1.4×10^{-1}	2.3×10^{-4}	8.5×10^{-5}

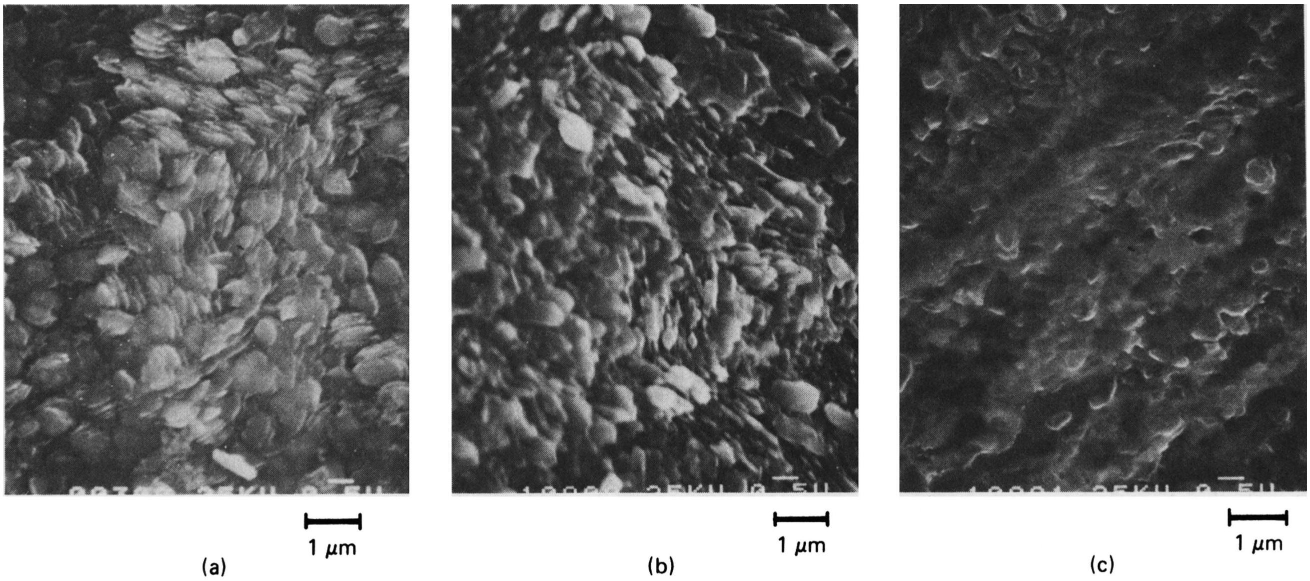

Fig. 3. Scanning electron micrographs of the test pieces: (a) after exposure in reactor water for 1000 h at 230°C, (b) after ultrasonic cleaning, and (c) after electrolytical descaling.

the deposition kinetics of ^{60}Co shown in Fig. 1 indicated that this crud did not stay in one place. In addition, the weight of deposited crud was very small compared with that of oxide film, e.g., it was <0.1% of oxide film formed after 1000-h exposure.

To identify the crystallographic phases in the oxide film, a carbon steel coupon, which was exposed for 4200 h, was observed by x-ray diffraction analysis. The data that were obtained showed magnetite as a major phase and hematite as a minor phase.

Comparison of Deposition Kinetics of Radionuclides

Figure 4 shows the accumulation of ^{58}Co and ^{51}Cr compared with ^{60}Co. The vertical axis shows the value of the deposited amount (μCi·m^{-2}) divided by the concentration in reactor water (μCi·m^{-3}). The accumulation kinetics of ^{58}Co were similar to those of ^{60}Co. However, the value for ^{51}Cr was a few orders of magnitude higher than that for the other two radionuclides. Furthermore, the amount of ^{51}Cr increased with time in spite of its short half-life (667 h). The above-mentioned difference in deposition kinetics was also observed among elemental chromium, cobalt, and nickel, as shown in Fig. 5. Chromium deposited more easily than cobalt and nickel.

DISCUSSION

It is generally accepted that a double magnetite layer forms on carbon steel in oxygen-free water at high temperatures above 250°C (Ref. 7). The layer grows on both sides of the original steel surface simultaneously. On the other hand, it is proposed that such a double layer would be nucleated by low conductivity neutral pH water with dissolved oxygen.[8] The corrosion proceeds via the following sequence:

$$6\mathrm{Fe} + \frac{7}{2}\,\mathrm{O_2} + 6\mathrm{H^+} \rightarrow \mathrm{Fe_3O_4} + 3\mathrm{Fe^{2+}} + 3\mathrm{H_2O}$$

$$2\mathrm{Fe^{2+}} + 2\mathrm{H_2O} + \frac{1}{2}\,\mathrm{O_2} \rightarrow \mathrm{Fe_2O_3} + 4\mathrm{H^+} \ .$$

Magnetite forms as an inner layer and hematite as an outer layer.

Taking these considerations into account, a model for the radiation buildup on carbon steel in reactor

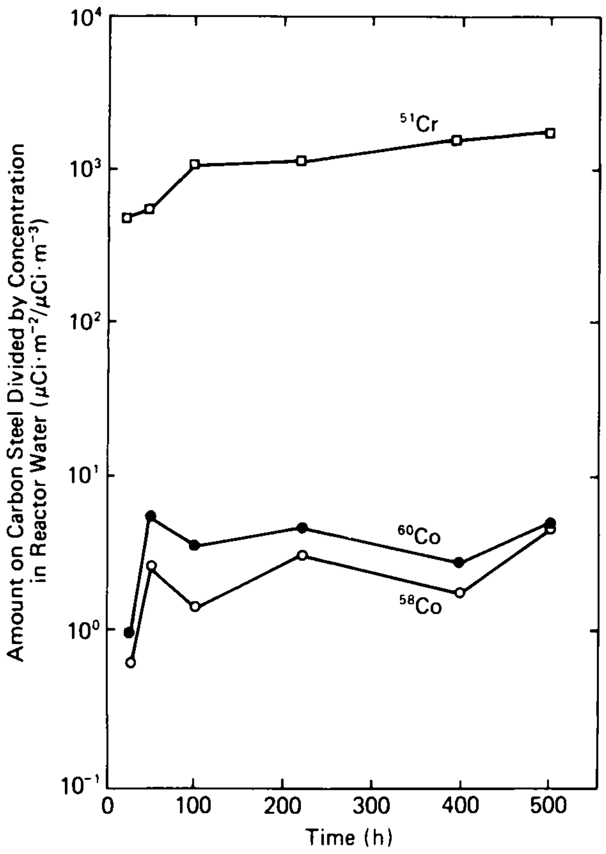

Fig. 4. Comparison of the accumulation kinetics of ^{60}Co, ^{58}Co, and ^{51}Cr on carbon steel exposed in reactor water at 230°C.

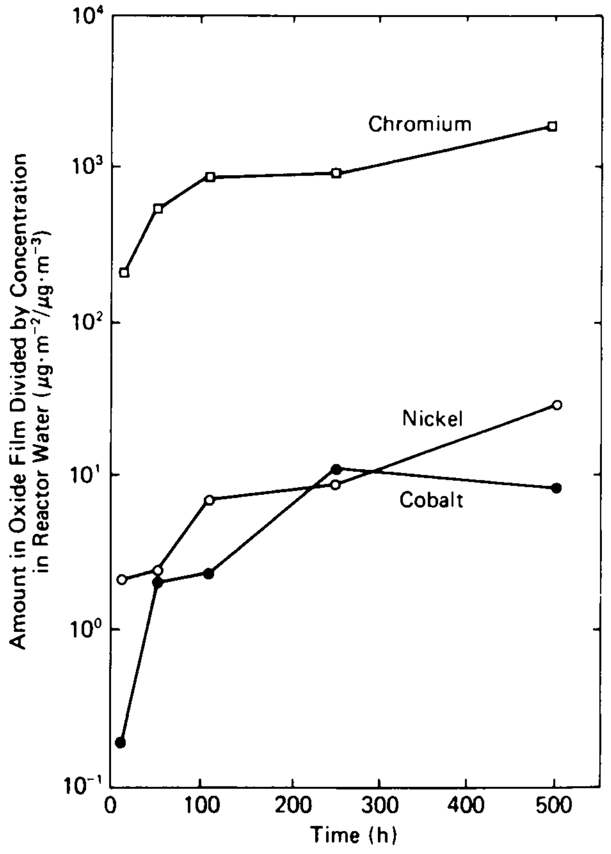

Fig. 5. Comparison of the accumulation kinetics of elemental metals (cobalt, nickel, and chromium) on carbon steel exposed in reactor water at 230°C.

water is depicted in Fig. 6. At the outer oxide and water interface (position A), hematite, which is estimated by observation with an SEM, grows outward. However, the growth of this layer is assumed to be depressed. If it grew extensively, the amount of ^{60}Co would have increased as a result of incorporation of suspended crud from the water. On the other hand, an inner layer, whose major phase is estimated as magnetite by x-ray diffraction analysis, grows inward following a linear law at the metal and inner oxide interface (position B). While a linear law best fits the film growth in this test, after long periods of oxidation, a parabolic or logarithmic law would seem to be more probable.

The experimental data show that ^{51}Cr is extensively incorporated into this inner layer, in comparison with ^{60}Co and ^{58}Co. This difference in kinetics is assumed to be due to the selectivity of oxide film for ion transmission. It is known that the oxide surfaces are charged in solution.[9] Therefore, the deposition rates of ions should be significantly affected by the surface charge of oxide film. If the oxide film assumes a positive fixed charge, the mobility of cationic species is depressed and that of anionic species is promoted. The reverse phenomenon occurs in the oxide film, which assumes a negative fixed charge. The deposition data show that oxide films formed on carbon steel tend to assume a highly positive fixed charge and be anion selective under the reactor water conditions.

By comparison, the radiation buildup on carbon steel differs significantly from that on stainless steel. This is assumed to be primarily due to the difference in the surface charges of oxides formed on these steels. The characteristics of oxide films are not the same in many respects for carbon and stainless steels. This is assumed to cause the difference in the surface charges. Under high-purity-water conditions like those of a BWR, the effect of migration, which is based on the surface charge of the oxide film, on the deposition kinetics of radionuclides must be considered in addition to diffusion. In addition, as the charge is dependent on solution pH, the deposition kinetics of radionuclides should be much affected by this parameter.

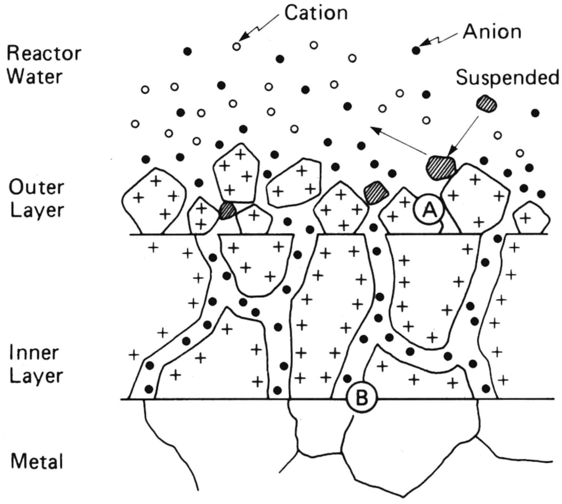

Fig. 6. Schematic illustration of radiation buildup on carbon steel.

SUMMARY

The deposition of ^{60}Co and other radionuclides on machine-polished carbon steel was evaluated in water of a commercially operating BWR. A major part of the radionuclides existed as soluble species.

The oxide film growth followed a linear law, but the amount of ^{60}Co always varied and did not increase even after 1000 h. The deposition kinetics of ^{58}Co were similar to those of ^{60}Co. However, the deposition coefficient of ^{51}Cr, which existed as an anionic species in the reactor water, was over two orders of magnitude larger than that of the other two cations, and the amount of ^{51}Cr showed an increasing trend up to 500 h.

Taking these results into account, the following model was established for the radiation buildup on flat surface carbon steel in high-purity reactor water. The growth rate of the outer layer was depressed, and the deposition and release of suspended crud took place continuously on this layer. The inner layer grew with time; however, cationic ^{60}Co and ^{58}Co were difficult to transmit through the positively charged oxide film and to incorporate into this layer, as compared with anionic ^{51}Cr.

ACKNOWLEDGMENTS

The authors want to thank the many people at The Chugoku Electric Power Company, Inc., Shimane Nuclear Power Plant, and Hitachi, Ltd., who assisted in this project. In particular, the following deserve individual recognition: K. Yonezawa and R. Goda for their work at the plant, M. Morishima and T. Kawakami for the facility operation and analysis of coupons, and A. Shiina for the design of the loop.

This work was sponsored by the Japanese BWR Owners' Group.

REFERENCES

1. G. ROMEO, "Characterization of Corrosion Products on Recirculation and Bypass Lines of a Boiling Water Reactor," *Proc. 7th Int. Congr. Metallic Corrosion*, **3**, 1456 (1978).

2. S. UCHIDA, M. KITAMURA, Y. MATSUSHIMA, K. YONEZAWA, K. OHSUMI, and M. MIKI, "Deposition of

Cobalt-60 on the Stainless-Steel Surface Used for the Primary Cooling System of a Boiling Water Reactor," *Nucl. Sci. Eng.*, **77**, 496 (1981).

3. W. E. BERRY and R. B. DIEGLE, "Survey on Corrosion Product Generation, Transport, and Deposition in Light Water Nuclear Reactors," EPRI NP-522, Electric Power Research Institute (1979).

4. T. HONDA, K. OHSUMI, and H. MATSUBAYASHI, "Radiation Buildup on Stainless Steel in a BWR Environment," *Trans. Am. Nucl. Soc.*, **43**, 342 (1982).

5. T. HONDA, M. IZUMIYA, A. MINATO, K. OHSUMI, and H. MATSUBAYASHI, "Radiation Buildup on Stainless Steel in a Boiling Water Reactor Environment," *Nucl. Technol.*, **64**, 35 (1984).

6. C. C. LIN, C. R. PAO, J. S. WILEY, and W. R. DEHOLLANDER, "Corrosion Product Transport and Radiation Field Buildup Modelling in the BWR Primary System," *Water Chemistry II*, British Nuclear Energy Society, Paper 46 (1980).

7. P. H. EFFERTZ, "Morphology and Composition of Magnetite Layers in Boiler Tubes Following Long Exposure," *Proc. 5th Int. Congr. Metallic Corrosion*, p. 920 (1972).

8. V. B. BORRIS, "Der Einfluß des Sauerstoffs fie des Neutralen Fahrweise," *VGB Kraftwerkstechnik*, **54**, *5*, 324 (1974).

9. G. A. PARKS and P. L. de BRUYN, "The Zero Point of Charge of Oxides," *J. Phys. Chem.*, **66**, 967 (1962).

HYDRAULICS OF BLOCKED ROD BUNDLES

HEAT TRANSFER AND FLUID FLOW

SHI-CHUNE YAO *Carnegie-Mellon University*
Department of Mechanical Engineering
Pittsburgh, Pennsylvania 15213

M. J. LOFTUS and L. E. HOCHREITER
Westinghouse Electric Corporation, P.O. Box 355
Pittsburgh, Pennsylvania 15230

Received February 23, 1983
Accepted for Publication November 28, 1983

The hydraulic results of a series of 21-rod bundle water experiments have been analyzed systematically. Models are established for the prediction of the pressure drop over unblocked bundles, grid spacers, coplanar concentric blockage, coplanar concentric blockage with bypass, noncoplanar concentric blockage, and noncoplanar nonconcentric blockage. The models can be extended to other bundles with similar characteristics. The comparisons of these models with the experimental results agree reasonably well.

INTRODUCTION

Under hypothetical nuclear accident conditions, the fuel cladding may become distorted or swell from the original shape in the high-temperature environment. In these circumstances, the hydraulic condition at this region is disturbed and the heat transfer behavior is also affected. Since the cooling of the fuel rods in this high-temperature region is important to the evaluation of reactor safety, the understanding of the hydraulic behavior of distorted bundles is of interest.

Although the fluid is usually a two-phase mixture during the calculated accident under this condition, the first step toward the fundamental understanding of the distorted bundle hydraulics is to investigate the single-phase flow in blocked bundles. The major concerns are the friction factor of the bundle without grid spacers, the loss coefficient of the grid spacers, and the loss coefficients of the swollen blockage of different shapes and different distributions. With this information, the local flow distribution near the blockages and the global flow distribution among subassemblies can be estimated, and then the heat transfer can be evaluated. For example, at extreme conditions the flow may either pass through the blockage zone or bypass the blockage such that the local heat transfer from unblocked bundles will be increased or decreased, respectively.

Although extensive studies have been conducted for the hydraulics in the normal bundles, the corresponding knowledge of blocked-bundle hydraulics is limited. There is also a great deal of interest in the loss coefficients of grid spacers. Due to the complexity of the spacer geometry, various models have been proposed for different types of grids.[1,2] However, a simple but general approach has been proposed by Rehme[2] (see Nomenclature on p. 453):

$$K_{gR} = C_v \epsilon^2 \tag{1}$$

for a Reynolds number above 10^5 and ϵ in the range of 0 to 1.

An experimental investigation has been performed with the support of the U.S. Nuclear Regulatory Commission, Electric Power Research Institute, and Westinghouse Electric Corporation through the FLECHT-SEASET (Ref. 3) program to provide a data base on flow blockage effects in rod bundles. Several 21-rod bundle configurations were studied to examine their hydraulic behavior under various conditions (see Table I).

The objective of the study in this paper is to establish simple formulas or models that can be used to predict the pressure drop and flow distribution at various conditions of blocked bundles and to provide an understanding of them.

EXPERIMENTAL SETUP AND PROCEDURE

A bundle containing 21 rods is tested for its hydraulic behavior using subcooled water. The cross-sectional view of this 21-rod bundle is shown in Fig. 1 with the triangular fillers inserted to achieve the proper

TABLE I

Conditions of the 21-Rod Bundle Experiments

Configuration	Blockage Description	Maximum Sleeve Strain Percentage[a]
A	Unblocked bundle[b]	---
B	Coplanar, over nine central rods	32.6
C	Coplanar, over whole bundle	32.6
D	Noncoplanar, concentric blockage	32.6
E	Noncoplanar, nonconcentric blockage	36
F	Noncoplanar, nonconcentric blockage	44

[a] Maximum strain is for the increase of perimeter at the location of maximum deformation.

[b] Rod diameter, 9.5 mm; casing i.d., 67.8 mm; hydraulic diameter of the bundle, 9.08 mm.

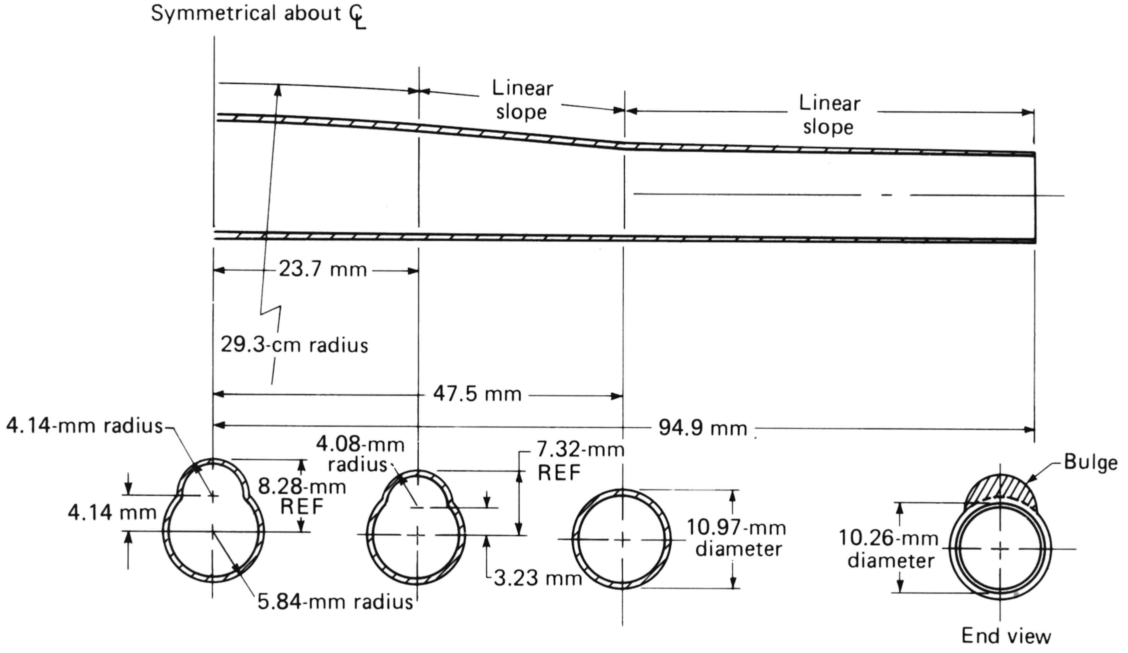

Fig. 1. Nonconcentric blockage sleeve.

flow area for the rod bundle. The bundle is 3.66 m long with grid spacers installed every 0.523 m. The grid spacers are in the form of ∼4.45-cm-long straight strips along the direction of the flow. The blockage ratio, when viewed from the flow direction, is ∼0.25, including the blocked area of the steam probes and the thermocouples attached to the grids. Individual values for the total grid blockage were used in Eq. (1).

Two types of sleeve blockages were studied. The concentric blockage (57 mm long) has the peripheral strain axially distributed in a cosine shape; therefore, the variation of the subchannel flow cross section is very gradual. The other type of blockage shape is nonconcentric (190.5 mm long), with a bulge occurring at one side of the concentric swelling. The detailed dimension of a typical nonconcentric blockage of this kind is shown in Fig. 1. Since the variation of the strain is significant near the bulge, the flow may separate downstream of the bulge. The detailed description of the blockages is also reported in Ref. 3. The blockages are centered at 1.85 m between the grids, which are at 1.569 and 2.092 m from the inlet. When the blockages are noncoplanar, the locations of the blockage midpoints and the subchannels in which the bulges are oriented are denoted in Fig. 2. A three-dimensional view for the physical arrangement of the noncoplanar, concentric blockages is shown in Fig. 3. The details of the 21-rod bundles are described in Ref. 3.

In the experiments, pressure drops are measured at 0.3-m increments along the bundle as shown in Fig. 4.

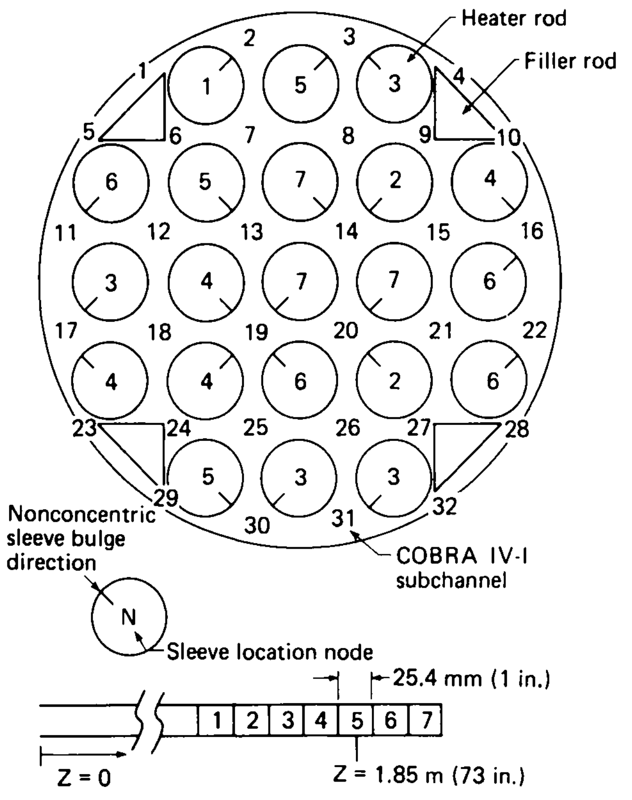

Fig. 2. Noncoplanar sleeve distribution and bulge direction for nonconcentric sleeves.

The rod and housing frictional loss as well as the loss coefficients for the grids and blockages are calculated from the measured pressure drop data:

$$K\frac{1}{2}\rho V_o^2 = (P_1 - P_2) + \frac{1}{2}\rho(V_1^2 - V_2^2) + \rho g(X_1 - X_2) \ , \qquad (2)$$

where

$$\begin{aligned} K &= fL/D && \text{for frictional losses} \\ &= Kg + \frac{fL}{D} && \text{for grid losses} \\ &= K_B + \frac{fL}{D} + Kg && \text{for blockage losses .} \qquad (3) \end{aligned}$$

The subscripts 1 and 2 are two typical locations of pressure measurement.

The different bundle configurations for each series of hydraulic tests are listed in Table I.

RESULTS AND DISCUSSION

Individual aspects of the hydraulic behavior of the blocked bundle are reviewed in this section of the paper. Models or correlations for the rod bundle, grid, and blockage pressure drops are established. Calculations using the models are performed for steam and water and are compared with the experimental data. All the information related to the entire bundle is based on the hydraulic diameter of the bundle.

Friction Factor

The friction factor data for the unblocked sections of the 21-rod bundles between grids and away from blockage are plotted in Fig. 5. Scattering of the data is observed over the entire Reynolds number range. The Moody friction factor for smooth pipes[4] is also shown in the figure, but its value is always lower than the data of the bundle friction factor. The 21-rod bundle configuration was modeled with the COBRA-IV-I code to assess the calculated pressure drop. Steam flow was used in the calculation; however, the Reynolds number range was the same as the water hydraulics tests. The Moody friction factor is used for the flow subchannels to predict the friction factor of the whole bundle. As shown in Fig. 5, the predicted bundle friction factor is close to the data of water but generally higher than the Moody friction factor of smooth tubes. The present bundle has a pitch-to-diameter ratio of 1.32. If the bundle is an infinite array, the friction factor of the bundle should be close to that of the Moody friction factor.[5] In the 21-rod bundle, one-third of the overall wetted perimeter is due to the fillers and housing. The increase of the friction factor in the present bundle is possibly due to the presence of irregular subchannels in the corners of the bundle, which causes nonuniform velocities in different subchannels. The flow at central subchannels will be greater than the bundle-averaged velocity. The frictional dissipation and the pressure drop is therefore higher. Another possible reason for the higher friction factor is the existence of turbulent wakes downstream of the grid spacers, which increase the wall frictional loss as compared with the flow in smooth tubes. Also the grid can induce an entrance region effect on the rods.

Grid Pressure Loss

The grid spacers in rod bundles can be of various complex geometries. For a first-order estimation of the grid loss coefficient, simple formulations based on abrupt contractions and expansions can be adopted. The loss coefficient of grid spacers without mixing vane in tube bundles has been correlated by Rehme[2] using Eq. (1) for Reynolds numbers beyond 10^5, where ϵ is the blockage ratio of the grid projection to the flow cross-sectional area. A detailed review of Rehme's data at low Reynolds number indicates that a more complete correlation for a wide Reynolds number range can be fitted by:

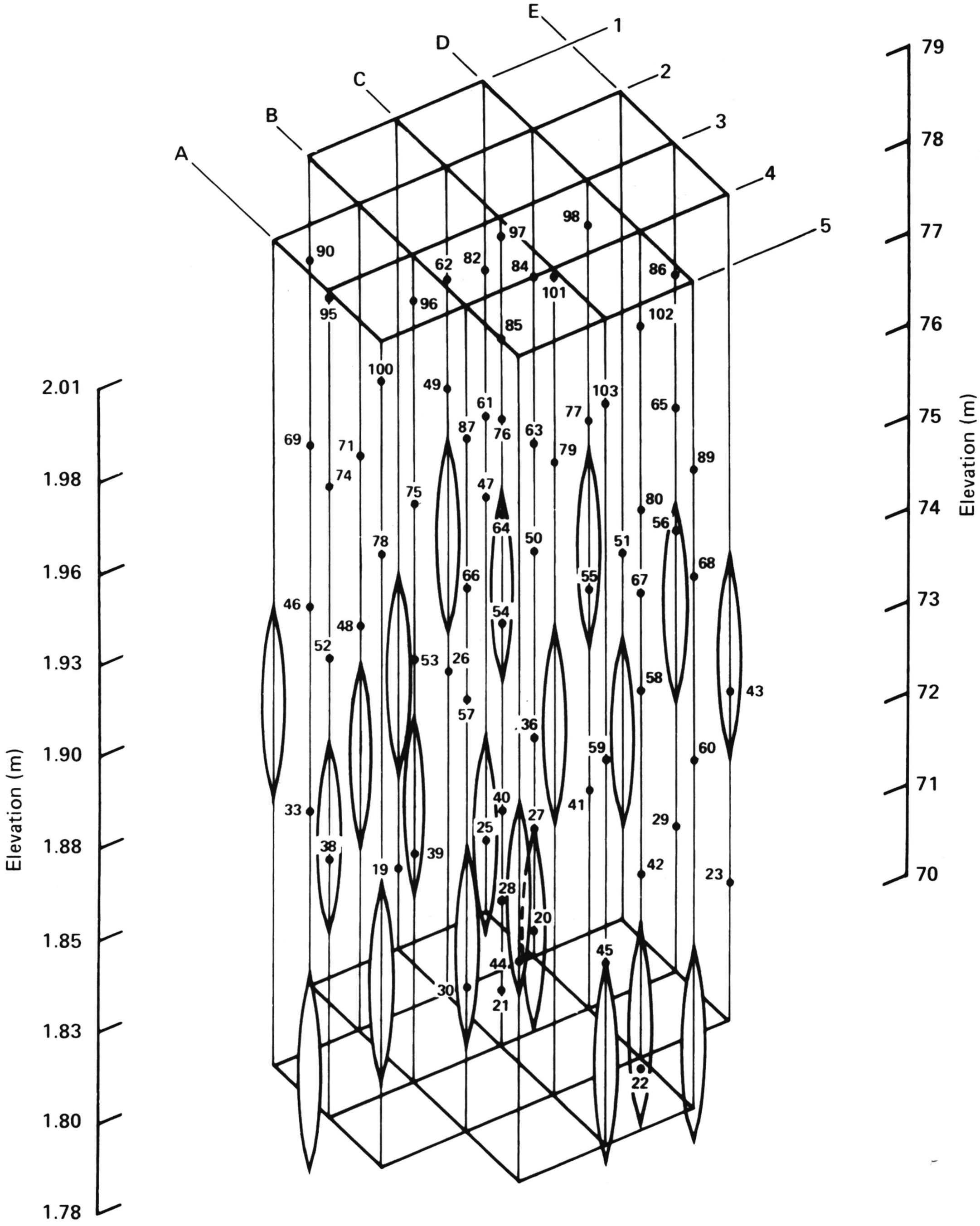

Fig. 3. Noncoplanar, concentric sleeve (configuration D) blockage distribution and rod instrumentation.

$$
\begin{aligned}
K_{gR} &= 196\,\mathrm{Re}^{-0.33}\epsilon^2 && \text{for } 10^3 < \mathrm{Re} < 10^4 \\
&= 41\,\mathrm{Re}^{-0.16}\epsilon^2 && \text{for } 10^4 < \mathrm{Re} < 10^5 \\
&= 6.5\epsilon^2 && \text{for } 10^5 < \mathrm{Re}\ , \qquad (4)
\end{aligned}
$$

where ϵ is in the range of 0 to 0.5. From the general comparison of this correlation with the data sets,[6] it is observed that a multiplier of 1.4 should be applied to Eq. (4). As pointed out by Rehme,[7] Eq. (4) is valid for grid spacers with a rounded leading edge, while a 40% factor must be applied to grid spacers with a sharp leading edge. Therefore, the appropriate form for grid loss in the present study of sharp-edged spacers becomes

$$K_g = 1.4 K_{gR}\ . \qquad (5)$$

Figure 6 shows the 21-rod bundle data for grid loss coefficients at four different elevations for different bundles compared to Eq. (5). The modified grid in

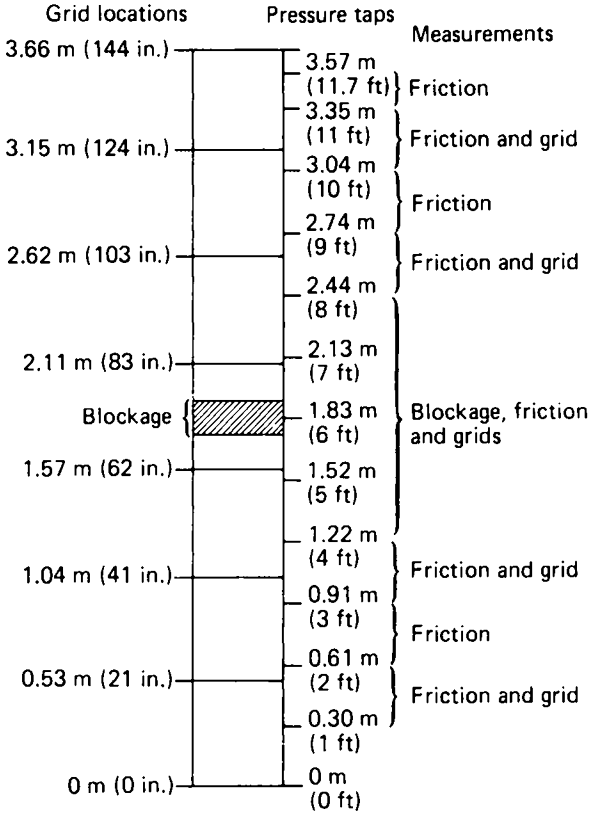

Fig. 4. Grid locations and pressure measurements.

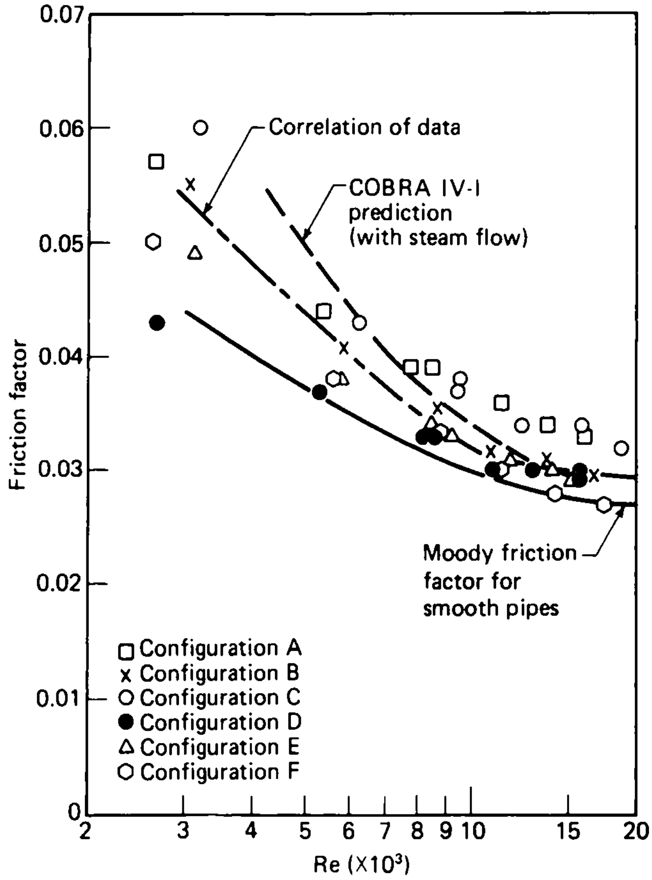

Fig. 5. Average bundle friction factor versus Reynolds number.

Fig. 6b refers to the removal of the dimples on the center nine rods. In general, Eq. (5) fits the data reasonably well within 20% for all the bundles at all the elevations except that of the grids at 2.615 m. At this particular location, the loss coefficient can be correlated by

$$K_g = 1.6K_{gR} \ . \tag{6}$$

The increase of the loss coefficient at this elevation in the experiment with configuration B-F is possibly because this grid is located downstream of the blockage zone. The high loss coefficient of configuration A, which has no blockage, is not clearly understood. The wakes generated by the blockages in the bundle have not decayed completely, so that a nonuniform velocity profile impacts the grid. Therefore, more pressure loss occurs at this grid elevation.

For general applications, Eq. (5) can be used for a first-order estimation for fully developed flow approaching a simple grid. Although this formulation is derived from the bundle-averaged condition, Eq. (5) can also be used in the subchannel analysis of the COBRA-IV-I program for bundles with blockages. The 21-rod bundle with grids was modeled with COBRA IV-I using the grid loss coefficient as given by Eq. (5) on a subchannel basis. That means the local subchannel value ϵ was used in the COBRA IV-I model. The predicted and measured grid loss coefficients at a 2.615-m elevation (downstream of the blockage zone) are compared in Table II for configurations D, E, and F. The COBRA-calculated pressure loss is slightly below the measurement but is reasonably close.

Coplanar Blockage over the Whole Bundle

The simplest case of a blocked bundle is that where all the blockages are at the same elevation of the bundle. If the blockage occurs at all the subchannels with the same amount of swelling on all the tubes, the flow passes straight through the blockage zone, and the situation is very similar to that of a grid spacer. For the case of smooth concentric blockage on the rods, the blockage so resembles a venturi rather than an orifice that the abrupt contraction/expansion grid model would predict the pressure loss. Since the concentric blockage studied here has a maximum angle of 3 deg with respect to the bundle axis, the possibility of flow separation is very small.[3] Therefore the equivalent loss coefficient for the smooth coplanar blockage can be correlated following the previous grid loss coefficient formulation. Only the first term on the right side of Eq. (2) is retained. The data for bundle C are shown in Fig. 7 and can be correlated by

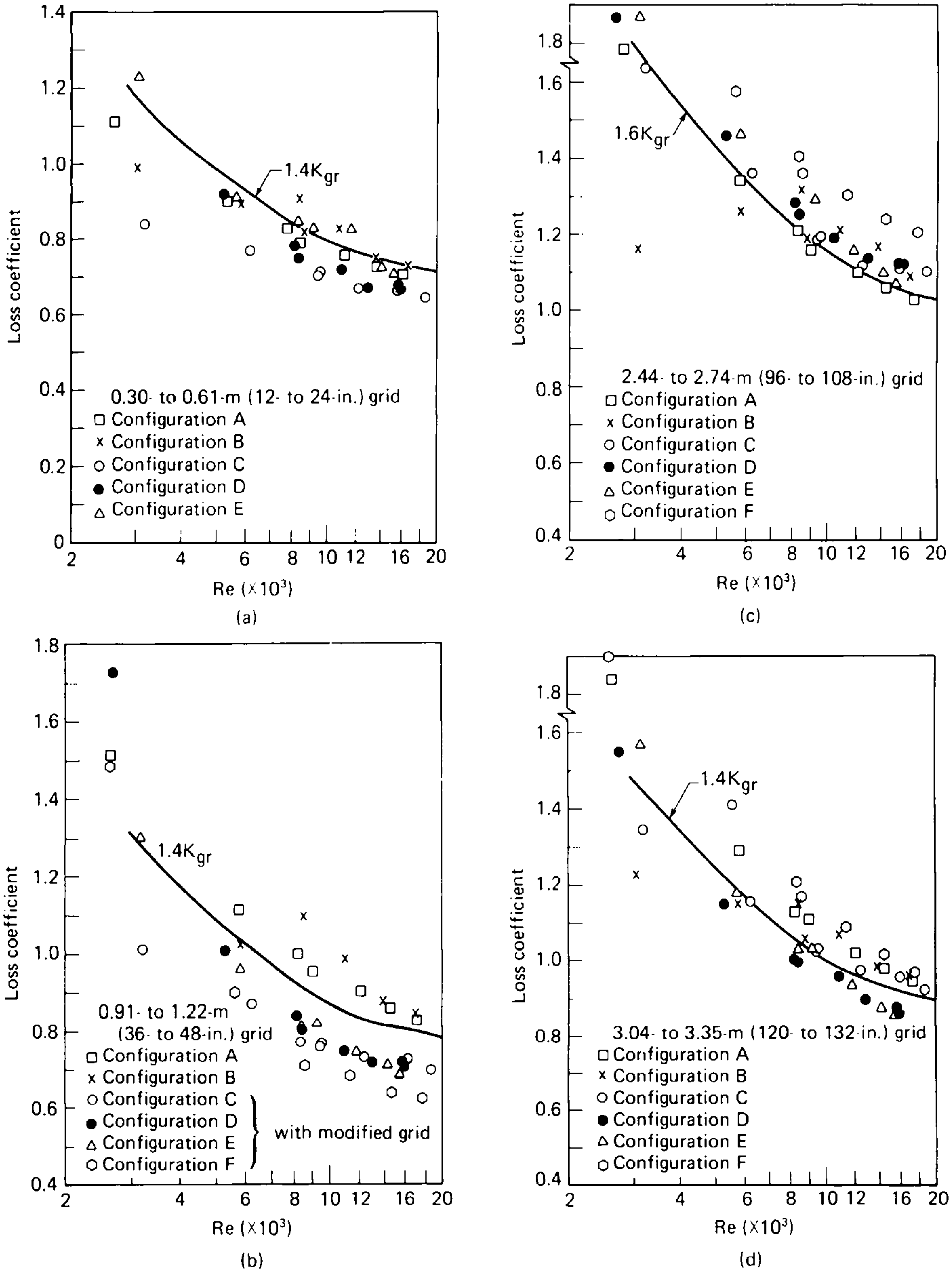

Fig. 6. Grid loss coefficient versus Reynolds number.

$$K_B = 0.7 K_{gR} \ . \tag{7}$$

It is expected that if the geometry of the coplanar blockage is different from the concentric blockages used in this experiment, the coefficient in Eq. (7) will be different from 0.7. However, due to the smooth venturi characteristic of the blockage, the coefficient is most likely to be <1.4 of the grid spacers.

TABLE II

Calculated and Measured* Hydraulic Information

	Reynolds Number	f		Kg (2.615 m)		K Blockage	
		Predicted[a]	Measured	Predicted	Measured	Predicted	Measured
Bundle D	4.8×10^3	0.0512	0.0385			0.408	0.38
Steam	8×10^3	0.0375	0.033			0.367	0.36
1.2×10^4		0.0315	0.030	1.00	1.1	0.327	0.34
Bundle D	5.3×10^3	0.0336	0.037	1.157	1.46	0.387	0.373
Water	1.5×10^4	0.0248	0.0293	0.820	1.121	0.285	0.325
Bundle E[b]	1.4×10^4	0.026	0.028	1.04	1.1	2.16	2.47
Bundle F[b]	1.4×10^4	0.026	0.028	1.03	1.1	3.07	2.9

*All the measured data are for water.

[a] The COBRA IV-I code using the MOODY friction factor in subchannels.

[b] The calculations here used the distributed K for blockage but, with the total of distributed K_B, equals $1.6K_{gR}$ instead of $1.4K_{gR}$, which is indicated in Eq. (12).

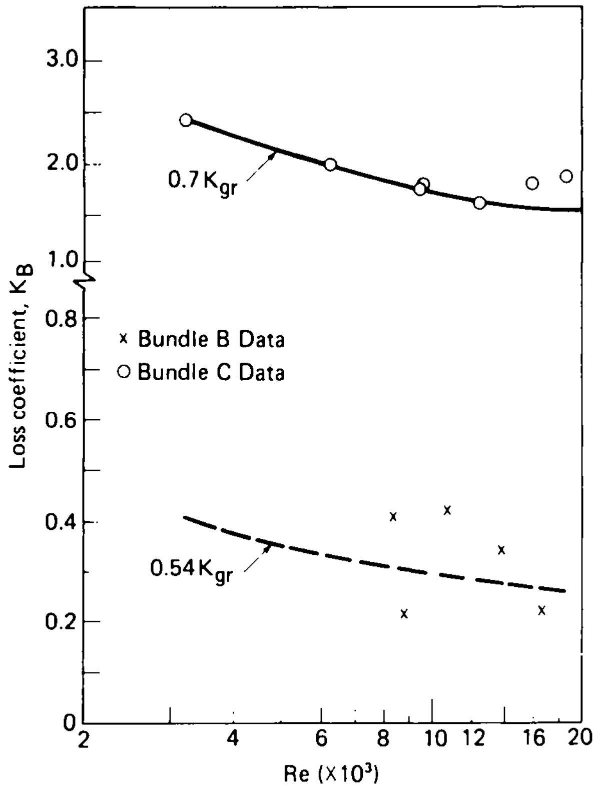

Fig. 7. Coplanar blockage loss coefficient versus Reynolds number.

Coplanar Blockage over Part of the Bundle

A more complicated condition is coplanar blockage with flow bypass, where the blockage covers part of the cross section of the bundle. The flow will bypass the blocked area and then merge again behind the blockage. Generally, the flow in the bypass area acts like that in an unblocked bundle; the flow passing through the blockage acts like that in a coplanar blockage over the whole bundle. In the analysis model, the cross-flow resistance is assumed to be negligible. The flow bypass near the blockage area is similar to the flow redistribution between two interconnected parallel tubes of different flow resistances. Therefore, the same axial pressure drop can be assumed for the blocked area and the bypass area.

Following this assumption, the flow redistribution can be calculated by using the unblocked bundle friction factor for the bypass area and by using the loss coefficient similar to Eq. (7) plus the unblocked bundle friction factor for the blocked area. The flow continuity can be written as

$$A_o V_o = A_B V_B + A_b V_b \ , \tag{8}$$

where

o = unblocked bundle

B = blocked portion of the bundle

b = bypass portion of the bundle that does not contain the blockage.

The extra pressure drops across this region in the bypass zone, and the bypass and blockage zones are assumed to be equal. The overall loss coefficient K_{Bp} will also be related to this pressure drop. Thus

$$\left(f\frac{L}{D} + K_{Bp}\right)\frac{1}{2}\rho V_o^2 = \left(f\frac{L}{D} + K_B\right)\frac{1}{2}\rho V_B^2$$

$$= f\frac{L}{D}\frac{1}{2}\rho V_b^2 \ . \tag{9}$$

Since the required formulas of friction factor f and loss coefficient K_B are readily available, the flow redistributions V_B and V_b and the overall loss coefficient K_{BP} of the whole bundle can be calculated.

A typical example of this problem is studied experimentally with bundle B, where the nine central rods of the 21 rods contain smooth concentric blockage at the same elevation. The calculated overall blockage loss coefficient of this bundle with the bypass is correlated from the data in Fig. 7 as

$$K_{Bp} = 0.54 K_{gR} \ . \qquad (10)$$

As expected, the blockage over part of the bundle has a loss coefficient less than that of the blockage over the whole bundle. For the pressure loss of concentric coplanar blockages with bypass, the parallel path model of Eq. (9) can be used as a first approximation.

Noncoplanar Concentric Blockage

A complex condition of a blocked bundle occurs when the swellings on the rods are situated at different elevations. A typical view of this noncoplanar situation is illustrated in Fig. 3. The local swelling of the tube changes the flow cross section of the adjacent subchannels into the form of converging and diverging passages. As stated before, for the concentric blockages, the angle of the swollen tube surface is always within 3 deg of the bundle axis. The possibility of flow separation, therefore, becomes very small,^{3} especially when the swelling on the adjacent rod is not at exactly the same elevation in the bundle.

For bundles D, E, and F, the blockages are distributed over an axial distance between grid spacers. In the blockage region, the flow cross section of the whole bundle is reduced, and the bundle-averaged velocity would be higher. Since the total surface area on the rods is increased, the averaged velocity will increase the frictional drag on the fluid and cause more pressure drop in the flow. In addition, if the flow channels are severely restricted, flow separation can occur and result in additional form drag.

Calculations of the COBRA-IV-I code have been performed for configuration D considering the locally increased surface area and reduced flow cross section of the subchannels in the blocked zone of the bundle. No form loss was calculated for the blockage. The Moody friction factor is used for the subchannels. Since the blockage is noncoplanar, the flow cross sections of the subchannels adjacent to a swollen blockage are not drastically reduced. For the maximum strain of 32% on a rod, the equivalent pitch-to-diameter ratio of the adjacent subchannel that has the other three nonswollen rods is 1.22. Therefore, it is possible that the Moody friction factor can be used for the slightly reduced subchannel with reasonable accuracy. The calculated loss coefficient of this kind of blockage in steam and water is compared with the experimental data of water in Fig. 8 as the lower curve. Good agreement has been obtained for the flow at various Reynolds numbers.

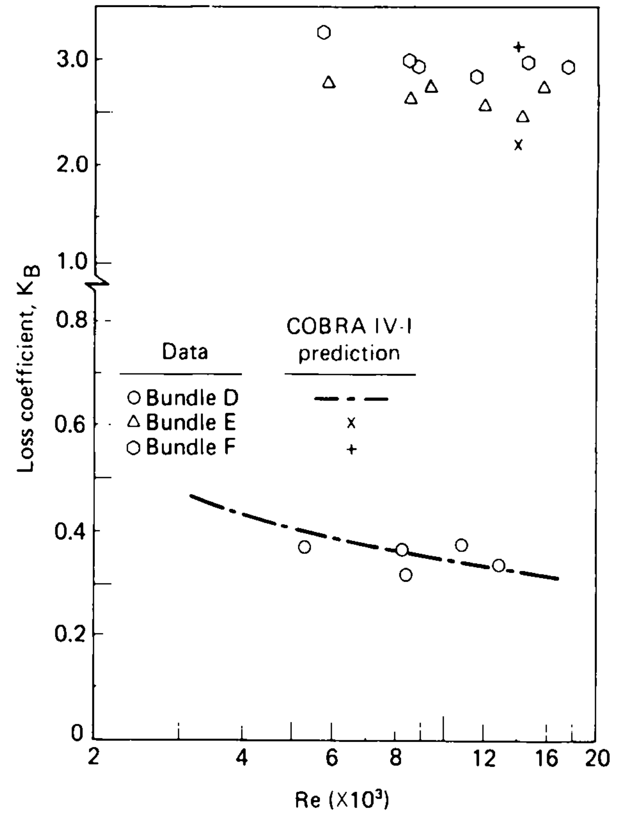

Fig. 8. Noncoplanar blockage loss coefficient versus Reynolds number.

Therefore, it can be concluded that the loss coefficient of noncoplanar concentric blockage is mainly caused by increasing the skin friction at the blockage zone of the bundle, and no additional form loss occurs.

Noncoplanar Nonconcentric Blockage

The geometry of the nonconcentric blockage referred to in this study is shown in Fig. 1. A small bump is formed on the top of a concentric swelling. The orientation of the bump is indicated in Fig. 2. The same type of subchannel analysis for the noncoplanar concentric blockages considering only the skin friction effect has been performed for the bundles of nonconcentric blockages. However, the calculated loss coefficients due to the increased skin friction were only ~25% of the experimental results. The difference between the calculated and measured loss coefficients of the nonconcentric blockage was attributed to the flow separation downstream of the bulge, especially when there was cross flow over the bulge.

The wakes generated at the bulge gradually decay along the stream. The distribution of the loss affects cross flow downstream of the bulge. No information is currently available for this loss distribution in bundles. However, the analogy of momentum and energy transport suggests that the existing information of heat transfer downstream of an obstruction in bundles can be used to estimate the form of loss distribution. It is the gradually decaying turbulence that causes the heat transfer augmentation at the wall and the pressure loss in the channel. The variation of the heat transfer augmentation downstream of grid spacers has been found to be in the form of exponential decay.[8] It was postulated that the pressure loss due to the bulge is also distributed in a similar functional form. An advantage of using a distributed pressure loss is that the subchannel computation program (e.g., COBRA-IV) will experience smooth variations of cross flows among the subchannels, which stabilize the computation and enhance the convergence of the solution.

The local loss coefficient of a nonconcentric blockage in a subchannel can be calculated like a grid spacer following Eq. (5). In the evaluation of flow blockage ratio ϵ for a subchannel, the total flow cross section is calculated at the location of the maximum bulge. The flow blockage area is calculated from the projection of the bulge beyond the concentric portion of the blockage. The total loss coefficient is then distributed downstream of the bulge. Following the heat transfer augmentation results[8] the general form was assumed to be

$$K_B = k\left(\frac{z}{D}\right) = \begin{cases} \frac{1}{2} & \text{for } 0 \le \frac{z}{D} \le \frac{z_1}{D} \\ \exp[-0.13(z - z_1)/D] \quad , & \\ & \text{for } \frac{z_1}{D} < \frac{z}{D} \le 20 \end{cases} \qquad (11)$$

where D is the hydraulic diameter of the bundle. The effective range of Z/D is between the maximum of the bulge, where z/D is 0, and the downstream location, where Z/D equals 20. The Z_1 is the axial increment of the subchannel computation. The assignment of $\frac{1}{2}$ for the first axial step behind the bulge is to give a smooth variation of the loss coefficient axially and can be considered as an empirical choice in the present study. After normalization, the local loss coefficient becomes

$$K_B\left(\frac{z_i}{D}\right) = 1.4K_{gR}\frac{\int_{z_i/D}^{z_{i+1}/D} k\left(\frac{z}{D}\right) d\left(\frac{z}{D}\right)}{\int_0^{20} k\left(\frac{z}{D}\right) d\left(\frac{z}{D}\right)} \quad , \qquad (12)$$

where K_{gR} is given in Eq. (4) with the blockage ratio ϵ referring to the projected cross-section area of the bulge, which induces the flow separation.

The distribution of the loss coefficient is shown schematically in Fig. 9. This distributed loss coefficient has been included in the calculation of COBRA-IV-I for configurations E and F in steam. Reasonable comparison of the calculated and experimental results at Reynolds number 14 000 is shown in Table II. Therefore, Eqs. (11) and (12) are recommended for noncoplanar nonconcentric blockages in bundles.

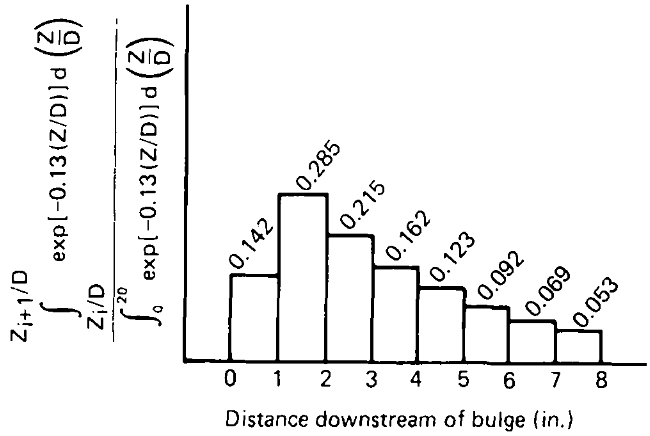

Fig. 9. Axial pressure loss coefficient distribution.

CONCLUSION

1. Moody's friction factor can be used in the subchannel analysis for the calculation of wall shear pressure drop in unblocked bundles over a wide Reynolds number range when the pitch-to-diameter ratio is not far from 1.3 as a first approximation. The larger the bundle the better the approximation will be.

2. The correlation of Rehme for the pressure drop over grid spacers has been corrected by an additional 40% for grids with sharp leading edges. The correlation has also been extended to the low Reynolds number flow.

3. For a bundle with coplanar concentric blockage over the whole cross section, the equivalent loss coefficient may be similarly evaluated as that of the grids, except that the geometry resembles the venturi instead of the orifice. Therefore the loss coefficient is lower.

4. For a bundle with coplanar concentric blockage over part of the bundle, some of the flow bypasses the blockage zone. The flow and pressure drop can be evaluated approximately, considering the whole bundle as two parallel channels, one of them blocked and the other unblocked.

5. For the bundle with noncoplanar concentric blockages, the pressure drop in the blockage zone can be calculated as the skin friction of an unblocked bundle, but with the surface area increased and flow area decreased due to the presence of blockages.

6. For bundles with noncoplanar nonconcentric blockages, the pressure loss coefficients can be considered as distributed resistance downstream of the bulge. The total loss coefficient of the bulge can be estimated in a way similar to the evaluation of grid loss coefficient.

7. These friction factor and loss coefficients can be used in a subchannel analysis of a blocked bundle. Local blockage ratio in each subchannel will be used. When the rods swell slowly, the instantaneous blockage ratio of each subchannel can be used for the quasi-steady process as a first approximation.

8. The present study is limited to single-phase hydraulics in deformed rod bundles. The research should be continued for two-phase nonequilibrium flow in bundles, which is also of great importance to reactor safety analysis.

NOMENCLATURE

A = flow cross section in the bundle

D = equivalent hydraulic diameter

f = friction factor

g = gravitational acceleration

k = form loss distribution function

K = form loss coefficient

L = axial length in the bundle

P = pressure of the bundle

Re = Reynolds number based on the bundle geometry

V = area-averaged axial velocity of the fluid

z = axial location measured from the maximum strain on a rod

Z = axial location, measured from the bundle entrance

Greek

ϵ = blockage ratio, defined as the projected cross-section area of the blockage divided by the original unblocked flow area

ρ = density of the fluid

Subscripts

b = bypass zone of a blocked bundle

B = blocked zone

Bp = overall bypassed blockage

g = grid spacer

gR = grid spacer correlation based on Rehme's correlation defined in Eq. (1)

o = original unblocked bundle

1 = axial location 1

2 = axial location 2

i = incremental axial location i

REFERENCES

1. A. N. DeSTORDEUR, "Drag Coefficients for Fuel-Element Spacers," *Nucleonics*, **19**, *6*, 74 (1961).

2. K. REHME, "Pressure Drop of Spacer Grids in Smooth and Roughened Rod Bundles," *Nucl. Technol.*, **31**, 314 (1977).

3. M. J. LOFTUS, L. E. HOCHREITER et al., "PWR FLECHT SEASET 21-Rod Bundle Flow Blockage Task Data and Analysis Report," NUREG/CR-2444, U.S. Nuclear Regulatory Commission (1982).

4. L. F. MOODY, "Friction Factors for Pipe Flow," *Trans. ASME*, **66**, *8*, 671 (1944).

5. J. MAREK, K. MAUBACK, and K. REHME, "Heat Transfer and Pressure Drop Performance of Rod Bundles Arranged in Square Arrays," *Int. J. Heat Mass Transfer*, **16**, 2215 (1973).

6. A. C. SPENGOS, "Tests on Models of Nuclear Reactor Elements IV, Model of Fuel Element Supports," UMRI-2431-4-P, University of Michigan (1959).

7. K. REHME, Institut für Neutronenphysik und Reaktortechnik, Kernforschungszentrum Karlsruhe, Private Communication (1981).

8. S. C. YAO, L. E. HOCHREITER, and W. J. LEECH, "Heat Transfer Augmentation in Rod Bundles Near Grid Spacers," *J. Heat Transfer, Trans. ASME*, **104**, *1*, 76 (1982).

AN IMPROVED MULTIDIMENSIONAL FINITE DIFFERENCE SCHEME FOR PREDICTING STRATIFIED HORIZONTAL PIPE FLOW

YASSIN A. HASSAN *Babcock & Wilcox Company*
Utility Power Generation Division, P.O. Box 1260
Lynchburg, Virginia 24505

JAMES G. RICE *University of Virginia*
Department of Mechanical & Aerospace Engineering
Charlottesville, Virginia 22903

JONG H. KIM *Electric Power Research Institute, Nuclear Power Division*
3412 Hillview Avenue, P.O. Box 10412, Palo Alto, California 94303

Received July 9, 1983
Accepted for Publication December 12, 1983

Numerical predictions of the three-dimensional temperature and velocity profiles of an experimental stratified horizontal pipe flow are performed. The experiment is one of a series of flow tests conducted at Argonne National Laboratory. A new accurate and stable skew-upwind differencing scheme is employed in the finite difference solution of the energy equation. The skew-upwind predictions are in excellent agreement with the experimental data as steady-state conditions are approached at the upstream test subsection. Comparisons between the conventional upwind and the skew-upwind schemes showed that the skew-upwind formulation provided a significant increase in the accuracy of temperature predictions.

INTRODUCTION

In many cases, the numerical procedures for two- and three-dimensional thermal and fluid mixing calculations often result in poor agreement with the experimental data.[1,2] In particular, the temperature predictions in stratified fluids are found to have large discrepancies with the experimental findings. These errors are due in large part to the common use of a one-sided upstream discretization, which may introduce nonphysical diffusion or numerical diffusion.[3]

Studies have shown that the artificial diffusion error has a deteriorating effect on the solution accuracy. Excessive numerical diffusion may obscure important physical processes. The artificial diffusion is most significant when the flow is skewed relative to the computational grid lines, and the absolute value of the mesh Peclet number, which is defined by

$$\mathrm{Pe} = \frac{V\Delta}{\Gamma} \ ,$$

(where V is the vector velocity, Δ is the mesh size in the direction of the velocity vector, and Γ is the effective diffusivity coefficient) exceeds the value of 2 (see Nomenclature on p. 461). This is certainly the case in most practical problems. One cure for this problem is to refine the grid until the finite difference discretization can be treated with a second-order accurate central difference approximation. This can be obviously prohibitively expensive if not precluded by computer time and storage limitations. The other alternative approach is to use a more accurate scheme than the conventional upwind approximation. The candidate formulation is the skew- or super-upwind differencing scheme.

The skew-upwind differencing scheme was originally developed by Raithby[4] and Lillington[5] separately. The scheme suffers from overshoot and undershoot instability difficulties in its original formulations. However, a new modified and more stable three-dimensional mass-weighted scheme has been developed and can be obtained from Refs. 6 and 7.

The purpose of this paper is twofold. First, a comparison is presented of predicted and measured results for an experimental thermally stratified flow in a horizontal pipe with a 90-deg elbow. The experiment is one of a series of stratified flow tests conducted at Argonne National Laboratory[8,9] (ANL). Second, a comparison is made between the temperature predictions using the conventional upwind and the skew-upwind schemes with the experimental data when a linear-downramp thermal transient (sudden reduction in inlet temperature) is superimposed on the constant inlet flow.

GOVERNING EQUATION AND NUMERICAL SCHEME

The transport equation for the convection-diffusion phenomena of a dependent variable ϕ in a three-dimensional Cartesian coordinate system can be cast in the following form[10]:

$$\frac{\partial}{\partial t}(\rho\phi) + \frac{\partial}{\partial x}(\rho u\phi) + \frac{\partial}{\partial y}(\rho v\phi) + \frac{\partial}{\partial z}(\rho w\phi) = \frac{\partial}{\partial x}\left(\Gamma\frac{\partial\phi}{\partial x}\right) + \frac{\partial}{\partial y}\left(\Gamma\frac{\partial\phi}{\partial y}\right) + \frac{\partial}{\partial z}\left(\Gamma\frac{\partial\phi}{\partial y}\right) + S \ , \quad (1)$$

where

Γ = diffusion coefficient

t = time

ρ = fluid density

u, v, w = velocity components in the x, y, and z directions, respectively.

The general variable ϕ can stand for a variety of different quantities, such as the mass fraction of a chemical species, the enthalpy or the temperature, a velocity component, or turbulent parameter as shown in Table I.

TABLE I

Types of Dependent Variable ϕ

Governing Equation	ϕ	Γ	S
x momentum	u	μ_{eff}	$-\frac{\partial P}{\partial x} + \rho g$
y momentum	v	μ_{eff}	$-\frac{\partial P}{\partial y}$
z momentum	w	μ_{eff}	$-\frac{\partial P}{\partial z}$
Energy	h	Γ_h	0
Continuity	1	0	0

In numerical fluid dynamics, the finite difference discretization is often derived by utilizing the control-volume approach. This can be accomplished by integrating the transport equation over the control volume. The common practice to approximate the convection terms at the cell surface is to use the upwind differencing scheme. As illustrated in Fig. 1, the value of the variable ϕ in the conventional upwind approximation at the west face is the upstream node value. This approximation can be represented by

$$\phi_w = \frac{1}{|u_w|}\{\phi_W[[u_w,0]] + \phi_P[[-u_w,0]]\} \ , \quad (2)$$

in which the symbol [[ ]] stands for the largest of the quantities contained within it. The skew-upwind scheme is aimed at reducing the error due to the streamline-to-grid skewness. In contrast to the pure-upwind scheme, the value of the dependent variable at the control volume surface is estimated by performing upwind differencing on the true streamline. Attention will be confined, for the purpose of describing the scheme, to the two-dimensional procedures. The surface-dependent value at the point w on the west face can be represented by the following compact equations:

$$\phi_w = \frac{\alpha_w}{|u_w|}[\phi_W[[u_w,0]] + \phi_P[[-u_w,0]]] + \frac{\beta_w}{|u_w|}[\phi_{SW}[[u_w,0]] + \phi_S[[-u_w,0]]] \ , \quad \text{if } V \geq 0 \quad (3)$$

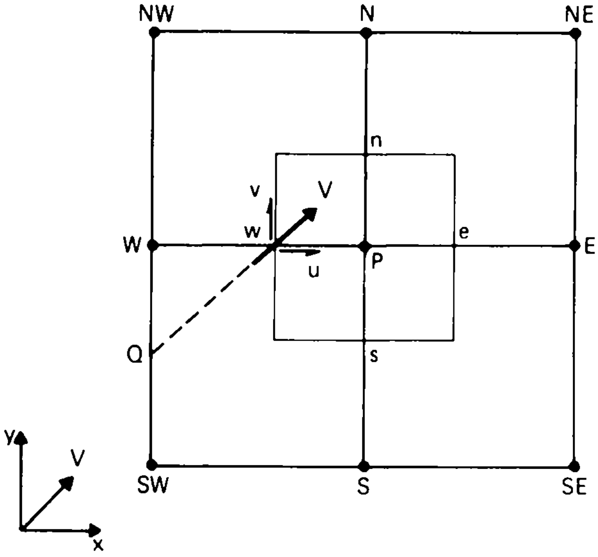

Fig. 1. Main volume arrangement.

and

$$\phi_w = \frac{\alpha_w}{|u_w|}\,[\phi_W[[u_w,0]] + \phi_P[[-u_w,0]]\,] + \frac{\beta_w}{|u_w|}\,[\phi_{NW}[[u_w,0]] + \phi_N[[-u_w,0]]\,] \ , \quad \text{if } \boldsymbol{V} < 0 \ , \tag{4}$$

where α_w and β_w are functions of the angle between the streamline and the grid line, and $\alpha_w + \beta_w = 1$. In two-dimensional situations, the scheme needs nine adjacent nodal points for the formulation as shown in Fig. 1. The formulation in three-dimensional situations is algebraically cumbersome since 27 adjacent nodal points are needed for the interpolation. In addition, two other weighting interpolation functions are introduced, e.g., γ_w and δ_w for the west face. Furthermore, the identity $\alpha_w + \beta_w + \gamma_w + \delta_w = 1$ holds.

Note that the skew-upwind scheme is only incorporated in the solution of the energy equation of the COMMIX-1A computer code[11] in the following analysis. The COMMIX-1A is a three-dimensional computer code developed by ANL. Numerical experimentation has shown that the numerical diffusion error is most significant in the energy equation in certain applications such as the mixing of hot and cold water in the cold leg and downcomer of a pressurized water reactor.[12]

THE MODEL AND TEST SIMULATION

A detailed description of the test can be obtained from Refs. 8 and 9. The horizontal stratified flow test section consists of two straight subsections with i.d. $D = 152.4$ mm (6 in.), connected by a 90-deg elbow with an i.d.-to-turning ratio of 0.5. The fluid enters the first horizontal section of length $L_1 = 7.47$ m, and turns through the 90-deg elbow to the other horizontal straight section of length $L_2 = 2.31$ m. The test section instrumentation consists of thermocouples to measure the temperature at various stations and dye-injection ports for flow visualization.

The COMMIX-1A computational model of the test section is depicted in Fig. 2. The model uses 1357 computational cells in three-dimensional Cartesian geometry over a nonuniformly distributed grid system, which corresponds to $I = 1$ to 7, $J = 1$ to 17, and $K = 1$ to 25. The subsections L_1, L_2, and the elbow are simulated using 717, 295, and 345 computational cells, respectively. The pipe circumference is modeled using irregular surface elements that combine to approximate the circular pipe cross section with a polygonal shape as shown in Fig. 3. The following assumptions are employed in this simulation:

1. The pipe wall is adiabatic.
2. The effective turbulent viscosity is taken as a constant value.
3. The fluid temperature is uniform over the inlet cross section.
4. The inlet velocity is uniform over the inlet cross section and throughout the whole transient.
5. The fluid exit boundary condition at subsection L_2 is treated as a continuative mass outflow boundary condition.[11]

RESULTS AND DISCUSSIONS

A selection of results for the simulation is presented in this section.

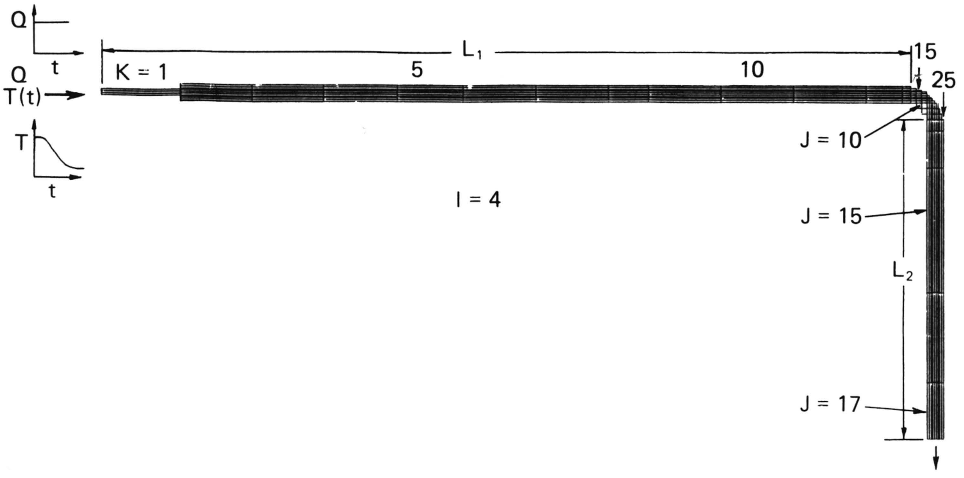

Fig. 2. The COMMIX-1A input model of stratified flow test facility.

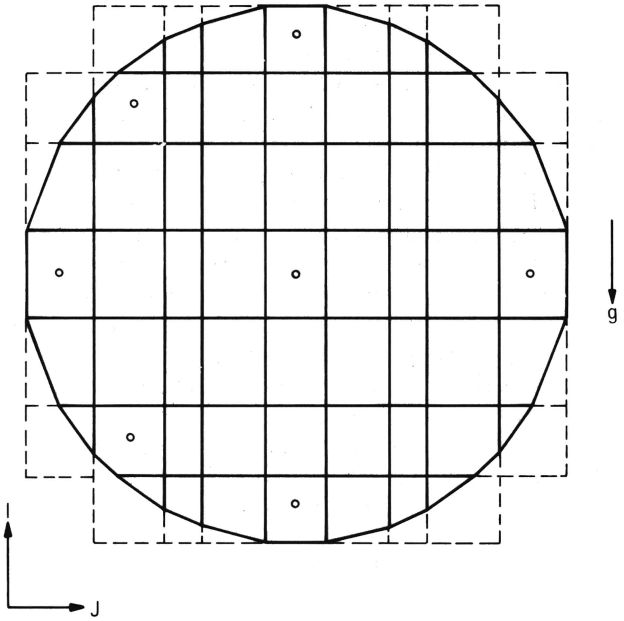

Fig. 3. Cross section of COMMIX-1A model.

Velocity Field Predictions

Prior to imposing an approximately linear thermal downramp on the constant flow at the test section inlet, the isothermal steady-state conditions are computed. Figures 4, 5, and 6 present the steady-state isothermal velocity profile at planes $I = 4$, 3, and 2, respectively. It is noteworthy that the flow field in the curved pipe differs greatly from that in the straight pipe. In a curved pipe, the centrifugal force of the fluid produces a cross-sectional pressure gradient. The faster moving fluid in the middle of the pipe at the core is shifted outward. The velocity distribution has a relatively gentle gradient as shown in Fig. 4, while in the thin "boundary layer" adjacent to the wall, the velocity distribution has a steep gradient. This behavior, predicted by COMMIX-1A, is typical of curved pipe velocity fields as observed by various investigators.[13,14]

Cross flow distributions for K partitions 10 and 12 upstream of the elbow are illustrated in Figs. 7 and 8, respectively. The secondary flow profiles downstream of the elbow are shown for $J = 14$ and 15 in Figs. 9 and 10, respectively. This secondary flow consists of a pair of distinguishable, classical counter-rotating helical vortices. The secondary flow pattern arises because of the centrifugal-induced gradient, drives the slower moving fluid near the wall inward, while the faster moving fluid in the core is swept outward. As shown in Fig. 8, the secondary flow begins to develop at partition $K = 12$ upstream of the elbow. This behavior is not unexpected since there is evidence that the influence of pipe curvature can propagate as many as 30 pipe diameters upstream of the onset of curvature.[15]

The effect of curvature is controlled by a characteristic Dean number, K, which is defined by[16]

$$K = \left(\frac{a}{R}\right)^{1/2} \mathrm{Re} \ , \tag{5}$$

where

a = pipe cross-sectional radius

R = radius of the curvature of the elbow

Re = Reynolds number.

The Dean number is the ratio of the square root of the product of the inertia and centrifugal forces to the viscous force. Since the secondary flow is induced by centrifugal forces and their interaction with viscous forces, K, is a good measure of the magnitude of the

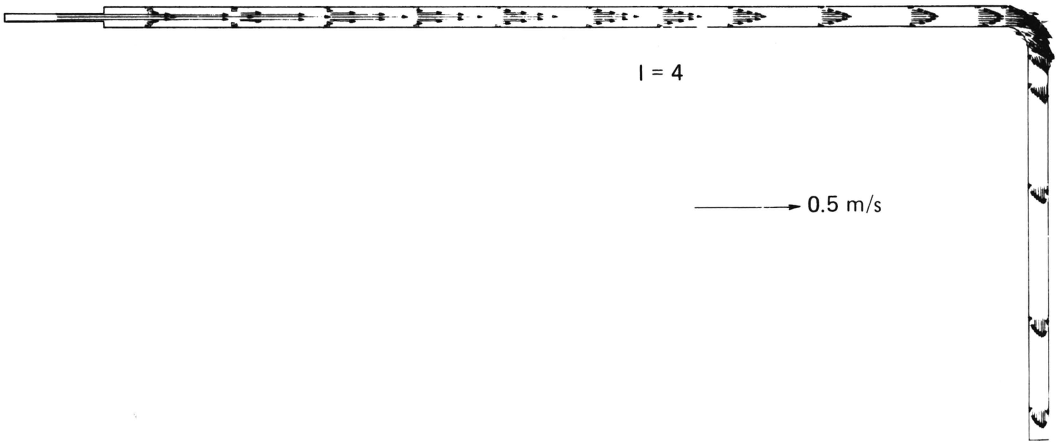

Fig. 4. Steady-state velocity profile at plane $I = 4$.

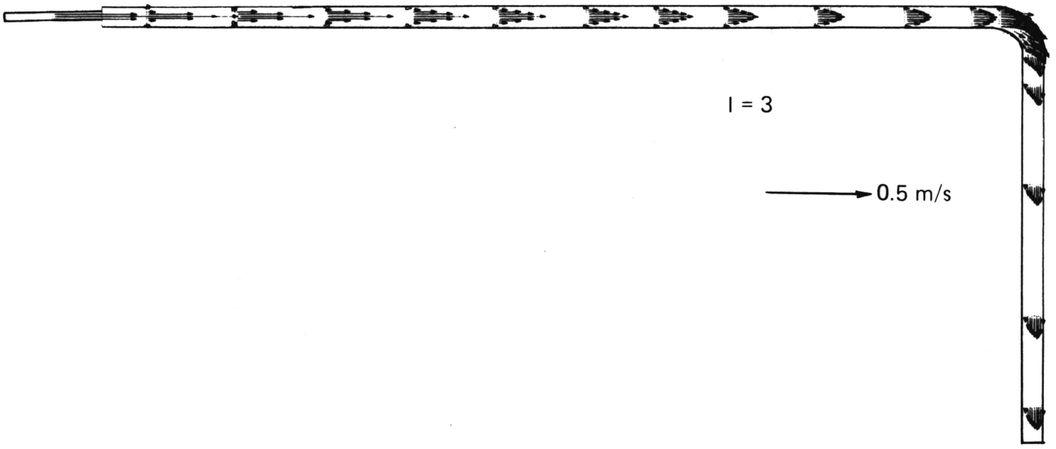

Fig. 5. Steady-state velocity profile at plane $I = 3$.

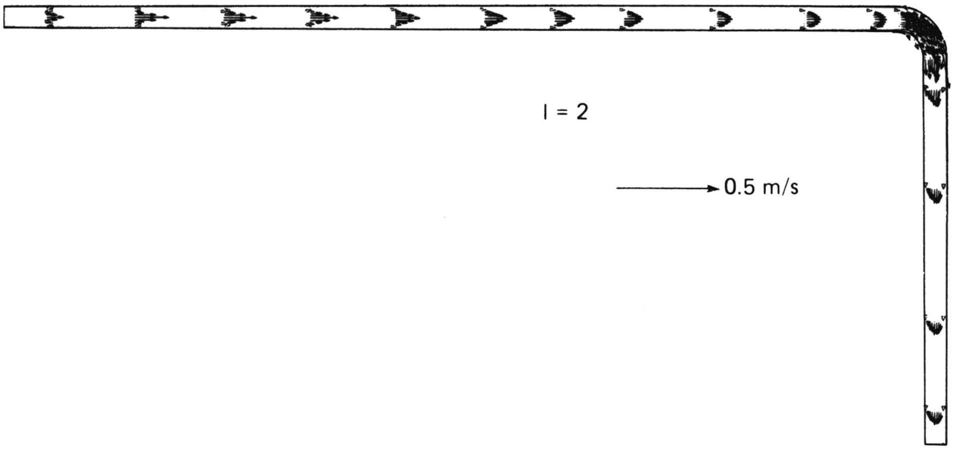

Fig. 6. Steady-state velocity profile at plane $I = 2$.

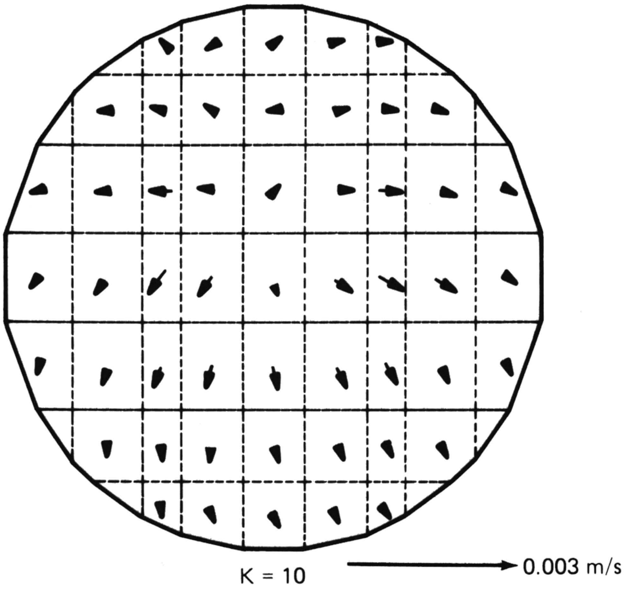

Fig. 7. Cross flow predictions at $K = 10$.

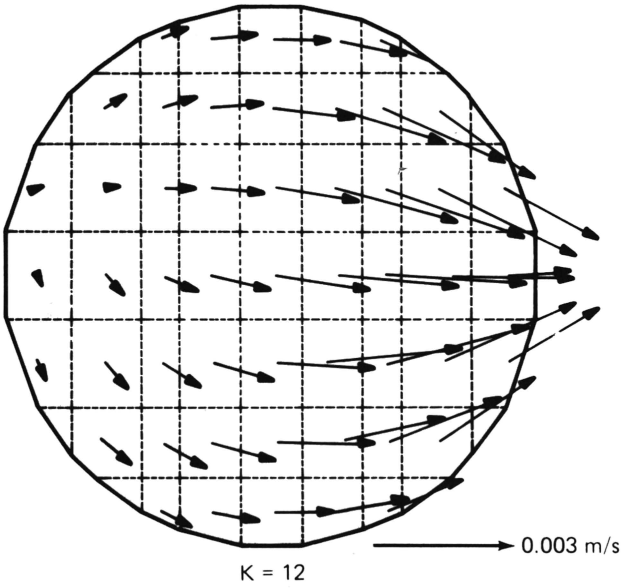

Fig. 8. Cross flow predictions at $K = 12$.

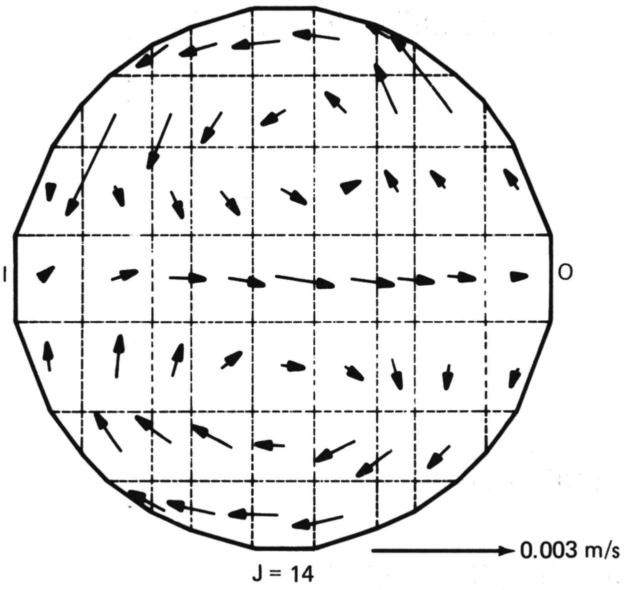

Fig. 9. Cross flow predictions at $J = 14$.

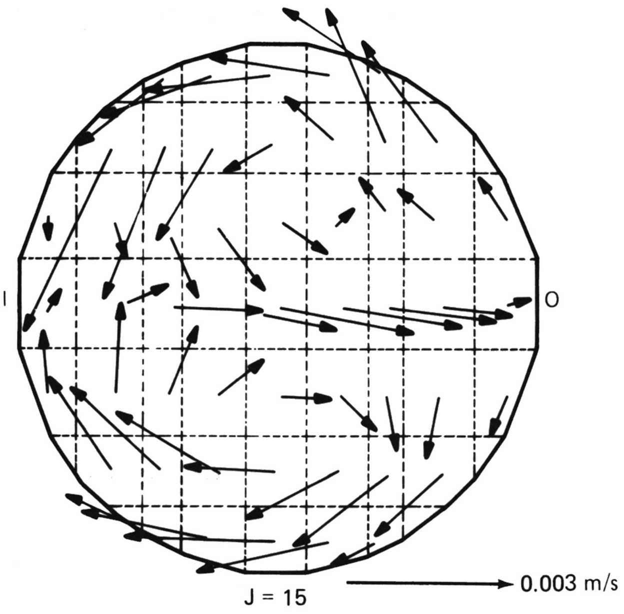

Fig. 10. Cross flow prediction at $J = 15$.

secondary flow. The Dean number for the subject experimental run was 12065. The COMMIX-1A predictions of the outward shift of the location of maximum axial fluid velocity and the secondary flow structure in the elbow are qualitatively consistent with the findings of other investigators.[13-15]

Figure 11 shows the velocity profiles at plane $J = 5$ for various transient times after the linear thermal downramp is superimposed on the constant pipe inlet flow. The cooler fluid entering the test section sinks toward the bottom of the pipe. This is due to the action of the gravity or the thermal buoyancy forces. As a result, the location of maximum velocity at the center of the pipe during the isothermal steady-state conditions shifts downward. Thus, the cooler incoming fluid accelerates along the bottom of the pipe, while the warmer fluid at the top is slowed. As the transient proceeds, the warm fluid at the top of the pipe stagnates and at 38.2 s undergoes a temporary flow reversal. The stagnation and flow reversal are also observed during the experimental course.

Temperature Predictions

Comparisons between the temperature predictions using the upwind and the skew-upwind finite difference schemes in the COMMIX-1A energy equation

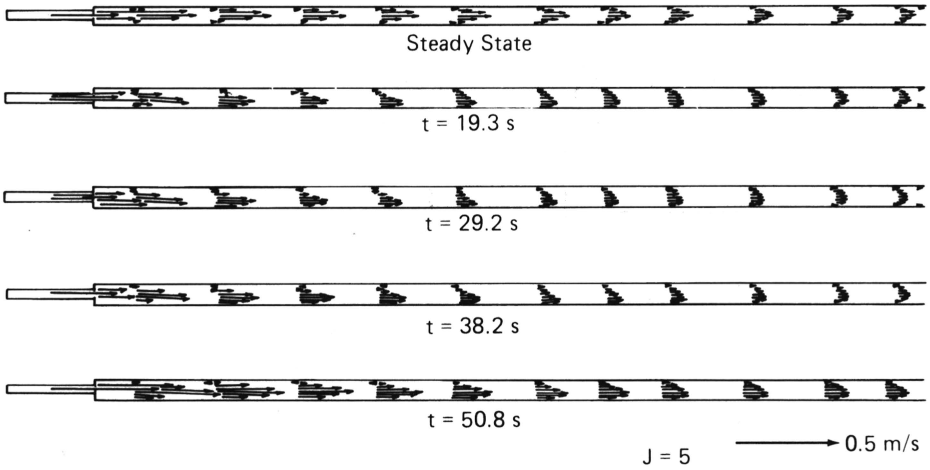

Fig. 11. Transient velocity profiles at plane $J = 5$.

and experimental data for station A are presented in Fig. 12. Good agreement is obtained with the experimental findings when the skew-upwind scheme is used. Moreover, it is found that the discrepancy between the conventional upwind and the skew-upwind solutions progressively increases as the transient time proceeds. It should be mentioned that the skew-upwind predictions are in excellent agreement with the experimental data when the steady conditions are approached.

Figure 13 depicts the comparison between the experimental data for station B, the conventional upwind and the skew-upwind finite difference solutions in the COMMIX-1A energy equation. Here again, better agreement with the data is obtained when the skew-upwind approximation is adopted. Note that neither the conventional upwind nor the skew-upwind scheme can predict the exact shape of the cold front at a transient time of ~10 s. This discrepancy may be due to two reasons: first, the large aspect ratio of the computational grid with a value of 68. Consequently, the use of a coarse streamwise grid resulted in a failure to adequately resolve the front of cold fluid passing the measurement point. This shortcoming can be alleviated by using a finer mesh displacement in the *z* direction. This solution may not be practical due to the increased computer storage requirements and run time. Second, since station B is downstream of station A, the temporal term error is compounded and the prediction of fluid temperature as the cold front passes is less accurate at station B than it was at station A. Once the cold front has passed and the temporal term in the energy equation has decayed, the results obtained using the skew-upwind scheme are in excellent agreement with the experimental data.

CONCLUSIONS

The isothermal steady-state velocity numerical predictions of the horizontal pipe flow with a 90-deg elbow are in qualitative agreement with the available experimental and numerical solutions. The secondary flow consists of a pair of counter-rotating helical vortices superimposed on the axial velocity downstream the elbow. The secondary flow pattern arises because of the centrifugal-induced gradient, and drives the slower moving fluid near the wall inward. The faster moving fluid in the core is swept outward. The transient velocity predictions show that the cooler fluid enters the test section and immediately sinks toward the bottom of the pipe. This is due to the action of gravity forces. As the transient proceeds, a reversal flow in the pipe is computed.

Comparison of the temperature predictions using the skew-upwind finite difference scheme in the energy equation is in excellent agreement with the experimental data when the steady-state conditions are approached. The pure-upwind scheme shows the effect of numerical diffusion. Note that neither the conventional upwind nor the skew-upwind scheme accurately captures the cold front at the early stage of the transient. This is due to the large streamwise diffusion introduced by the coarse-mesh spacing in the streamwise direction. More studies are needed to reduce this type of truncation errors.

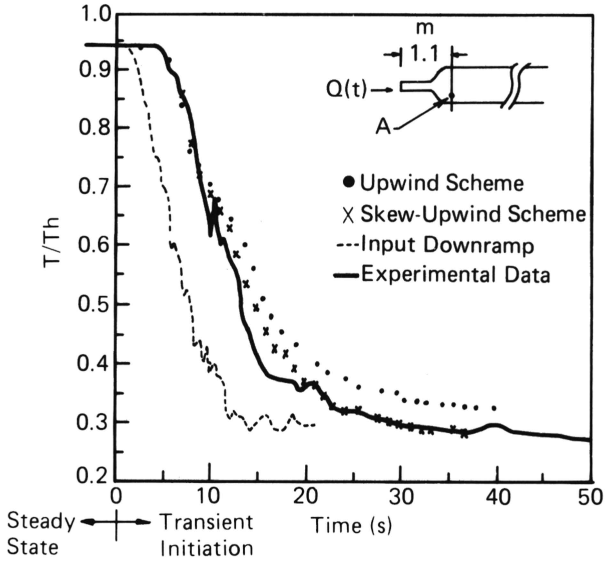

Fig. 12. Comparison between experimental data and predictions of the temperature at station A using the upwind and skew-upwind schemes.

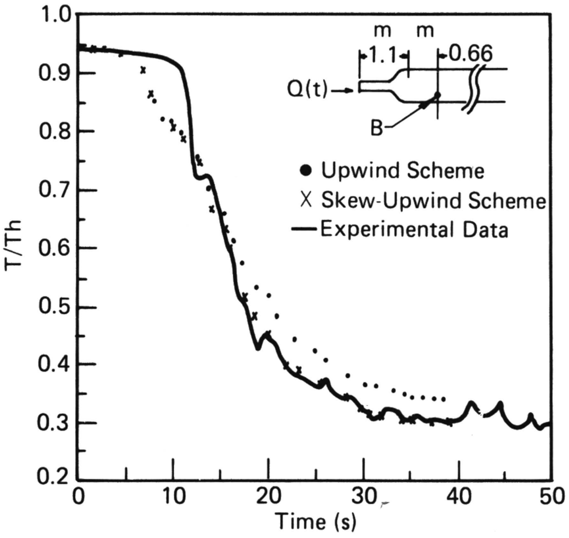

Fig. 13. Comparison between experimental data and predictions of the temperature at station B using the upwind and skew-upwind schemes.

NOMENCLATURE

a = pipe cross-sectional radius
D = pipe i.d.
g = gravitational acceleration
h = enthalpy
K = Dean number
p = pressure
P = main control volume
Pe = Peclet number
R = radius of the elbow curvature
Re = Reynolds number
S = source term, Eq. (1)
t = time
u, v, w = velocity components in the x, y, and z directions, respectively
V = total velocity vector
x, y, z = Cartesian coordinate system
$\alpha, \beta, \gamma, \delta$ = weighting interpolation functions
Γ = diffusion coefficient
ρ = fluid density
ϕ = dependent variable, Eq. (1)
Δ = mesh size
μ_{eff} = effective viscosity, Table I

Subscripts

P = main control volume
w = west fact
$W, \ldots NW, \ldots$ = denote neighbor nodes surrounding the main control volume P, Fig. 1

ACKNOWLEDGMENTS

The authors wish to acknowledge the technical contributions afforded to them by K. E. Kasza and T. M. Kuzay from ANL during the course of the present study.

This work is supported by the Electric Power Research Institute, Nuclear Power Division.

REFERENCES

1. B. P. LEONARD, "A Stable and Accurate Convective Modelling Procedure Based on Quadratic Upstream Interpolation," *Comput. Methods Appl. Mech. Eng.*, **19**, 59 (1979).

2. Y. A. HASSAN, J. H. KIM, and J. G. RICE, "Reduction of Numerical Diffusion Errors in Thermal Mixing Predictions," *Trans. Am. Nucl. Soc.*, **44**, 261 (1983).

3. P. J. ROACHE, *Computational Fluid Dynamics*, Hermosa, Albuquerque, New Mexico (1972).

4. G. D. RAITHBY, "Skew Upstream Differencing Schemes for Problems Involving Fluid Flow," *Comp. Meth. Appl. Mech. Eng.*, **9**, 153 (1976).

5. J. N. LILLINGTON, "A Vector Upstream Differencing Scheme for Problems in Fluid Flow Involving Significant Source Terms in Steady-State Linear Systems," *Int. J. Numer. Methods Fluids*, **1**, 3 (1981).

6. Y. A. HASSAN, J. G. RICE, and J. H. KIM, "A Stable Mass-Flow-Weighted Two-Dimensional Skew Upwind Scheme," *Num. Heat Transfer*, **6**, *4*, 395 (1983).

7. Y. A. HASSAN, J. G. RICE, and J. H. KIM, "A Stable Three-Dimensional Skew Upwind Scheme," submitted for publication in *Numer. Heat Transfer*.

8. K. E. KASZA and T. M. KUZAY, "The Influence of an Elbow on Horizontal Pipe Flow Thermal Stratification," *Trans. Am. Nucl. Soc.*, **43**, 780 (1982).

9. K. E. KASZA, J. P. BOBIS, and W. P. LAWRENCE, "Overview of Thermal-Transient-Induced Buoyancy Phenomena in Pipe and Heat Exchanger Flows," presented at 74th annual meeting of AICHE, New Orleans, 1981.

10. S. V. PATÁNKAR, *Numerical Heat Transfer and Fluid Flow*, McGraw-Hill Book Company, Inc., New York (1980).

11. W. T. SHA, H. M. DOMONUS, R. C. SCHMITT, J. J. ORAS, and E. I. H. LIN, "COMMIX-1A: A Three-Dimensional Transient Single-Phase Component Computer Program for Thermal-Hydraulic Analysis," NUREG/CR-0785, ANL-77-96, Argonne National Laboratory (Sep. 1978).

12. Y. A. HASSAN, J. G. RICE, and J. H. KIM, "Comparison of Measured and Predicted Thermal Mixing Tests Using Improved Finite Difference Technique," *Nucl. Eng. Design*, **76**, *2*, 153 (1983).

13. M. P. SINGH, "Entry Flow in a Curved Pipe," *J. Fluid Mech.*, **65**, Part 3, 517 (1974).

14. Z. ZAPRYANOR, Ch. CHRISTOV, and E. TOSHEV, "Fully Developed Laminar Flow and Heat Transfer in Curved Tubes," *Int. J. Heat Transfer*, **23**, 873 (1980).

15. H. ITO, "Friction Factors for Turbulent Flow in Curved Pipes," *J. Basic Eng.*, **81D**, 123 (1959).

16. H. SCHLICHTING, *Boundary-Layer Theory*, 7th ed., p. 626, McGraw-Hill Book Company, Inc. (1979).

COMPARATIVE STUDY OF MEASUREMENTS BY MEANS OF GAMMA THERMOMETER STRINGS WITH FISSION CHAMBER MEASUREMENTS

FISSION REACTORS

TECHNICAL NOTE

CHARLES HANTOUCHE *Electricité de France*
Direction des Etudes et Recherches, 6, quai Watier
F-78400 Chatou, France

Received July 2, 1983
Accepted for Publication November 28, 1983

A comparison of local linear power densities measured with a gamma thermometer string (GTS) and with a fission chamber shows important discrepancies at the extremities of the assembly. The cause was revealed by a simulation of axial power distribution. These discrepancies appear to arise from inaccurate knowledge of the axial position of the GTS in the assembly.

Using the method of fictitious displacement of a GTS, it was possible to reduce these discrepancies to <3.7%. One method of reducing this disadvantage could be to include the GTS in the fuel assemblies in the factory. By this way, it would be possible to eliminate passages for the string through the bottom of the core vessel.

INTRODUCTION

Up to now, the nuclear state of a pressurized water reactor has been followed by two types of instrumentation[1]:

1. movable internal instrumentation (fission chambers)
2. fixed external instrumentation (boron-deposit ionization chambers).

We have been working on a new type of detector, "gamma thermometer string" (GTS), which includes nine gamma thermometers on the length of the fuel assembly. The GTS is a fixed internal measurement instrument.[2,3] To assess its reliability, it is necessary to compare the values measured with it to those obtained from current measuring instruments.

Boron-deposit ionization chambers permit continuous followup of the axial offset of the overall power in the core, while fission chambers give a precise picture of the local linear power density (of one assembly) in the core. Since a GTS measures local linear power density, the comparison can only be between the values measured by a GTS and a movable fission chamber in an assembly. At present, three reactors (BUGEY 5, TRICASTIN 2, and TRICASTIN 3) are equipped with these two types of detectors.

EXPERIMENTAL COMPARISON

The g values given by a GTS are converted in units of linear power density (in watts per centimetre) by the SERIN calculation code.[a] The values measured by a fission chamber are converted into the same power units by the CAMARET calculation code.[b]

The GTS axial position (and, consequently, the location of the nine gamma thermometers) is evaluated in terms of expansion parameters in the core; the fission chamber can be located exactly when it is passing in front of the assembly grids.

Thus, the nine measurements given by the nine gamma thermometers at estimated axial positions, correspond to nine measurements made by a fission chamber for the same axial positions. Tables I, II, and III and Fig. 1 summarize the results of our comparisons for three GTSs placed in three different assemblies of the three reactors mentioned above.

The discrepancies ϵ are calculated in percent as follows:

$$\epsilon(\%) = \frac{P_c - P_t}{P_c} \times 100 \ ,$$

where

P_t = average local linear power density measured with a gamma thermometer[4]

P_c = average local linear power density measured with the fission chamber.

Conclusion

On the one hand, one observes that for these three cases the GTS, in the axial positions indicated, underestimates the average linear power density at the bottom of the core and overestimates it at the top. On the other hand, it is known

---

[a] A calculation code developed by the Electricité de France (EDF) Studies and Research Division.

[b] A code developed by the EDF Equipment Division.

TABLE I

Measurements of Local Linear Power Density in the D5 Assembly of BUGEY Unit 5

Calculated Axial Positions (m)	Values Measured by the Gamma Thermometers, P_t (W/m)	Values Measured by the Fission Chamber, P_c (W/m)	Discrepancy, ϵ (%)
0.456	1.525	1.571	+3.0
0.840	1.937	1.970	+1.7
1.230	2.044	2.003	-2.0
1.616	2.104	2.100	-0.2
2.001	2.118	2.044	-3.5
2.388	1.926	1.912	-0.7
2.775	1.996	1.930	-3.4
3.162	1.674	1.652	-1.3
3.550	1.079	1.050	-2.8

TABLE II

Measurements of Local Linear Power Density in the G14 Assembly of TRICASTIN Unit 2

Calculated Axial Positions (m)	Values Measured by the Gamma Thermometers, P_t (W/m)	Values Measured by the Fission Chamber, P_c (W/m)	Discrepancy, ϵ (%)
0.411	1.581	1.650	+4.2
0.805	2.007	1.951	2.9
1.200	2.101	2.070	-1.5
1.590	2.080	2.070	-0.5
1.979	2.035	1.989	-2.3
2.375	1.815	1.871	+3.0
2.763	1.917	1.850	3.6
3.161	1.751	1.741	0.6
3.548	1.242	1.150	-8.0

that there are fairly important power gradients at the extremities of fuel assemblies, while in the middle (fourth and fifth positions of the gamma thermometers) the power variation is small.

Thus, if the estimate of the axial position of a GTS is 1% away from its true position, the comparison (and consequently the reliability of gamma thermometers) is likely to be distorted, and there will be discrepancies of varying amounts, depending on the pattern of the axial distribution of power, between the values measured by the two instruments at the extremities of the assembly.

The axial position is presently calculated in terms of the expansion parameters of the GTS. An error of a few centimetres in 3.7 m (the active length of the core) is possible. A simulation of axial distribution of power is thus necessary to ascertain the effect of the discrepancies caused by errors in the axial position of a GTS on the measurements.

TABLE III

Measurements of Local Linear Power Density in the D7 Assembly of TRICASTIN Unit 3

Calculated Axial Positions (m)	Values Measured by the Gamma Thermometers, P_t (W/m)	Values Measured by the Fission Chamber, P_c (W/m)	Discrepancy, ϵ (%)
0.402	0.648	0.733	+11.6
0.789	1.033	1.075	+3.9
1.184	1.288	1.293	+0.4
1.573	1.417	1.430	+0.9
1.970	1.462	1.410	3.7
2.362	1.310	1.247	5.1
2.753	1.204	1.174	-2.6
3.151	0.940	0.920	-2.2
3.544	0.589	0.498	18.3

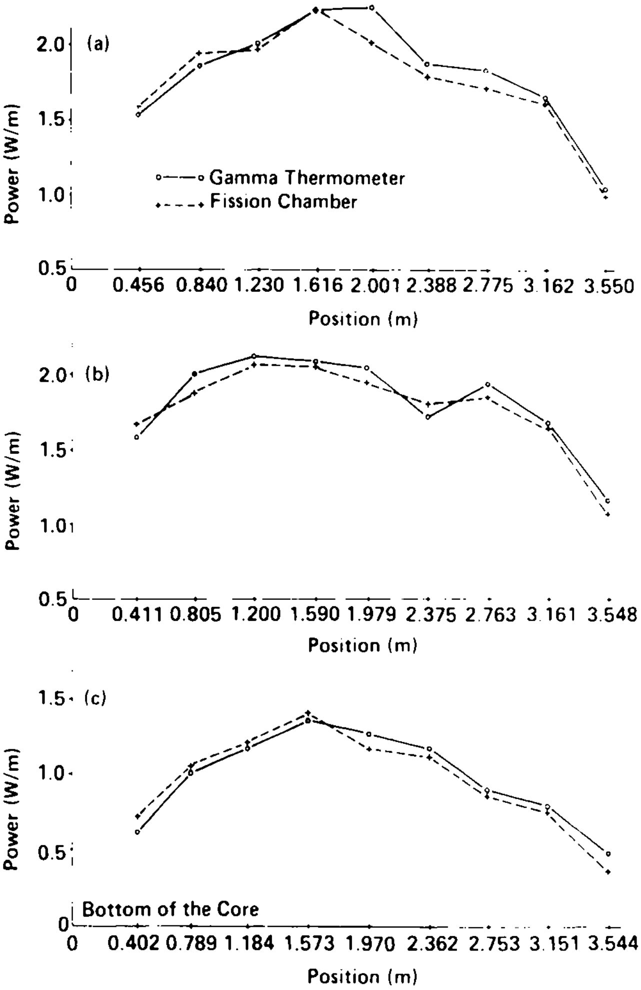

Fig. 1. Axial distribution of power in (a) the D5 assembly of BUGEY 5, (b) the G14 assembly of TRICASTIN 2, and (c) the D7 assembly of TRICASTIN 3, measured by GTS and fission chamber.

SIMULATION OF AXIAL POWER DISTRIBUTION

The conditions for this simulation are as follows:

1. The axial distribution is assumed to be perfectly sinusoidal.
2. The initial axial position of a GTS is assumed to be known (reference state).

Displacement of the string (and consequently of the nine gamma thermometers) upward or downward in the assembly simulates various possible cases of error in estimating the axial position. Table IV and Fig. 2 summarize the calculations for the different displacements made. They give the discrepancies for each gamma thermometer between the measurements without displacement and with displacements of the GTS.

We find that an error of ±1.25% in the axial position introduces a comparison error of ±10.5% in the measurements for the top of the core and of ±12% in those for the bottom of the core. The absolute values of the comparison discrepancy fall off toward the middle of the assembly.

Experimentally, we found the same orders of magnitude for the discrepancies between the *g* values measured by a GTS and those measured by a fission chamber (considered as the reference values).

From this it can be concluded that an error in estimating the axial position of a GTS even as small as 1 cm (0.25%) can introduce a comparison error of ~2.4% in the values given by the gamma thermometers at the extremities. This is why it is so important to know the axial position of a GTS to within a few millimetres.

METHOD USED FOR DETERMINING THE AXIAL POSITION OF A GTS

Our aim is to determine the real axial position of the GTS in the assembly. For this, we make nine measurements with the gamma thermometers and then we send the fission chamber to nine positions, supposedly those of the gamma thermometers, and make nine measurements. This gives us

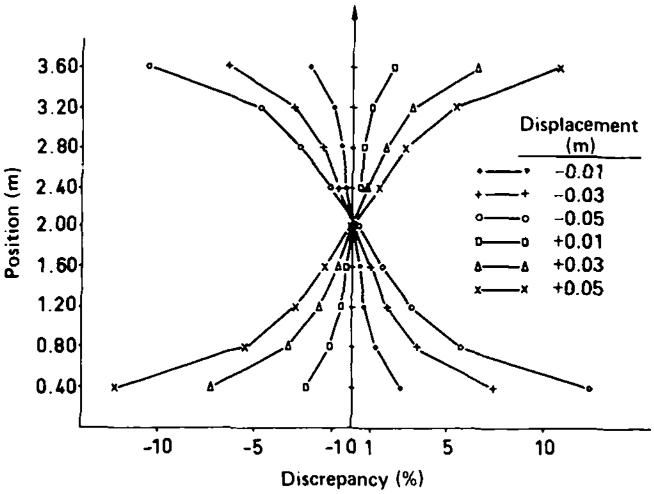

Fig. 2. Discrepancies for each gamma thermometer for different displacements.

TABLE IV

Discrepancies Calculated for Different Displacement

Fictitious Displacement (m)	Displacement Error Over 4 m (%)	Discrepancy First Gamma Thermometer (%)	Discrepancy Second Gamma Thermometer (%)	Discrepancy Third Gamma Thermometer (%)	Discrepancy Fourth Gamma Thermometer (%)
-0.01	-0.25	+2.4	+1.1	+0.6	+0.3
-0.03	-0.75	+7.2	+3.3	+1.8	+0.9
-0.05	-1.25	+12.1	+5.6	+3.0	+1.4
0	0	0	0	0	0
+0.01	+0.25	-2.4	-1.1	-0.6	-0.3
+0.03	+0.75	-7.2	-3.3	-1.7	-0.8
+0.05	+1.25	-12.0	-5.4	-2.9	-1.3

Fictitious Displacement (m)	Displacement Error Over 4 m (%)	Discrepancy Fifth Gamma Thermometer (%)	Discrepancy Sixth Gamma Thermometer (%)	Discrepancy Seventh Gamma Thermometer (%)	Discrepancy Eighth Gamma Thermometer (%)	Discrepancy Ninth Gamma Thermometer (%)
-0.01	-0.25	+0.02	-0.2	-0.5	-1.0	-2.1
-0.03	-0.75	+0.08	-0.7	-1.6	-3.0	-6.3
-0.05	-1.25	+0.20	-1.1	-2.6	-4.9	-10.4
0	0	0	0	0	0	0
+0.01	+0.25	-0.02	+0.2	+0.5	+1.0	+2.1
+0.03	+0.75	-0.03	+0.7	+1.6	+3.0	+6.3
+0.05	+1.25	-0.02	+1.2	+2.7	+5.1	+10.6

discrepancies that are positive or negative following the considered gamma thermometer but discrepancies that are correlated in the aggregate. As seen in the previous section, this may be interpreted by an error in the positions of the gamma thermometers.

Considering the results of this first set of measurements, we calculate a supposed error of position of the GTS (plus or minus a few centimetres) and for a second time send the movable fission chamber to nine new positions. For example, the calculations show that each gamma thermometer is −20 mm lower than theoretical, so we send the movable fission chamber to nine positions displaced of −20 mm in relation to the nine initial positions.

This new measurement gives us nine new discrepancies lower than the first. This process may be repeated until each discrepancy is lower than a few percent. This method has been applied to the three strings mentioned above. Figure 3 and Tables V, VI, and VII show the errors made for the axial positions of these strings.

Through this method, it is possible to reduce the discrepancies between all the respective values measured with the two instruments to <3.7%. The accuracy with which the new position is determined is ±2 mm, because the variation of the discrepancy is a trivial <2 mm of displacement.

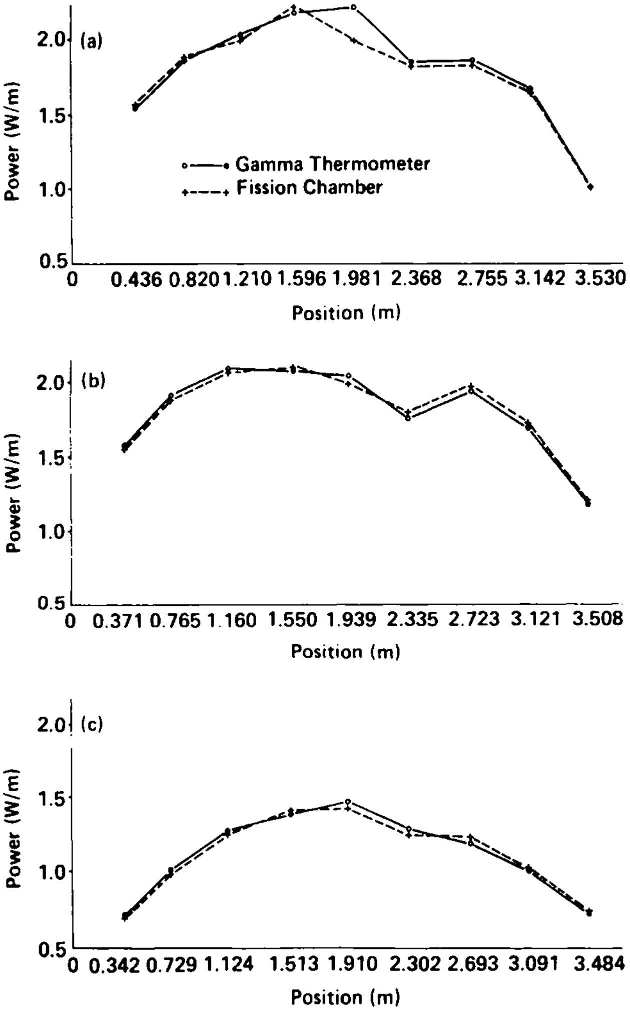

Fig. 3. Axial power distribution for (a) assembly D5 of BUGEY 5 with a fictitious displacement of 0.02 m (−0.5%), (b) assembly G14 of TRICASTIN 2 with a fictitious displacement of 0.04 m (−1.0%), and (c) assembly D7 TRICASTIN 3 with a fictitious displacement of 0.06 m (−1.5%).

Conclusion

This method can only be used when a reactor is instrumented with both types of detectors. Thus, for a reactor fitted with gamma strings only, it is not usable. It is therefore necessary to find a suitable solution for such cases.

SOLUTIONS FOR DETERMINING THE AXIAL POSITION OF A GTS

Because of the importance of the influence of the axial position of the gamma thermometer, it is necessary to find a method to accurately determine this position. Two types of solution can be envisaged:

1. *a posteriori* repositioning by nuclear measurements
    a. close to the grids[4]
    b. by moving the control rods.
    - Since the influence of the grids is small, the positioning accuracy will be low. This solution is therefore not suitable.
    - The solution using movement of the control rods is perfectly suitable when the GTS is associated with a rodded fuel assembly. Unfortunately this is not the case with all gamma strings.
2. *a priori* repositioning by factory inclusion of a GTS in a fuel assembly.

Setting to factory a GTS would appear to be a solution that should give very accurate information on the position of the various gamma thermometers in relation to the fuel. This

TABLE V

Measurements of Local Linear Power Density of the D5 Assembly at BUGEY 5 with a Fictitious Displacement of the GTS of 0.02 m (−0.5%)

Axial Positions Displaced (m)	Values Measured with the Gamma Thermometers, P_t (W/m)	Values Measured with the Fission Chamber, P_c (W/m)	Discrepancy, ϵ (%)
0.436	1.525	1.530	+0.3
0.820	1.930[a]	1.938	+0.4
1.210	2.044	2.034	−0.5
1.596	2.104	2.110	+0.3
1.981	2.118	2.044	−3.5
2.368	1.916[a]	1.902	−0.7
2.755	2.000[a]	1.992	−0.4
3.142	1.674	1.665	−0.5
3.530	1.079	1.090	+1.0

[a] Variation due to the nearness or remoteness of a grid from the horizontal plane of a gamma thermometer (Ref. 4).

TABLE VI

Measurements of Local Linear Power Density of the G14 Assembly at TRICASTIN 2 with a Fictitious Displacement of the GTS of 0.04 m (−1.0%)

Axial Positions Displaced (m)	Values Measured with the Gamma Thermometers, P_t (W/m)	Values Measured with the Fission Chamber, P_c (W/m)	Discrepancy, ϵ (%)
0.371	1.581	1.574	−0.4
0.765	1.930	1.920	−0.5
1.160	2.105	2.101	−0.2
1.550	2.081	2.085	+0.2
1.939	2.030[a]	1.995	−1.8
2.335	1.761[a]	1.771	+0.6
2.723	1.898[a]	1.892	−0.3
3.121	1.751	1.760	+0.5
3.508	1.242	1.240	−0.2

[a] Variation due to the nearness or remoteness of a grid from the horizontal plane of a gamma thermometer (Ref. 4).

TABLE VII

Measurements of Local Linear Power Density of the D7 Assembly at TRICASTIN 3 with a Fictitious Displacement of the GTS of 0.06 m (−1.5%)

Axial Positions Displaced (m)	Values Measured with the Gamma Thermometers, P_t (W/m)	Values Measured with the Fission Chamber, P_c (W/m)	Discrepancy, ϵ (%)
0.342	0.648	0.645	−0.5
0.729	1.025[a]	1.021	−0.4
1.124	1.306	1.300	−0.5
1.513	1.417	1.421	+0.3
1.910	1.450[a]	1.424	−1.8
2.302	1.300[a]	1.291	−0.7
2.693	1.235[a]	1.240	+0.4
3.091	0.940	0.950	+1.0
3.484	0.589	0.591	+0.3

[a] Variation due to the nearness or remoteness of a grid from the horizontal plane of a gamma thermometer (Ref. 4).

solution, which requires developments in connection technology, would also make it possible to eliminate passages through the bottom of the core vessel.

CONCLUSION

The difficulty found, at present, in determining the axial position of a GTS in an assembly may explain some discrepancies noted when comparing values measured by gamma thermometers with those measured by fission chambers. An error of 1% in the position can lead to comparison discrepancies from 3 to 18%, depending on the pattern of axial distribution.

Under these conditions, a fictitious displacement of the axial position of the GTS has made it possible to reduce to <3.7% the difference between the measurements made with the two instruments.

In cases where a core is instrumented with gamma strings only, it is not possible to reposition the strings using the fission chambers; to get over this problem it would be possible to include the GTS in the fuel assembly during manufacture, which would also offer the advantage of eliminating the passages through the bottom of the core vessel.

REFERENCES

1. "Instrumentation du réacteur," DPT-SPT No. 323, Electricité de France (1977).

2. M. BARBET and M. GUILLERY, "A New Advanced Fixed In-Core Instrumentation for a PWR Reactor," *Nucl. Instrum. Methods*, **185**, 377 (1981).

3. P. GUILLERY, G. BERAUD, and M. BARBET, "Le thermomètre gamma, nouvelle instrumentation fixe pour la mesure de la puissance locale d'un réacteur PWR," SM-265/63, International Atomic Energy Agency (1982).

4. C. HANTOUCHE, "La constitution de la densité d'échauffement d'un thermomètre γ," to be published in *Nucl. Instrum. Methods* (1983).

BOOK REVIEWS

Selection of books for review is based on the editor's opinions regarding possible reader interest and on the availability of the book to the editor. Occasional selections may include books on topics somewhat peripheral to the subject matter ordinarily considered acceptable.

Neutron Radiography, Proceedings of the First World Conference, San Diego, California, December 7-10, 1981

Editors	John P. Barton and Peter von der Hardt
Publisher	D. Reidel Publishing Company, Hingham, Massachusetts (1983)
Pages	1073
Price	$136.00
Reviewer	Raymond L. Murray

It has been suggested that the applications of radiation and radioisotopes might someday be more important economically than nuclear power. This book tends to support that thesis, at least in the case of neutron radiography, which appears to be well and prospering. It is being applied in many interesting and beneficial ways, ranging from the study of seed germination and root growth in the soil to the observation of a running gas turbine engine at Rolls-Royce, with a great deal of bread-and-butter work in nuclear fuel inspection. Although the principle has been known for several decades, the application has grown rapidly in only the last few years.

A good conference proceedings starts with an elementary review of the subject, including historical background. This allows the reader to determine the degree of his interest in the topic, to gain a smattering of knowledge, or to learn enough to be able to read the papers profitably. This book admirably meets those criteria by providing several introductory papers by authorities in the field, including the two editors of the volume.

We learn from the book that neutron radiography is related to ordinary photon radiography as neutron diffraction is to x-ray diffraction. It is the wave property of particles that is exploited to reveal new and different aspects of the interior of the medium through which the neutrons pass. The scattering of neutrons in hydrogenous materials or absorption in certain isotopes gives a different view than the interaction of photons with heavy elements. As discussed in the book, the principal neutron sources are nuclear reactors, accelerators of deuterons, and radioisotopes, such as ^{124}Sb, ^{241}Am, ^{242}Cm, and especially ^{252}Cf. Neutrons of several energies may be used—"cold," thermal, epithermal or resonance, and fast—each having special virtues in applications. The image detectors incorporate strong neutron absorbers, such as (a) boron, which yields alpha particles that activate phosphors, or (b) gadolinium, which releases gamma rays that produce electrons by internal conversion. An alternative is the track-etch method, using alpha particles or fission fragments to cause damage in nitrocellulose films. This technique has the advantage of being insensitive to gamma rays (as from irradiated nuclear fuel) and ordinary light.

The proceedings consist of a total of 140 papers from 80 centers in 20 countries. The papers are generally brief and are grouped into 13 parts. Among these are: experiences at laboratories around the world; fuel inspection studies, biological applications; and real-time studies. A workshop was held at the end of the conference, with sessions discussing standards for the general industry and the nuclear industry.

Neutron radiography is routinely applied to the inspection of both new fuel and spent fuel. It can detect defects in fresh fuel, such as variations in size or enrichment, and can provide details in irradiated fuel on internal cracking or melting and on hydriding or failure of cladding. It is widely used in industry in conjunction with ordinary x rays to provide complementary views of an opaque object. Displayed in the proceedings are a number of contrasting photographs made by the two methods. One dramatic example is an explosive bolt used in the Apollo space program. The bolt contains plastic, glass, metal, and explosive compounds, each of which reacts differently to x rays and neutrons. Neutrons are also beginning to be used for computerized axial tomography ("CAT scans") for inanimate objects, such as nuclear fuel. It appears that the fast neutron dose is too high for the radiography of living human beings.

The proceedings appear to be a valuable contribution to the literature in several ways—(a) as a record of a historical event, the first international conference on the subject, (b) as a compendium of information on uses, techniques, and problems, (c) as a source of useful theoretical methods, both analytic and Monte Carlo, and (d) as a bibliographic source, with special value in providing names of organizations and people throughout the world that are working in the field.

Many different type styles and formats are represented in the book, since it was prepared by photographing the authors' contributed papers. Although not as attractive as some proceedings, these contain the important information, and thus the heterogeneity is acceptable. However, use of the book would have been enhanced by including a subject index, admittedly an additional onerous chore for the editors.

Some of the interesting applications one finds by scanning the volume are:

1. study of hydrogen absorption by palladium
2. determination of aluminum corrosion in aircraft structures
3. nondestructive testing of complex laminated composites for flaws in the adhesives being used
4. control of the assembly of test reactor components
5. preparation of the burnup profiles of reactor control rods and blades
6. study of two-phase flow
7. investigation of bone tissue in animals.

The scope and variety of the applications reported in the proceedings suggest that there are many other applications waiting to be made by imaginative and enterprising researchers. In contrast with the situation in basic neutron and nuclear physics, which requires a high-flux reactor, it appears that an intermediate power research/training reactor in the 5- to 250-kW range is adequate to do many valuable studies in neutron radiography.

The cost of the book is prohibitive for many individual readers, and even a university departmental library would think twice before buying it. Science historians tell us that Gutenberg invented the printing press to eliminate the high cost of books that were copied by hand, sometimes as much as a half-year's income to a professional to acquire a large reference book. The modern era needs a similar breakthrough. Perhaps the computer will soon serve that function by providing convenient and inexpensive access to needed information.

Dr. Raymond L. Murray received his first degree in science education at the University of Nebraska, where he also took a master's degree in physics. His doctorate was from the University of Tennessee. During World War II, he contributed to uranium isotope separation research and production at Berkeley and Oak Ridge. He has been a faculty member at North Carolina State University since 1950, assisting in the establishment of the first nuclear engineering curriculum and the first university nuclear reactor. He served as Burlington Professor of Physics, as head of the nuclear engineering department for 11 years, and currently is Professor Emeritus. He has published a number of research papers on reactor theory and design analysis, has written textbooks in nuclear engineering and basic physics, and serves as a consultant to industry on reactor design and nuclear safety. He has been a member and chairman of the North Carolina Radiation Protection Commission. His current studies involve nuclear reactor analysis related to the Three Mile Island-2 recovery and to uranium resource extension, the application of microcomputers to nuclear problems, and public information on nuclear energy, especially radioactive waste management.

Irradiation Technology

Editors	Peter von der Hardt and Heinz Röttger
Publisher	D. Reidel Publishing Company, Hingham, Massachusetts (1983)
Pages	759
Price	$100.00
Reviewer	K. Linga Murty

This book is a collection of papers presented at the International Topical Meeting at Grenoble, France, September 28-30, 1982, with the main theme of in-pile testing. These conference proceedings concentrated on thermal reactor experiments, while the earlier American Nuclear Society conference held in Salt Lake City, Utah, in April 1982, emphasized fast and fusion reactor experiments. The papers contained information on various aspects of nuclear reactor instrumentation, facilities available throughout the world for radiation experiments, as well as some typical in-pile test results on fuel, structural, and other materials. Since the main thrust of the proceedings is on irradiation testing—facilities, techniques, etc.—very few results are presented. Thus, some of the articles were quite general with descriptions of the available facilities, while others contained relatively more in-depth technical information. The book is divided into seven major sections: Light Water Reactors (Sessions I through IV), LWR Instrumentation (Session V), Fast Breeder Reactors (Session VI), Instrumentation (Session VII), Gas Cooled and Fast Breeder Reactors (Session VIII), Miscellaneous (Session IX), followed by papers presented in a poster session—a total of 110 papers. The majority of articles was from European countries and Japan; there are two papers from Canada and only one from the United States. A range of reactor-related topics including thermal-hydraulics, neutronics, and materials aspects were included in the proceedings, and thus this is an excellent book for people looking for facilities for irradiation testing. The book was excellently produced and often contains some detailed drawings of instrumentation as well. The disheartening aspect of the book is that there are many papers in German and French, albeit the majority of them are in English. It would have been better if at least the summaries or abstracts were printed in all three languages. Researchers in the nuclear reactor field will find the book very informative and useful. Some of the technical details are interesting and informative. I enjoyed reading, in particular, the varied experiences of nuclear reactor fuel following in-pile testing and the different techniques and approaches of various organizations. Distinctly absent in the papers are studies on nuclear pressure vessel steels, perhaps since data on these are available through reactor surveillance capsule programs.

K. Linga Murty (MSc, physics, Andhra University, India, 1963; MS, 1967, and PhD, 1970, materials science and engineering, Cornell University) is an associate professor in the nuclear engineering and materials engineering departments at North Carolina State University, Raleigh, and has been involved in research on the effects of aggressive environment and neutron exposure on the mechanical properties and fracture characteristics of metals. He has been actively pursuing research on creep and mechanical anisotropy of Zircaloy and embrittlement of nuclear pressure vessel steels. He is currently involved in studies on synergistic effects of dynamic strain-aging and neutron-induced defects on properties of steel, and on the improvement of mechanical properties of metals through laser surface treatment and ion implantation.

AUTHOR INDEX

nuclear technology®

Volume 65, Numbers 1 through 3
April, May, and June 1984

CITATIONS ARE BY PAGE NUMBER
*DENOTES BOOK REVIEWER

SUBJECT INDEX

nuclear technology®

Volume 65, Numbers 1 through 3
April, May, and June 1984

CITATIONS ARE BY PAGE NUMBER AND ISSUE

BOOK REVIEW INDEX

ENS European Nuclear Society nuclear technology®

Volume 65, Numbers 1 through 3
April, May, and June 1984

CITATIONS ARE BY PAGE NUMBER

Author	*Title*	
Barton, John P., and Peter von der Hardt, Eds.	Neutron Radiography	467
Burke, J. J., R. Mehrabian, and V. Weiss, Eds.	Advances in Metal Processing	354
Chicken, John C.	Nuclear Power Hazard Control Policy	170
Clerman, Robert J., Rajani Joglekar, Robert P. Ouellette, and Paul N. Cheremisinoff	Biotechnology and Energy Use (Electrotechnology Series, Vol. 8)	169
Foner, Simon, and Brian B. Schwartz, Eds.	Superconductor Materials Science (Metallurgy, Fabrication and Applications), Series B: Physics	169
Grathwohl, Manfred	World Energy Supply	356
Lewins, Jeffery, and Martin Becker, Eds.	Advances in Nuclear Science and Technology—Vol. 14, Sensitivity and Uncertainty Analysis of Reactor Performance Parameters	355
Nichols, R. W., Ed.	Advances in Non-Destructive Examination for Structural Integrity	356
Plesset, Milton S., Novak Zuber, and Ivan Catton, Eds.	Transient Two-Phase Flow	357
Reed, C. B.	The Coal Era in the United States: A Study of Our Viable Alternatives	168
Stamm'ler, R., and M. J. Abbate	Methods of Steady-State Reactor Physics in Nuclear Design	358
Taborek, J., G. F. Hewitt, and N. Afgan	Heat Exchangers—Theory and Practice	170
von der Hardt, Peter, and Heinz Rottger, Eds.	Irradiation Technology	468